



**University of
Nottingham**

UK | CHINA | MALAYSIA

**Developing a Novel Sensor Technology
for Detecting Neural Activity Based
on Surface Plasmon Resonance**

by Carmel Howe

A thesis submitted to the University of Nottingham
for the degree of Doctor of Philosophy

March 2018

ABSTRACT

One of the main goals of contemporary systems neuroscience is to understand how sensory inputs are processed, networks are formed and the resulting functional outputs. To achieve this, a recording technique is required that can detect action potentials with single-cell resolution for a long period of time across a large network. Current imaging techniques available are limited in at least one of the four elements needed to fulfil this aim (a) the technique needs to be able to detect every action potential (b) from every neuron (c) for a long period of time (d) from an entire network. Neural activity has been shown to produce fast intrinsic optical signals that are the result of refractive index changes causing light scattering and birefringence associated with membrane depolarisation. To date no one has successfully managed to exploit these intrinsic optical signals in a practical robust recording system. Surface plasmon resonance (SPR) is a technique that can detect extremely small changes in refractive index and is capable of detecting this membrane localised refractive index change with a high spatio-temporal resolution. This thesis describes the design and development of an imaging system based on surface plasmon resonance to detect the refractive index change of a cell membrane during neural activity.

This thesis, first theoretically examines the different processes that occur during neural activity that could affect the resulting SPR response. The change in refractive index and therefore, light intensity was calculated considering the reorientation of

dipoles and ion flux during an action potential.

The theoretical light intensity changes are very small so consideration, measurement, quantification, and minimisation of noise sources, along with application of signal detection theory, were explored.

The planar gold surfaces required to produce surface plasmon resonances were characterised and the imaging system was shown to be sensitive enough to detect these small refractive index changes. There were no visible light intensity changes after recording the optical response from one action potential. This led to the development of the experimental protocol and a data analysis tool was developed to align and average over a number of action potentials to reduce the noise floor as much as possible and increase the signal-to-noise ratio. Unfortunately, it was determined to a high degree of certainty that no action potentials were detected by the planar gold SPR sensors. It was hypothesised the SPR signal from these cell membrane localised refractive index changes was averaged across the relatively large surface area of the planar gold sensor which was why no response was detected.

A novel sensor design was investigated by reducing the gold sensor size to that of one cell to improve coupling or isolation of the plasmons to a single cell.

SPR at planar metal/dielectric interfaces and localised SPR for metal nanoparticles have both been extensively studied, but it is less clear what happens to the optical properties at the micrometer scale. Gold patterns of different sizes in the micrometer range were therefore, produced using photolithography. Typical SPR responses were observed for all gold microstructures, however, as expected they were not as sensitive and were wider than that of the planar gold controls. This phenomenon became more pronounced as the length of the gold structure decreases, as expected because of the spatial constriction of the propagating surface plasmon. Although the sensitivity of the micron-sized gold surfaces was less than that of the planar gold surface, with the latter unable to detect these refractive index changes. The process still suggested that the SPR technique could be successfully implemented to detect individual action potentials. Reducing the sensor size to that of one cell could improve coupling and stop the signal being averaged across the sensor. Unfortunately, it was determined to a high degree of certainty that no action potentials were detected by the gold microstructure SPR sensors.

Declaration of Authorship

I, Carmel Leah Howe, declare that this thesis titled, "Developing a Novel Sensor Technology for Detecting Neural Activity Based on Surface Plasmon Resonance" and the work presented in it are my own. I confirm that:

- This work was done wholly or mainly while in candidature for a research degree at this University.
- Where any part of this thesis has previously been submitted for a degree or any other qualification at this University or any other institution, this has been clearly stated.
- Where I have consulted the published work of others, this is always clearly attributed.
- Where I have quoted from the work of others, the source is always given. With the exception of such quotations, this thesis is entirely my own work.
- I have acknowledged all main sources of help.
- Where the thesis is based on work done by myself jointly with others, I have made clear exactly what was done by others and what I have contributed myself.

Signed:

Date:

Publications arising from this PhD:

- Carmel L. Howe, T. M. Fromhold, Noah A. Russell, “Surface plasmon resonance on gold microstructures”, Proc. SPIE 10509, Plasmonics in Biology and Medicine XV, 105090R (23 February 2018); doi: 10.1117/12.2300953

Publications in preparation:

- Carmel L. Howe, Sidahmed A. Abayzeed, Kevin F. Webb, Noah A. Russell, “Surface plasmon resonance imaging of excitable cells”
- Carmel L. Howe, Kevin F. Webb, T. M. Fromhold, Noah A. Russell, “Functional imaging of primary hippocampal rat neurons using surface plasmon resonance”

ACKNOWLEDGEMENTS

First and foremost I would like to thank my supervisors Dr. Noah Russell and Professor Mark Fromhold for their support and encouragement, both scientific and personal. I really appreciate the opportunities I have been given.

I would like to thank my friends and colleagues, past and present from the lab, especially to Chris Towlson for being the best post-doc in existence and for all the electrophysiology jokes. Thank you to Dhruma Thakker for training me in the cell culture techniques, and to Nitzan Herzog and Hala Dhowre for helping me out in times of need. Thank you Jamie Williams for keeping me sane, and to Alexander Johnstone, Sebastiaan Van Nuffel, Rob Clay, Houda Sahaf, Solomon Idinyang, Benjamin Paul and everyone else for the assistance and chats these past years.

My sincere thanks go to Sidahmed Abayzeed, whose advice regarding the SPR instrumentation and theory has proved extremely valuable.

Massive thanks to everyone in the Physics clean room facility, including Jaspinder Chauhan, Dave Taylor, and Chris Mellor for all the help and advice regarding the microstructures, and who provided me with access to their laboratories and facilities.

Last but not least, I would like to send massive thanks to all my family and friends. Luca, you are amazing and have been my rock. I cannot thank you enough. My

Eurotrippers; Edd, James, Stefan, and Michelle. Thank you for all the weekend trips to Europe. Pete and Sally thank you for the support. Thank you to my family, Mum, Ade, Lucas, Lola, Ziggy, and Missy.

I would also like to acknowledge the contribution of the IMechE Whitworth Senior Scholarship Award and the Engineering and Physical Science Research Council in supporting this research.

CONTENTS

Abstract	i
Declaration	iii
Acknowledgements	v
List of Figures	xii
List of Tables	xviii
Glossary of Abbreviations	xx
Physical Constants	xxii
1 Introduction	1
1.1 Motivation	1
1.2 The Brain, Neurons and Action Potentials	2
1.2.1 Neurons	2
1.2.2 The Action Potential	3
1.3 Neural Activity Detection	6
1.3.1 Electrical Detection	7
1.3.2 Optical Detection	9

1.3.3	Comparison	13
1.4	Surface Plasmon Resonance	17
1.4.1	SPR Sensors	17
1.4.2	SPR Imaging	19
1.4.3	Beyond Extended Planes	22
1.5	Microscopy Fundamentals	26
1.6	Noise, Sources and Detectors	27
1.6.1	Measures of Noise in Signals	27
1.6.2	Types of Noise	28
1.6.3	Detectors	30
1.6.4	Detection of Signals in Noise	32
1.7	Aims and Objectives	36
1.7.1	Thesis Structure	37
2	Methods	39
2.1	Ethics	39
2.2	Materials, Equipment and Software	39
2.3	Substrate Preparation	39
2.3.1	Pre-Treatment	40
2.3.2	Silanisation	40
2.4	Planar Gold	40
2.4.1	Evaporation System	40
2.5	Fabrication of Microstructures	41
2.5.1	Photomask	41
2.5.2	Photolithography	41
2.6	Functionalisation of the Surface	42
2.6.1	AUT on Planar Gold	42
2.6.2	PEI on Microstructures	43
2.7	Cell Culture	43
2.7.1	Harvesting, Plating and Feeding	43
2.7.2	Live Dead Cell Viability	44
2.8	Surface Analysis	45
2.8.1	Ellipsometry	45
2.8.2	Profilometry	45

2.8.3	Microscopy	45
2.9	Imaging Systems	45
2.9.1	Measurement Conditions	45
2.9.2	Back Focal Plane	48
2.9.3	Total Internal Reflection Microscopy	49
2.9.4	Reflection and Transmission Microscopy	50
2.9.5	Surface Plasmon Resonance	50
2.10	Noise and Efficiency	51
2.11	Sensitivity Experiments	51
2.12	Electrophysiology	52
2.12.1	Electrophysiology Recordings	52
2.13	Validating SPR / Electrophysiology Experiments	53
2.13.1	Procedure	55
3	Detecting Neural Activity Using Surface Plasmon Resonance	58
3.1	Theory	59
3.1.1	Excitation of Surface Plasmons	66
3.2	SPR Response in a Multi-Layer System	76
3.2.1	Assumptions and Determination of Parameters	76
3.2.2	Solution of the N-layer model	79
3.3	Ion Flux During Action Potential	84
3.4	Chapter Conclusions	88
4	System Characterisation	90
4.1	Noise Measurements	91
4.1.1	Light Source Noise	91
4.1.2	Optical Efficiency	92
4.1.3	Detector Noise	94
4.1.4	Minimum Detectable Refractive Index Change	102
4.2	Temperature Dependence	106
4.3	Determination of the Angle of Incidence	106
4.4	Chapter Conclusions	112
5	Planar Gold Surfaces	116

CONTENTS

5.1	Planar Gold Characterisation	117
5.1.1	SPR Response	117
5.1.2	Sensitivity to Refractive Index Changes	121
5.2	Detection of Neural Activity	127
5.2.1	Triggering and Recording One Action Potential	128
5.2.2	Increasing the SNR	136
5.2.3	Planar Results	144
5.3	Chapter Conclusions	151
6	Microstructures	154
6.1	Photomask Design	155
6.1.1	Cell Morphology	155
6.1.2	Design	156
6.2	Optimisation of Photolithography Protocol	157
6.2.1	Reversal Bake Optimisation	158
6.2.2	Experimental Design	158
6.3	Microstructure Characterisation	162
6.3.1	Microscopy	162
6.3.2	Profilometry	164
6.3.3	SPR Response	164
6.3.4	Chemical and Mechanical Resistance	171
6.4	Microstructure Functionalisation	173
6.4.1	Cell Viability	173
6.4.2	Effect of PEI Layer on SPR Signal	177
6.5	Detection of Neural Activity	177
6.5.1	10 × 10 Microstructure	178
6.6	Chapter Conclusions	188
7	Discussions and Conclusions	192
7.1	Conclusions	201
7.2	Potential Future Work	202
	Bibliography	204
	Appendices	229

A	Supplementary Information for Chapter 2	230
A.1	Materials, Equipment and Software	230
A.1.1	Chemical, Solvents and Materials	230
A.1.2	SPM Components	233
A.1.3	Equipment	234
A.1.4	Software	235
A.2	Media and Solutions	235
A.3	Experimental Pipeline	236
B	Supplementary Information for Chapter 4	238
B.1	Specifications	238
B.1.1	EPIX Camera	238
B.2	Noise and Filters	239
C	Supplementary Information for Chapter 5	241
C.1	Figures	241
D	Supplementary Information for Chapter 6	248
D.1	Microfabrication Methodology	248
D.1.1	Gold Deposition onto Glass	248
D.1.2	Photolithography	249

LIST OF FIGURES

1.1	An illustration of a neuron	3
1.2	An action potential	4
1.3	Diagram of angular and intensity modulation SPR sensor modalities.	18
1.4	Plasmonic Scales.	25
1.5	Summing the simulated time-aligned signal epochs corrupted with random noise improves the SNR.	33
1.6	Verifying the SNR improvement.	33
1.7	Gaussian probability density functions for detection	35
2.1	Schematic of the SPM that was developed.	46
2.2	Photo of the SPM that has been developed.	47
2.3	Triggering Setup.	54
2.4	Procedure for the SPR and electrophysiology experiments.	57
3.1	Plot of the real and imaginary parts of the dielectric constant as a function of wavelength.	62
3.2	Geometry for SPP propagation at a single, flat interface between a metal and a dielectric.	64

LIST OF FIGURES

3.3	Propagation length for SPP and decay lengths in the dielectric and metal as a function of the wavelength of the incident light for a gold/air and gold/water interface.	65
3.4	Theoretical angular responses for p - and s - polarised light for a gold/air and gold/water interface.	67
3.5	Wave-vector of a photon with a grazing incidence in air and that of a PSPP at a gold/air interface as a function of the angular frequency.	67
3.6	Illustration of the two most common ATR configurations.	68
3.7	Angular response as a function of wavelength for gold and silver.	71
3.8	SPR Curves for Au, Ag, Cu, Pd, and Li in air with a film thickness of 50 nm	73
3.9	Theoretical SPR responses for different thicknesses of Au.	75
3.10	Theoretical SPR responses for changing the Au layer thickness by $\pm 10\%$ with water as the dielectric.	76
3.11	Model of the multi-layer system. The model is simplified to a five-layer model comprising of glass/gold/extracellular solution/membrane/cytosol. $n = [1.52, \varepsilon(\omega), 1.37, 1.5, 1.35]$	77
3.12	Ψ and Δ for silanised glass and untreated glass measured using ellipsometry.	78
3.13	Angular response solved using the N-layer model and increasing the gap distance between the gold surface and cell membrane from 0 to 300 nm in 20 nm steps.	82
3.14	SPR angle minimum taken from Figure 3.13.	82
3.15	Affect on the gradient of the SPR dip with increasing gap distance.	83
3.16	Theoretical angular SPR response when the refractive index of the cell membrane changes by $\pm 1.5 \times 10^{-3}$	85
3.17	Summary of the $\Delta\theta/\Delta n$ for angular modulation and $\Delta R/\Delta n$ for intensity modulation schemes.	86
3.18	Angular response before and after changing the plasma frequency.	87
4.1	Time and frequency domain traces of the light source noise taken with the EPIX camera.	93
4.2	Model of a single pixel.	95
4.3	Measured mean gray values as a function of the exposure time.	97

LIST OF FIGURES

4.4	The average value of each pixel for the signal, dark image, and difference.	100
4.5	The average area uniformity for the differential image.	101
4.6	The effect on the gain factor with increasing the gap distance.	103
4.7	Improvement in the minimum detectable ΔR and Δn after signal averaging.	105
4.8	Illustration of the method employed to determine the angle of incidence at the sample plane by scanning a focused SLED across the BFP.	108
4.9	Resulting scans with different solvents on glass.	109
4.10	Distance from Origin vs. Critical angle for characterising the BFP. .	110
4.11	Comparison of the polynomial curve fitting with the sine condition. .	111
5.1	Representative ellipsometry figure.	118
5.2	Representative BFP images and SPR responses for the different thicknesses of gold.	120
5.3	Gradient of the angle scans shown in Figure 5.2d calculated using $\Delta \tilde{R} = \Delta \tilde{R} / \Delta \theta$	121
5.4	Refractive index variation as a function of both temperature and salinity.	123
5.5	Time series plots of changing the bulk refractive index on the surface of planar gold with NaCl, KCl, and NaF.	124
5.6	Summary of the normalised change in light intensity as a function of the refractive index.	126
5.7	Representative images of the sample. Cells have been cultured on planar gold and have been imaged 14 DIV.	130
5.8	Representative SPR responses for cells and gold/ECS.	131
5.9	Recordings from electrophysiology of the applied current pulse and resulting membrane voltage.	132
5.10	Plot of light intensity over time for all pixels for one AP.	134
5.11	The average across all pixels for one action potential.	134
5.12	Comparison of the average intensity distribution values across all pixels from the SPR images after processing and white Gaussian noise.	135
5.13	The average across all pixels for 500 action potentials from the pseudo data.	138

LIST OF FIGURES

5.14	Flow chart of the data analysis.	139
5.15	Comparison of the pseudo-data values for the intensity from the average across all pixels and white Gaussian noise.	141
5.16	Resulting figures from the cross correlation of “AP” and “noise + AP” for increasing amplitudes of AP hidden in noise.	143
5.17	Summary of the peak of the cross correlation as a function of the AP amplitude	143
5.18	Spectral coherence estimate for “AP” and “noise + AP”.	144
5.19	Processed electrophysiology voltage recordings for 1000 triggered APs on planar gold surfaces.	145
5.20	The average across all pixels for 1000 action potentials from the planar results.	146
5.21	Representative figure computing the cross correlation amplitude between the SPR response and electrically recorded membrane voltage for 1000 AP repeats on a planar gold sensor.	147
5.22	Representative figure comparing the histogram of the SPR response to that of white Gaussian noise.	148
5.23	Spectral coherence estimate for the relation between the SPR response and electrically recorded membrane voltage for 1000 AP repeats on a planar gold sensor.	149
5.24	Summary of the resultant amplitude from the cross correlation analysis for the planar sensors.	150
5.25	Estimated noise floor from the planar repeats compared with theory.	151
6.1	Microscopy and threshold binary image of primary rat hippocampal neurons 2 DIV.	156
6.2	S/N Ratios to quantify the variability of the independent parameters from the Taguchi array.	161
6.3	Results from the one-way ANOVA for each variable vs. the average number of successful attempts.	163
6.4	Representative brightfield images of the nine microstructures post lift-off.	165
6.5	Representative BFP image and SPR response for the 10×16 gold microstructures.	166

LIST OF FIGURES

6.6	Representative BFP image and SPR response for the 10×10 gold microstructures.	166
6.7	Representative BFP image and SPR response for the 6×16 gold microstructures.	167
6.8	Representative BFP image and SPR response for the 6×10 gold microstructures.	167
6.9	Representative BFP image and SPR response for the 6×6 gold microstructures.	168
6.10	θ_{sp} summary for the microstructures and planar controls.	169
6.11	Gradient maximum summary for the microstructures and planar controls.	169
6.12	Time series plots of changing the bulk refractive index on the surface of the gold microstructures with NaCl.	172
6.13	Summary of the normalised change in light intensity as a function of the refractive index for each of the microstructures.	172
6.14	Brightfield and fluorescent images from the cell viability assay for AUT treated surfaces.	174
6.15	Brightfield and fluorescent images from the cell viability assay for PEI treated surfaces.	175
6.16	Brightfield images of the cells on the PLL surfaces.	176
6.17	Live/dead cell viability assay summary	176
6.18	Representative images of the sample. Cells have been cultured on planar gold and have been imaged 14 DIV.	179
6.19	Representative SPR responses for cells and gold microstructure / ECS.	180
6.20	Processed electrophysiology voltage recordings from the microstructures.	181
6.21	Time series plot of the average intensity as a function of time averaged across all pixels in the ROI.	182
6.22	Cross-correlation results for 400 APs on the 10×10 microstructure.	183
6.23	Comparison of the intensity values from the average across all pixels and white Gaussian noise.	184

LIST OF FIGURES

6.24	Spectral coherence estimate for the relation between the SPR response and electrically recorded membrane voltage for 400 AP repeats on the 10×10 microstructure.	185
6.25	Summary of cross correlation amplitudes for the different number of repeats 10×10 microstructure.	187
6.26	Estimated noise floor from the microstructure repeats compared with theory.	189
7.1	The cross correlation amplitudes of both the planar gold and microstructures across all the repeats.	201
B.1	Effect of filtering on the shape of the action potential.	239
B.2	Difference between the bias images for determining the read noise.	240
C.1	Raw electrophysiology voltage recordings from the pseudo-data.	242
C.2	Processed electrophysiology voltage recordings for the pseudo-data.	242
C.3	The raw SPR and voltage recordings and combined pseudo data before any processing.	243
C.4	The average across all pixels for one action potential from the pseudo data after the control area had been subtracted from the ROI.	243
C.5	False colour plot of light intensity over time for all pixels.	244
C.6	Time series traces of the pseudo-data: “noise + AP”	244
C.7	Cross-correlation standard result from the pseudo-data.	245
C.8	Frequency domain traces of the average membrane voltage and the row average from the optical, SPR recordings.	246
C.9	Normalised and subtracted FFT traces.	247

LIST OF TABLES

1.1	Approximate Concentrations and Nernst equilibrium potentials for a Mammalian Neuron.	5
1.2	Summary of the available action potential detection technologies and their limitations.	16
1.3	Comparison of LSPR and SPR sensors. Reproduced from Mayer and Hafner (2011).	24
1.4	Conditional probability matrix	34
2.1	Photomask Design Details	41
2.2	The solvents that were used to determine the angle of incidence, their refractive indices at 680 nm, and corresponding critical angle.	49
2.3	Procedure to dilute or concentrate the media on the sensor for the desired change in refractive index.	52
3.1	Parameters used to reproduce the data of Johnson and Christy (1972) for gold and silver. Values taken from Le Ru and Etchegoin (2008).	61
3.2	$\Delta R/\Delta\theta$ in air for the different thicknesses of gold.	74
4.1	Measured temperature of the coverslip and ambient at the start and after 20 mins of use with SLED or LED.	107

LIST OF TABLES

4.2	Table of the refractive index, critical angle (θ_c), and measured distance from the origin for each solvent.	110
4.3	Comparison of the other curve fitting results for determining the angle of incidence.	111
5.1	Resonance angles θ_{sp} and gradient maximum amplitude ($\Delta\tilde{R}/\Delta\theta$) values for theoretical (T) and experimental (E) data.	121
5.2	Estimated noise floor from the planar repeats.	150
6.1	Results from the analysis of cell morphology of cultured neurons at 2 DIV.	156
6.2	Dimensions of structures on Photomask.	157
6.3	Experimental runs designed using a Taguchi array	159
6.4	Populated version of Table 6.3 and results giving the average number of successful attempts for each run.	160
6.5	SPR angle (θ_{sp}) and gradient maximum ($\Delta\tilde{R}/\Delta\theta$) for the 50 nm planar controls and microstructures.	170
6.6	The sensitivities for the 10×16 , 10×10 , and $6 \times 6 \mu\text{m}$ microstructures.	171
6.7	Estimated noise floor from the microstructure repeats.	188

GLOSSARY OF ABBREVIATIONS

AgCl	Silver chloride
ATP	Adenosine triphosphate
ATR	Attenuated total internal reflection
a.u.	Arbitrary unit
AP	Action Potential
BFP	Back focal plane
DI	Deionised water
DIV	Days <i>in vitro</i>
ECS	Extracellular solution
FFT	Fast Fourier transform
FPS	Frames per second
ICS	Intracellular solution
LED	Light emitting diode
NA	Numerical aperture
PSPP	Propagating surface plasmon-polariton
PSD	Power spectral density
RIU	Refractive index unit
RMSE	Root mean square error
ROI	Region of interest

SLED	Super-luminescent diode
SNR	Signal-to-noise ratio
SP	Surface plasmon
SPP	Surface plasmon polariton
SPM	Surface plasmon microscope
SPR	Surface plasmon resonance
SSE	Sum of squared errors of prediction
TIR	Total internal reflection

PHYSICAL CONSTANTS

Name	Symbol	Value
Avogadro's number	N_A	$6.022 \times 10^{23} \text{ mol}^{-1}$
Boltzmann's constant	k	$1.381 \times 10^{-23} \text{ J K}^{-1}$
Electron charge	q	$1.602 \times 10^{-19} \text{ C}$
Electron mass	m	$9.109 \times 10^{-31} \text{ kg}$
Faraday's constant	F	$96,490 \text{ C mol}^{-1}$
Planck's constant	h	$6.626 \times 10^{-34} \text{ m}^2\text{kg}^{-1}\text{s}^{-1}$
Speed of Light	c	$2.998 \times 10^8 \text{ ms}^{-1}$
Vacuum permittivity	ϵ_0	$8.854 \times 10^{-12} \text{ A}^2\text{s}^4\text{kg}^{-1}\text{m}^{-3}$

CHAPTER 1

INTRODUCTION

1.1 Motivation

Our comprehension of the brain and its functions is far from complete, despite the enlightening research performed by neuroscientists. Improving our understanding of the brain is necessary to make progress against the challenges that we currently face. These challenges include discovering preventative medicines or treatments to neurological diseases and disorders including Alzheimer's and dementia that are associated with the deterioration of the brain, disorders such as epilepsy, or applying the learned techniques to machine learning.

Neurons form networks and send electrical signals between each other called action potentials (Hodgkin and Huxley, 1939; Barnett and Larkman, 2007; Bloom et al., 2009). We lack a complete understanding of how information is encoded into spatio-temporal patterns or how they give rise to behaviour or cognition. In order to attempt to decode these signals and understand brain function, it is first necessary to monitor a whole network of neurons and record all the action potentials, for an extended period of time. Here lies the problem; the current technology available

can only detect the signalling activity of a small number of individual neurons, or, on a larger scale electrical activity from specific regions of the brain at low resolution for example, functional magnetic resonance imaging (Huettel et al., 2004; Glover, 2011; Chow et al., 2017), positron emission tomography (Phelps et al., 1985; Bailey et al., 2005), electroencephalography (Niedermeyer and da Silva, 2005; Parvizi and Kastner, 2018), and magnetoencephalography (Hämäläinen et al., 1993; Baillet, 2017). Therefore, in order to develop an understanding of how a population of neurons is organised, exchanges and processes information a new sensing technology is required, one that has single cell resolution and can be used long-term over a whole network. The development of such a sensor is the aim of the work in this thesis.

1.2 The Brain, Neurons and Action Potentials

1.2.1 Neurons

Neurons are electrically excitable cells¹ that transmit information via electrical and chemical signals throughout the nervous system. Neurons are formed of three main parts; a cell body (soma), dendrites, and the axon, shown in Figure 1.1. The soma contains the nucleus and other organelles for cell maintenance. The dendrites are considered to be the input to the neuron and receive incoming signals from other neurons; these inputs can be excitatory or inhibitory. The axon is the output of the neuron and forms synapses onto dendrites of neighbouring neurons to create a neuronal network to transfer information throughout the nervous system. The diameter of the soma ranges from 4 μm for a granule cell to 100 μm for a motor neuron in the spinal cord (Spruston et al., 1999).

Neurons can be categorised into three types: primary-sensory neurons are attached to sensory surfaces, for example, skin, the retina, and in the ear; motor neurons connect to muscles, and interneurons (the most common) transmit information between the sensory and motor neurons.

¹Note: cell is used throughout this thesis to describe an unidentified cell-type for example when it is not clear whether the cell in question is a neuron or glial cell.

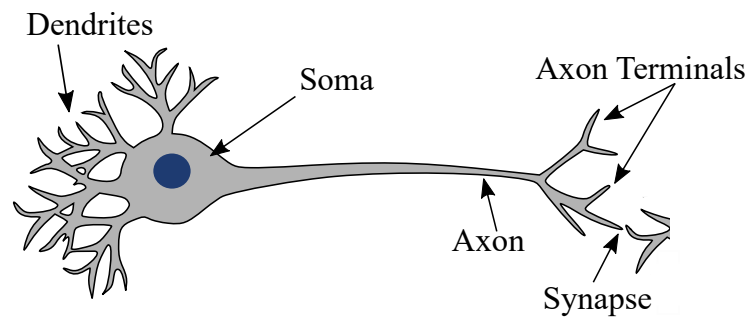


Figure 1.1: An illustration of a neuron. The main parts are labelled. The signalling propagates from the dendrites to the axon.

1.2.2 The Action Potential

Hodgkin and Huxley (1939) were the first to directly record the membrane potential change across the membrane of a giant squid axon. The membrane potential change is now known as the action potential (AP) and illustrated in Figure 1.2. Using an intracellular micro-electrode inserted into the axon they measured a resting membrane potential of around -60 mV and in subsequent experiments with Bernard Katz (Hodgkin and Katz, 1949; Hodgkin et al., 1952) it was discovered that the AP results from transient changes in the sodium (Na^+) and potassium (K^+) ions across the neuronal membrane during a ~ 2 msec reversal in polarity of the transmembrane potential.

The resting membrane potential (V_m) is maintained by an unequal distribution of ions between the intra- (V_{in}) and extracellular (V_{out}) spaces, where $V_m = V_{in} - V_{out}$ (Kandel, 2012). The extracellular space has an excess of positive Na^+ ions and a low concentration of K^+ ions; the opposite is true of the intracellular space. The approximate ion concentrations for a mammalian neuron are defined in Table 1.1 (Bear et al., 2006). This heterogeneity in concentration distribution between the intra V_{in} and extracellular V_{out} space is maintained by ion channels and adenosine triphosphate (ATP)-dependent pumps in the neuronal membrane. Both the channels and pumps regulate the distribution and movement of ions across the membrane in response to certain electrical, mechanical, or chemical stimuli. Ion channels are permeable to specific ions and only allow passive diffusion across the membrane as

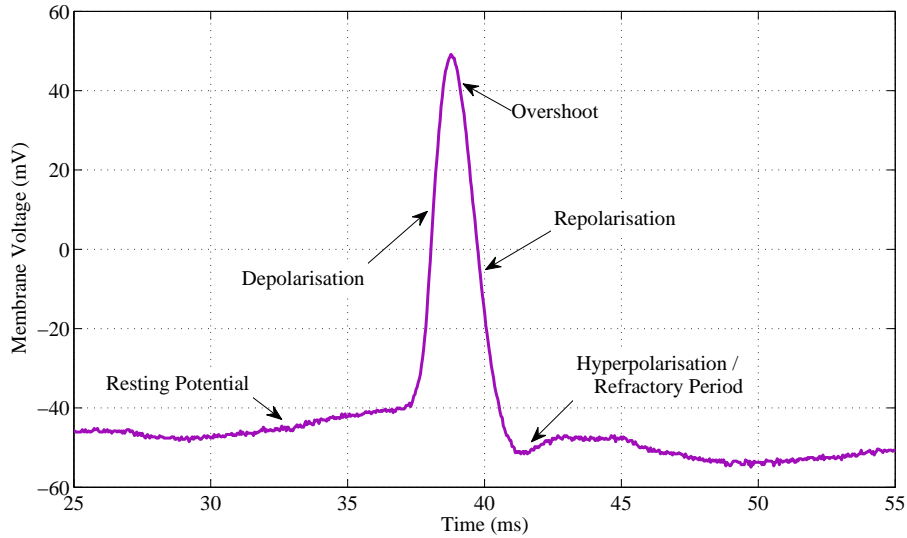


Figure 1.2: An action potential, recorded using an intracellular microelectrode. The main parts are labelled.

a result of an electrochemical gradient that is formed from differences in electrical charge and ion concentrations on either side of the membrane. The ATP-dependent pumps breakdown ATP to release energy for transporting ions across the membrane, against the concentration gradient. Most commonly the ATP pumps are returning Na^+ and Ca^{2+} ions from inside the neuron to the extracellular space during the repolarisation stage of an action potential (Bear et al., 2006).

The membrane potential and concentration gradient for each ion generates a force which maintains an electrical and chemical equilibrium, called the reversal potential. Each ion has its own specific reversal potential that defines which direction they flow when an ion channel opens and at what membrane potential they reach their electrochemical equilibrium. The ionic equilibrium potential for each ion (E_{ion}) can be determined using the Nernst equation (Purves et al., 2012):

$$E_{ion} = \frac{RT}{zF} \ln \frac{[ion]_o}{[ion]_i} \quad (1.1)$$

where R is the gas constant, T is the temperature in Kelvins, F is Faraday's constant, z is the charge of the ion, $[ion]_i$ and $[ion]_o$ are the ionic concentrations inside and outside of the cell, respectively. The extracellular potential (V_{out}) is defined as zero

so the membrane potential at rest is equal to V_{in} , around -60 mV due to the high concentration of K^+ ions and its low ionic equilibrium potential. The intra- and extracellular concentrations for each ion including the equilibrium potentials are given in Table 1.1.

Table 1.1: Approximate Concentrations and Nernst equilibrium potentials for a Mammalian Neuron. Values from Bear et al. (2006)

Ion	Extracellular Concentration (mM)	Intracellular Concentration (mM)	E_{ion} at 37°C (mV)
K^+	5	100	-80
Na^+	150	15	62
Ca^{2+}	1	0.0001	123
Cl^-	110	13	65

An action potential is caused by the rapid depolarisation of the membrane of a neuron, where the inside of the membrane becomes positively charged compared to the outside. At rest, the membrane potential is around -60 mV and both the voltage-gated Na^+ and K^+ channels are closed. Incoming currents from neighbouring dendrites open the Na^+ channels and the electrochemical gradient results in a Na^+ influx to the neuron, causing the membrane to depolarise. If this depolarisation reaches a threshold level, commonly -45 mV (Barnett and Larkman, 2007) then the voltage sensitive Na^+ channels completely open and the voltage peaks around +40 mV. When the membrane is depolarised, the intracellular K^+ (which has a low equilibrium potential) flows out of the neuron to the more negative potential. As more of the voltage-sensitive K^+ channels open, the membrane potential is brought back to its resting state by the efflux of K^+ ions during the repolarisation stage. The undershoot occurs because the voltage-gated K^+ channels stays open longer than needed (Barnett and Larkman, 2007). A refractory period (between 3 – 5 msec) follows where the voltage-gated channels remain inactive and no action potential can be generated. This is to allow the Na^+ and K^+ pumps to reverse the ion distribution across the membrane back to baseline conditions and also stops the AP propagating backwards.

1.3 Neural Activity Detection

One of the primary goals of contemporary systems neuroscience is to understand how sensory inputs are processed; networks are formed and the resulting functional outputs. This system-level approach can be applied to higher-level functions such as learning, behaviour, and neuropsychology. To achieve this, an imaging technique is required that can detect every action potential from every neuron in a large population to observe correlations in space and time between stimulus and response. Any experience can alter how the brain functions (Kolb and Whishaw, 1998; Kolb and Gibb, 2011; Butz and van Ooyen, 2013; Sale et al., 2014) so it is essential that detection can be performed long-term.

For a sensor to be capable of detecting every action potential from every neuron in a relatively large population for a long period of time the measurement targets of the sensor are as follows:

1. Considering the action potential is on the order of 1 msec, i.e., the highest frequency of interest (B) is 1 kHz, and the Nyquist-Shannon sampling theorem, which states that the sample-rate must be larger than $2B$ samples/second (Nyquist, 1928; Shannon, 1949). Therefore, the sensor must sample the action potential at a sampling-rate higher than 2 kHz resulting in a **temporal resolution** of at least 0.5 msec.
2. The sensor will need to have single-cell spatial resolution. The typical area of a mammalian neuron soma is around $80 \mu\text{m}^2$ (Meitzen et al., 2011). If the soma is assumed to be a perfect circle this gives a diameter of around $10 \mu\text{m}$. To fulfill the Nyquist-Shannon sampling theorem the **spatial resolution** needs to be at least half of this ($5 \mu\text{m}$) so an imaging a square area of $25 \mu\text{m}^2$.
3. From a large network in this case is relative. The required **spatial extent** will be assumed to be the size of a microculture, with an area of 1mm^2 .
4. For a long period of time is also relative. Therefore, the required **temporal extent** will be assumed to be more than one week of continuous recording.

This section will discuss some of the current technologies available for detecting action potentials. They can be categorised into the following groups: (a) intracellu-

lar electrical recordings using sharp or patch electrodes, (b) extracellular electrical recordings including Microelectrode Arrays (MEAs), (c) optical imaging using extrinsic fluorescent indicators or genetically encoded indicators, (d) optical imaging of intrinsic signals including changes in light scattering, absorption, and refractive index, (e) other methods designed to detect neural activity from very large populations by functional magnetic resonance imaging (fMRI), positron emission tomography (PET), electroencephalography (EEG), and magnetoencephalography (MEG). The following sections will describe techniques (a) – (d), separated into electrophysiological and optical techniques. (e) is not in the scope of this thesis as the techniques are not suitable for single neuron AP activity detection. The lack of spatial resolution, which is on the order of mm^3 for fMRI (Goense et al., 2016), and MEG (Hedrich et al., 2017), and up to cm for EEG (Burle et al., 2015) is a fundamental limit of these technologies.

1.3.1 Electrical Detection

Intracellular

Neher and Sakmann (1976) were the first to use a glass micropipette to form a high resistance seal on the cell membrane of frog skeletal muscle leading to currents being detected through single ion channels. Intracellular recordings are very accurate with a signal-to-noise ratio (SNR) that allows cellular and sub-cellular properties to be resolved, including the currents of individual ion channels whose amplitudes are on the order of one pA (Standen et al., 1987). Intracellular recordings also have a high temporal resolution down to $5 \mu\text{s}$ (Sontheimer and Olsen, 2007), and when the sampling-rate is over 25 kHz intracellular recordings can discern synaptic currents (Hamill et al., 1981; Anson and Roberts, 1998). Intracellular membrane patches, however, are invasive to the cell and the damage to the cell membrane limits the recording time to hours.

The necessity for accurate and precise control when using intracellular techniques along with the bulkiness of current micromanipulators and patch-clamp systems limits the number of simultaneous recordings to about 12 (Perin et al., 2011). Planar patch-clamp systems have been developed for automated, high-throughput patch-clamp of *in vitro* cells used for drug testing and discovery (Dunlop et al., 2008).

Extracellular

Extracellular recordings were first performed by using a microelectrode outside of the cell (Weale, 1951). Hubel et al. (1957) inserted a thin metallic wire into a cats spinal cord where sharp fluctuations in the potential were detected that was synchronous with AP activity in a nearby cell. The potential difference is thought to be due to local ionic currents in the vicinity of the cellular membrane during an AP. The ions that pass across the membrane during an AP are constrained to a thin surface layer of about 1 nm close to the membrane by the electrical attraction to the oppositely charged ions on the other side of the membrane (Alberts, 2017). Extracellular recordings only occur in close proximity to the neurons and are the result of the summation of the electric currents from multiple nearby cells (not just neurons), called local field potentials (Buzsáki et al., 2012). The one-on-one connection with the neuron is lost and can make it difficult to isolate individual neurons. However, extracellular recordings are non-invasive enabling long-term recording for days and months (Potter and DeMarse, 2001; Spira and Hai, 2013). Thomas et al. (1972) were the first to record signals from cultured cardiomyocytes harvested from embryonic chicks using planar MEAs. An array of 2×15 gold electrodes was developed that could detect signals of approximately 1 mV. Commercially available MEAs typically come in a pattern of 8×8 or 6×10 electrodes, but due to the relatively large electrode spacing ($>30 \mu\text{m}$), not all the electrical activity from the entire neuronal population can be detected. The size of the individual electrodes on an MEA is limited by the impedance. A larger electrode will have a larger impedance, resulting in a smaller SNR. Passive MEAs have a limited spatial extent to at most 1.5 mm^2 (Litke et al., 2004; Shew et al., 2010; Taketani and Baudry, 2010). It is difficult to scale up an MEA because each electrode needs to have its own circuitry. This is an inherent problem of the technology, and is one that is unlikely to be resolved even if components become smaller.

Efforts to increase the spatial resolution have been achieved by (a) integrating active electronic components onto the device in the form of transistors (Hutzler et al., 2006; Poghossian et al., 2009) or CMOS-based technology (Frey et al., 2009; Berdondini et al., 2009; Bakkum et al., 2013) or by (b) combining intra- and extracellular techniques with mushroom shaped electrodes (Spira and Hai, 2013), nanopillars (Zhou et al., 2016) or electroporation (Dipalo et al., 2017) to encourage the neuronal mem-

brane to engulf the electrode allowing pseudo-intracellular recordings. The latter, however, is limited by the number of neurons that can be recorded to tens of neurons. Using active electronic components has improved the density and the number of electrodes because unlike passive MEAs the performance does not depend on impedance (Obien et al., 2014). Some devices have nearly 30,000 electrodes resulting in single-cell analysis without averaging and sub-cellular resolution after averaging (Müller et al., 2015). Both passive and active MEAs have demonstrated a temporal resolution of submillisecond down to microsecs depending on the number of functional electrodes during a recording (Hutzler et al., 2006; Berdondini et al., 2009).

However promising, to derive any meaningful information from *in vitro* cultures it is usual that a single cell or set of cells is stimulated, either electrically (Standen et al., 1987; Tanamoto et al., 2015) or optically (Fenno et al., 2011; Deisseroth, 2015) and the response from the network is recorded. For all electrical, extracellular techniques, simultaneous electrical stimulation and recording cause stimulation artefacts, where the stimulation signal is detected on all electrodes of the array. These artefacts can be several orders of magnitude greater than APs resulting in the saturation of the recording amplifier, which in turn causes the detection electrode unable to detect anything for at least 2 msec and nearby electrodes for half a msec (Tateno and Nishikawa, 2014). Considering the latency of the AP can be as short as 100 μ sec (Sekirnjak et al., 2008) and the average AP duration is 1 msec this saturation could result in the electrodes missing the invoked activity.

1.3.2 Optical Detection

Optical recording methods have a distinct advantage over electrical recording as they do not suffer from the previously discussed electrical artefacts and are easier to scale up with only the objective lens field of view limiting the recording area. Optical recording techniques can be either intrinsic or extrinsic. Intrinsic signals are activity-dependent optical changes, including changes in scattering, absorption and refractive index. Extrinsic optical effects are due to fluorescent changes of externally applied dyes.

Extrinsic Signals

Extrinsic signals are the result of changes in fluorescence following the addition of an externally applied dye. The dyes can either be voltage-sensitive or calcium indicators and both can be synthetic or genetically encoded.

Voltage-sensitive dyes (VSDs) are membrane-bound and respond proportionally to the membrane potential. They can be applied internally with a micropipette or to the extracellular media to stain all the neurons in a population. Salzberg et al. (1973) were one of the first to use VSDs to monitor activity from a single neuron from the leech ganglia. However, the photodynamic damage limited the duration of the experiments, and the recordings suffered from a poor SNR. More recently activity from hundreds of individual neurons has been detected simultaneously (Zochowski et al., 2000). Baker et al. (2005) measured the activity of up to 50% of the approximately 1000 cells in a mollusc ganglion. VSDs have fast, sub-millisecond temporal resolution (Ferezou et al., 2006; Grinvald et al., 2016) and can track the AP accurately, and they have a high spatial resolution (20 – 50 μm), the latter being limited by the optical scattering of the emitted fluorescence (Orbach and Cohen, 1983; Peterka et al., 2011; Grinvald et al., 2016). VSDs are limited because depending on the preparation they may respond differently. This means that many dyes need to be tested to optimise the response (Baker et al., 2005). Also, due to the dye being membrane-bound and the membrane being essentially a 2D surface the number of fluorophores available to excite is limited. The AP is fast, so a large number of photons are needed for a reasonable SNR. The SNR can be improved by increasing the power of the light source, and therefore the number of photons but this will increase the rate of bleaching and the speed of photo-damage of the cell thus reducing the experimental time. Also, VSDs have a small temporal extent because they are very toxic and cannot be used for recording times of more than ten mins (Grienberger and Konnerth, 2012). Genetically encoded voltage indicators (GEVI) have been developed but in their current form display poor properties including a low SNR, slow kinetics and cytotoxicity (Looger and Griesbeck, 2012; Rad et al., 2017).

Action potential activity leads to Ca^{2+} influx causing the intracellular concentration to rise from 50 – 100 nM at rest to levels that are 10 to 100 times larger (Table 1.2).

Calcium indicators manipulate this and respond to changes in the calcium in the cytoplasm. Synthetic, chemical calcium indicators are a combination of a fluorophore with a calcium-selective binding molecule. These indicators have a very good SNR, and rapid kinetics so are currently the optical method of choice (Paredes et al., 2008; Grienberger and Konnerth, 2012). They can be loaded using sharp or patch micropipettes to detect the AP activity of individual cells, but methods have been developed to image activity in larger populations. These methods, however, are laborious and can be damaging to the cells (Tian et al., 2009; Looger and Griesbeck, 2012).

Alternatively, genetically encoded calcium indicators (GECI) have demonstrated the ability to image the spiking activity of hundreds to several thousands of neurons with single-cell resolution for up to 80% of neurons reported (Cossart et al., 2003; Ahrens et al., 2013). It is even possible to detect individual action potentials without the need to average (Smetters et al., 1999). However, the duration of a typical calcium signal is on the order of 100 msec meaning in fast-spiking neurons individual action potentials can be challenging to resolve (Chen et al., 2013; Peron et al., 2015). GECIs can be loaded using viral transfection or in-utero electroporation, but this causes cell damage (Grienberger and Konnerth, 2012). Compared to chemical indicators, GECIs are functional longer than synthetic, chemical indicators but suffer from a lower SNR, photostability, and calcium affinity (Tian et al., 2009).

Both chemical and genetically encoded calcium indicators are slower to respond compared to VSDs and are biased to suprathreshold responses ultimately limiting their temporal resolution (Homma et al., 2009). Similarly to VSDs, calcium indicators suffer from bleaching and photo-toxicity (Grienberger and Konnerth, 2012; Looger and Griesbeck, 2012).

Intrinsic Signals

Neural activity has been shown to produce both fast and slow light scattering signals. The increased metabolism that occurs during neural activity causes slower haemodynamic events that can be monitored through the light absorption of both oxy- and deoxy-haemoglobin. This change in haemoglobin can be detected non-invasively using near-infrared spectroscopy and diffuse optical tomography (Villringer and Chance, 1997; Lloyd-Fox et al., 2010; Torricelli et al., 2014). However,

because these signals are slow (on the order of 4 – 10 secs) and indirect (Glover, 2011; Mayer et al., 2014), they are unsuitable for detecting fast neural activity with single event resolution.

Fast optical changes are the result of light scattering and birefringence changes that are associated with membrane depolarisation. First demonstrated by Hill and Keynes (1949), the opacity of a crab leg nerve was shown to increase by about 1 part in 500 for 250 impulses during stimulation. The authors questioned whether the light scattered by the nerve was due to changes in the optical properties of the membrane or by changes in the viscosity of the axoplasm. This led to further experiments using the giant axon of the squid. Cohen et al. (1968) linked the change in light scattering to the firing of action potentials observing a time lag of 0.25 msec between the optical and electrical events. The hypothesis was that the light scattering was due to a small increase in the volume of the nerve fibres resulting in a reduction of the internal refractive index. Similarly, the birefringence change was assumed to be directly dependent on the membrane potential of the axon and was caused by the polarisation and alignment of protein molecules associated with the membrane. Studies in the subsequent years confirmed the results (Cohen et al., 1968, 1969; Salzberg et al., 1977), and further characterised the resulting optical signal with respect to the membrane currents and voltages (Cohen et al., 1972a,b).

The mechanisms underlying this fast change in the intrinsic light scattering and birefringence properties of cells during action potentials remains uncertain. Along with being associated to mechanical events (Tasaki et al., 1968, 1980; Yao et al., 2005; Yang et al., 2017), studies have linked this phenomena to molecular (Landowne, 1985, 1993) and electrical events (Stepnoski et al., 1991). Foust and Rector (2007) compared the optical scattering and birefringence measurements from a lobster nerve to that from a VSD during electrical activity. It was suggested that cellular swelling might cause the scattering but cannot be the origin for the birefringence changes because a time-lag was observed between the scattered and birefringence signal. The authors showed the birefringence signals closely follow changes in the membrane potential and were not affected by cellular swelling, implying that birefringence is dependent on both molecular and electrical changes resulting in a larger resultant signal (Foust and Rector, 2007; Schei et al., 2008; Badreddine et al., 2016). The detection of the intrinsic optical changes of neuronal cells have also been reported

in single cultured neurons (Stepnoski et al., 1991; Graf et al., 2009), brain slices (MacVicar and Hochman, 1991; Lee and Kim, 2010), intact cortical tissue (Grinvald et al., 1986; Rector et al., 1997), and even *in vivo* (Gratton et al., 1995; Zepeda et al., 2004; Lu et al., 2017). The latter, however, has been tempered by negative results (Steinbrink et al., 2000, 2005; Radhakrishnan et al., 2009; Chiarelli et al., 2013) concluding that the SNR is too low to detect brain cortex activity through the intact head reliably.

The problem to overcome regarding intrinsic optical imaging is that the resultant signal from the refractive index change is very small. Enough photons are needed to surpass shot noise and obtain a SNR of one, i.e., the level of the signal matches that of the noise. Even more photons will be required to obtain better SNRs. Methods to increase the sensitivity to intrinsic optical signals have been developed including optical coherence tomography *in vitro* (Lazebnik et al., 2003; Akkin et al., 2010; Yeh et al., 2015), phase-sensitive laser interferometry *in vitro* (Akkin et al., 2004; Fang-Yen et al., 2004, 2006; LaPorta and Kleinfeld, 2012) and surface plasmon resonance *in vitro* (Kim et al., 2008) and *in vivo* (Kim et al., 2012).

1.3.3 Comparison

Detecting the APs of single neurons in a network with a reasonable spatio-temporal resolution is a challenge for contemporary neuroscience and could be argued is limiting our progress in understanding brain dynamics. As described in the previous sections the techniques currently available to complete this are limited in at least one of the four elements needed to fulfil this aim (a) the technique needs to be able to detect every AP (b) from every neuron (c) for an extended period of time (d) from a large population. The current technologies are summarised in Table 1.2.

Intracellular recordings have a temporal resolution high enough to resolve synaptic currents with high SNR and the spatial resolution to see cellular and sub-cellular properties. However, they can only record from a small number of cells and once the cell membrane is damaged, the recording time is limited. Extracellular recording with passive MEAs have a larger spatial extent, but in doing so, they lose spatial resolution as the contact with individual neurons is lost and can therefore, only detect APs and LFPs from multiple cells. Active arrays demonstrate electrode densities large enough to resolve individual APs from neurons, but single-cell selectivity is

challenging as the axons from neighbouring neurons are interlaced and may grow over or under the soma of the neuron closest to the electrode. Note: this is also a problem for passive MEAs. Electrical recording techniques also suffer from stimulation artefacts which could result in APs being missed from fast responding neurons.

Optically imaging voltage or calcium transients using extrinsic dyes are mixed in their abilities to fulfil this aim. Voltage-sensitive dyes have a high spatio-temporal resolution and can be used for the imaging of large populations but have a poor SNR and the photodynamic damage limits the duration of experiments. Calcium indicators are most commonly used for cell activity measurements because they have high spatio-temporal resolution, high SNR, and can be used in large populations. Like VSDs though they are phototoxic.

Measuring the fast intrinsic optical signals caused by electrical activity results in recordings that have a high spatio-temporal resolution. No external dyes are being used, so they also have a high spatio-temporal extent. However, current measurements report average SNRs and have only been demonstrated for use with large nerve bundles. An alternative technique is required that can use the advantages that come with intrinsic optical imaging while improving the SNR for detecting individual APs from neurons *in vitro*.

An Alternative?

Action potentials give rise to fast optical changes in the cell membrane, which are seen as refractive index changes. Various methods can be used to detect the refractive index change of the membrane during electrical activity including surface plasmon resonance (SPR). The resonance conditions for SPR highly depend upon the permittivity of what is on the surface of the sensor. So, any change on the surface that changes the refractive index will thus shift the resonance conditions resulting in a change in the reflected SPR signal. SPR in principle can meet all the requirements needed to detect electrical activity. However, its limitation is that it is a surface technique, therefore, predominately used for measuring the binding kinetics of biomolecules to ligands on the surface. There are some isolated examples of SPR being used to image living cells and detecting neural activity; these are discussed in Section 1.4.2. SPR can be seen as a comparable technique to total internal reflection fluorescence microscopy (TIRF). TIRF has been demonstrated to be effective

for live cell imaging (Axelrod, 2001; Mattheyses et al., 2010) but is limited in that it still requires dyes to be injected into the cell. A more detailed description of the theory of total internal reflection is given in Chapter 3.

This raises the question if it would be possible to use SPR and microfabrication techniques to detect the refractive index changes of a neuronal membrane during electrical activity. If it is possible, SPR would have a number of advantages over current technologies. It would provide a sensitive, label-free imaging technique that could image a large number of cells in real-time for longer periods of time.

Table 1.2: Summary of the available action potential detection technologies and their limitations.

		Temporal		Spatial		SNR	Reference
		Resolution	Extent	Resolution	Extent		
Electrical Recording	Intracellular	++ (ⁱ)	-- (max few hours)	++ (ⁱ)	- (max ~12 neurons ⁱⁱ)	++	i (Hamill et al., 1981) ii (Perin et al., 2011)
	Extracellular	- (LFPs rather than single APs)	++ (> months ⁱ)	- (~30 μm ⁱⁱ)	+ (1.5 mm^2 ⁱⁱⁱ)	-	i (Müller et al., 2015) ii (Potter et al., 2006) iii (Litke et al., 2004)
Optical Recording		+ (2 - 12 kHz ⁱⁱⁱⁱ)	++	+ (Sensor pitch < 10 μm ^{ii,i})	++ (70 mm^2 ⁱⁱⁱ)		i (Eversmann et al., 2003) ii (Hutzler et al., 2006) iii (Johnson et al., 2013)
	Extrinsic	++ (Individual APs ⁱ)	- (photodamage ⁱⁱ)	+ (20 - 50 μm ^{i,iii})	++ (> Hundreds ^{i,iii})	-	i (Peterka et al., 2011) ii (Grienberger and Komnerth, 2012) iii (Baker et al., 2005)
		+ (Slower to respond than VSDs ⁱ)	- (photodamage ⁱⁱ)	++ ($\leq 80\%$ neurons ⁱⁱⁱ)	++ (> Hundreds ^{iii,iv})	++	i (Honma et al., 2009) ii (Grienberger and Komnerth, 2012) iii (Ahrens et al., 2013) iv (Cossart et al., 2003)
	Intrinsic	++ (Individual APs ^{i,ii})	++ (≤ 1 year ⁱⁱ)	++ (Limited by the optical resolution ⁱⁱⁱ)	++ (Limited by the optical field-of-view ⁱⁱⁱ)	+ SNR 5-10 _ⁱ	i (Stepnoski et al., 1991) ii (Bonhoeffer and Hübener, 2016) iii (Graf et al., 2009)

1.4 Surface Plasmon Resonance

1.4.1 SPR Sensors

Neural activity has been shown to produce fast optical signals that are the result of light scattering and birefringence changes associated with membrane depolarisation (Cohen et al., 1968; Stepnoski et al., 1991). Surface plasmon resonance sensors have highly sensitive resonance conditions which make them capable of detecting this membrane localised refractive index change with a high spatio-temporal resolution. SPR has been demonstrated to detect APs from a large rat sciatic nerve (Kim et al., 2008) but there is no literature using traditional SPR in dissociated, cultured neurons. If using SPR for AP detection in dissociated, cultured neurons then it will have considerable advantages over other detection methods, including higher sensitivity, label-free, and minimal cellular damage due to the low light levels required for SPR, which will allow detection to be performed long-term.

Surface plasmon resonance occurs when p -polarised light couples to the free electrons in a metal generating an evanescent field in both the metal and dielectric. The evanescent wave decays into the dielectric for about 100 – 200 nm, which is known as the decay length. Assuming the decay length is the same across the whole metal surface this defines the sensing volume. This resonance condition appears as a sharp dip in the reflected light as shown in Figure 1.3, and is dependent upon the angle of incidence, light wavelength, and refractive index of the dielectric.

A surface plasmon is a charge-density oscillation occurring at the interface between a noble metal, such as gold or silver, and a dielectric (Maier, 2007). So, when there is a change in the refractive index of the dielectric medium, the dispersion relation of the surface plasmon is altered. The change in refractive index alters the characteristics of the light wave coupled to the surface plasmon and ultimately shifts the resonance conditions. The sensitivity is measured in Refractive Index Units (RIU) which is the minimum detectable change of refractive index by the sensor. This allows SPR to be used as a sensor by measuring the reflected light intensity changes using a detector. The theory is explained in more detail in Chapter 3.

There are four SPR sensor modalities; angular modulation (AM), wavelength modulation (WM), intensity modulation (IM), and phase modulation (PM). Angular

modulation uses monochromatic light to excite the SPs, and the excitation of the SPs can be seen as a dip in the angular spectrum. The detector senses a shift in the angle where the reflected light intensity is at a minimum. AM modulation has been commercialised by Biacore and resulted in SPR sensors with high detection levels down to 10^{-7} RIUs. Wavelength modulation uses collimated light containing multiple wavelengths to excite the SPs, and the excitation of the SPs can be seen as a dip in the wavelength spectrum. A refractive index resolution down to 10^{-7} RIUs has been demonstrated (Nenninger et al., 2002). Intensity modulation fixes the angle of incidence and wavelength and measures the strength of the coupling between the light wave and the SP; detection is achieved by measuring the change in the intensity of the reflected light, also shown in Figure 1.3. The detection of small refractive index changes over a relatively large volume has been successful on some sensors based on an intensity modulation scheme down to 10^{-6} RIUs (Sepúlveda et al., 2006; Campbell and Kim, 2007). Finally, phase modulation, similar to IM,

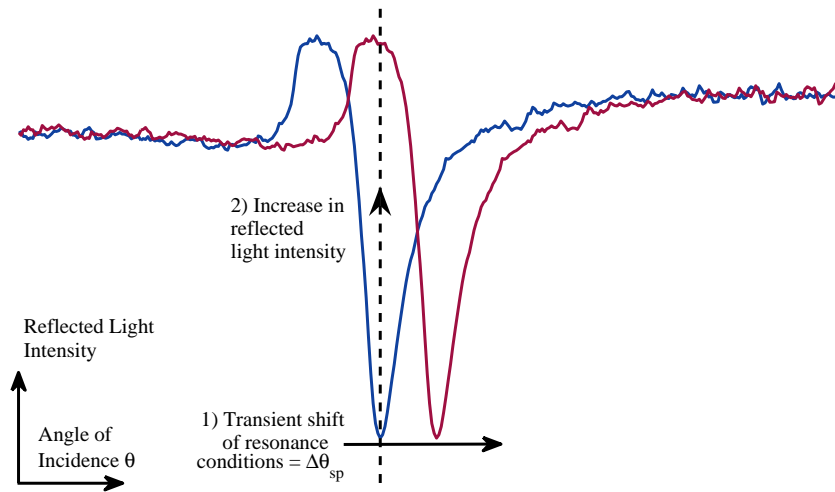


Figure 1.3: Diagram of angular and intensity modulation SPR sensor modalities. In an angular modulation SPR sensor modality the change in resonance conditions, for example the refractive index of dielectric is detected by monitoring the change in the resonance angle, θ_{sp} . In an intensity modulation scheme the angle of incidence is fixed and when θ_{sp} changes the detector sees an increase or decrease in light intensity.

has a single angle of incidence and wavelength but the detector senses a shift the phase of the reflected light. PM modulation has demonstrated a refractive index resolution down to 10^{-6} RIU (Notcovich et al., 2000; Wu et al., 2003).

1.4.2 SPR Imaging

Surface plasmon resonance is typically used for measuring the binding kinetics of biomolecules to ligands on the surface (Phillips and Cheng, 2007; Homola, 2008; Yanase et al., 2010; Abadian et al., 2014; Su and Wang, 2018). However, there are examples of SPR being used to image living cells and detect neural activity. The configurations and methodologies introduced will be described in more detail in Section 3.1.1.

Giebel et al. (1999) imaged cell/substrate contacts of living cells in culture by exciting surface plasmons. They used primary goldfish glial cells cultured on aluminum (15 nm) coated glass. Cell-substrate distances were quantified by imaging cells at various angles of incidence, reconstructing the SPR curves from an analysis of 200 images, and fitting the data. Jamil et al. (2008) reported similar results using a high numerical-aperture (NA) microscope objective (NA = 1.45 for fixed samples in air, and NA = 1.65 for live cells in media) to image the cell surface interface of HaCaT cells cultured on gold with a high spatial resolution without losing contrast or z -resolution. Wang et al. (2012) also reported the imaging of cell-substrate contacts of human epithelial cells (SH-EP1) on gold with sub-cellular resolution using a high NA microscope objective. Furthermore, they investigated the response of the cells to hypertonic stimulation where it was observed the light intensity decreased in cell regions lasting for ~ 4 mins.

Peterson et al. (2009) used SPR imaging to quantify the deposition of protein by vascular smooth muscle cells (vSMC) seeded on regions of extracellular matrix protein (fibronectin) on gold as a function of cell density and distance from the cell periphery. It was possible for the protein patterned regions as well as cell-substrate contacts to be imaged. Peterson et al. (2014) more recently used a high NA microscope objective (100 \times , NA = 1.65) to image five cell types (mice fibroblasts, 3T3; human liver carcinoma, HepG2; kidney epithelial, Vero; vascular smooth muscle, A10; and adenocarcinomic alveolar basal epithelial, A549) and used a digital light projector to pattern the angle of the incident excitation on the samples. Sub-cellular

components including focal adhesions, the nucleus, and cellular secretions were imaged. SPR imaging has on average a detection limit of 10 pg/ml (Nguyen et al., 2015).

Action Potential Detection Using SPR

In preliminary experiments Baac et al. (2005), reported an SPR system that could be used for action potential detection by investigating the electrochemical modulation of the SPR effect without neurons. The resulting SPR signals were electrochemically modulated following the applied field frequency to demonstrate their set-up was capable of measuring resonance angle shifts of $\sim 10^{-3}$ deg. They suggested that using multi-cell photodiodes resonance angle shifts of 10^{-4} to 10^{-5} deg could be detected. Kim et al. (2008) demonstrated a low noise SPR sensor that could be used for extracellular, optical detection of neural activity without requiring signal averaging. The authors used a rat sciatic nerve closely adhered to a gold surface. A biphasic stimulation pulse was applied to the distal (knee) end of the nerve, and both electrical and optical SPR signals were simultaneously recorded at the proximal end (spinal cord). The resulting SPR responses showed a strong correlation with the electrical recording with an SNR of about 4:1. To confirm that the responses were the result of neural activity a nerve blocker was applied and both the electrical and SPR responses degraded within 20 minutes of application. The cause of the resulting SPR response is unclear, and it was suggested that cellular swelling rather than the change in membrane potential could have caused the response. It is also possible that movement of the axon caused the response during stimulation. Kim et al. (2012) extends findings by Kim et al. (2008) by simultaneously detecting SPR and electrical neural activity from the rat somatosensory cortex *in vivo* evoked by electrical stimulation on the forepaw. The evoked signals were detected optically with a gold-coated optical fibre and electrically using a tungsten wire electrode, both inserted into the cortex. The resulting optical SPR signals suffered from a poor SNR and required signal averaging of 500 to 2000 repeats. The SPR signals consisted of mainly low-frequency components that can be attributed to local field potentials from many neighbouring neurons rather than individual action potentials. To confirm the SPR responses were from neural activity a voltage-gated sodium channel blocker was applied. Following the application of the blocker the second

peak diminished and the first peak increased in amplitude. The authors theorise the reason for the first peak increasing in magnitude is due to the reorientation of dipoles and activation of channels other than sodium. They concluded that by using gold-coated optical fibres, large evanescent waves, and consequently a high sensitivity could be produced near the probe.

The limitations in these isolated reports of detecting neural activity with SPR is that they have not been widely replicated. Some studies lack adequate positive and negative controls. For example, the Kim et al. (2008) study control experiment demonstrating the effects of a nerve blocker has no optical response present without toxin. Also, the optical responses do not resemble the electrical and could be the result of artefacts, indirect effects or something else.

Novel plasmonic-based imaging techniques have been developed to detect AP activity. Liu et al. (2017) reported a plasmonic-based electrochemical impedance (P-EIM) microscope capable of P-IEM detection of single APs from embryonic rat hippocampal neurons without signal averaging. P-EIM works by applying an AC potential to the metal surface and the SPR signal changes with respect to the amplitude and phase outputs. The AC component of the SPR response gives the electrochemical impedance (Lu et al., 2011). The authors simultaneously recorded electrical responses using traditional patch clamp and P-EIM recordings with a 10 μ sec temporal resolution and single cell spatial resolution. A decrease in the plasmonic response after the application of tetrodotoxin to inhibit the Na^+ channels and block AP initiation was reported. The authors concluded that the responses they were expecting theoretically were about 30 times smaller than what was observed and attributed this to structural changes in the membrane causing birefringence. Plasmonic ellipsometry has also shown some promise. Sohrabi and Hamidi (2017) demonstrated ellipsometric responses to different mediums which could be applied to detecting electrical activity.

However, it may be possible to detect action potentials from individual, cultured neurons using SPR. Yanase et al. (2014) stated that SPR sensors detect only an average of refractive index changes in the presence of thousands of cells, similar to the local field potentials detected by MEAs. Kim et al. (2008) detected APs from a rat sciatic nerve and Liu et al. (2017) have detected single APs from dissociated,

cultured neurons using P-IEM but there is no literature using traditional SPR. If it was possible SPR has considerable advantages over other AP detection methods, including higher sensitivity, label-free, and minimal cellular damage due to the low light levels required for SPR, enabling long-term detection.

1.4.3 Beyond Extended Planes

Detecting refractive index changes during neural activity using SPR does have some advantages over other imaging techniques. However, one potential limitation is that the resulting responses are averaged over the entire volume. Averaging over an entire volume could result in a lower SNR, potentially impeding single-cell resolution. Methods of minimising the sensor area to increase localisation are explored including localised surface plasmon resonance using nanoparticles and SPR on micron-sized structures.

Localised SPR

When a metallic particle is smaller than the wavelength of the incident light the planar approximation is no longer valid and the description of the dispersion relationship (3.11) become irrelevant. Instead of being continuous modes, the EM modes exist for discrete values of ω . These modes are called localised surface plasmons and are non-propagating excitations of the conduction electrons of metallic structure coupled to the EM field (Maier, 2007).

Mie theory (Mie, 1908) provides a solution to Maxwell's equations that describe the scattering and absorption of EM radiation by spherical particles. The cross sections for scattering and absorption (C_{sca} and C_{abs}) can be derived from the Poynting-vector (Bohren and Huffman, 1983). The cross-section of the LSP mode of the sphere is dependent on the permittivity of the metal chosen ($\varepsilon(\omega)$), the environment (ε_m), and the radius of the sphere (a).

$$C_{sca} = \frac{8\pi}{3} k^4 a^6 \left| \frac{\varepsilon(\omega) - \varepsilon_m}{\varepsilon(\omega) + 2\varepsilon_m} \right|^2 \quad (1.2)$$

$$C_{abs} = 4\pi k a^3 \text{Im} \left| \frac{\varepsilon(\omega) - \varepsilon_m}{\varepsilon(\omega) + 2\varepsilon_m} \right| \quad (1.3)$$

where k is the incoming wavevector given by $k = 2\pi/\lambda$. For small particles with $a \ll \lambda$, the efficiency of absorption dominates over the scattering efficiency (Mayer

and Hafner, 2011). Together these form the expression for the extinction cross section:

$$C_{ext} = 9 \frac{\omega}{c} \varepsilon_m^{3/2} V \frac{\varepsilon_2}{[\varepsilon_1 + 2\varepsilon_m]^2 + \varepsilon_2^2} \quad (1.4)$$

where V is the particle volume. The extinction cross section will be maximum at a frequency where $\varepsilon_1 \approx -2\varepsilon_m$. This explains the dependence of the LSPR extinction peak on the surrounding environment. The sensitivity to ε_m comes from the slope of the real part of the dielectric function. The imaginary part of the dielectric function is related to the peak resonance broadening (damping) that is observed (Mayer and Hafner, 2011). At this frequency, the absorption and scattering will be very large. These small particle approximations only strictly apply to very small particles (<10 nm diameter), but it still gives an accurate prediction of ε_m for larger particles. As the particles size increases the LSP peak frequency given by $\omega_{max} = \omega_p / \sqrt{(2\varepsilon_m + 1)}$ redshifts and more plasmon damping occurs. For gold and silver nanoparticles, therefore, the resonance occurs in the visible region.

As with SPR, LSPR resonances are sensitive to the environment and can be used to detect refractive index changes, typically in shifts in the resonant wavelength ($\Delta\lambda$). The sensitivity is measured in Refractive Index Units (RIU) which is the minimum detectable change of refractive index by the sensor. The resonant wavelength is dependent on the refractive index sensitivity of the nanoparticles (m), the difference in the refractive index induced by absorption (Δn), the absorption layer thickness (d), and the EM-field decay length (l_d).

$$\Delta\lambda_{max} = m\Delta n[1 - e^{-2d/l_d}] \quad (1.5)$$

Monitoring the shift in the peak wavelength is an effective way to sense refractive index using the LSPR technique. The decay length of the EM field into gold is of the order of 20 nm which results in larger changes of λ_{max} for binding events closer to the spheres surface even though the bulk refractive index sensitivity is smaller than that for PSPPs. The shorter decay length for LSPR results in a smaller sensing volume per particle and is the reason LSPR is not as sensitive to bulk refractive index changes compared to SPR (Jatschka et al., 2016). Table 1.3 compares LSPR and SPR sensors.

The dependence of the plasmon response on the nanoparticles size, shape, composition, and dielectric properties of the surrounding medium is well documented in

Table 1.3: Comparison of LSPR and SPR sensors. Reproduced from Mayer and Hafner (2011).

	LSPR	SPR
Bulk dielectric sensitivity (nm/RIU)	10^2	10^6
Sensing distance (nm)	10	1000
Temperature sensitive?	No	Yes
Simple instrumentation?	Yes	No

literature (Hulst and van de Hulst, 1957; Bohren and Huffman, 1983; Link and El-Sayed, 1999, 2000; Scaffardi et al., 2004; Willets and Van Duyne, 2007). It is evident that scattering efficiency increases with increasing nanoparticle size, and conversely the absorption efficiency decreases. Larger nanoparticles tend to have high sensitivities, but their peaks are broadened by multipolar excitations and radiative damping (Mayer and Hafner, 2011).

Zhang et al. (2009) detected changes in the spiking activity of cultured rat hippocampal neurons by monitoring the LSPR resonance shift of a gold nanoparticle array. Neurons were cultured on top of a gold nanoparticle array where each nanoparticle is 160 nm in diameter, 40 nm in height, and with a lattice constant of 400 nm. The neurons were chemically stimulated and a photodiode was used to detect the resonance change in the transmitted or scattered light for both single spike activity and a burst of activity. An adequate signal-noise ratio was reported in a real-time experiment with millisecond temporal resolution. It is evident that the signals obtained are typical of the signals that would be obtained from extracellular electrode recordings or using voltage-sensitive dyes. The amplitude of the signals varied neuron to neuron, and attributed this to the distance between the neurons and the array. However, detection of electrical activity of neurons using LSPR has not since been replicated. A problem with this study is that the neurons were chemically stimulated, so there is no positive control or electrically recorded response to compare to.

Microscale SPR

Both SPR and LSPR have been studied extensively individually, but it is unclear what happens to the optical properties of SPs at the micrometer scale less than

or equal to the propagation length ($\sim 20 \mu\text{m}$ for gold/water interface), Figure 1.4. Research has been performed to find out how SPs are affected by lateral confinement.

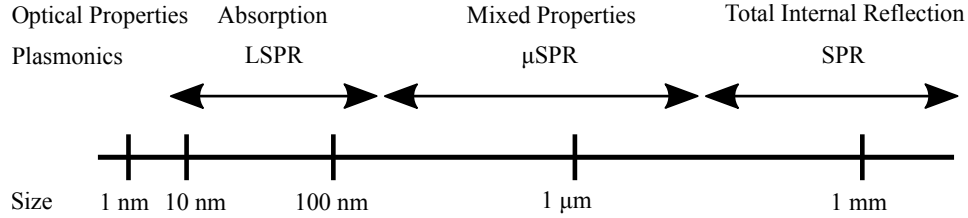


Figure 1.4: Plasmonic Scales.

Lamprecht et al. (2001) measured the SP propagation in silver and gold thin films (70 nm) with structure widths ranging from 54 to 1 μm . The propagation lengths were measured using a high NA objective lens detecting the detecting stray light emitted from the SP. For both silver and gold, the propagation length decreases with decreasing lateral stripe width because the propagation length is inversely proportional to the imaginary part of imaginary part of the wave-vector of the plasmon (k_x). The decreasing propagation length is expected because the radiation damping due to the SP scattering on the lateral stripe edges should increase with decreasing stripe widths. Live et al. (2008) fabricated gold triangles with base lengths ranging between 200 nm to 1.5 μm using nanosphere lithography. The optical properties were measured with a wavelength modulated attenuated total internal reflection (ATR) configuration for SPR and transmission spectroscopy for LSPR. All the gold triangles demonstrated an LSPR response. As the base length was increased, the response transitioned to a regime where there was both an LSPR and a short-range SPR mode present. The larger gold triangles between 500 nm – 1.5 μm have SPR and total internal reflection (TIR) responses, with the SPR absorption peak around $\lambda = 800 \text{ nm}$. Refractive index sensitivities from 11 to 50 nm/RIU are reported. Live and Masson (2009) further investigated the SPR/LSPR properties of gold triangles with base lengths of 700, 950, and 1800 nm and microhole arrays with a 3 μm periodicity and hole diameters of 2.2, 2.0, and 1.6 μm . For all the triangles the LSPR response was in the near infrared. The SPR responses of the gold triangles had two absorption peaks at $\lambda = 525$ and 800 nm and a transmission maximum at $\lambda = 600 \text{ nm}$. The 800 nm peak varies with the size and aspect ratio of the triangle, while the 525 nm peak remains relatively invariable. Bulk refractive index sensitivity

was measured using different concentrations of sucrose solution. The peak observed at $\lambda = 800$ nm is not very sensitive to the refractive index with <100 nm/RIU. The transmission maximum at 600 nm, however, significantly shifts in wavelength with increasing refractive index. After forming a 16-mercaptohexadecanoic acid monolayer on the $1.8 \mu\text{m}$ triangle array, the large shift of the SPR wavelength (13 ± 3 nm) was attributed to a shorter penetration depth of the SPP of 24 nm, which is comparable to the 20 nm penetration depth observed in LSPR (Malinsky et al., 2001). The microhole arrays with the smallest holes, 2.0 and $1.6 \mu\text{m}$ were reported to have an SPR peak that is sharper and more intense than planar gold film. The microhole arrays were also reported to be more sensitive than planar gold, with 3700 ± 400 nm/RIU and 3300 ± 350 nm/RIU for the microhole arrays with a diameter of 2.0 and $1.6 \mu\text{m}$, respectively, within the refractive index range of 1.33 – 1.39 and, 2971 ± 286 nm/RIU for planar 50 nm gold within the same RI range. Similar results were reported by Live et al. (2010) using gold triangles with base lengths between 275 nm and $2 \mu\text{m}$.

1.5 Microscopy Fundamentals

This section will briefly cover some of the microscopy terms that will be used throughout this thesis.

Field of view: The field of view defines the diameter of the viewable area in mm (Hecht, 2016).

$$\text{FOV} = \frac{\text{Sensor Size}}{\text{Magnification}} \quad (1.6)$$

Numerical aperture: The numerical aperture (NA) describes the ability of the microscope objective to collect or emit light (Abbe, 1873; Hecht, 2016). It can be defined using

$$\text{NA} = n \sin \theta \quad (1.7)$$

where n is the refractive index of the medium between the objective lens and the sample, and θ is the maximum angle. The NA is important because it defines the **spatial resolution** of a lens. The spatial resolution refers to the ability for the microscope objective to distinguish between two closely spaced points or the minimum detectable distance between two closely spaced points (Born and Wolf,

2013). The spatial resolution can be defined with the Abbe limit

$$d = \frac{\lambda}{2\text{NA}} \quad (1.8)$$

where λ is the imaging wavelength (Abbe, 1873; Born and Wolf, 2013).

1.6 Noise, Sources and Detectors

The minimum level of detection in almost every area of measurement is determined by the level of noise. Random noise is made up of many independent sources some of which can be reduced or eliminated from measurements with filtering and proper grounding, some forms, however, are unavoidable and caused by fundamental physical processes.

A thorough understanding of noise sources will help improve the optical recordings with the aim of reducing or eliminating the need to filter or signal average. This section will introduce some of the causes of noise from both light sources and detectors and then go onto describe some commonly used post-processing techniques that can be used to filter or average out unwanted noise.

1.6.1 Measures of Noise in Signals

This section will define some of the commonly used terms for characterising noise in systems.

Signal-to-Noise Ratio: The signal-to-noise ratio (SNR) is the ratio of the signal power to the noise power and can be defined as

$$\text{SNR} = 10 \log_{10} \frac{V_s^2}{V_n^2} \quad (1.9)$$

where V_s and V_n are the signal and noise voltages in rms, respectively (Horowitz et al., 2015). If the variances are known the SNR can be defined as (1.10) assuming that the signal and noise are both mean-zero.

$$\text{SNR} = \frac{\sigma_{\text{signal}}^2}{\sigma_{\text{noise}}^2} \quad (1.10)$$

Dynamic Range: The dynamic range is closely related to the SNR and measures the ratio of the strongest signal and the minimum detectable signal (generally the noise) (Janesick, 2007; Horowitz et al., 2015).

Noise Floor: The noise floor can be thought of as the minimum detectable power or the level of background noise in a signal. The noise floor is calculated by summing all the noise sources (N_i) within the system, and because each source of noise is independent the total noise is added in quadrature:

$$N_{total} = \sqrt{N_1^2 + N_2^2 + \dots N_n^2} \quad (1.11)$$

1.6.2 Types of Noise

In a perfect world, only the desired signal would be present in recordings. In reality, there are fluctuations in the signal due to noise, or interference from equipment. The amplitude of the noise level will ultimately lower the dynamic range and sensitivity of the detector, which in turn will limit the minimum signal that can be detected with any certainty.

Johnson (Thermal) Noise

Johnson noise, also called thermal noise is generated by random electron movements in a conductor. The moving electrons lose energy as they collide with other atoms in the material. These collisions average to zero, but the fluctuations form Johnson noise (Vaseghi, 2008). The amplitude distribution is Gaussian with a flat (white) spectrum. The thermal noise voltage can be calculated using

$$V_{thermal} = \sqrt{4kTRB} \quad (1.12)$$

where k is Boltzmann's constant, T is the absolute temperature in Kelvin, R is the resistance, and B is the bandwidth. The thermal noise associated with a 50 k Ω electrode measuring action potential activity from neurons with a 5 kHz bandwidth at 37 °C is approximately 2 μ V. Johnson noise sets the lower limit (noise floor) on the noise voltage in any piece of equipment that has resistance, for example, the light source, detector, or amplifier. This noise can be reduced by cooling the equipment.

Shot Noise

Light and electric current consist of the movement of discrete particles, photons, and electrons, respectively. Shot noise is a fundamental noise limit which arises from statistical fluctuations in light intensity or current (Janesick, 2007; Paschotta

et al., 2008). The number of particles arriving in a time interval (x) follows a Poisson probability model:

$$P(x) = \frac{N^x e^{-N}}{x!} \approx \frac{1}{\sqrt{2\pi N}} \exp \frac{-x^2}{2N^2} \quad (1.13)$$

where N is the mean number of interacting particles (Yates and Goodman, 1999; Murphy, 2001). The right side invokes the central limit theorem, which states that given a sufficiently large N , the Poisson distribution can be approximated as Gaussian with a mean of N and a standard deviation of \sqrt{N} . A device is shot noise dominant when the amount of shot noise is much greater than other noise sources in the system, therefore, you need a large number of interacting particles (N), which in turn will increase the SNR and lead to better system performance. Shot noise is temperature and frequency independent. In optics, shot noise describes the fluctuation in the number of photons detected including the random conversion of photons to photo-electrons in the detector. The conversion from photons to electrons is related by the quantum efficiency and described further in Section 1.6.3 (Janesick, 2007). When the electronic charges act independently of each other, the photocurrent can be expressed as

$$i_n(rms) = \sqrt{2qI_{dc}B} \quad (1.14)$$

where q is the electron charge, I_{dc} is the current and B is the measurement bandwidth. Shot noise power can be defined as

$$P_{shot} = i_n(rms)^2 \cdot R_L = 2qI_{dc}BR_L \quad (1.15)$$

where R_L is the load on the shot noise current.

Flicker Noise

Flicker noise ($1/f$) is present in electronic devices at low frequencies (<100 Hz). At higher frequencies flicker noise is masked by noise from other sources. It is caused by the random fluctuation of electron flow associated with direct current. Flicker noise has a pink-shaped spectrum that varies with $N(f) = 1/f$ (Voss, 1979).

Interference

Interference can arise from electromagnetic noise or burst noise. Electromagnetic noise is picked up from other electronic devices and is most commonly from mains interference (50 Hz), which has a narrow spectrum and constant amplitude. Burst

noise is a brief pulse with broad spectrum occurring at random times and durations (Vaseghi, 2008).

Acoustic noise is another source of interference and is caused by moving sources, for example, air-conditioning, an optical table, or doors opening and closing, etc. Interference can often be eliminated with adequate isolation, grounding, and other controls (Vaseghi, 2008).

Relative Intensity Noise

Relative intensity noise (RIN) describes the instability in the optical power of an active semiconductor device, i.e., a laser or Superluminescent Light Emitting Diode (SLED) and is caused by spontaneous emission (Paschotta et al., 2008). The optical power of a laser or SLED can be expressed as

$$P(t) = \bar{P} + \Delta P(t) \quad (1.16)$$

where \bar{P} is the average power and $\Delta P(t)$ is a fluctuating quantity with a mean zero value. RIN can be defined as the ratio between the fluctuating quantity and the average power and is measured in dB/Hz (Paschotta et al., 2008). Statistically, this can be described with a power spectral density (PSD), which depends on the frequency:

$$S_I(f) = \frac{2}{\bar{P}^2} \int_{-\infty}^{\infty} (\Delta P(t)\Delta P(t + \tau)) \exp(i2\pi f\tau) d\tau \quad (1.17)$$

An RMS value can be calculated for specific measurement bandwidths by integrating the PSD over an interval of frequencies (Paschotta, 2009).

1.6.3 Detectors

Some important parameters for characterising cameras are discussed in this section. Many of the terms can be applied to any photosensitive device including photodiodes, and photomultipliers. These parameters will be discussed further in Chapter 4.

Quantum efficiency: defines how efficient the sensor is at converting incident photons to electrons, and is usually expressed as a percentage. It is a function of the wavelength (Janesick, 2007).

Read noise: is the noise generated by the electrons of the camera as the charge in the pixels gets transferred (Janesick, 2007; Photometrics, 2015).

Dark Current: thermal energy that is generated in the silicon of the detector. Increasing the temperature of the detector increases the dark current. Therefore, the simplest way to minimise the dark current is by cooling the detector. Dark current can be seen as a shot noise source (Janesick, 2007; Hecht, 2016).

Dark noise: statistical variation in the number of electrons generated within a pixel in the absence of photons (electron equivalent of photon shot noise). The dark noise is calculated as $n_d = \sqrt{I_d/\tau}$ where I_d is the dark current, and τ is the integration time (Janesick, 2007; Hecht, 2016).

Fixed pattern noise: any noise associated with the non-uniformity in each pixel's sensitivity. FPN increases linearly with the signal and is consistent spatially across all pixels in a detector (Janesick, 2007).

Readout noise: the number of electrons generated by the electronics when the pixel's charge is transferred from the pixel (Janesick, 2007).

Responsivity

The responsivity is a ratio of the generated photocurrent and incident optical power (A/W) (Paschotta et al., 2008). It can be expressed as

$$R = \eta \frac{q}{h\nu} \approx \eta \frac{\lambda(\mu m)}{1.23985} \quad (1.18)$$

where $h\nu$ is the photon energy, q is the electron charge, and η is the quantum efficiency.

Noise Equivalent Power

The noise-equivalent power (NEP) measures the sensitivity of a detector system and is defined as the signal power that gives an SNR of 1 with a bandwidth of 1 Hz (Paschotta et al., 2008).

$$\text{NEP}(W/\sqrt{Hz}) = \frac{N_0}{R} \quad (1.19)$$

where N_0 is the noise spectral density (PSD of noise in W/Hz) and R is the responsivity of the detector (A/W). Therefore, a detector with a small NEP is more sensitive. The SNR can be improved with the square root of the averaging time.

1.6.4 Detection of Signals in Noise

Detection of signals hidden in noise will require signal processing and can be completed in the time domain or frequency domain. There are many methods available to reduce the noise and this section briefly introduces some of the techniques employed during this PhD project.

Signal Averaging

Signal averaging is a digital technique used to separate a repetitive signal from noise without distorting the signal. Signal averaging assumes:

- The signal and noise are uncorrelated
- The timing of the signal is known
- The noise is random and has a mean zero value
- A signal is present

We can assume a waveform of continuous random, white Gaussian noise, “noise”, $N(t)$ that combines with a signal, $S(t)$ to give a waveform of “noise + signal” ($f(t)$).

$$f(t) = S(t) + N(t) \tag{1.20}$$

Signal averaging works by splitting $f(t)$ into epochs and summing them with the aim that the noise adds destructively and reduces while the signal builds up, as illustrated in Figure 1.5. The signal-to-noise ratio increases with the \sqrt{N} , where N is the number of epochs or repeats, shown in Figure 1.6 (Hassan and Anwar, 2010).

Signal Detection Theory

Signal detection theory was developed in the 1950’s for electronic communication systems (Marcum, 1960). It has since been applied to a whole range of disciplines from analysing psychophysical experiments (Swets, 1964) to forming error matrices in machine learning (Stehman, 1997). Optical detection of APs is a problem of signal detection because it is more important to detect when the event occurred rather than the exact waveform. At every time point, there are two possibilities: H_0 , the null hypothesis, that no AP occurred; and H_1 , the alternative hypothesis is that an AP did occur.

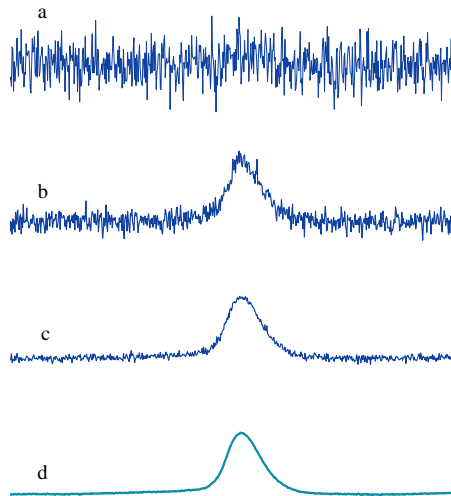


Figure 1.5: Summing the simulated time-aligned signal epochs (d) corrupted with random noise (a) improves the SNR. The result of averaging 100 of these time epochs is in (b), and (c) is after 1000 repeats. The data was generated using experimental whole-cell patch recordings and random, white noise added using MATLAB.

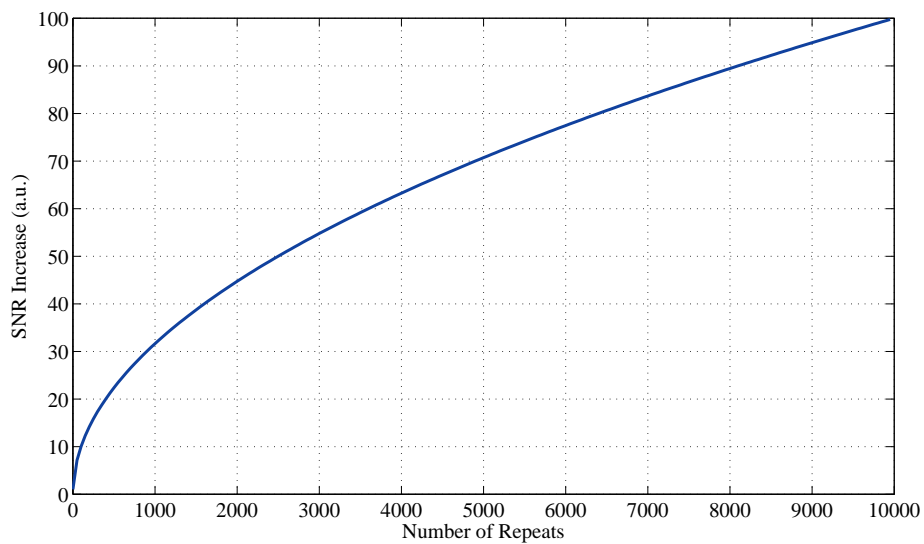


Figure 1.6: Theoretically verifying the SNR improvement as the number of repeats (N) increases.

Considering the signal from the previous section (1.20). By assumption the “noise” distribution has a mean, μ_n of 0 and standard deviation, σ_n of 1. The “signal + noise” distribution, μ_s and σ_s depends upon the strength of the signal (or SNR). When a “noise + signal” distribution is detectably different from the noise, i.e., has a SNR of one, the two distributions are separated by a discriminability index (d'). The discriminability index (d') is measured by taking the difference between the means of the “noise” and the “signal + noise” distributions. When the standard deviations are equal $\sigma_n = \sigma_s$, d' can be calculated using (1.21).

$$d' = \frac{(\mu_s - \mu_n)}{\sigma_n} \quad (1.21)$$

As the SNR decreases the amount of overlap between the two distributions increases and the signal becomes harder to detect using this method.

Taking this into account it at every time point there are four possible outcomes:

- True positive (TP) - an AP was stimulated and an AP was detected
- False negative (FN) or miss - an AP was stimulated and an AP was not detected
- False positive (FP) - no AP was stimulated and an AP was detected
- True negative (TN) - no AP was stimulated and no AP was detected

The conditional probability matrix, Table 1.4 takes into account whether stimuli were present or absent and summarises all eventualities that can occur.

Table 1.4: Conditional probability matrix

	Respond "Present"	Respond "Absent"
Stimulus Present	True Positive (TP)	False Negative (FN) (Type II error)
Stimulus Absent	False Positive (FP) (Type I error)	True Negative

The Neyman-Pearson decision rule sets a threshold to decide whether an AP has occurred or not, illustrated in Figure 1.7. If the signal goes above this threshold, then an AP has occurred, and the hypothesis H_1 is true. This threshold is set

arbitrarily and is a trade-off between the acceptable level of false positives (false alarms) and false negatives (missed events) (1.22).

$$\mathfrak{R}(\text{threshold} = \theta) = P_{FP}(\theta) + P_{FN}(\theta) \quad (1.22)$$

A higher threshold is more specific, i.e., has less false positives but more false negatives and is therefore, more likely to miss an AP occurring. Conversely, a lower threshold is more sensitive, i.e., has more false positives but less false negatives so is more likely to incorrectly identify noise as an AP (Wickens, 2002; Sjulson

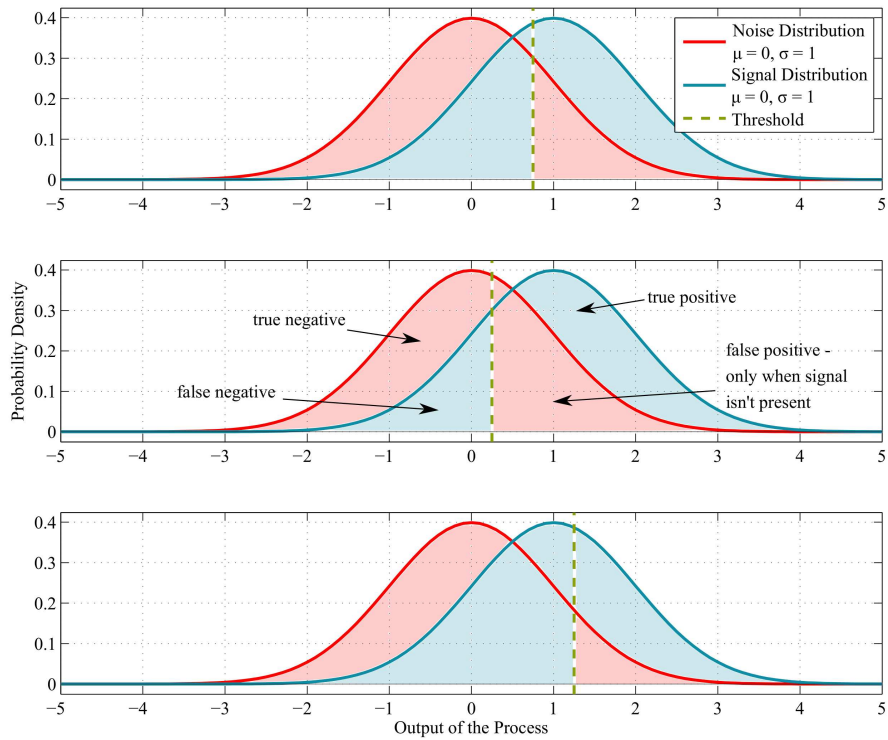


Figure 1.7: Gaussian probability density functions for detection. The vertical line is the arbitrarily set threshold. Responses lower than this threshold are absent; those higher are present. Figures show the effect of moving the threshold value. A lower threshold value (middle) shows more true positives being detected but also more false positives. A higher threshold value (bottom) shows more true positives being missed but there are less false positives.

and Miesenböck, 2007; Vaseghi, 2008). The curve on the left (red) is the “noise” distribution, and the curve on the right (blue) is for the “signal + noise” distribution. The figure is split into four areas that correspond to true positives, false positives, true negatives, and false negatives. Moving the threshold to a lower or higher value changes the ratio of false positives to false negatives.

1.7 Aims and Objectives

The ability to detect action potentials with single-cell resolution, for a long period of time, across a large network is important for advancing our understanding of the brain. The technologies that currently exist, however, are limited in this aim. Based on the literature, surface plasmon resonance theoretically appears to be a promising alternative. The technique is sensitive to refractive index changes on the surface of the metal, which are present during neural activity and SPR sensors have demonstrated the ability to detect small refractive index changes, down to 10^{-6} RIUs in an intensity modulation scheme (Sepúlveda et al., 2006; Campbell and Kim, 2007). SPR has distinct advantages over other detection techniques as optical techniques are not susceptible to the same issues that electrically based techniques are. SPR is a label-free technique, avoiding problems with fluorescent dyes such as bleaching and toxicity. There are isolated reports of LSPR and SPR detecting neural activity, but they lack adequate controls and have not been replicated. The sensitivity of SPR sensors could be improved by using LSPR or a combination of SPR and LSPR in micron-sized structures as a means of signal amplification (Live et al., 2008; Live and Masson, 2009; Live et al., 2010). However, it is anticipated that these signals will be very small and will require consideration, measurement, quantification, and minimisation of noise sources and application of signal detection theory.

Aim

The aim of this PhD project was to develop a sensor that could detect every action potential, from every neuron in a relatively large network for a long period of time.

Objectives

The objectives to fulfill this aim are as follows:

- Estimate the size of the signal that occurs during an action potential.
- Determine the noise floor of the system to ensure the signal can be detected.
- Measure the angular and intensity surface plasmon resonance responses of the planar gold sensors.
- Culture primary rat hippocampal neurons on the planar gold sensors and detect refractive index changes using surface plasmon resonance.
- Develop a protocol to fabricate the gold microstructures.
- Measure the angular and intensity surface plasmon resonance responses of the gold microstructure sensors.
- Culture primary rat hippocampal neurons on the gold microstructure sensors and detect refractive index changes using surface plasmon resonance.

1.7.1 Thesis Structure

Surface plasmon resonance could be a viable technique to be able to detect every action potential with single-cell resolution for an extended period of time. The SPR sensors developed in this thesis were used to monitor cultured neuronal networks, during neuronal development and regeneration processes. To achieve the aims and objectives of this PhD, the project was divided into four sections which correspond to the experimental chapters.

Chapter 4 theoretically determines the refractive index changes of an action potential signal. The refractive index change on the gold surface during electrical activity was modelled and the reflected light intensity changes on an SPR sensor were computed. The effect of varying the distance between the neuron and the surface was investigated. Finally, the minimum detectable signal that will be required of the sensor was calculated.

Chapter 5 characterises the sensitivity of the system concerning the noise. The noise floor of the system was estimated by calculating the various sources of noise

from the light source and detector. The minimum detectable signal for the system was determined and the refractive index and light intensity changes from chapter 3 were compared, to confirm the system was theoretically capable of detecting APs before and after signal averaging. The effect of the SLED and LED on the temperature of the coverslip was investigated. Additionally, an equation was derived to determine the angle of incidence at the sample with respect to the position of the focused SLED on the back focal plane.

Chapter 6 introduces a planar gold SPR sensor. The optical properties and sensitivity of these sensors were characterised to ensure they were capable of detecting small refractive index changes. Primary rat hippocampal neurons were cultured on the planar gold surfaces. The neurons were electrically stimulated while the optical SPR response was simultaneously recorded to demonstrate light intensity changes arising from neural activity. Patch clamping was used to stimulate the neuron and validate the SPR response as it is the most accurate method for recording and inducing action potentials. The protocol and analysis methods employed are introduced and described in detail.

Chapter 7 introduces and develops a new sensor. Microstructures were fabricated using photolithography. The motivation for developing microstructures was because extracellular, electrical recording (MEAs) are currently the best method available to detect every action potential from every neuron for a long time. MEAs are only lacking in their spatial resolution because of the restrictions on the size of the electrodes because smaller electrodes will result in a higher impedance and lead to a poor SNR. Developing a “plasmonic MEA” would enable us to place more electrodes thus improving the spatial resolution. The reduction of the SPR sensor size will constrict the propagation length of the SPP and result in a less sensitive SPR response (Live and Masson, 2009). The optical properties of the microstructures were investigated to find whether they support surface plasmons. Furthermore, the microstructures needed to be sensitive to refractive index changes. The microstructures sensitivity to refractive index changes was confirmed experimentally by recording the sensitivity of the samples with different concentrations of an electrolyte solution. After characterising the plasmon response of the microstructures, neurons were cultured on the gold stripes, and the experiments from chapter 5 were repeated.

CHAPTER 2

METHODS

2.1 Ethics

All primary neural cells used for experiments were obtained in accordance with guidelines set out in the code of practice for humane killing under Schedule 1 of the UK Home Office Animals (Scientific Procedures) Act 1986, and approved by the University of Nottingham Animal welfare and Ethical Review body.

2.2 Materials, Equipment and Software

For a comprehensive list of materials, equipment and software used please refer to Appendix A.1.

2.3 Substrate Preparation

In the following sections, a detailed description of the preparation processes for the sensors, and the equipment used is explained.

2.3.1 Pre-Treatment

The as received glass coverslips were sonicated for 10 – 15 minutes in 10% Decon90 then rinsed with deionised water (DI) and sonicated for a further 5 minutes in DI before being dried using a nitrogen (N_2) steam. The coverslips were then sonicated in acetone, methanol and isopropanol (IPA) for 10 mins each. Following the solvent wash the coverslips were subjected to an oxygen plasma treatment at 0.25 mbar, at 50 W for 10 minutes.

2.3.2 Silanisation

The glass coverslips were treated with (3-mercaptopropyl)trimethoxysilane (MPTS) to present thiol groups prior to thermal metal evaporation. Silanisation was performed immediately after pre-treatment. The MPTS deposition solution was prepared by mixing 1% v/v MPTS solution in anhydrous toluene. When the clean glass coverslips were removed from the plasma oven the coverslips and rack were immersed in pure toluene for 1 minute. The rack and coverslips were transferred to the MPTS solution and left at room temperature for at least 30 minutes. Following immersion the coverslips were rinsed in pure toluene, then IPA, and dried with N_2 . The coverslips were left to bake on a hotplate at 100 °C for at least one hour but ideally overnight.

2.4 Planar Gold

2.4.1 Evaporation System

The MPTS glass coverslips were coated with ~50 nm thick gold by thermal metal evaporation. The gold thickness is critical and the effect on the SPR response for a difference of $\pm 10\%$ is shown in Section 3.1.1. Gold evaporation was carried out using an Edwards E306A thermal evaporator. Gold wire was placed in a filament and the chamber was pumped down to 10^{-1} mbar with a rotary pump, then to 10^{-7} mbar with an oil diffusion pump, while being cooled with liquid nitrogen. A current of ~30 A was passed through the filament so the metal melts and evaporates onto the glass coverslips held above the source with rare earth magnets. An Intellemetrics IL100 quartz crystal microbalance was used to estimate the evaporation rate and

film thickness.

2.5 Fabrication of Microstructures

2.5.1 Photomask

The photomask was designed using AutoCAD and exported to a GSDII file to send for fabrication by Compugraphics Jena GmbH (Germany), see Table 2.1 for the photomask design details. A quartz mask was required because the mask aligner generates a 365 nm wavelength of light (*i*-line). Quartz also has the advantage of a much lower coefficient of thermal expansion.

Table 2.1: Photomask Design Details

Mask Size (inch)	$3 \times 3 \times 0.060$
Material Type	Quartz
Min Critical Feature Size (μ)	2.0
Critical Dimension Tolerance (μ)	± 0.25
Defectivity (cm^{-2})	0.5
Defect Size (μ)	0.5

2.5.2 Photolithography

The gold patterns were fabricated in a clean room with an image reversal process. The process was optimised and this procedure is described below. The optimisation steps and results can be found in Section 6.2. The treated glass coverslips were held onto the spin coater chuck by vacuum. An image reversal photoresist, AZ 5214E was spun onto the coverslips at 4000 rpm for 30 seconds to give a uniform layer of about 1.4 μm . The edge beads were removed with a cotton bud soaked in acetone to ensure that a close contact was formed between the photomask and substrate. The substrate was baked on a hotplate at 110°C for 50 sec to remove the water from the photoresist. The imaging resist was exposed for 3 sec with a light intensity of 9.2 mW/cm² using a Karl Suss MBJ3 mask aligner. The mask aligner generates an ultraviolet light with a wavelength of 365 nm using a high-pressure mercury-vapour lamp. The substrate underwent a post-exposure bake on a hotplate at 120°C for 2

mins. A flood exposure was performed on the substrates without a mask for 30 sec. Finally the substrates were developed in concentrated AZ 726 MIF for 25 sec. The patterned coverslips were then placed in the thermal evaporator for gold deposition. Post evaporation the coverslips were soaked in Dimethyl Sulfoxide (DMSO) at 60°C for approximately one hour before rinsing with DMSO and DI to remove the excess photoresist.

2.6 Functionalisation of the Surface

Primary cells need to be able to bind to the surface in order to survive and neuronal cells can not grow directly on untreated glass or gold. The cell culture needs a non-toxic surface, and because cell-surface interaction is actually an interaction between cells and surface bound proteins, the surface needs suitable protein adsorption properties.

2.6.1 AUT on Planar Gold

The surface chemistry of gold can be modified using thiol-containing molecules to form a self-assembled monolayer on the surface (Ulman, 2013; Jans et al., 2009). Thiols on gold, for example, 11-Amino-1-undecanethiol hydrochloride (AUT) make the strongest bond and are known to be very stable (Arya et al., 2009).

Therefore, for cell based experiments on planar gold, the coverslips were treated with AUT to generate a self-assembled monolayer (Palyvoda et al., 2007). The gold coverslips were solvent cleaned, followed by an oxygen plasma treatment (as outlined in Section 2.3.1 without sonication). The AUT was dissolved in ACS grade Ethanol at 1 mM, which was then poured into an immersion cylinder to completely cover the gold. Immersion time was not less than 18 hours. Following immersion the solution was drained from the cylinder and the gold was thoroughly rinsed, first with ethanol to remove the bulk AUT solution, and then with distilled water to remove the cytotoxic ethanol. The coverslips were dried thoroughly with N₂ before plating.

2.6.2 PEI on Microstructures

AUT was used to modify gold surfaces with amine groups to generate cell adhesive areas. The microstructures fabricated were predominantly glass with at most one third of the $300 \times 300 \mu\text{m}$ area being gold. Therefore, an alternative to AUT was required. Poly(ethyleneimine) (PEI) was chosen after a cell viability assay was performed on both glass and gold surfaces. The methods are outlined in Section 2.7.2 and the results given in Section 6.4.1. PEI is a polymer that binds to the surface through electrostatic interactions and covers the surface with positively charged amino acids and has been proven to provide a strong attachment between the cell and the surface (Wiertz, 2010; Sun et al., 2012).

The microstructures and the planar gold controls were solvent cleaned. The PEI solution was diluted in DI to a concentration of 0.1% and briefly sonicated to fully dissolve the PEI. Before applying to the solvent cleaned surfaces the solution was sterile filtered. A 0.5 mL drop was applied to each coverslip and left for two hours at room temperature. After two hours the PEI was discarded and the coverslips were rinsed three times with DI before being left immersed in DI for at least another two hours. Finally the DI was removed and the coverslips were left to dry overnight (Lelong et al., 1992; Bledi et al., 2000).

2.7 Cell Culture

Recipes for media and solutions can be found in Appendix A.2.

2.7.1 Harvesting, Plating and Feeding

The hippocampi were dissected from E18 Wistar rat embryos following a standard protocol (Kaech and Banker, 2006). The hippocampi were enzymatically dissociated in 2 ml Hanks balanced salt solution, 200 μl of Trypsin and 20 μl of DNase at 37°C for 30 minutes. Then 100 μl Trypsin Inhibitor was added to inactivate the trypsin. The cells were washed in fresh neurobasal medium twice and 20 μl of DNase was added before preparing the cell suspension. The cell suspension was prepared by gently titrating the solution using a glass, fire-polished Pasteur pipette until there was no visible tissue. The disassociated cells were placed in a centrifuge and spun down at $250 \times g$ for 5 minutes to wash the cells. The pellet was then re-suspended in

fresh neurobasal medium. The concentration of the cell suspension was calculated using a haemocytometer and diluted to a concentration of 300,000 cells per ml.

The primary rat hippocampal neurons were plated on the functionalised coverslips (gold or microstructures) at double density or higher ($\sim 150,000$ cells per coverslip). The cell suspension was left in the incubator for 30 minutes to allow the neurons to adhere to the surface after which an additional 1.5 ml of fresh neurobasal medium was added to each well plate. The cultured neurons were stored in an incubator at 37°C , with high humidity to prevent the media drying out, with 5% CO_2 mixed into the air and O_2 maintained at atmospheric levels (20 – 21%).

The day after the preparation all the medium was removed and replaced with fresh. Thereafter, the cultures were fed every four days for two weeks by removing $750\ \mu\text{l}$ and adding $1000\ \mu\text{l}$ of fresh medium to compensate for evaporation. If the cultures were fed for any longer, cell processes began to break down and they deteriorated quickly. For the SPR/electrophysiology validation experiments (Section 2.13), the neurons were left to mature for at least two weeks before experimentation. In general the *in vitro* cultures could be kept for approximately 3 – 5 weeks before the osmolarity of the media became too high and caused cell shrinkage.

2.7.2 Live Dead Cell Viability

Live dead staining was performed on neurons cultured on gold patterned glass coverslips at 12 DIV to assess the viability of the different surface functionalisation methods. Calcein (Excitation/Emission 494/517 nm) and Propidium Iodide (Excitation/Emission 536/617 nm) were used to stain the live and dead cells, respectively. The Calcein and Propidium Iodide were added to the media at a concentration of 0.1%. The samples were left in the incubator for 30 minutes before taking fluorescence images on the Nikon Eclipse Ti inverted microscope using a $10\times$ objective (NA = 0.25) and the QuantEM:512SC EMCCD camera. Post-processing was performed using Image-J.

2.8 Surface Analysis

2.8.1 Ellipsometry

The thickness of the gold coverslips was measured with a spectroscopic ellipsometer at a fixed incident angle (70°) and with a wavelength range between 380 – 900 nm.

2.8.2 Profilometry

The thickness of the microstructures was measured using a stylus profilometer (KLA-Tencor Alpha Step D-120) at a speed of 0.05 mm/sec, a scan length of 0.4 mm, and a force of 8.0 mg. Data levelling was done in software and post-processing in MATLAB.

2.8.3 Microscopy

Brightfield images were taken on a Nikon Eclipse Ti inverted microscope with a $10\times$ magnification objective ($NA = 0.25$). The images were captured on a Hamamatsu ORCA-Flash4.0 V2 Digital CMOS camera. The images were analysed and processed in Image-J.

2.9 Imaging Systems

The custom built imaging system (Surface Plasmon Microscope, SPM) that has been developed can be used to image using a variety of different techniques including Total Internal Reflection (TIRM), Surface Plasmon Resonance (SPR), Reflection, and Transmission microscopy, shown in Figures 2.1 and 2.2. The rig was mounted on a floating optical table (Thorlabs) to minimise mechanical noises. The different imaging modalities will be described in the following sections.

2.9.1 Measurement Conditions

Conditions were standardised and maintained for all experiments throughout the project to ensure consistency and increase reproducibility.

Temperature: Performed at room temperature around 20°C .

Camera bit depth: Number of bits set as high as possible to minimise quantisation

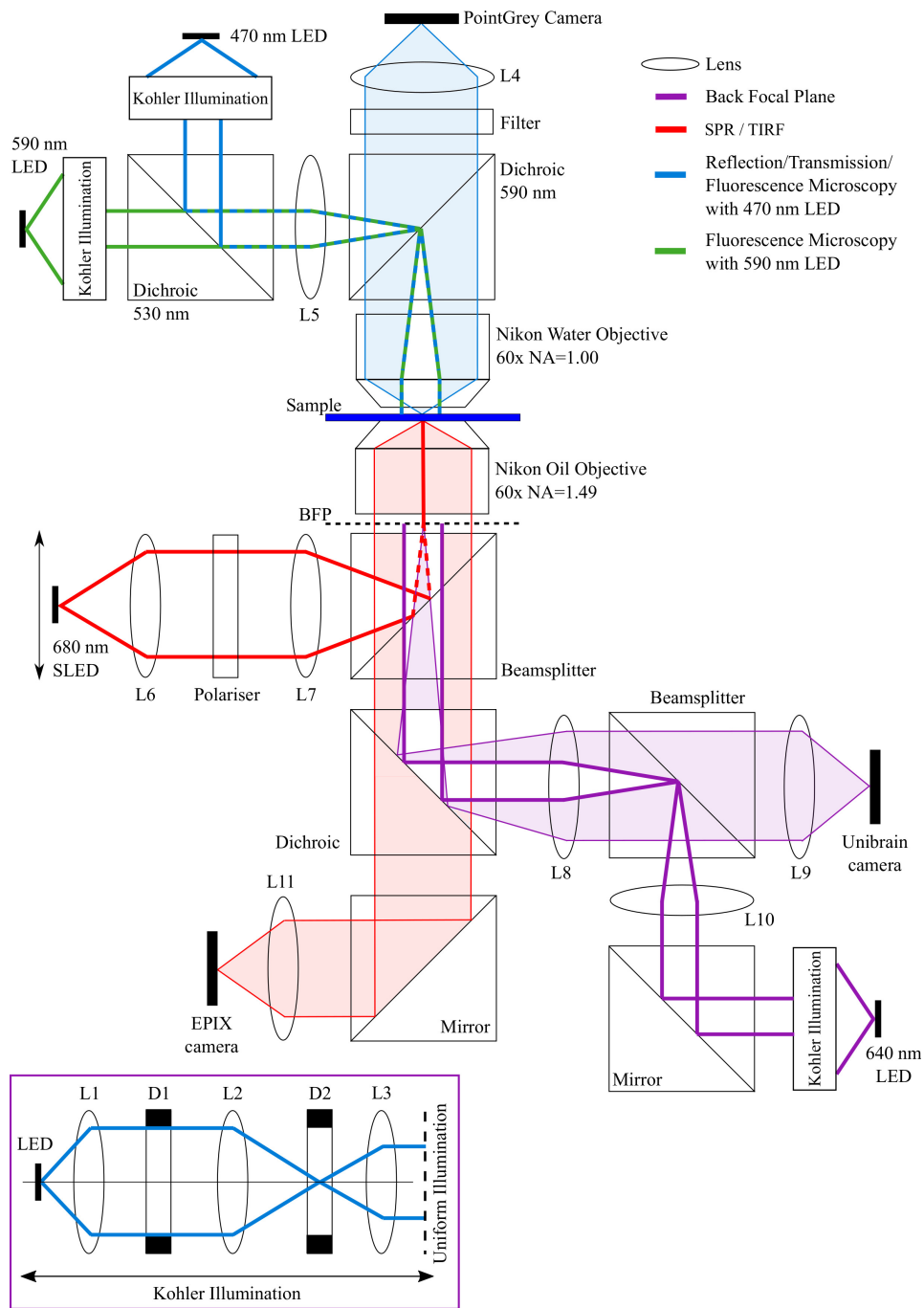


Figure 2.1: Schematic of the SPM that was developed. Several imaging modalities can be exploited and the optical pathways have been traced on the figure. Imaging pathways are shaded and illumination pathways are have the darker line. All wavelengths chosen were appropriate and will be explained in text. The component information is given in Appendix B.1.

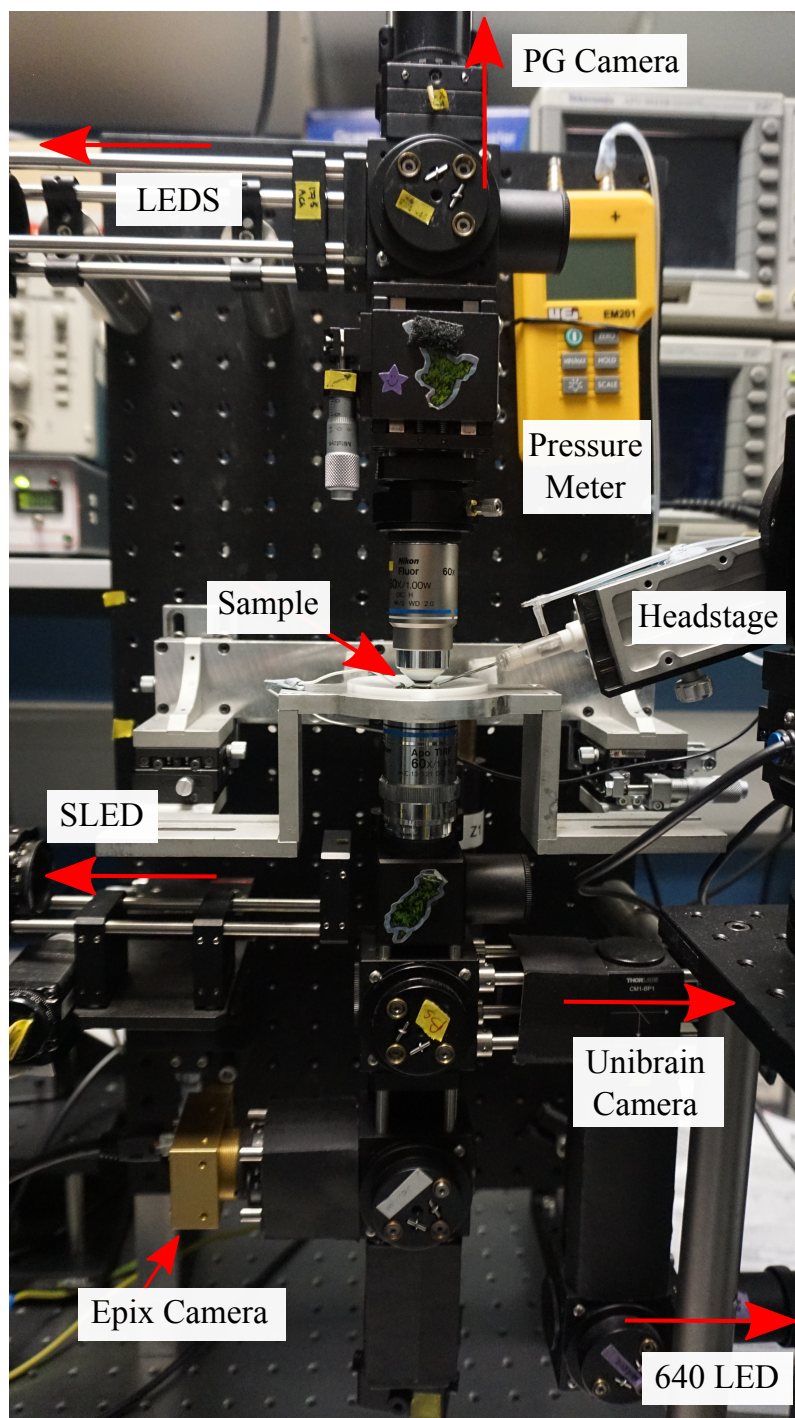


Figure 2.2: Photo of the SPM that has been developed.

effects. Recorded using 10 bits, saved as 8-bit to ensure compatibility between software.

Camera Gain: Gain set to one.

Camera Exposure: Maximum allowed for SPR/Ephys experiments and set to 0.124 msec for everything else.

In order to reduce noise, optical pathways were enclosed in black card and the lights were turned off to minimise the impact of stray light.

2.9.2 Back Focal Plane

The 640 nm LED was used in conjunction with Kohler illumination to illuminate the back focal plane of the Nikon Oil Objective lens (CFI Apo TIRF 60× Oil, Nikon, NA = 1.49) with uniform light (Keller, 1998). The back focal plane was monitored on the Unibrain camera (Fire-iTM from Unibrain Inc.).

Determination of the Angle of Incidence

The angle of incidence of the SLED on the sample was calculated through the sine condition of an aplanatic optical system (Richards and Wolf, 1959):

$$d = f \sin \theta \tag{2.1}$$

Where d is the offset of the laser from the optical axis of the objective in pixels, f is the focal length of the objective, and θ is the angle of incidence. The angle of incidence was determined using the relative displacement from the critical angle using solvents of different known refractive indices on glass, detailed in Table 2.2. The critical angle is the angle where all the light is totally internally reflected. The theory of total internal reflection is described in Section 3.1.1.

The critical angle was calculated from the relative displacement:

$$d - d_0 = f(\sin \theta - \sin \theta_0) \tag{2.2}$$

where d_0 and θ_0 are the reference offset and the reference angle, respectively. Each solvent was added to the substrate in turn and the focused 680 nm SLED was scanned across the BFP with the stepper motor moving at 0.1 mm/sec. The radial position of the focused SLED at the BFP then relates to angle of incidence at the sample

plane (Burghardt, 2012). The reflected light was imaged using the EPIX camera at 24 fps with an exposure time of 0.124 msec. The resulting intensities detected at the EPIX camera were processed in MATLAB. The reflected light intensity was plotted with respect to the radial position of the SLED along the x -axis. The position where all light is reflected, i.e., being totally internally reflected was exported and related to the critical angle for each solvent. Literature values for gold were used (Johnson and Christy, 1972).

Table 2.2: The solvents that were used to determine the angle of incidence, their refractive indices at 680 nm, and corresponding critical angle.

Solvent	n (@ 680 nm)*	Calculated θ_c with glass ($n = 1.52^{**}$)
Air	1.000	41.15
Methanol	1.325	60.91
Water	1.331	61.27
Acetone	1.357	63.35
Ethanol	1.359	63.59
Isopropanol	1.381	64.96
Toluene	1.497	77.92

* References: Methanol, Isopropanol, and Toluene (Moutzouris et al., 2014). Water (Hale and Querry, 1973). Acetone (Rheims et al., 1997). Ethanol (Kedenburg et al., 2012).

** See Section 3.2.1.

2.9.3 Total Internal Reflection Microscopy

Total internal reflection microscopy was achieved using the 640 nm LED uniformly illuminating the back focal plane of the sample. The aperture diaphragm (D1) within the Kohler illumination was closed so no angles above the critical angle were illuminated. The reflected light was imaged using the Unibrain camera.

2.9.4 Reflection and Transmission Microscopy

Reflection microscopy was performed using the 470 nm LED reflecting off the sample and imaged on the Point Grey Grasshopper camera. Transmission microscopy was performed using the 470 nm LED transmitting through the sample to the EPIX camera.

2.9.5 Surface Plasmon Resonance

The SPM that has been developed uses a high NA objective (Nikon, 60 \times , NA = 1.49) lens and is able to exploit both angular and intensity modulation. Angular modulation was achieved using the 680 nm super luminescent diode (SLED), which generates light that is focused onto the sample through the objective lens. SLEDs have a high spatial coherence but a short temporal coherence, which allows the output to be focused to a very tight spot (Hitzenberger et al., 1999; Deng and Chu, 2017), without suffering from the effects of laser speckling (Dainty, 2013). The p -polarised light from the SLED excites the surface plasmons. The most common methods to excite surface plasmons are described in Section 3.1.1. The focused SLED beam was scanned across the back focal plane of the sample, changing the angle of incidence on the sample using a stepper motor moving at 0.1 mm/sec. The reflected light was imaged on the EPIX camera at 24 fps, with an exposure time of 0.124 msec to provide reflection values as a function of angle of incidence. Regions of interest were selected on the surfaces using Image-J and the z -axis profile was exported to MATLAB.

Intensity modulation was performed in much the same way but the angle of incidence (θ) was fixed at the angle with the steepest gradient (around 30% of the minimum, θ_{spr} and θ_c). The reason for this is discussed further in Section 2.13.

The field of view was increased to 350 \times 250 μm by mismatching the objective and tube lens, which reduced the effective magnification of the objective. The focal length of the tube lens used was 60 mm instead of 200 mm, so the new magnification was calculated using

$$\text{Magnification} = \frac{f_2}{f_1} \quad (2.3)$$

where f_1 is the focal length of the objective and f_2 is the focal length of the tube lens. The focal length of the tube lens, f_2 should be 200 mm as defined on the

datasheet and given the magnification is $60\times$, f_1 will be 3.33 mm. By mismatching the tube lens and objective the magnification will change. Using the new tube lens length of 60 mm the actual magnification can be calculated as $18\times$.

2.10 Noise and Efficiency

The noise floor of the imaging system was found by identifying the noise source with the highest value. The noise values from the the SLED (RIN) and the EPIX camera were measured. An SLED was used over other available light sources, for example a laser, because, in theory, it has extremely low noise (Foust et al., 2008). The shot noise of the SLED was calculated by measuring the output power from the SLED using a power meter and determining the standard deviation. The noise fluctuation over time (RIN) was recorded by focusing the SLED in total internal reflection mode on the SPM with glass with the angle of incidence set so all light is being reflected to the EPIX camera. The noise was calculated from the standard deviation. The dark current of the EPIX camera was measured by covering the camera sensor and the noise fluctuation was recorded using the software at 250 Hz for 15 seconds. The specifications for the EPIX camera can be found in Appendix B.1.

2.11 Sensitivity Experiments

Sensitivity experiments were performed on the planar gold surfaces and microstructures to determine the minimum refractive index change (sensitivity) that could be detected. Different concentrations of Sodium Chloride (NaCl) salt solutions were added to a chamber on top of a gold coverslip whilst the SPR intensity response was measured. The NaCl solutions were used at a reference osmolality of 302 mOsm to be comparable with extracellular solution resulting in a reference refractive index of 1.3342. Deionised water was added to the sample first to find the reflection gradient maximum and the SLED was positioned here for the entirety of the experiment. While keeping all other parameters fixed, the refractive index of the media was adjusted using different concentrations of salt solutions, detailed in Table 2.3. The reference concentration was returned to between each step to ensure that the change in light intensity was not due to drift. The change in refractive index was calibrated with an Abbe Refractometer (Anton Paar, Abbemat 200). The reflected

light from the sample plane was recorded using the EPIX camera at 100 Hz. To allow the solution to stabilise, 30 – 60 seconds was left between each step. The resulting intensities were exported using Image-J and further analysis was performed in MATLAB. The resulting plot is ΔR as a function of the refractive index (n) of the dielectric. The experiments were repeated on planar gold with Potassium Chloride (KCl) and Sodium Fluoride (NaF) to investigate the cause of the long transients seen in the responses.

Table 2.3: Procedure to dilute or concentrate the media on the sensor for the desired change in refractive index.

Refractive Index*	Concentration** (g/l)	C_{add} ***
1.3342	1.000	-
1.3340	0.868	0
1.3342	1.000	2
1.3344	1.132	2
1.3342	1.000	0

* The refractive indices shown are for the NaCl solutions. .

** The concentration is normalised to the reference refractive index of the starting refractive index. A concentration of '1' corresponds to a reference osmolality of 302 mOsm. This osmolality was chosen to be comparable with extracellular solution resulting in a reference refractive index of 1.3342.

*** C_{add} indicates the added solution; '0' for DI water and '2' for 19 g/l of the salt solution.

2.12 Electrophysiology

2.12.1 Electrophysiology Recordings

Intracellular recordings and stimulation were performed with glass micropipettes pulled with a pipette puller from Sutter Instruments (Heat 525, Pull 0, Vel 65, Time 250, Pressure 500, Ramp 525, and Program Loop 1) using fire-polished Borosilicate glass with filament also from Sutter Instruments (O.D. 1.5 mm, I.D. 1.10 mm, Length

10 cm) to obtain a pipette resistance between 5 – 8 M Ω . The pipette resistance defines the diameter of the tip of the pipette (Standen et al., 1987; Sherman-Gold, 1993). If the tip diameter is too large, i.e., has a small resistance then a small cell could be sucked into the pipette. Conversely, a pipette with a large resistance, the tip diameter will be too small and it could be difficult to get a G Ω seal or debris in the solution could easily get trapped and block the pipette (Standen et al., 1987; Sherman-Gold, 1993). Pipettes were filled with ICS: 105 mM KCl, 10 mM HEPES, 2 mM Na₂-ATP, 2 mM Mg-ATP, 10 mM Na₂ Phosphocreatine, and 1 mM EGTA (243 mOsm and pH 7.4) (Clark and Barbour, 1997) and fitted to the electrode holder containing a silver chloride (AgCl) wire. An AgCl ground electrode was placed in the extracellular solution containing 110 mM NaCl, 3 mM KCl, 10 mM HEPES, 15 mM Glucose, 2 mM MgSO₄, and 2 mM CaCl₂ (pH 7.4). The osmolality of the ECS was matched to the cell media before the experiment. Whole cell recordings were performed with a seal resistance of \sim 2 G Ω . The membrane potential was held at -60 mV during current clamp. All experiments were performed at room temperature. Signals were amplified with an AxoPatch 200A amplifier (Axon Instruments), and converted to a digital signal using a National Instruments DAQ. WinWCP was used for data acquisition and analysis. Results were analysed in MATLAB.

2.13 Validating SPR / Electrophysiology Experiments

To validate that the optical response imaged by the SPR was caused by neural activity it was necessary to induce an action potential in the neuron being imaged. Whole-cell patch clamp was used to stimulate the target cell whilst the electrical (intracellular recording) and optical responses (extracellular) were recorded simultaneously. The full experimental pipeline of the steps and methods needed to reach this stage can be found in Appendix A.3.

To synchronise the electrophysiology and optical recordings, the electrophysiology software (WinWCP) and EPIX camera were externally triggered. WinWCP was triggered at 5 Hz to begin stimulating the neuron whilst recording the voltage across the membrane. The neuron was triggered at 5 Hz because some reports have assumed an average rate of AP spiking at 5 Hz (Sharpeykar, 2010; Harris et al., 2012). The EPIX camera software was triggered at 8 kHz to capture images of the SPR response

at the same time. Two function generators were used. The first function generator outputs a continuous 5 Hz pulse for x amount of cycles. This is the master trigger and the output goes to the input (TTL) of the second function generator. The second function generator requires both channels. Channel 1 triggers the electrophysiology stimulation and recording at the same frequency as the master trigger. Channel 2 triggers the EPIX camera to capture images at 8 kHz for a set amount of time as determined by the stimulation protocol used. The pulse duration and amplitude for all triggers was $62.5 \mu\text{secs}$ and 1.75 V, respectively. The setup is illustrated in Figure 2.3.

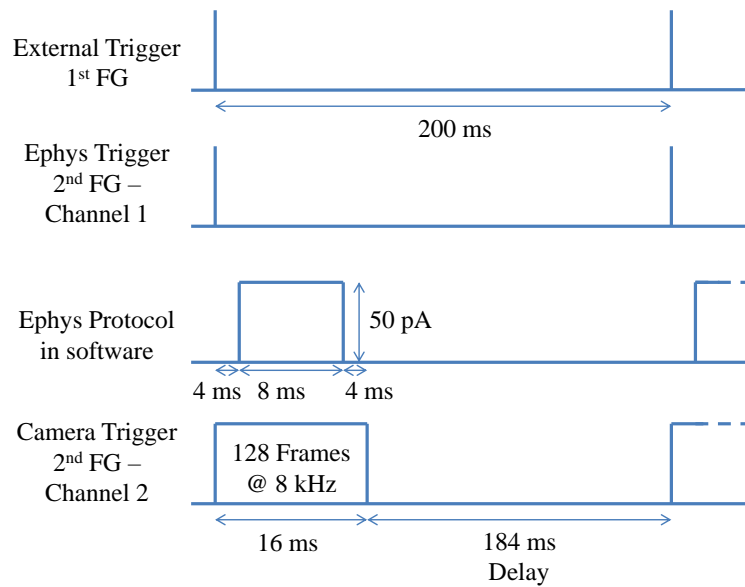


Figure 2.3: Triggering Setup. The 1st function generator acts as a master trigger to synchronise the electrophysiology and camera software. As soon as the master function generator triggers the camera starts capturing images at 8 kHz. The electrophysiology software has a 4 msec delay before the protocol is started.

To stimulate an action potential, depolarising current pulses with amplitude between 50 – 80 pA for 26 – 42 msec at 32 kHz were applied in current clamp mode. The software recorded the voltage across the membrane for the entire protocol. The triggering of the EPIX camera was set to save images at 8 kHz (125 μsec temporal resolution) for the entire recording duration of the electrophysiology protocol. Therefore, the number of images required increased with increasing the time of the

electrophysiology stimulation protocol.

To allow such a high frame rate the region of interest being imaged was restricted. At the smallest an area of 48×48 pixels was imaged. The distance of one pixel on the image can be calculated using (2.4), where the size of one pixel on the EPIX camera is $9.9 \mu\text{m}$ (Appendix B.1) and the magnification is $18\times$ as $0.55 \mu\text{m}$.

$$\text{distance} = \frac{\text{pixelsize}}{\text{magnification}} \quad (2.4)$$

Therefore, the total area imaged was $26.4 \times 26.4 \mu\text{m} = \sim 700 \mu\text{m}^2$. As shown in Section 6.1.1 the average diameter for a neuron is $\sim 13 \mu\text{m}$, therefore, it was possible to image one whole neuron and surrounding area of extracellular matrix as a control. The exposure time can at most be the inverse of the frame rate $1/8000 = 0.125$ msec, to ensure no frames were missed the exposure time was set to be less than this at 0.124 msec.

2.13.1 Procedure

The procedure to image the SPR response while simultaneously stimulating the neuron of interest with whole cell patch clamp is as follows. The letters correspond to steps from the flowchart in Figure 2.4. First, a neuron was selected using reflection microscopy and then using transmission microscopy imaged on the EPIX. For the experiments using microstructures, the neuron chosen needed to be engulfing a gold area.

(a) To set up the SPR, the z -axis of the sample holder was adjusted to ensure the gold surface was in focus with the SLED. An angle scan was performed (Section 2.9.5) and then the region of interest was selected. Using the ROI and the histogram tool in the EPIX software, the angle of incidence was adjusted to ensure that it was at the most sensitive point of the SPR curve ($\sim 50\%$). The EPIX settings were configured to allow the camera to be externally triggered.

(b) The Ephys hardware was then setup. The pipette was filled with ICS and loaded onto the headstage. Positive pressure was applied, and the micro-manipulator was used to insert the pipette into the ECS. If the pipette resistance at this point was not between $2 - 10 \text{ M}\Omega$ then this step was repeated. If the pipette resistance was acceptable, then the micro-manipulator was used to go cell-attached. If a suitable

G Ω seal was achieved then a sharp negative pressure was applied to go whole-cell.

(c) If recording whole-cell was successful then the ephys software was switched to current clamp and spontaneous activity was recorded. To select which stimulation protocol to use, a protocol that injected current for 1000 msec in steps of 10 pA between 10 and 100 pA was used to determine how responsive the neuron was to stimulation. The current step protocol gave the electrophysiology recording time and current injection amplitude to be used for the following stimulations.

(d) If the cell was electrically active and responsive to stimulation, then the stimulation and imaging protocols were setup.

(e) After the stim/imaging protocol and before saving it was necessary to check if the ephys or SPR had dropped any frames. The latency of the APs was also checked to ensure that a suitable stimulation protocol was being used. The software was changed to detect spontaneous activity again. If the neuron was still alive, then the experiments were repeated. If the neuron had died, then the procedure was started from the beginning.

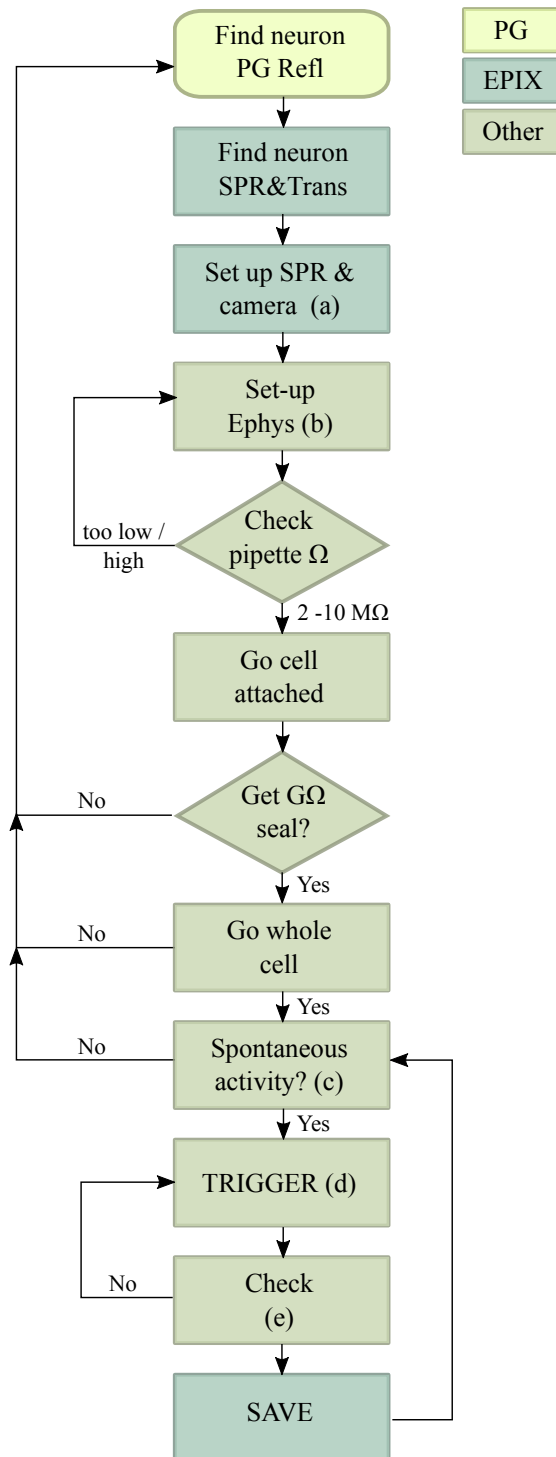


Figure 2.4: Procedure for the SPR and electrophysiology experiments.

CHAPTER 3

DETECTING NEURAL ACTIVITY USING SURFACE PLASMON RESONANCE

Neural activity induces fast intrinsic optical signals that are the result of light scattering and birefringence changes associated with action potentials and postsynaptic potentials (Cohen et al., 1968; Stepnoski et al., 1991; Foust and Rector, 2007). The refractive index changes of a neuronal membrane during electrical activity are likely to be very small, so, it is crucial to estimate the size of these signals to know whether the SPR system is capable of detecting them. This chapter will first introduce the theory surrounding the principle of SPR, and a model will be developed to understand what signals the system needs to detect. First, the equations necessary to model the angular response are derived, and a simple, three-layer model is introduced considering a glass/metal/dielectric configuration. The method of exciting the plasmons and choice of metal will be explained.

In reality, however, the model will need additional layers to account for the cell membrane and cytosol. The N-layer model required will be developed, and the transfer matrix method will be described and used to solve the system. The gap distance between the cell and substrate is never a fixed value, so the N-layer model

will be used to understand the effect of increasing the gap distance between the neuron and the surface. Next, the gap distance will be fixed, and the angular and intensity responses for SPR as a function of the change of refractive index will be evaluated. These results will determine the minimum detectable signals that the SPR system needs to be capable of resolving to detect electrical activity successfully.

The ion flux that occurs during an action potential sees a huge exchange of Na^+ and K^+ ions from inside the cell to the extracellular solution. The work of Clay (2017) is built upon to understand the effect of ion flow during an action potential, and its effect on the metal surface to confirm the estimated refractive index change of the neuronal membrane and associated light intensity changes.

3.1 Theory

Optical Properties of Noble Metals

Metallic bonding occurs because the positively charged ions in a metal atom repel each other and form a solid crystalline structure that is held together by a negatively charged electron cloud. This negatively charged electron cloud can be defined as a solid-state plasma and is what governs the optical properties of noble metals including Gold (Au), Silver (Ag), and Copper (Cu), etc. The Drude model is the simplest model to describe the optical response of an electron in an atom, bound by a force with a resonant frequency, ω_0 (Drude, 1900). The dielectric function of a metal defines the permittivity of a material as a function of space or frequency. According to the Drude model the dielectric function is given by (3.1).

$$\varepsilon(\omega) = \varepsilon_\infty \frac{ne^2}{m\varepsilon_0 \omega^2 + i\gamma_0\omega} \quad (3.1)$$

where $i = \sqrt{-1}$, e is the electronic charge, m is the mass of an electron, and ε_0 is the vacuum permittivity. γ_0 is the damping term, which corresponds to the collision rate of free electrons within the crystal or impurities, and is small for ω of interest here. The optical response of the positive ions in the crystal contributes to a constant background real dielectric function $\varepsilon_\infty \geq 1$ (Le Ru and Etchegoin, 2008), and n is the number of free electrons. The number of free electrons (n) in gold can be calculated using

$$n = \frac{Z\rho}{A} N_A \quad (3.2)$$

where N_A is Avogadro's number, ρ is the mass density, and A is the atomic mass. The mass density and atomic mass for gold are $19,300 \text{ kg m}^{-3}$, and 197 g/mol , respectively. Given the number of conduction electrons (Z) per gold atom is one, the density of conduction electrons can be calculated as $5.9 \times 10^{28} \text{ m}^{-3}$. Using the number of free electrons, the natural oscillation frequency of the free-electron-plasma charge known as the plasma frequency can be written as:

$$\omega_p = \sqrt{\frac{ne^2}{m\varepsilon_0\varepsilon_\infty}} \quad (3.3)$$

Combining (3.1) and (3.3), the dielectric function can be rewritten as:

$$\varepsilon(\omega) = \varepsilon_\infty \left(1 - \frac{\omega_p^2}{\omega^2 + \gamma_0^2} \right) + i \left(\frac{\varepsilon_\infty \omega_p^2 \gamma_0}{\omega(\omega^2 + \gamma_0^2)} \right) \quad (3.4)$$

and can be simplified to

$$\varepsilon(\omega) = \varepsilon_1(\omega) + i\varepsilon_2(\omega) \quad (3.5)$$

where ε_1 is the real part of the dielectric function and represents the polarisation and anomalous dispersion, ε_2 is the imaginary part of the dielectric function and represents the energy lost, i.e., absorbed in the medium. As γ_0 is small compared to ω , the plasma frequency is obtained from the condition $\varepsilon_1 \approx 0$ for $\omega = \omega_p$. For a good plasmon supporting metal in the visible/NIR wavelengths $\omega < \omega_p$, $\varepsilon_1 < 0$, and ε_2 is also small. To conclude, for a metal to be plasmon supporting, the real part of the dielectric function, ε_1 is negative in the wavelength range of interest (VIS/NIR), and the imaginary part, ε_2 is small.

At optical frequencies (400 – 700 nm) the dielectric function can be determined experimentally via reflectivity studies and the determination of the complex refractive index is given by:

$$\varepsilon_1 = n^2 - k^2 \quad (3.6)$$

$$\varepsilon_2 = 2nk \quad (3.7)$$

$$n^2 = \frac{\varepsilon_1}{2} + \frac{1}{2} \sqrt{\varepsilon_1^2 + \varepsilon_2^2} \quad (3.8)$$

$$k = \frac{\varepsilon_2}{2n} \quad (3.9)$$

where n is the real part of the complex refractive index and k is the extinction coefficient (Hecht, 2016).

The analytical model for gold can be written as:

$$\begin{aligned} \varepsilon_{Au}(\lambda) = & \varepsilon_{\infty} \left(1 - \frac{1}{\lambda_p^2 \left(\frac{1}{\lambda^2} + \frac{i}{\mu_p \lambda} \right)} \right) \\ & + \sum_{n=1,2} \frac{A_n}{\lambda_n} \left[\frac{e^{i\phi_n}}{\frac{1}{\lambda_n} - \frac{1}{\lambda} - \frac{i}{\mu_p}} + \frac{e^{-i\phi_n}}{\frac{1}{\lambda_n} + \frac{1}{\lambda} + \frac{i}{\mu_p}} \right] \end{aligned} \quad (3.10)$$

where the parameters needed to calculate the dielectric function for gold and silver according to the Drude model are in Table 3.1, $\lambda_p = 2\pi c/\omega_p$. The analytical model for gold is derived in full in Le Ru and Etchegoin (2008).

Table 3.1: Parameters used to reproduce the data of Johnson and Christy (1972) for gold and silver. Values taken from Le Ru and Etchegoin (2008).

	ε_{∞}	λ_p (nm)	μ_p (nm)	A_1	ϕ_1	λ_1 (nm)	μ_1 (nm)	A_2	ϕ_2	λ_2 (nm)	μ_2 (nm)
Au	1.54	143	14500	1.27	$-\pi/4$	470	1900	1.1	$-\pi/4$	325	1060
Ag	4.00	282	17000								

For light with a wavelength of 680 nm, the real part of the complex refractive index and the extinction coefficient for gold are, $n = 0.135$, and $k = 3.88$. The dielectric constants are $\varepsilon_1 = -15.051$, and $\varepsilon_2 = 1.052$. The corresponding graphs for the real and imaginary parts of the dielectric function can be plotted as a function of wavelength, which were experimentally verified by Johnson and Christy (1972) and are shown in Figure 3.1. The differences between the theoretical and experimental plots are the result of two interband transitions at 330 and 470 nm that are not accounted for by the Drude model (Etchegoin et al., 2006). It can be seen that gold can support plasmons at wavelengths greater than 600 nm, where $\varepsilon_1 < 0$ and ε_2 is small¹.

¹Note: all the MATLAB code for the theory and experimental analysis has been uploaded to Github - github.com/carmelh/thesis

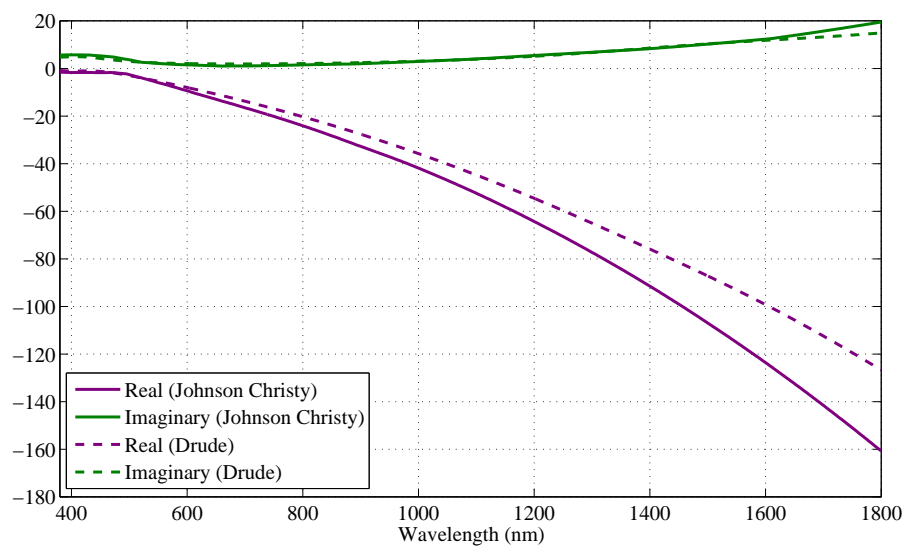


Figure 3.1: Plot of the real and imaginary parts of the dielectric constant as a function of wavelength. The experimental values from Johnson and Christy (1972) are plotted against the theoretical values from the Drude-Lorentz model. Parameters for the Drude-Lorentz model are taken from Rakić et al. (1998).

What is a Plasmon?

A plasmon is a quantum quasi-particle representing the elementary excitations, or modes, of the charge density oscillations in a plasma (Le Ru and Etchegoin, 2008). It is useful here to remember the definition of a photon as a quantum particle representing the elementary excitations, or modes, of the free electromagnetic field oscillations (Le Ru and Etchegoin, 2008), i.e., a plasmon is to the plasma charge density what photons are to the electromagnetic field. A plasmon is a quasi-particle because it is always lossy and highly interacting. When an electromagnetic wave propagates in a medium that is optically responsive with a relative dielectric function, $\varepsilon \neq 1$, the energy of the wave is shared between the electromagnetic field oscillations and the internal excitations of the medium. These modes are known as polaritons. Furthermore, if the optical response of a metal in the VIS and NIR is dominated by the interaction of light with the free-electron plasma, then the electromagnetic waves in a metal are called plasmon-polaritons (Le Ru and Etchegoin, 2008). Another family of plasma modes exist in thin films called surface plasmons. Surface plasmons correspond to longitudinal charge density waves propagating at a metal/dielectric interface. These charge density waves cannot exist without being associated with a transverse electromagnetic wave (e.g., a photon). Therefore they should be called surface plasmon-polaritons (SPPs) (Le Ru and Etchegoin, 2008). SPPs can come in several different modes: propagating, localised, radiating, non-radiating, bound, virtual, or evanescent. Only propagating and localised modes will be discussed in this thesis (For localised modes see Section 1.4.3).

Propagating Surface Plasmon-Polaritons

SPPs are electromagnetic excitations propagating at an interface between a metal and dielectric, evanescently confined in the perpendicular direction (Maier, 2007). The simplest geometry is that of a single, flat interface between a scattered wave in the dielectric with wave-vector $k'_1 = k_x e_x + k'_{1z} e_z$ and a transmitted wave in the metal with wave-vector $k_2 = k_x e_x + k_{2z} e_z$, illustrated in Figure 3.2.

The dispersion relation describes the effect of dispersion in a medium as a function of the wave travelling within that medium (Hecht, 2016). For propagating surface

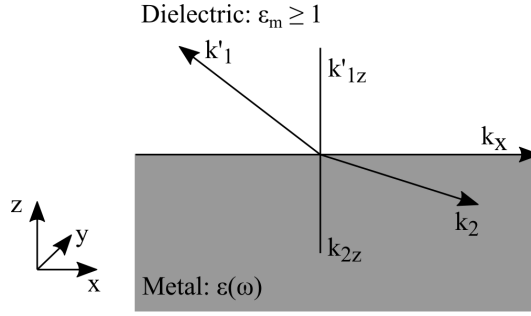


Figure 3.2: Geometry for SPP propagation at a single, flat interface between a metal and a dielectric. k_1 and k_2 are two TM waves at the interface in the dielectric and metal, respectively. Evanescent field decay occurs along the z -axis in both the metal and dielectric. EM propagation occurs along the x -axis (L_x). The dispersion relations in each medium, along with the boundary conditions result in the dispersion relation for PSPPs (3.11).

plasmon-polaritons (PSPPs) the dispersion relation can be written as:

$$k_x = k_0 \sqrt{\frac{\varepsilon(\omega)\varepsilon_m}{\varepsilon(\omega) + \varepsilon_m}} \quad (3.11)$$

where k_0 is the wave-vector of a propagating wave in a vacuum given by $k_0 = \omega/c$ (c is the speed of light in a vacuum), and ε_m is the permittivity of the dielectric medium. The exact nature of each mode will depend on whether the wave-vector components k_x , k_{1z} , and k_{2z} , are real or complex. If the wave-vector in the direction is real, then the mode will correspond to a propagating wave, on the other hand, if the wave-vector is imaginary, the mode is evanescent with an exponential decay of the intensity. In the ideal case with a non-absorbing metal ($\varepsilon_2 = 0$), its dielectric constant will be real at frequencies smaller than the plasma frequency (ω_p). Providing $\varepsilon(\omega) < -\varepsilon_m$, k_x will be real and both k'_{1z} , and k_{2z} will be imaginary, resulting in a propagating surface wave with an evanescent wave perpendicular to the interface. The travelling SPPs are damped by an absorption in the metal and the field intensity decays as $e^{-2|\text{Im}(k_x)x|}$. This field intensity decay is called the propagation length (3.12), and is generally on the order of 10 and 100 μm in the visible region depending on the metal/dielectric configuration (Maier, 2007). The field intensities in the z direction decay as $e^{-2|\text{Im}(k'_{1z})z|}$ in the dielectric and as $e^{-2|\text{Im}(k_{2z})z|}$ in the metal. The field intensity decays in the z direction are known as the decay length

and can be expressed as (3.13) and (3.14) in the dielectric and metal, respectively.

$$L_x = \frac{1}{2\text{Im}(k_x)} \quad (3.12)$$

$$L_{z1} = \frac{1}{2\text{Im}k_{2z}} \quad (3.13)$$

$$L_{z2} = \frac{1}{2\text{Im}k'_{1z}} \quad (3.14)$$

The decay length in the metal is very small, and on the order of $\sim 10 - 15$ nm. In the dielectric, the decay length is smaller than one wavelength and more than two orders of magnitude shorter than the propagation length along the surface (L_x). Figure 3.3 shows the propagation (x -axis) and decay lengths (z -axis) for a gold/air interface and for a gold/water interface. For a wavelength of 680 nm at a gold/air interface this gives L_x , L_{z1} , and L_{z2} to be 29.2, 0.297, and 0.0199 μm , respectively. Likewise, for a gold/water interface this gives L_x , L_{z1} , and L_{z2} to be 18.27, 0.22, and 0.0197 μm , respectively.

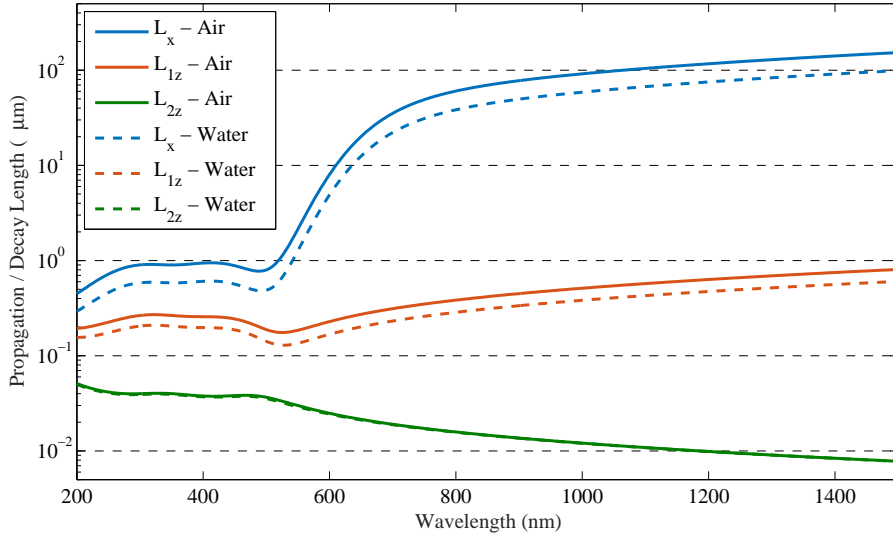


Figure 3.3: Propagation length of the SPP along x , L_x , and decay lengths along z , away from the interface in the dielectric and metal, L_{zd} , and L_{zm} , respectively as a function of the wavelength of the incident light for a gold/dielectric interface. The propagation and decay lengths have been normalised by λ .

No surface modes exist for s -polarised light; only p -polarised. P -polarised light oc-

occurs when the incident radiation has its electric vector in the plane of incidence. For p -polarised light, the magnetic (\mathbf{H}) vector has only one component, H_y tangential to the interface (transverse magnetic radiation), and the electric (\mathbf{E}) vector has components E_x normal, and E_z tangential to the interface. S -polarised light occurs when the incident radiation has its electric vector orthogonal to the plane of incidence. For s -polarised light, the \mathbf{E} vector has only one component, E_y tangential to the interface (transverse electric radiation), and the \mathbf{H} vector has components H_x normal, and H_z tangential to the interface. The components of the vectors for p - and s -polarised light mean that s -polarised light cannot create charge at an interface, whereas p -polarised can. Figure 3.4 confirms this theoretically using the Fresnel equations. The Fresnel equations describe the behaviour of light at a single interface between two media of different refractive indices. The theoretical reflection amplitudes for p - and s -polarised light can be written as (3.15) and (3.16), respectively.

$$r_p = \frac{-n_1 \cos \theta_2 + n_2 \cos \theta_1}{n_1 \cos \theta_2 + n_2 \cos \theta_1} \quad (3.15)$$

$$r_s = \frac{n_1 \cos \theta_1 - n_2 \cos \theta_2}{n_1 \cos \theta_1 + n_2 \cos \theta_2} \quad (3.16)$$

$$(3.17)$$

where θ_1 and θ_2 are the angles of the incident light and the resulting reflected and refracted light, respectively. These reflection amplitude coefficients are related to the reflectance (R) by $R = |r|^2$ (Hecht, 2016).

3.1.1 Excitation of Surface Plasmons

SPPs cannot be excited directly with incident light because the wave-vector of the light ($k = k_0 \sqrt{\varepsilon_m}$) on the dielectric side of the interface is less than the PSPP mode (k_x). Figure 3.5 shows the wave-vector of a photon with a grazing incidence and the dispersion relation (3.11). It can be seen that at no point (apart from the origin) the two wave-vectors intersect.

Several techniques have been devised to introduce the missing momentum and excite the PSPP, the following section will discuss the attenuated total reflection (ATR) configuration.

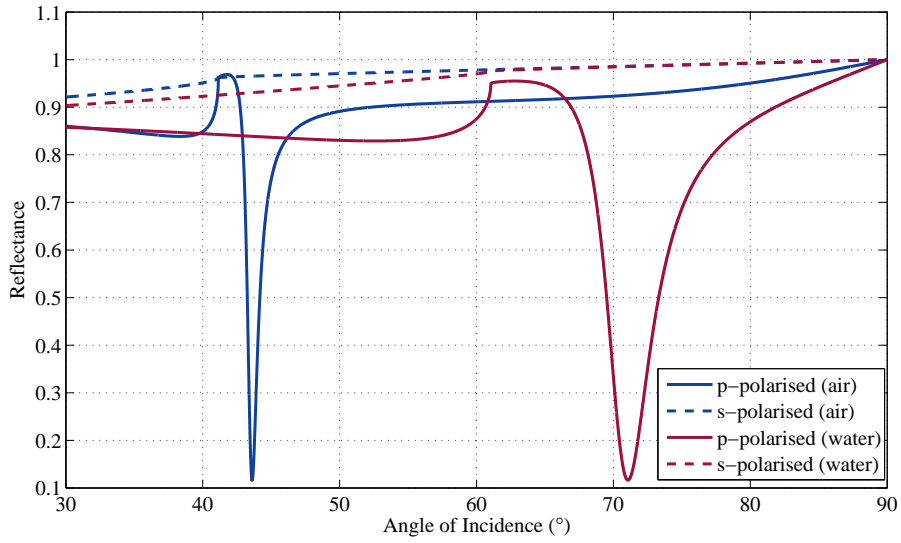


Figure 3.4: Theoretical angular responses for p - and s - polarised light for a gold/air and gold/water interface. Modelled using a three-layer model: glass/gold/dielectric.

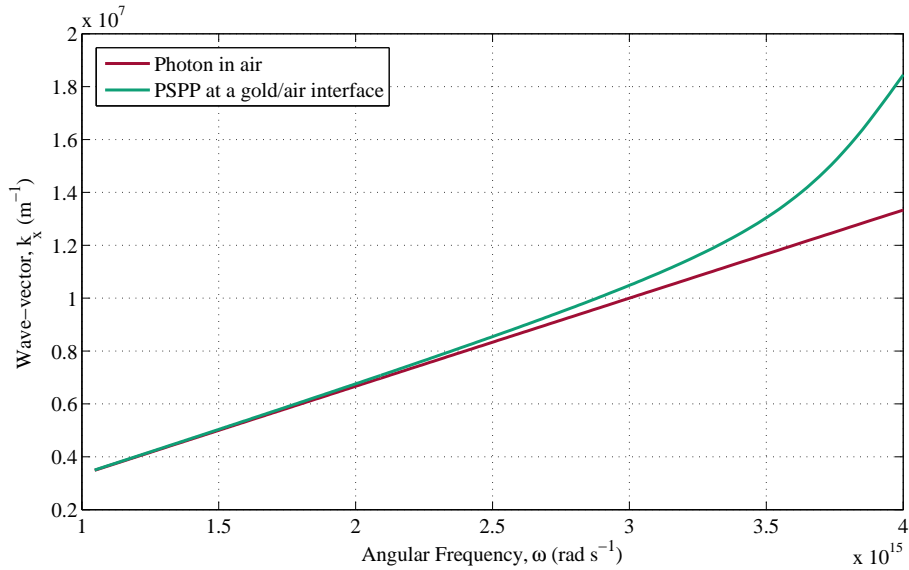


Figure 3.5: Wave-vector of a photon, k_x with a grazing incidence in air ($\epsilon_m = 1$) and that of a PSPP, k at a gold/air interface as a function of the angular frequency. The values to calculate the dielectric function for gold are taken from Johnson and Christy (1972).

Attenuated Total Reflection Configuration

The attenuated total reflection configuration is one method that has been developed to excite PSPPs. Total internal reflection occurs when an incident electromagnetic wave hits a planar interface with an optically less dense medium, i.e., a medium with a lower refractive index n , with an angle of incidence higher than the critical angle (θ_c). The critical angle is defined by Snell's law, where

$$n_1 \sin \theta_1 = n_2 \sin \theta_2 \quad (3.18)$$

$$\theta_c = \sin^{-1} \frac{n_2}{n_1} \quad (3.19)$$

Snell's Law describes the relationship between the angle of the incident light (θ_1) and the resulting reflected and refracted light (θ_2) (Hecht, 2016). \tilde{n}_i is the complex refractive index for each medium given by $\tilde{n} = n + ik$ where n and k are the real and imaginary parts of the refractive index, respectively. The transmitted wave is evanescent. As the wave-vector in the optically dense medium is larger, then this transmitted wave can excite PSPPs. The two most common ATR configurations are the Otto configuration (Otto, 1968) and the Kretschmann method (Kretschmann and Raether, 1968), both shown in Figure 3.6.

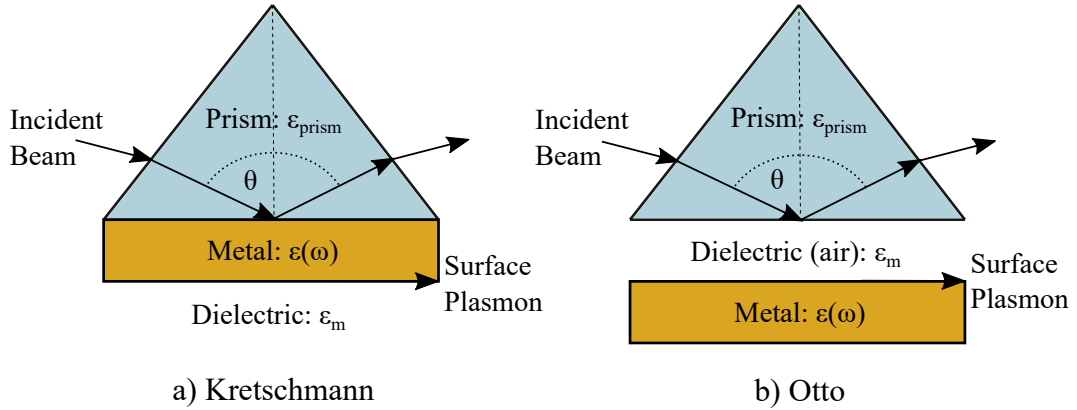


Figure 3.6: Illustration of the two most common ATR configurations. The Otto configuration and the Kretschmann method. The Otto configuration uses a prism on top of a metal surface with a small air gap. The Kretschmann configuration has a thin metal film is deposited on top of a prism surface.

The Otto configuration uses a prism on top of a metal surface with a small air gap ($\sim 1 \mu\text{m}$), so has the configuration prism/dielectric/metal. However, this gap is difficult to control, so the Kretschmann configuration uses the metal itself to deliver the photons. Here a thin metal film is deposited on top of a prism surface, so has a configuration prism/metal/dielectric. The film thickness is smaller than the dielectric gap in the Otto configuration, due to the stronger decay of the evanescent field in the metal. The film thickness must remain larger than the decay length in the metal, L_{2z} to avoid strong coupling between the two interfaces. Both of these methods use the evanescent wave to excite the PSPP modes. Resonance occurs when the wave-vectors match, $k_x = k$, so the coupling condition for an ATR configuration is given by:

$$\sqrt{\varepsilon_{prism}} \sin \theta = \sqrt{\frac{\varepsilon(\omega)\varepsilon_m}{\varepsilon(\omega) + \varepsilon_m}} \quad (3.20)$$

where ε_{prism} is the permittivity of the prism. This equation can be rearranged to determine the SPR angle (3.21). The SPR angle (θ_{sp}) is the angle where resonance occurs and thus the angle of minimum reflectivity. The resonance condition and θ_{sp} are dependent on the wavelength of the light because the wavelength affects the permittivity of the metal, and the refractive index of the dielectric.

$$\theta_{sp} = \sin^{-1} \sqrt{\frac{\varepsilon(\omega)\varepsilon_m}{\varepsilon_{prism}(\varepsilon(\omega) + \varepsilon_m)}} \quad (3.21)$$

The Kretschmann ATR configuration is one of the most popular methods for exciting surface plasmons. The Kretschmann configuration allows a large field of view (up to cm). However, the physical constraint of the prism limits the numerical aperture and magnification of the system and results in the technique having a reduced spatial resolution (Huang et al., 2007). Also, in this configuration, when the incident angle is scanned the prism distorts the SPR images and causes them to move. Using a high NA objective lens instead of a prism overcomes the issues of spatial distortion by keeping the object plane parallel to the image plane (Stabler et al., 2004; Huang et al., 2007). This method also allows higher magnification, and because of the high NA, the resolution of the imaging is diffraction limited ($\sim 300 \text{ nm}$). However, if the resolution is diffraction limited then the field of view will be $< 100 \mu\text{m}$.

Characterising the Sensitivity

Yeatman (1996) produced a model for characterising the sensitivity of an SPR sensor. He stated that the smaller the imaginary part of the refractive index, i.e., less loss from the material the sharper the resonance dip. By observing the change in the theoretical reflection amplitude concerning the angle of incidence, the sensitivity of the sensor will be at its highest when the slope $\Delta R/\Delta\theta$ is greatest. By manipulating gradient maximum, the sensitivity of a material can be described as the minimum detectable change by changing the refractive index of the medium on the surface. Yeatman expressed the minimum detectable change in the dielectric as:

$$\Delta n_{min} = \frac{1.3Nn^3\varepsilon_2}{\varepsilon_1^2} \quad (3.22)$$

where N is the noise term, given as optical power at the receiver/incident optical power, and n is the refractive index of the dielectric, for example, air or water (Yeatman, 1996). This Δn_{min} is describing the sensitivity of the sensor to bulk refractive index changes and is not valid for the model adopted in this thesis. The sensor will need to detect membrane localised refractive index changes rather than bulk.

The refractive index unit (RIU) is an arbitrary unit that characterises the sensitivity of an SPR sensor as a change in the refractive index of the fluid medium, Δn :

$$RIU = \frac{\Delta R}{\Delta n} \quad (3.23)$$

where ΔR is the change in the reflection amplitude. The resolution of most SPR sensors is in the range of 10^{-5} to 10^{-6} RIU (Hoa et al., 2007). The limit of detection is limited by the shot noise, which is a statistical fluctuation of photon density from the light source (see Section 1.6.2) or the electronic variation in the detector. To consider the noise term, (3.23) must be multiplied by the noise equivalent power at the receiver, σ :

$$RIU = \frac{\sigma}{\Delta R} \Delta n \quad (3.24)$$

The method just discussed to characterise sensitivity does not take into account spatial resolution, which is just as important as sensitivity, and there is a trade-off between them. The resolution is given by:

$$\chi_c = \frac{0.14n^2}{n_0^3 k} \lambda \quad (3.25)$$

where χ_c is the characteristic length of the plasmon which differs from the decay length of the plasmon by an arbitrary factor. The resolution is dependent on the wavelength, and this explains the curve in Figure 3.7, where silver has a steeper and more defined area of reflectance compared to gold.

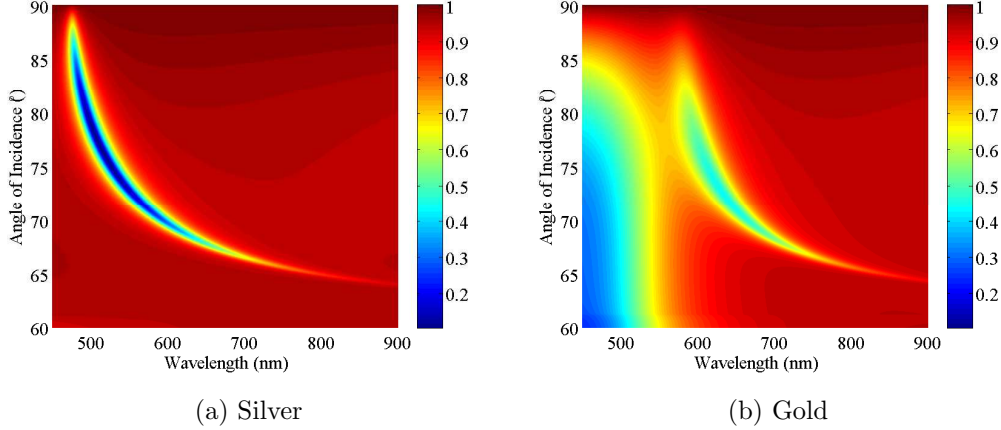


Figure 3.7: Angular response as a function of wavelength for gold and silver. The metal layer for both was 50 nm. The parameters needed to compute the dielectric function for both metals can be found in Table 3.1. The colourbar represents the reflectivity value between 0 and 1.

Metal and Thickness Sensitivity

The choice of the metal-wavelength combination influences the size of the displacement when a chemical reaction alters the resonance conditions (3.21). The displacement occurs when the properties of the dielectric layer on top of the metal layer change resulting in a new ε_m . The new ε_m then causes the resonance angle and potentially the gradient of the slope to change. If the reflection coefficient is measured at a fixed angle, as is the case in an intensity modulation scheme, the sensitivity constant or gradient of the slope (S) is given as:

$$S = \frac{\Delta R}{\Delta \theta} \frac{\Delta \theta_{sp}}{\Delta d_3} \quad (3.26)$$

where d_3 is the thickness of the dielectric. $\Delta R/\Delta \theta$ is taken where the reflection coefficient is 0.5 because this is where the reflection gradient is at its maximum. For angular modulation set-ups, i.e., where the change in plasmon angle is determined

the sensitivity is given by:

$$S^* = \frac{\Delta\theta_{sp}}{\Delta d_3} E \quad (3.27)$$

where E is the experimental sensitivity to detect the position of the minimum. de Bruijn et al. (1992) reported the experimental sensitivities for different metals including (but not limited to) aluminium, copper, gold, and silver as a function of wavelength. It was reported that silver at 800 nm is the best for fixed angle measurements (S). For sensors where the value of θ_{sp} is to be determined (S^*), a short wavelength should be used with the choice of metal being less critical. Similar results for fixed angle measurements were reported by Akimoto et al. (1999).

Islam et al. (2011) investigated the performance of different metal films such as gold, silver, and aluminium for use in SPR biosensors based on the Kretschmann configuration. The thickness of a protein on the metal surface was varied to examine the shift of the plasmon dip for each metal. The authors concluded that although silver has the sharpest plasmon dip, the sensitivity of the angular shift was greatest for gold, where it was almost two times that of silver and aluminium. Theoretical SPR curves for gold, silver, copper, palladium, and lithium with a fixed 50 nm thickness are computed in Figure 3.8 using the Fresnel equations.

Figure 3.8 shows that silver, gold, and copper are good for plasmonics. palladium presents too much absorption, and aluminium would only be suitable for applications in the UV. Lithium has plasmon-supporting properties but reacts violently in water making it unsuitable for many applications (Rycenga et al., 2011). Gold is used throughout this project because it is biologically inert, has excellent resistance to oxidation, corrosion, and it lends itself readily to surface chemistry treatments. Silver, even though it has the better SPR response is cytotoxic and oxidises easily (Tauran et al., 2013).

Gwon and Lee (2010) studied the spectral and angular response of an SPR sensor based on the Kretschmann configuration using different thicknesses of gold films (30, 52, and 70 nm). SPR sensitivity is shown to be highly dependent on the thickness of the gold film. In thinner films, the reflection amplitude recovered slowly after θ_{sp} , whereas for thicker films (>50 nm) the dynamic range between the minimum and maximum reflectance becomes smaller. A gold film thickness of about 50 nm was deemed to be the most sensitive regarding sharpness and recovery of the reflection

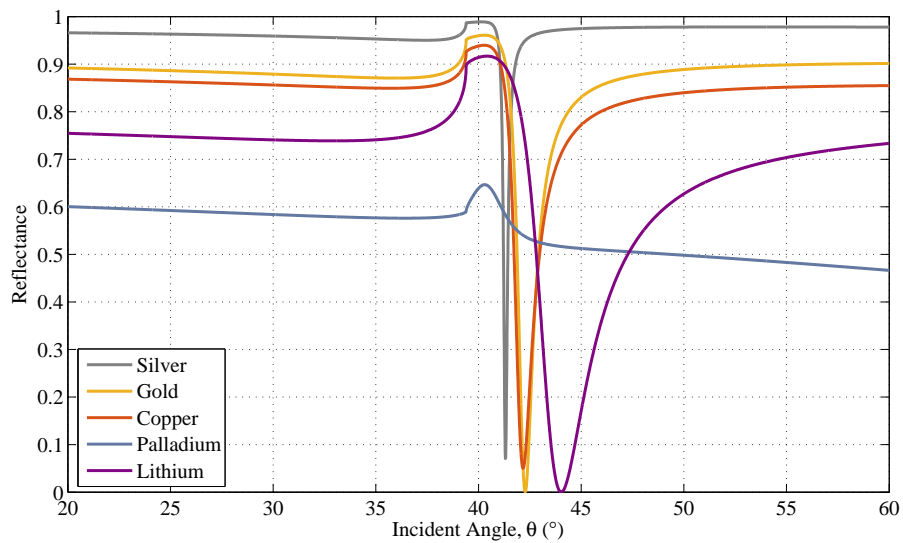


Figure 3.8: Theoretical reflection amplitude vs. angle of incidence for silver, gold, copper, palladium, and lithium in air ($\epsilon_m = 1$) with a film thickness of 50 nm at 680 nm. n_{prism} is 1.52 at 680 nm. The increase in the reflected light intensity before the SPR dip is caused by total internal reflection. Dielectric constant values for silver, gold, and copper are from Johnson and Christy (1972). palladium from Johnson and Christy (1974), and lithium from Rasigni and Rasigni (1977).

amplitude near θ_{sp} . Figure 3.9 shows the theoretical SPR responses for different thicknesses of gold with air ($n = 1$) and water ($n = 1.33$) as the dielectric and a wavelength of 680 nm confirming that 50 nm has the sharpest response. As expected, when changing the dielectric to water the θ_{sp} to a higher angle and the theoretical $\Delta\tilde{R}/\Delta\theta$ reduces.

Using Figure 3.9 the theoretical $\Delta\tilde{R}/\Delta\theta$ for a gold/air and a gold/water interface can be calculated. The theoretical $\Delta\tilde{R}/\Delta\theta$ and the corresponding angle are detailed in Table 3.2.

Table 3.2: $\Delta R/\Delta\theta$ in air for the different thicknesses of gold.

Thickness (nm)	Dielectric = Air ($n = 1$)		Dielectric = Water ($n = 1.33$)	
	$\Delta\tilde{R}/\Delta\theta$	θ_{max} ($^\circ$)	$\Delta\tilde{R}/\Delta\theta$	θ_{max} ($^\circ$)
0 (glass)	30.4	41.1	24.2	61.3
30	0.284	42.9	0.070	68.0
50	1.540	42.8	0.339	70.3
70	3.037	42.8	0.534	71.2

The quartz crystal microbalance used to calculate the thickness on the evaporator is unreliable and is usually within $\pm 10\%$. The gold thickness was changed by $\pm 10\%$ and the resulting angular SPR responses are shown in Figure 3.10. The amplitude of the gradient maximum changes by $\pm 30\%$ when the gold metal thickness changes by 10%. The amplitude of the gradient maximum increases as the gold thickness increases so it is preferable to keep the gold at 50 nm or slightly thicker rather than thinner.

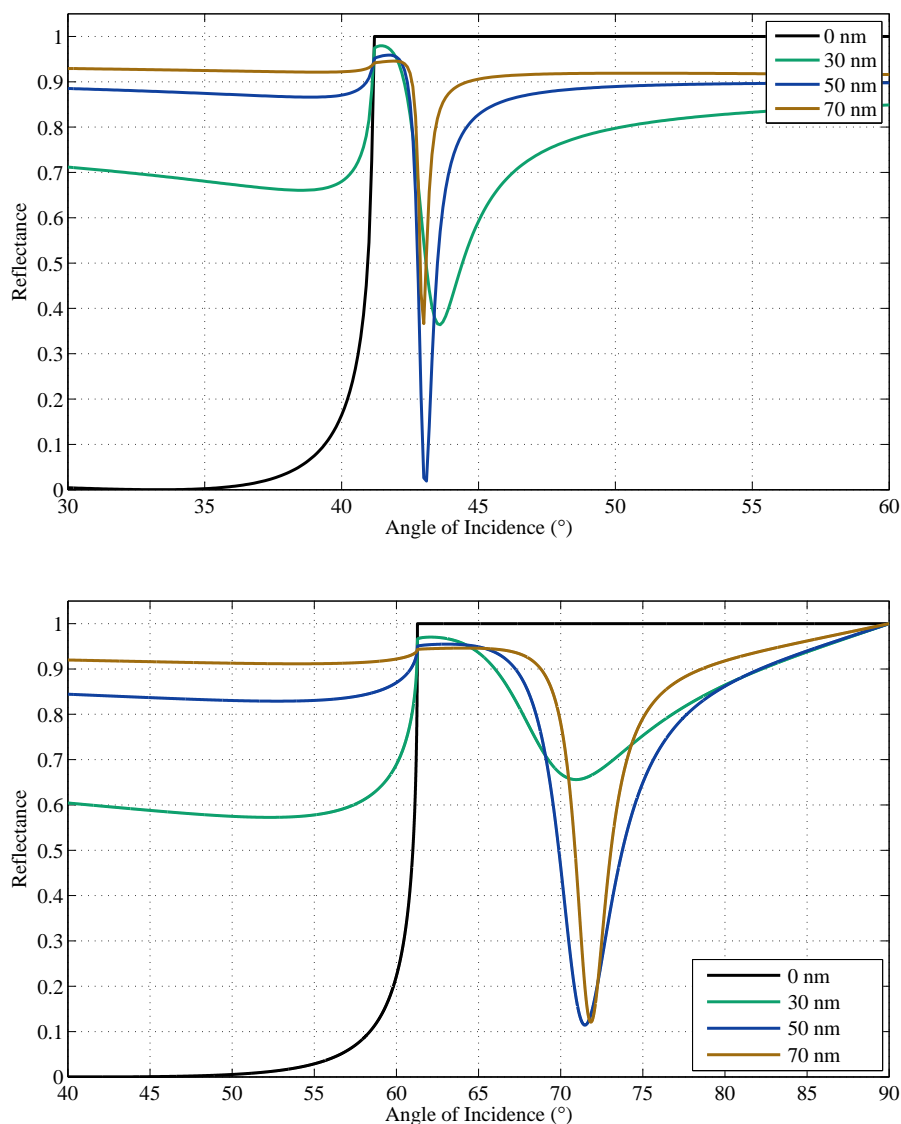


Figure 3.9: Theoretical SPR responses for increasing Au layer thickness with air (top) and water (bottom) as the dielectric ($\lambda = 680$ nm). The SPR response is less sharp and recovers slowly for a thinner layer, whereas for a thick layer the response is sharp but the dynamic range between the minimum and maximum reflectivity values is smaller. 50 nm is optimum at 680 nm.

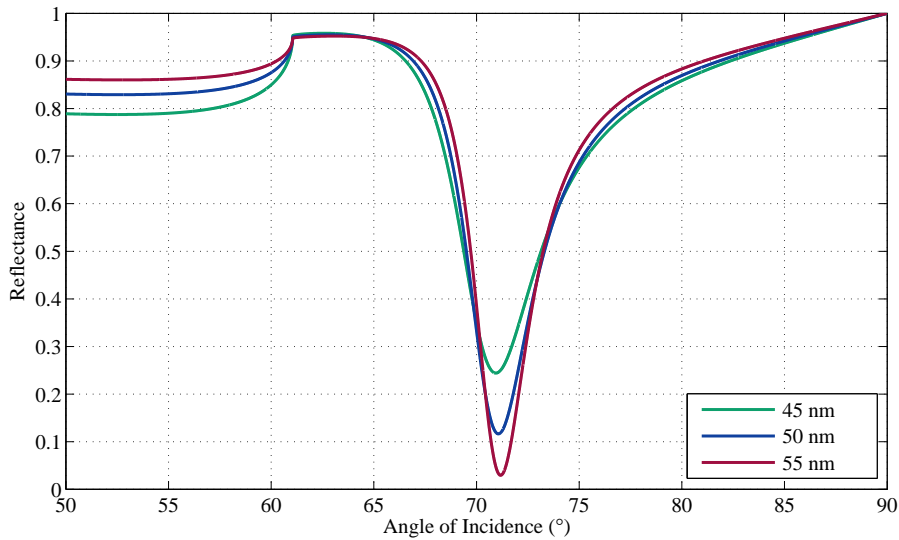


Figure 3.10: Theoretical SPR responses for changing the Au layer thickness by $\pm 10\%$ with water as the dielectric ($\lambda = 680$ nm).

3.2 SPR Response in a Multi-Layer System

Calculating the angular SPR response for a three-layer model is a relatively simple problem to solve using the Fresnel equations. The results from the three-layer model are shown in Figure 3.4 and Figure 3.9. The model here, however, is more complicated because additional layers are required to account for the adhesion layers, and because changes in the cell membrane are going to be detected the cell membrane itself needs to be considered. Therefore, a multi-layer system needs to be solved. The transfer matrix method (Hansen, 1968) has been used to analyse the wave propagation through each layer in the model as illustrated in Figure 3.11. In the subsequent subsections, the assumptions and determination of parameters for each layer are outlined, and the transfer matrix is developed and ultimately solved.

3.2.1 Assumptions and Determination of Parameters

At present, the model illustrated in Figure 3.11 has seven layers, and therefore, the transfer matrix method would need to solve seven matrices. Ellipsometry has been performed on the glass and adhesion layers to ensure accurate values are being used

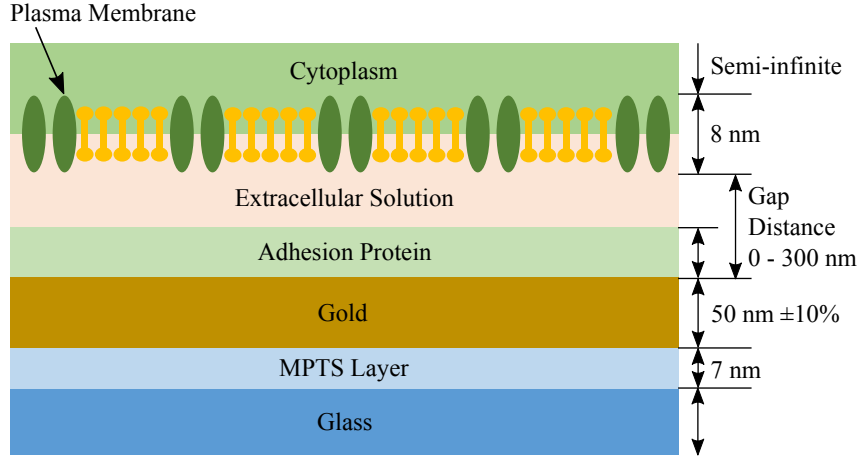


Figure 3.11: Model of the multi-layer system. The model is simplified to a five-layer model comprising of glass/gold/extracellular solution/membrane/cytosol. $n = [1.52, \varepsilon(\omega), 1.37, 1.5, 1.35]$.

and in some cases, layers can be neglected thus simplifying the model.

Refractive Index of MPTS Coated Coverslips

Ellipsometry was performed on the MPTS coated glass coverslips and modelled using a Cauchy dispersion relation, given by:

$$n(\lambda) = B_0 + \frac{B_1}{\lambda(\mu m)^2} \quad (3.28)$$

where B_0 and B_1 are coefficients that are determined by using a non-linear least squares fitting of the experimental Ψ and Δ . Ellipsometry measures the complex reflectance ratio given as $\tan \Psi \exp^{i\Delta}$. Ψ is the ratio of the p - and s -polarised light amplitudes, and Δ is the phase difference induced by the reflection, $\Delta = \delta_1 - \delta_2$, where δ_1 is the phase difference before, and δ_2 is the phase difference after.

The MPTS coverslips were prepared according to Section 2.3.1. Measurements were made on three different coverslips. Figure 3.12 shows the Ψ and Δ of the silanised glass and untreated glass overlap. The refractive index for the glass coverslips at 680 nm SLED is 1.52. The overlap is probably because of the similar refractive indices and small thickness of the MPTS monolayer, which has previously been measured at around 7 nm (Liu et al., 2009). Therefore, it is not possible to reliably retrieve the refractive index and thickness of the MPTS monolayer so will be neglected from

the model.

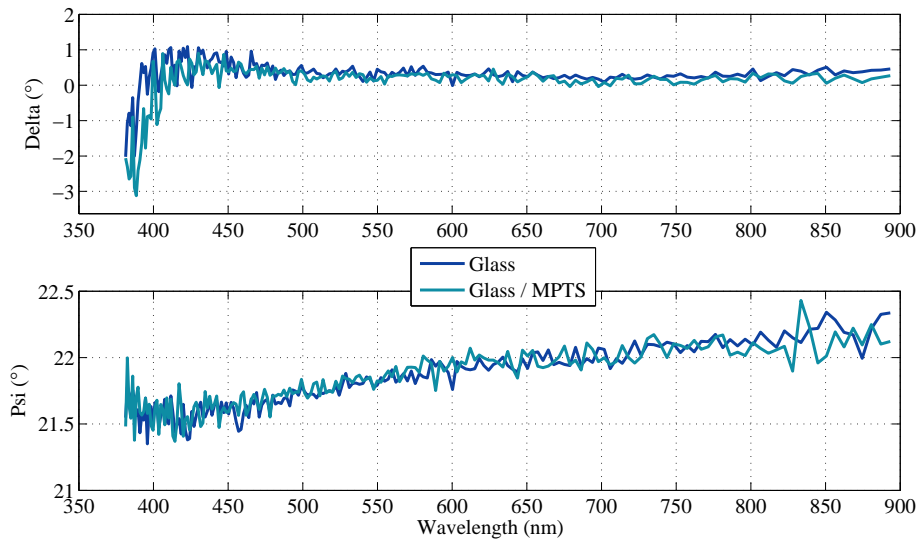


Figure 3.12: Ψ and Δ for silanised glass and untreated glass measured using ellipsometry. The overlap between the two traces means that it is impossible to reliably retrieve the refractive index information for the MPTS layer.

Cell Matter

The refractive index of the extracellular solution prepared using Section 2.12.1 was measured using an Abbe refractometer as 1.34.

Cell membranes are composed mostly of lipids and proteins which have refractive indices in the range of 1.46 – 1.54 (Meyer, 1979). Therefore, in this model, a refractive index of 1.5 was used for the membrane. The thickness of the membrane is generally between 5 and 10 nm (Campbell et al., 1996; Gentet et al., 2000; Hine et al., 2009; Breedlove et al., 2010) so here has been assumed to be 8 nm. The refractive index for the cytosol of cells was assumed to be 1.35 as previously reported in literature (Duck, 2013).

The model has now been simplified to a five-layer model comprising of glass/gold/extracellular solution/membrane/cytosol, where $n = [1.52, \varepsilon(\omega), 1.37, 1.5, 1.35]$.

3.2.2 Solution of the N-layer model

Hansen (1968) provides a general solution for an N -layer model using the transfer matrix method. The transfer matrix method is a technique used for analysing wave propagation in a one-dimensional system. At a single interface between two different media with different refractive indices, the behaviour of light can be described using the Fresnel equations. When considering multiple interfaces at each interface some of the light will be partially reflected and partially transmitted. The transfer matrix method works by describing the outgoing waves regarding the incoming waves with a simple matrix operation for each layer. Finally, the transmission and reflection amplitudes can be determined from these matrices.

As previously mentioned the Fresnel equations describe the behaviour of light at a single interface between two media. When incident light reaches an interface of two media with different refractive indices some of the light is reflected and some is refracted (or transmitted). Snell's Law (3.18) describes the relationship between the angle of the incident light (θ_1) and the resulting reflected and refracted light (θ_2) given by $\tilde{n}_1 \sin \theta_1 = \tilde{n}_2 \sin \theta_2$. \tilde{n}_i is the complex refractive index for each medium given by $\tilde{n} = n + ik$ where n and k are the real and imaginary parts of the refractive index, respectively. The refractive index relates to the permittivity of the material using Equations (3.6) – (3.9).

The Fresnel equations represent the ratio of reflected (r) and refracted (t) light. For p - and s - polarised light the Fresnel coefficients for the reflected light are given by (3.15) and (3.16), respectively. The Fresnel coefficients for the transmitted light are

$$t_p = \frac{2n_1 \cos \theta_1}{n_1 \cos \theta_2 + n_2 \cos \theta_1} \quad (3.29)$$

$$t_s = \frac{2n_1 \cos \theta_1}{n_1 \cos \theta_1 + n_2 \cos \theta_2} \quad (3.30)$$

The reflectance (R) is related to (3.15) and (3.16) by $R_i = |r_i|^2$ (Hecht, 2016). The transmittance (T) however, is related by

$$T_i = \frac{n_2 \cos \theta_2}{n_1 \cos \theta_1} |t_i|^2 \quad (3.31)$$

In the general case described by Hansen (1968), with $N - 1$ surfaces of discontinuity there is a characteristic matrix (M_k where $k = 1, 2, \dots, N - 1$) for each space. The

tangential electric fields U_k and V_k at the first boundary $z = z_1 = 0$, are related to those at the final boundary $z = z_{N-1}$ by:

$$\begin{bmatrix} U_1 \\ V_1 \end{bmatrix} = M_2 M_3 \dots M_{N-1} \begin{bmatrix} U_{N-1} \\ V_{N-1} \end{bmatrix} = M \begin{bmatrix} U_{N-1} \\ V_{N-1} \end{bmatrix} \quad (3.32)$$

For p -polarised light at a boundary, k , $U_k = H_y^0$ and $V_k = E_x^0$. The characteristic matrix is given by:

$$M_k = \begin{bmatrix} \cos \beta_k & -i \sin \beta_k / q_k \\ -i q_k \sin \beta_k & \cos \beta_k \end{bmatrix} \quad (3.33)$$

where

$$q_k = (\mu_k / \bar{\epsilon}_k)^{1/2} \cos \theta_k \quad (3.34)$$

$$\mu_k \cong 1 \quad (3.35)$$

$$q_k = (\mu_k / \bar{\epsilon}_k)^{1/2} \cos \theta_k \cong \frac{(\bar{\epsilon}_k - n^2 \sin^2 \theta_1)^{1/2}}{\bar{\epsilon}_k} \quad (3.36)$$

$$\beta_k = \frac{2\pi}{\lambda_0} \tilde{n}_k \cos \theta_k (z_k - z_{k-1}) = (z_k - z_{k-1}) \frac{2\pi}{\lambda_0} (\bar{\epsilon}_k - n^2 \sin^2 \theta_1)^{1/2} \quad (3.37)$$

The Fresnel equations for the reflection and transmission coefficients for p -polarised light can be rewritten as

$$r_p = \frac{E_{y1}^{0r}}{E_{y1}^{0t}} = \frac{(M_{11} + M_{12}q_N)q_1 - M_{21} + M_{22}q_N}{(M_{11} + M_{12}q_N)q_1 - M_{21} + M_{22}q_N} \quad (3.38)$$

$$M_{ij} = \left(\prod_{k=2}^{N-1} M_k \right)_{ij} \quad i, j = 1, 2 \quad (3.39)$$

$$t_H^p = \frac{2q_1}{(M_{11} + M_{12}q_N)q_1 - M_{21} + M_{22}q_N} \quad (3.40)$$

$$t_E^p = \frac{\mu_N n_1}{\mu_1 \tilde{n}_N} t_H^p \quad (3.41)$$

which relate to the reflectance (R) and transmittance (T) by

$$R_p = |r_p|^2 \quad (3.42)$$

$$r_p = R_p^{1/2} e^{i\phi_p^r} \quad (3.43)$$

$$\phi_p^r = \arg(r_p) \quad (3.44)$$

$$T_p = \frac{\mu_N \operatorname{Re}(\tilde{n}_N \cos \theta_N / \tilde{n}_N^2)}{\mu_1 n_1 \cos \theta_1 / n_1^2} |t_H^p|^2 \quad (3.45)$$

$$\phi_p^t = \arg(t_E^p) \quad (3.46)$$

Using the above equations and the analytical formula for the permittivity, $\varepsilon(\omega)$ of gold (3.10) the transfer matrix can be solved for the five-layer model in Figure 3.11.

It is reported that cell/substrate distances vary between 10 – 150 nm depending on the cell type and adhesion protocol used (Giebel et al., 1999; Son et al., 2017), so the effect of the gap distance between the gold surface and cell membrane was investigated. The gap distance was increased from 0 to 300 nm in steps of 20 nm, and the transfer matrix was solved to give the angular response, Figure 3.13. As expected, as the gap distance increases, θ_{sp} decreases exponentially as shown in Figure 3.14. An exponential curve was fitted where $f(x) = a \exp(bx) + c \exp(dx)$. $a = 2.80$, $b = -0.0125$, $c = 69.8$, and $d = -2.40 \times 10^{-5}$. Goodness of fit: SSE: 0.00399, R-square: 0.9997, Adjusted R-square: 0.9996, and RMSE: 0.0182.

The decrease in θ_{sp} is because the gold surface senses the bulk refractive index, meaning layers 3 (ECS), 4 (membrane), and 5 (cytosol) combine. Increasing the gap distance and moving the higher refractive index membrane away from the gold surface decreases the bulk refractive index and consequently decreases the resonant angle (θ_{sp}). The gradient ($\Delta R/\Delta\theta$) of the SPR dips, as shown in Figure 3.15 decreases as the gap distance increases for the same reason.

The intensity of reflected light during an action potential changes linearly with the membrane potential (Stepnoski et al., 1991). It has been hypothesised that the rearrangement of the dipoles during electrical activity causes the refractive index change. For a small change in membrane potential, the refractive index changes by

$$\Delta n = n \frac{\Delta V}{d} \quad (3.47)$$

where ΔV is the change of voltage during an AP, d is the thickness of the membrane, and n is the nonlinear index. The nonlinear index has been determined for the squid giant axon by Stepnoski et al. (1991) as $(1.2 \pm 0.4) \times 10^{-4}$ nm/mV. Using (3.47) and assuming the nonlinear index is the same for a mammalian neuron with a membrane thickness of 8 nm and an AP range of 100 mV, Δn will be 1.5×10^{-3} .

Using the five-layer model, the gap distance between the cell and gold surface was fixed at 30 nm and the refractive index of the membrane was changed by $\pm\Delta n$. The distance between the cell and surface is on average 30 nm (Braun and Fromherz, 1998; Giebel et al., 1999). The resonant angle i.e. the angle at which the theoretical

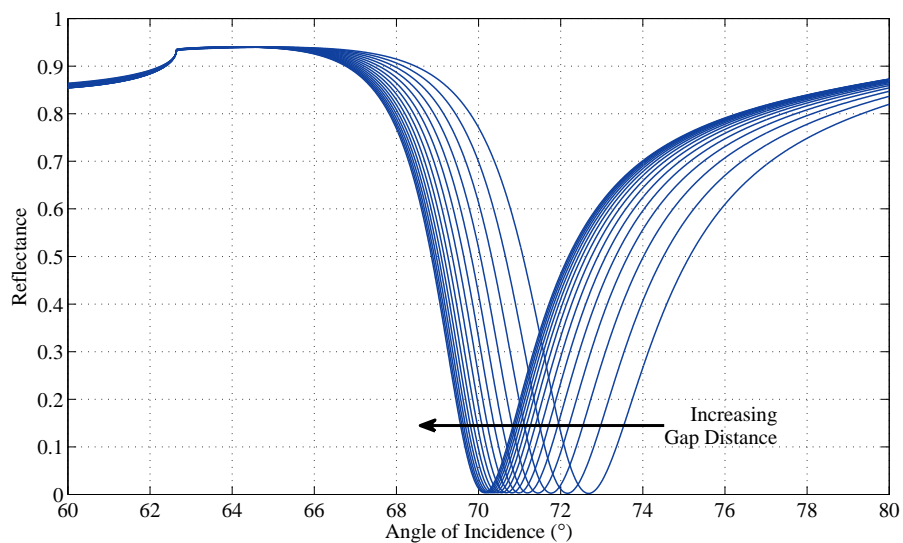


Figure 3.13: Angular response solved using the N-layer model and increasing the gap distance between the gold surface and cell membrane from 0 to 300 nm in 20 nm steps.

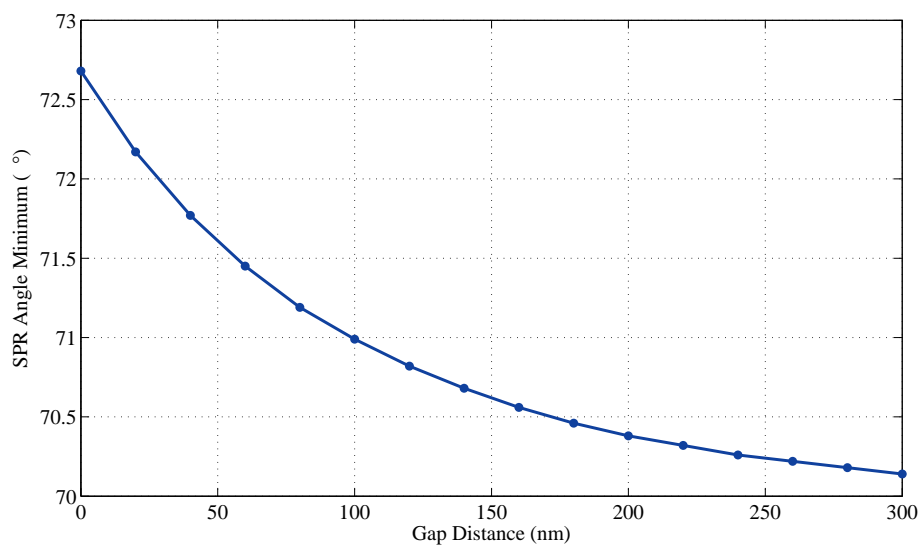


Figure 3.14: SPR angle minimum taken from Figure 3.13. The curve decays exponentially where $f(x) = a \exp(bx) + c \exp(dx)$. $a = 2.33$, $b = -0.0116$, $c = 70.3$, and $d = -1.31 \times 10^{-5}$. Goodness of fit: SSE: 0.000287, R-square: 1, Adjusted R-square: 1, and RMSE: 0.00481.

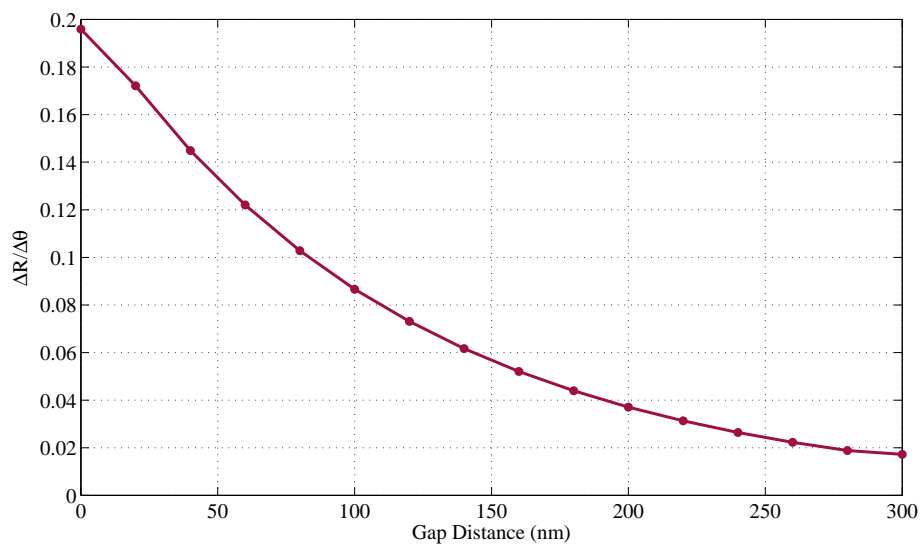


Figure 3.15: Affect on the gradient of the SPR dip ($\Delta R/\Delta\theta$) with increasing gap distance from Figure 3.13. The curve decays exponentially where $f(x) = a \exp(bx) + c \exp(dx)$. $a = -0.0756$, $b = -0.00575$, $c = 0.275$, and $d = -0.00749$. Goodness of fit: SSE: 2.69×10^{-5} , R-square: 0.999, Adjusted R-square: 0.999, and RMSE: 0.0015.

reflection amplitude is at a minimum changes by $\Delta\theta_{sp} = \pm 0.0089^\circ$ as shown in Figure 3.16, resulting in a required angular sensitivity of $\Delta\theta/\Delta n = 5.93$. The reflection minimum value changes by $\Delta R_{min} = \pm 5.93 \times 10^{-6}$. The inset in the top plot in Figure 3.16 is a closer view of the SPR minimum showing the tiny change. The gradient of each refractive index was plotted, and the difference between the largest and smallest value was exported. The average gradient amplitude, $\Delta R/\Delta n$ is $3.804 \times 10^{-3} \pm 4.39 \times 10^{-6}$ and the difference between the peak θ is ± 0.004 . There was no statistically significant difference between the groups regarding the sensitivity or the gradient of the SPR response as determined by one-way ANOVA; $F(1, 3000) = 0.05077, p = 0.822$.

However, in an intensity modulation SPR scheme the light source is fixed at the gradient maximum, in this case around 50%. So, a refractive index change of $\Delta n = 1.5 \times 10^{-3}$ at the 50% point ($\theta = 70.5^\circ$) of the SPR dip will result in the theoretical reflection amplitude changing by $\Delta R = \pm 3.1 \times 10^{-3}$, shown in the bottom plot of Figure 3.16. $\Delta R/\Delta n = 3.1 \times 10^{-3}/1.5 \times 10^{-3} = 2.067$ RIU. The SPR system will need to be able to detect fractional light intensity changes of $\Delta R = \pm 3.1 \times 10^{-3}$. Whether or not this light intensity change is feasible is investigated in the following chapters.

Now, the gap distance between the cell and gold surface was increased from 0 to 150 nm, and the refractive index of the membrane was changed by $\pm \Delta n = 1.5 \times 10^{-3}$. Figure 3.17 summarises the $\Delta\theta/\Delta n$ for angular modulation, and $\Delta R/\Delta n$ for intensity modulation schemes. As expected, the required sensor will need to be more sensitive to detect refractive index changes as the cell moves further away from the surface. Also, the figure confirms that an angular modulation scheme is more sensitive than an intensity modulation, agreeing with literature. However, experimentally it is more difficult to monitor θ_{sp} at fast sampling rates, which is why an intensity modulation scheme is used in this thesis.

3.3 Ion Flux During Action Potential

The ion flux that occurs during an action potential involves the exchange of about 2×10^6 Na^+ and K^+ ions from inside the cell to the extracellular solution causing the membrane potential to change by ~ 100 mV. In reality, this is only 0.0003% –

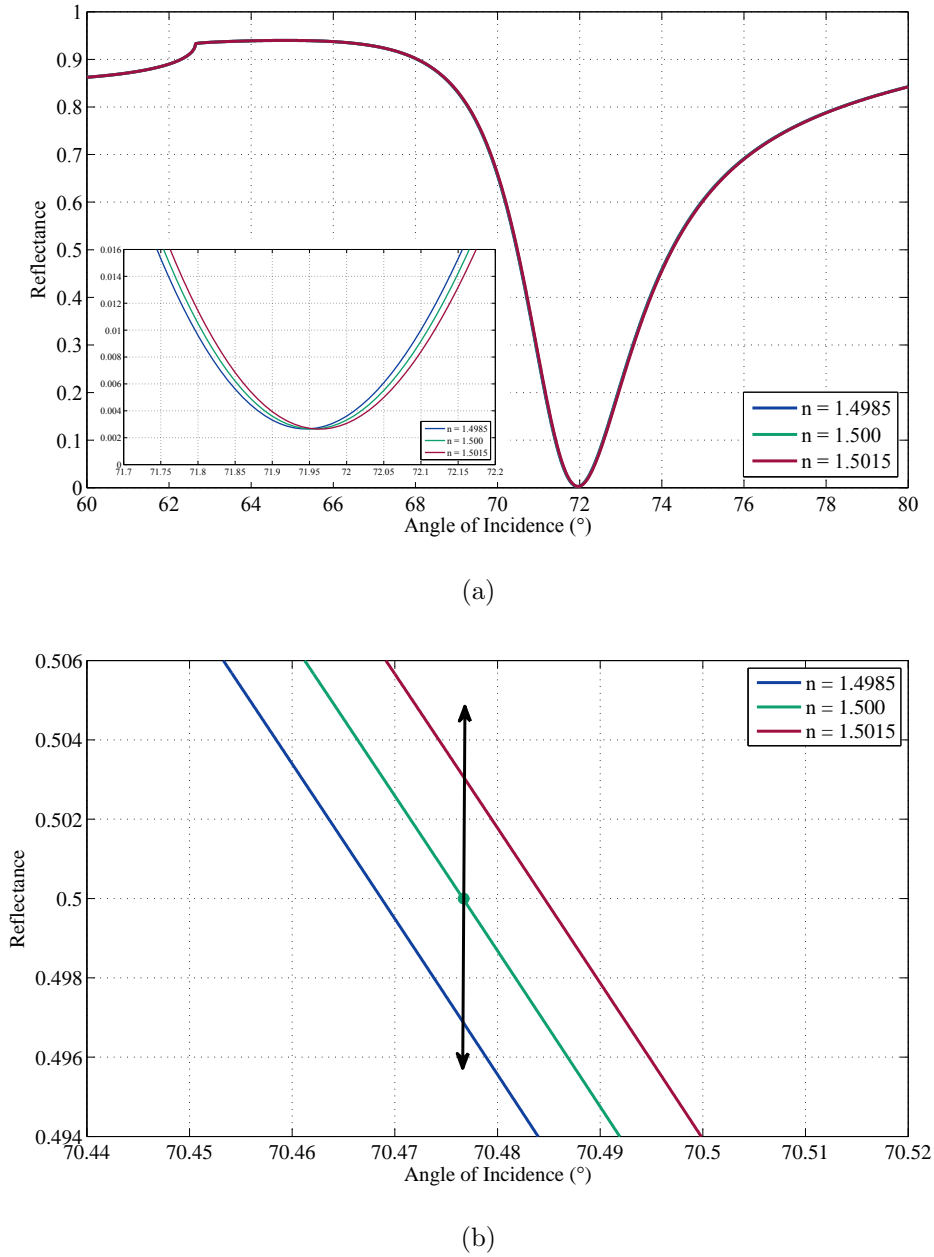


Figure 3.16: (a) Theoretical angular SPR response when the refractive index of the cell membrane changes by $\Delta n = \pm 1.5 \times 10^{-3}$ with a cell/substrate distance of 30 nm. The reflected light intensity increases around 62.5° due to TIR. The inset in (a) is a closer view of the SPR minimum. θ_{sp} changes by approximately $\pm 0.089^\circ$. (b) is a closer view of the 50% point or gradient maxima. The theoretical reflection amplitude changes by $\Delta R = \pm 3.1 \times 10^{-3}$.

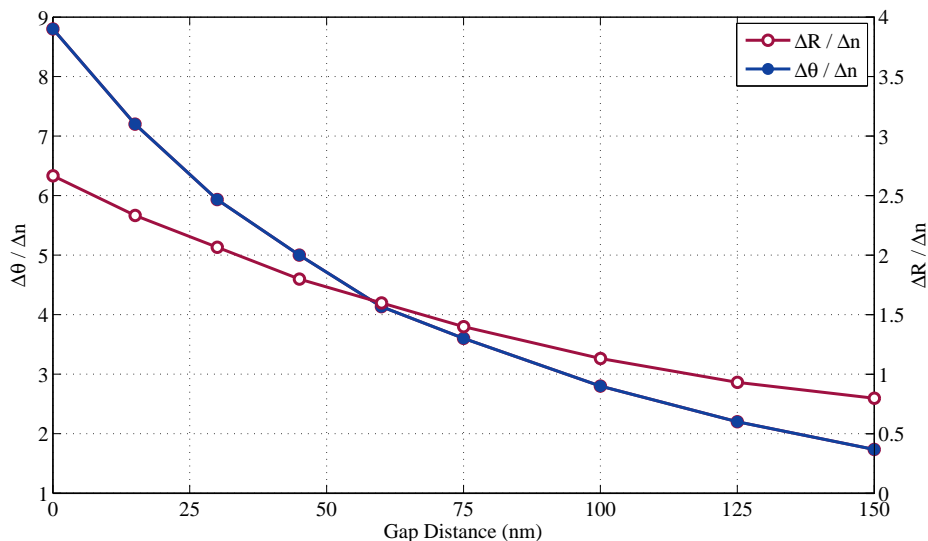


Figure 3.17: Summary of the $\Delta\theta/\Delta n$ for angular modulation and $\Delta R/\Delta n$ for intensity modulation schemes.

0.03% of the total number of K^+ ions in the cytosol and 0.06% of the bulk Na^+ ions (Lodish et al., 2000). However, given the small surface area this ion flux occurs in, it has a considerable impact on the electric field, which changes by around $10^7 - 10^8$ V/m. Could the electric field generated during an AP from a neuron near the surface affect the free electrons in the gold film and cause a larger shift in the resonance angle?

Clay (2017) modelled the ion flow during an AP and the effect on a nearby gold surface. The AP and the electric field generated was calculated using the Hodgkin-Huxley equations, and the concentration of electrons in the thin gold film were modelled using the drift-diffusion equations (Hodgkin and Huxley, 1952). Assuming that the charge density calculated by Clay (2017) represents a change in the density of electrons, the difference in the plasmon frequency (ω_p) of the gold surface during an AP can be calculated using (3.3).

Clay (2017) found the maximum charge density was on the order of $\Delta\rho \approx 3000$ Cm^{-3} , corresponding to a change in the electron number density of 2×10^{22} m^{-3} . The initial concentration of electrons was calculated in Section 3.1 as 5.9×10^{28} m^{-3}

so this is a fractional change of 10^{-6} . Substituting this fractional change ($n - \Delta n$) into (3.3), and using the original $\omega_p = 1.1078 \times 10^{16}$ rad/s. The change in plasma frequency can be calculated as $\Delta\omega_p \approx 2 \times 10^9$ rad/s.

The analytical model for the dielectric function of gold (3.10), and the previously computed theoretical SPR response for a three-layer model were used to change the plasma frequency. Changing the plasma frequency by 2×10^9 rad/sec does not change the SPR angle from $\sim 44.9^\circ$, but the intensity at the gradient maximum changes by -1.203×10^{-6} , shown in Figure 3.18. This change in the gradient maximum

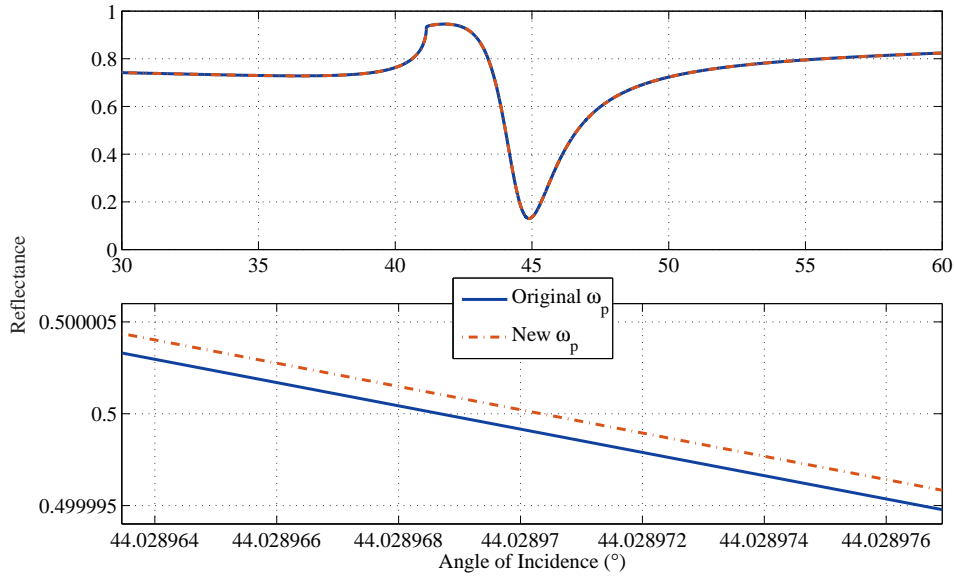


Figure 3.18: Angular response before and after changing the plasma frequency by 2×10^9 rad/s. The intensity at the gradient maximum changes by -1.203×10^{-6} .

is three orders of magnitude smaller than that calculated in the previous section as $\pm 3.1 \times 10^{-3}$. An explanation for this difference could be due to the diffusion equation,

$$l = \sqrt{2Dt} \quad (3.48)$$

where the diffusion coefficient (D) of Na^+ ions in water at room temperature is $1.33 \times 10^{-5} \text{ cm}^2\text{s}^{-1}$. Resulting in an average diffusion distance during the 2 msec (t) action potential for Na^+ ions is $2.3 \mu\text{m}$. However, it has been reported that the ions that cause an AP are held within 1 nm of the membrane surface by electrical attraction to their counterions on the opposite side of the membrane (Alberts, 2017).

It is likely that the movement of ions during an action potential has some effect on the SPR response as this will occur within the evanescent field but less than the changes in the membrane itself. The SPR sensors sensitivity to refractive index changes in the bulk medium is investigated in Chapter 5.

3.4 Chapter Conclusions

This chapter introduced the theory of SPR sensors. The model of the sensor and cell system was formulated. A multi-layer system needed to be solved and therefore, the transfer matrix method was used to analyse the wave propagation through each layer in the model. The assumptions and determination of parameters for each layer were outlined, and the transfer matrix was developed and solved, giving the theoretical SPR response for the model.

The effect of the cell/substrate distance was investigated. The gap distance was increased, and the transfer matrix was solved giving the angular response. When increasing the gap distance the SPR resonance angle moved to smaller angles, exponentially. It can be explained because SPR senses the bulk refractive index and increasing the gap distance moves the higher refractive index membrane away from the gold surface, which decreases the bulk refractive index and consequently decreases the resonant angle. The response will, therefore, be stronger the closer the cell is to the surface.

Using the five-layer model and fixing the gap distance between the cell and gold surface at 30 nm the refractive index of the membrane was changed by $\pm\Delta n$. In an intensity modulation SPR scheme, the detector is fixed at the 50% point, or the angle where the reflection gradient is at a maximum. A refractive index change of $\Delta n = 1.5 \times 10^{-3}$ at the 50% point ($\theta = 70.5^\circ$) of the SPR dip will result in the theoretical reflection amplitude changing by $\Delta R = \pm 3.1 \times 10^{-3}$. Resulting in $\Delta R/\Delta n = 3.1 \times 10^{-3}/1.5 \times 10^{-3} = 2.067$ RIU.

The gap distance between the cell and gold surface was increased from 0 to 150 nm while the refractive index of the membrane was changed by $\pm\Delta n = 1.5 \times 10^{-3}$. As expected, the results showed that the sensor will need to be more sensitive to be capable of detecting refractive index changes as the cell moves further away from

the surface.

Following on from the work of Clay (2017), the ion flux during an AP affected the plasma frequency of the gold surface. With this, the analytical model for the dielectric function of gold (3.10) and the previously computed theoretical SPR response for a three-layer model were solved. It was found that by just considering the ion flux the SPR angle does not change but the intensity of the gradient maximum changes by -1.203×10^{-6} . The gradient maximum considering the ion flux is three orders of magnitude smaller than that calculated previously considering the refractive index change as $\Delta R = \pm 3.1 \times 10^{-3}$. SPR is known to detect refractive changes, and it is likely that the movement of ions during an action potential has some effect on the SPR response if it occurs within the evanescent field.

The value for the refractive index change of $\Delta n = 1.5 \times 10^{-3}$ was chosen. It is more physically plausible that the refractive index change of the cell membrane is being detected more than the ion flux. This refractive index change results in a reflection change of $\Delta R = \pm 3.1 \times 10^{-3}$. In the next chapter the theoretical noise floor and detection limit of the SPR system will be determined. In Section 5.1.2 the sensitivity to refractive index changes of the planar gold surfaces will be experimentally measured.

CHAPTER 4

SYSTEM CHARACTERISATION

This chapter outlines the measurements performed to characterise and calibrate the custom-built SPM before experiments were performed. First the noise floor of the system was quantified, to determine whether the change in refractive index during an action potential of $\Delta n = 1.5 \times 10^{-3}$ could be detected. The noise from both the light source and detector were experimentally measured, and the minimum detectable reflection and refractive index signal were estimated. To ensure long-term recording could be performed, the temperature of the coverslip was monitored to confirm the SLED and LED do not affect the temperature. Finally, how the position of the focused SLED on the back focal plane relates to angle of incidence at the sample plane was determined. An equation fitting was fixed so future measurements could be validated.

4.1 Noise Measurements

4.1.1 Light Source Noise

Consideration of the light source noise was necessary because the signal to be detected was very small. A low noise source was required, that was ideally shot noise limited. The SNR will limit the precision or repeatability of the measurements, so to maximise the signal, as many photons as possible were needed for the ROI and exposure time to obtain an SNR of one. The refractive index and light intensity changes were expected to be very small so the noise was needed to be as low as possible to maximise the chances of detecting the electrical activity using SPR. The shot noise from the SLED was determined by calculating the standard deviation of the number of photons arriving per second (x). Shot noise follows a Poisson probability model, as described in Section 1.6.2, where the central limit theorem states that given a sufficiently large number of interacting particles, N , the Poisson distribution can be approximated as Gaussian with a mean of N and a standard deviation of \sqrt{N} . The standard deviation shows that the variance of the number of photons depends on the expected photon count (Hasinoff, 2014).

$$N_{shot} = \sqrt{N} = \sqrt{\frac{P\lambda}{hc}} \quad (4.1)$$

The total power of the SLED was measured using a power meter (PM100D from Thorlabs) as 1.1 mW across the entire 71 mm² sensor area (beam diameter $\varnothing = 9$ mm). The energy from a photon at 680 nm is $E_{ph} = hc/\lambda = 2.92 \times 10^{-19}$ J (1.823 eV), therefore there was a total of 3.77×10^{15} photons per second emitted from the SLED. Using (4.1) the shot noise of the SLED is therefore, 61.4×10^6 . The shot noise puts an ultimate limit on what can be measured. The absolute sensitivity threshold is the number of photons required to get a signal equivalent to the noise observed by the sensor, or to get an SNR of one. The absolute sensitivity threshold defines the minimum amount of photons needed to detect any signal. The system throughput needed to be determined because the maximum number of photons arriving at the detector is what is important when calculating the minimum detectable signals. The shot noise of the number of photons per pixel per sample time at the detector will determine the limit of detection. Then, assuming the system is shot noise limited the minimum detectable signal resulting in an SNR of one can be calculated. The

optical efficiency of the SPM is calculated in Section 4.1.2.

Analysis of the harmonic components in the temporal noise of the light source was conducted by measuring the noise from the SLED at all frequencies up to 8 kHz. The time series recordings were transformed to the frequency domain to determine which frequencies were present in the light source, so that filtering could be considered. An SLED was used over other available light sources because, in theory, it has extremely low noise (Foust et al., 2008). Figure 4.1 shows representative time series and frequency domain traces of the light source noise recordings for different sampling frequencies. The main source of noise in the SLED is at ~ 100 Hz, which is evident in both the time series trace (d) and frequency domain trace (c). The 100 Hz noise is an artefact and should not be there. It possibly comes from the power supply unit of the SLED, and as such it could not be removed. Attempts to remove the noise using filters was considered. However, APs are made up of frequencies ranging from 500 – 5000 Hz, assuming the duration and rise time of the AP is 2 msec and 0.2 msec, respectively and because the noise from the light source affects the low-frequency rather than the high frequency this low-frequency noise should not affect the measurements. Notch and bandpass filters were considered but are not used in this work because the 3 dB cut-off would be at 500 Hz and there would still be noise present at 100 Hz. The noise will be reduced, but this depends on the type and order of the filter used. Additionally, when using a bandpass filter between 500 – 5000 Hz, the shape of the AP is altered and could be misinterpreted in analysis, see Figure B.1 in Appendix B.2. Other noise reduction techniques were employed, see Section 5.2.2.

The noise of the SLED was measured by calculating the standard deviation as 0.226 ± 0.0588 DN ($n = 8$). A method of relating the digital grayscale value (DN) to number of photons is derived in Section 4.1.3.

4.1.2 Optical Efficiency

Having lots of photons and a shot noise limited source is of little use if the photons do not reach the detector. Therefore, the number of photons arriving at the detector needs to be measured.

To calculate the optical efficiency of the system both the power from the SLED and

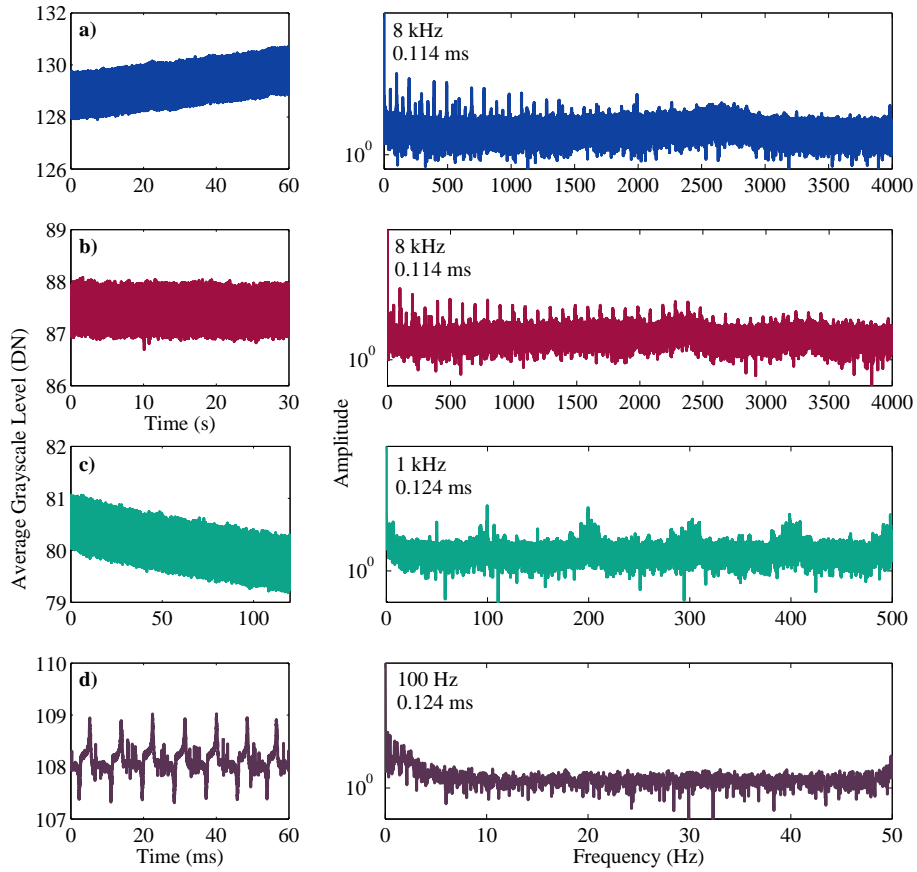


Figure 4.1: Time and frequency domain traces of the light source noise taken with the EPIX camera. The exposure times for each frequency are on the frequency domain traces. The main light source noise is apparent in the time trace (d) at 100 Hz and in the frequency domain trace at 1 kHz (c). The standard deviation of the noise is 0.226 ± 0.0588 DN ($n = 8$).

the power arriving at the detector was measured. The total power (at 680 nm) from the SLED was measured as 1.1 mW. The total power at the detector, after passing through the optical system, was measured using a glass coverslip as the sample with the SLED positioned so that all the light was undergoing TIR as $8.5 \mu\text{W}$. The ratio of the output and input power and therefore, the optical efficiency is 7.73×10^{-3} . This large loss is explained by the number of lossy optical components in the optical pathway of the SPM, and is necessary because of the design. The optical pathway as seen in Figure 2.1 shows the optical path from the SLED to the detector. The beam splitters and the objective lens give the most significant losses and the light beam travels through each twice. The amount of photons arriving at the detector per second is 2.91×10^{13} . The shot noise of the incident photons at the detector gives the ultimate limit to sensitivity assuming the system is SN limited. However, the noise of the detector is still unknown.

4.1.3 Detector Noise

This section will characterise the fundamental noise sources that affect the performance of the detector, these are signal shot noise, fixed pattern noise, and read noise. *Signal shot noise* is related to the interaction of photons with the detector, which produces a variance in the signal that differs pixel-to-pixel. *Fixed pattern noise* (FPN) defines the non-uniformity in each pixel's sensitivity. The *read noise* defines all other noise sources that are not related to the signal.

The number of incident photons at the detector can be converted to electrons or grayscale values (DN) or vice versa using the photon transfer method (Janesick, 2007). This section will derive a method of converting between photons, electrons and digital grayscale values. Figure 4.2 illustrates the steps for a sensor to convert photons to grayscale values.

The number of photons incident on a pixel will depend on the exposure time, the light intensity reaching the detector, and the fill factor of the pixel. The area of a pixel in an image sensor consists of a light-sensitive area along with transistors, electrodes and/or registers. The fill factor is the ratio of the light-sensitive area to the total area of the pixel. During the exposure time, an average number of photons are incident on a pixel in the sensor. The efficiency of the system to convert these incident photons to electrons is called the Quantum Efficiency, η (4.2). The quantum

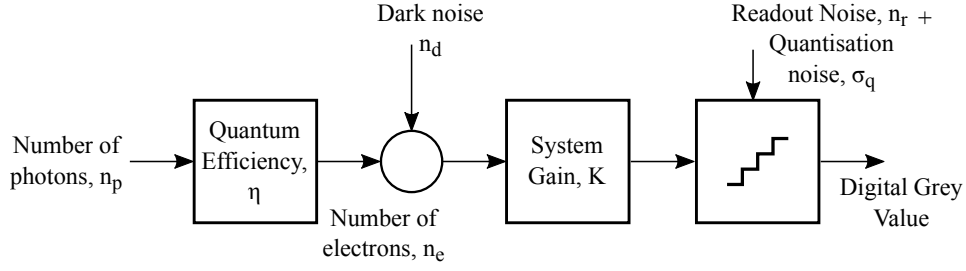


Figure 4.2: Model of a single pixel and the processes required to convert photons to a digital grey value.

efficiency is the ratio of the average number of interacting photons per pixel μ_e , to the average number of incident photons, μ_p during the exposure time and tends to include the fill factor. The average number of electrons (N_{e^-}) generated per pixel as a function of incident photons is given by (4.3), where η_i is the quantum yield. For silicon, and photon energy ranges between 1.14 to 3.1 eV (1000 nm to 400 nm) only one electron will be generated, therefore, the quantum yield will be one. Photon energies greater than this will generate multiple electrons.

$$\eta(\lambda) = \frac{\mu_e}{\mu_p} \quad (4.2)$$

$$N_{e^-} = \eta \cdot \eta_i \cdot \mu_p = \eta_i \cdot \mu_e \quad (4.3)$$

The number of electrons (μ_e) in each pixel is converted into a voltage, amplified, and turned into a digital signal using an analog-to-digital converter (ADC). This process is assumed to be linear and can be described with the system gain, K (4.4) with units DN/e^- , where e_{sat}^- is the saturation capacity of a single pixel and ADU is the bit depth of the ADC. The mean digital grayscale value (DN), μ is given by (4.5), where μ_d is the mean dark grayscale value.

$$K = \frac{e_{sat}^-}{ADU} \quad (4.4)$$

$$\mu = \mu_d + K\mu_e \quad (4.5)$$

Combining (4.2) and (4.5) results in the linear relation between the mean grayscale value and the number of photons converted during the exposure time on the pixel. This equation can be used to simply convert incident photons to the grayscale value or vice versa.

$$\mu = \mu_d + K\eta\mu_p \quad (4.6)$$

Signal Shot Noise

To determine the signal shot noise, the power per pixel is measured and the photon shot noise at the detector will be estimated. Additionally, the shot noise in terms of electrons will be calculated. To convert incident photons to electrons, the quantum efficiency as quoted by the camera manufacturer will be experimentally confirmed. However, because raw data from a camera system is measured in grayscale values the photon transfer method will be employed to calculate the system gain and convert the measured grayscale value to electrons and photons (Janesick, 2007).

To calculate the power per pixel, the power at the detector was measured through a 1 mm diameter pinhole (area = 0.79 mm²) as 0.55 μ W. Note this indicates that the illumination is not uniform. The power in a 20 mm² sensor area was previously measured as 8.5 μ W and the power measured through the pinhole is nearly twice the average. The fixed pattern noise that quantifies the spatial variation in the pixels under uniform illumination in the camera is investigated in a later section. The power per pixel can be calculated. The pixel size of the EPIX CMOS camera is 9.9 μ m, giving an area of 98.01 μ m². Therefore, there are 8015 pixels within the area of the 1 mm pinhole and the power per pixel is $0.55 \times 10^{-6} / 8015 = 6.86 \times 10^{-11}$ W. This results in $2.35 \times 10^8 \pm 15300$ photons per pixel per second (results given as signal \pm shot noise) or $29.1 \times 10^3 \pm 171$ photons per pixel per sampling frequency, assuming a 8 kHz sampling frequency and 0.124 ms exposure time.

The quantum efficiency of the sensor is used to convert incident photons to electrons. To confirm the quantum efficiency as specified by the camera manufacturer, the temporal response of a small number of pixels were recorded. Two recordings were made; the first, to measure the grayscale values as a function of exposure time for the average signal, and the second to measure the dark noise at the same exposure times. The measurements were performed using the SPM set up in total internal reflection to ensure the values measured were at their maximum. 50 equally spaced exposure times were measured between 0.02 and 1.6 ms. The EPIX camera imaged an area of 200 \times 200 at 250 Hz for 15 seconds. The dark image at every exposure time used was also measured in the same way.

The image stacks for each exposure time were imported to MATLAB. The mean grayscale value, μ was calculated for both the signal and dark (μ_d) values across all

the pixels at each exposure time by averaging over all rows and columns to give a vector of μ over time, Figure 4.3. The mean dark image was independent of exposure time and measured as 31.207 ($\sigma = 7.35 \times 10^{-4}$) DN, which includes a black offset. The standard deviation of the dark images defines the level of dark noise in the detector. The dark noise was calculated as 0.0354 ($\sigma = 7.35 \times 10^{-4}$) DN.

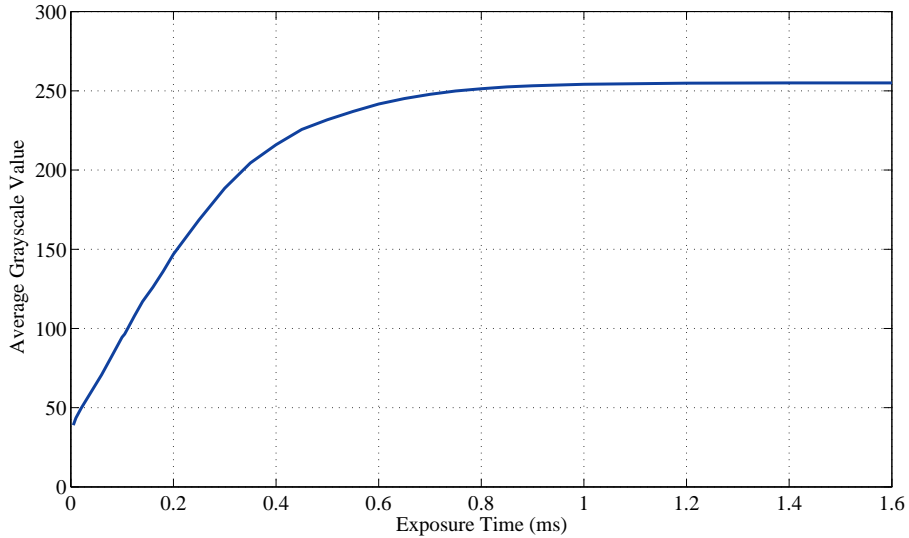


Figure 4.3: Measured mean gray values as a function of the exposure time. $\mu_{y,dark}$ at all exposure times was an average of 31.207 ($\sigma = 7.353 \times 10^{-4}$) DN.

The quantum efficiency defines how efficient the sensor is at converting incident photons to electrons and needs to be confirmed before the grayscale values (DN) can be converted to meaningful units. Figure 4.3 demonstrates that the camera appears to be 50% saturated, i.e., has a DN of 128 at an exposure time around 0.18 ms. The number of photons per pixel for an 0.18 ms exposure time can be calculated using the number of photons per pixel per second determined earlier as $2.35 \times 10^8 \times 0.16 \times 10^{-3} = 42.3 \times 10^3 \pm 206$. The full well capacity of the pixel quantifies how many electrons an individual pixel can store before it saturates. In the sensor datasheet, Appendix B.1 this is quoted as $35,000e^-$. When the sensor is 50% saturated, $42.3 \times 10^3 \pm 206$ photons/pixel/sample should convert to $17500e^-$. In fact, the experimentally measured quantum efficiency at 680 nm is $17500/42.3 \times 10^3 = 41.4\%$. The quantum efficiency quoted in the datasheet is 45%. The datasheet quotes

the peak quantum efficiency and will vary slightly depending on the wavelength. Assuming the quantum efficiency is 41.38%, at 8 kHz there will be $12.06 \times 10^3 \pm 110$ electrons/pixel. Therefore, the *signal shot noise* at 8 kHz (σ_s) is 110 electrons/pixel.

The noise of the SLED and dark noise of the detector have both been quoted in grayscale values with the units DN. To derive any meaningful information, these grayscale values need to be converted to electrons or photons. To convert between the two the system gain needs to be established. The system gain indicates how many electrons are needed to observe a change in the 8-bit grayscale value of the camera. Using (4.4), where the single pixel's saturation capacity is defined in the sensor datasheet as $35,000e^-$, and the bit depth is 255 (2^8). The system gain (K) is, therefore, 137. The number of electrons per pixel per sample time was calculated as $12.06 \times 10^3 \pm 110$, which will result in a grayscale value of around $88 + \mu_{y,dark} = 119$ DN. Figure 4.3 shows the measured grayscale value at 8 kHz was around 108 DN. The difference can be explained by the system gain not being exactly 137 as the pixel's saturation capacity is not 100% reliable. To saturate the detector at an 8 kHz sampling frequency $2 - 3\times$ more photons are needed. This was unfortunately not available with the light source being used. Introducing a higher power laser could have been an option but this could have added more noise (shot noise & relative intensity noise), which we wanted to keep to a minimum. Lasers, in their very nature, have larger relative intensity noise compared to SLEDs (Zhuravleva et al., 2005; Foust et al., 2008). The lower noise of an SLED is due to the wider spectrum of radiation used (Zhuravleva et al., 2005). Now, using the system gain, the dark noise, and (4.5) the conversion between grayscale values and photons is simple.

Fixed Pattern Noise

The illumination was previously found not to be uniform. The fixed pattern noise (FPN) defines the spatial variation or non-uniformity in each pixel under uniform illumination in the camera and consists of two elements. One is the dark signal non-uniformity (DSNU), which is an offset of the detector output when there is no illumination. The other is the photo response non-uniformity (PRNU), which is due to non-uniform responsivity and gain of the pixels. FPN is fixed because it is the same pattern, image to image (Janesick, 2007). First, the dark signal non-uniformity

(DSNU) needed to be quantified to determine if the non-uniformity in the pixel was due to the light source or FPN. Later PRNU will be described.

To quantify the DSNU FPN, the EPIX camera imaged an area of 200×200 at 250 Hz for 15 seconds at an exposure time where the sensor is 50% saturated under constant illumination. Earlier the camera was found to be 50% saturated at an exposure time of 0.18 ms. The image capture was repeated to find the dark image, where the sensor was covered at the same exposure time and images recorded. The average value of each pixel for the signal and dark image was computed to average out the temporal noise and are shown in Figure 4.4 (a) and (b), respectively. The dark noise was subtracted from the images under uniform illumination, Figure 4.4 (c). The column FPN is noticeable in Figure 4.4 (c). The EPIX camera is a CMOS image sensor and these sensors read out the charge in columns. The column FPN noise is caused by the variation in the column amplifier parameters, for example, the offset voltage, and the transistor threshold voltage, which will vary column to column. The pixels with higher values towards the outside of Figure 4.4 are present in other images and therefore, due to vignetting or non-uniformity in the light source. The ROI for cell-based experiments is almost always in the center of the field of view so will not be affected by this.

The average area uniformity for the differential image is evaluated in the histogram in Figure 4.5. The average area uniformity for the differential image fits a lognormal distribution, meaning the logarithm of the variable (X) is normally distributed, where $Y = \log(X)$ (Johnson et al., 1994), with a mean of 97.5 and variance 869. The goodness of fit values are R-square = 0.997, and RMSE = 23.6. The average pixel values for the 50% saturated image, dark, and differential image are 128 ± 28.9 , 31.2 ± 5.37 , and 97.4 ± 28.5 DN, respectively. The histogram and standard deviation show that the light source incident on the sensor has poor uniformity as an ideal uniformity would have one bar. The standard deviation and therefore, the DNSU FPN for the differential image is 25.8 DN, corresponding to $3540e^-$.

To eliminate the DNSU FPN or non-uniformity in the light source, subtracting two images or signal averaging will remove the noise as it is present in all images (Gardner, 2012; Liu et al., 2015). The average pixel values after subtracting two images is 0.889 ± 1.55 DN. Resulting in a corrected FPN of $212e^-$. The FPN regime begins

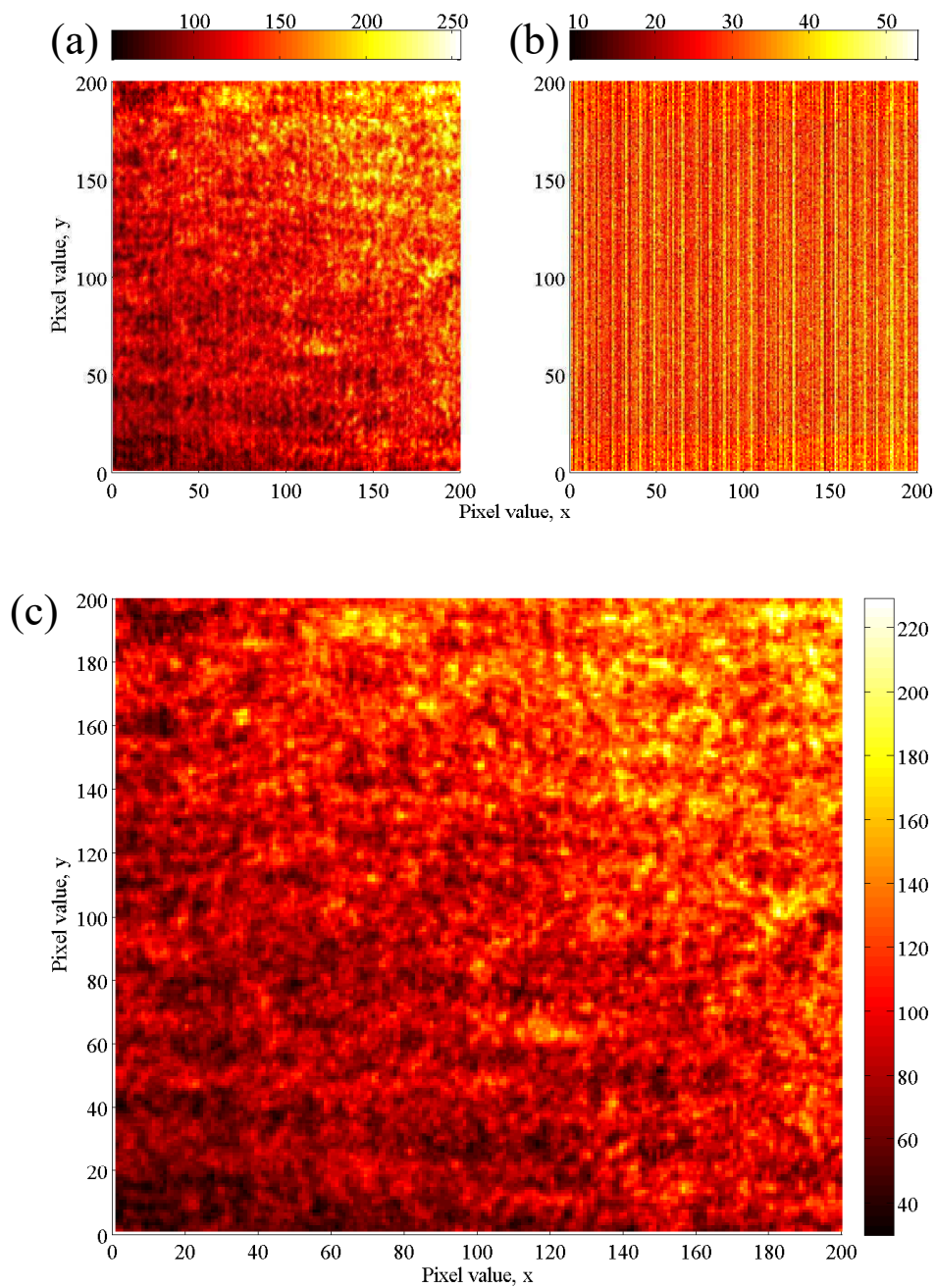


Figure 4.4: The average value of each pixel for the signal (a) and dark image (b). The dark noise was subtracted from the signal to give the differential (c). The colourbars are the intensity in digital grayscale values.

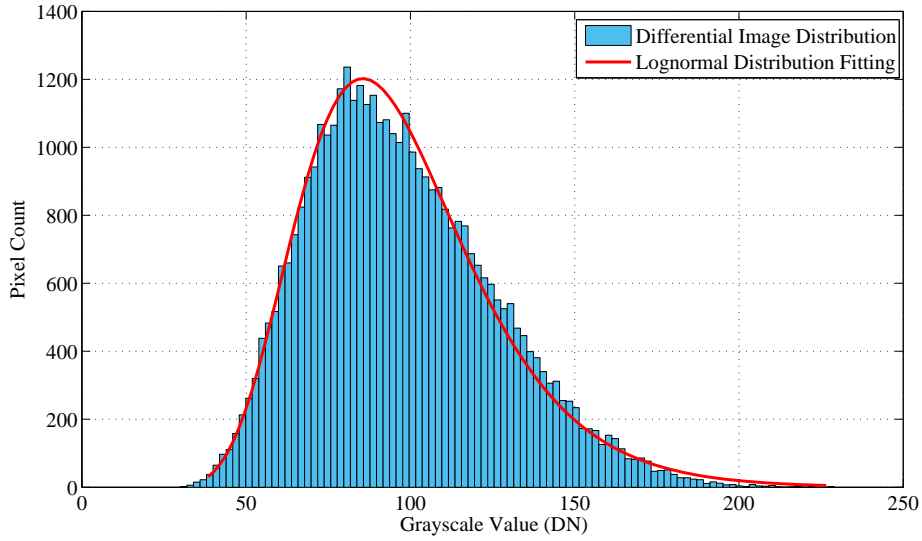


Figure 4.5: The average area uniformity for the differential image. The differential image fits a lognormal distribution, where $R\text{-square} = 0.997$, and $\text{RMSE} = 23.6$. The average pixel values for the differential image is 128 ± 28.9 DN.

at a signal level of approximately $10 \times 10^3 e^-$ for CMOS sensors (Janesick, 2007). It was previously estimated that there would be $12.06 \times 10^3 \pm 110$ electrons/pixel at 8 kHz and, therefore, the signal will possibly be within the FPN regime. FPN is spatial noise so is applied across the whole image. Methods to reduce the FPN by subtracting dark images and signal averaging are discussed in Section 5.2.2. Additionally, a shorter exposure time could be used to reduce the number of electrons per pixel but this will reduce the amount of signal available.

The PRNU is due to non-uniform gain and responsivity in the sensor caused during the manufacturing process. This results in slight variations in how each pixel converts photons to electrons (Janesick, 2001; Li and Li, 2012). The effect of the PRNU on the detector output is similar to a scaling factor, which is non-uniform pixel to pixel. The magnitude of the PRNU can be reduced by using uniform illumination on the camera and normalising the images using a look-up table (Janesick, 2001; Li and Li, 2012).

Read Noise

The read noise defines how much noise is present due to the electronics transferring the charge from the pixels to the camera. All the system components contribute to this noise. The read noise (σ_r) was determined by calculating the difference between two bias images with the shortest exposure time (0.003 ms) (Photometrics, 2015). Using MATLAB, two images were subtracted from one another to give the difference, Figure B.2 and the standard deviation of the differential image was calculated. Using (4.7), the *read noise* is therefore, $8.36e^-$ and since the read noise is added to each pixel as it is read out, the noise is added per sample.

$$\sigma_r = \frac{\sigma_{diff}K}{\sqrt{2}} \quad (4.7)$$

Total Noise

The total noise can now be calculated by adding the different noise sources in quadrature. The shot noise (σ_s) was 110 electrons/sample/pixel, and the read noise (σ_r) was calculated to be $8.36e^-$. The dark noise (σ_d) for the detector was calculated from the standard deviation of a dark image as 0.0354 DN, corresponding to about $5e^-$. The DNSU FPN (σ_{fpn}) for the differential image is $212e^-$ but this is across the whole sample and per pixel will be negligible. The total noise per pixel in the detector is $\sigma = \sqrt{\sigma_s^2 + \sigma_r^2 + \sigma_d^2 + \sigma_{fpn}^2} = 110e^-$ and is shot noise limited.

The minimum detectable signal (ΔR_{min}) per pixel can now be calculated using N_{e^-}/σ as one part in 109 with an SNR of one.

4.1.4 Minimum Detectable Refractive Index Change

In Chapter 3 it was determined that during an action potential the refractive index of the cell membrane will change by $\Delta n = 1.5 \times 10^{-3}$ resulting in a theoretical, fractional light intensity change of $\Delta R = \pm 3.1 \times 10^{-3}$ and a theoretical $\Delta R/\Delta n$ of 2.067. Whether or not the sensor developed can detect this minimum detectable refractive index change is essential. The minimum detectable refractive index change can be determined, first by calculating the gain factor, which is given by (4.8) and based on (3.26), where d_3 is Δn .

$$G = \frac{\Delta R \Delta \theta}{\Delta \theta \Delta n} \quad (4.8)$$

The theoretical $\Delta\theta/\Delta n$ for the five-layer model can be seen in Figure 3.17. As expected, $\Delta\theta/\Delta n$ becomes less sensitive as the gap distance between the cell and sensor surface increases. The theoretical $\Delta R/\Delta\theta$ or the gradient of the SPR dip in air for planar gold is calculated from the gradient maximum in Figure 3.9 as 1.54. Similarly, the gradient maximum were obtained from the five-layer model as the gap distance was increased. The effect on the gain factor as a function of $\Delta\theta/\Delta n$ and $\Delta R/\Delta\theta$ was investigated. Each individual line in Figure 4.6 is from changing $\Delta R/\Delta\theta$ as a function of $\Delta\theta/\Delta n$. As the gap distance increases, the effective bulk refractive index decreases because the larger refractive index of the membrane has less effect, and the resulting gain factor increases. The gain factor is at a maximum for planar gold with air as the dielectric. However, planar gold in air for this situation is not realistic. A gap distance of 30 nm is assumed (Braun and Fromherz, 1998; Giebel et al., 1999; Toma et al., 2014).

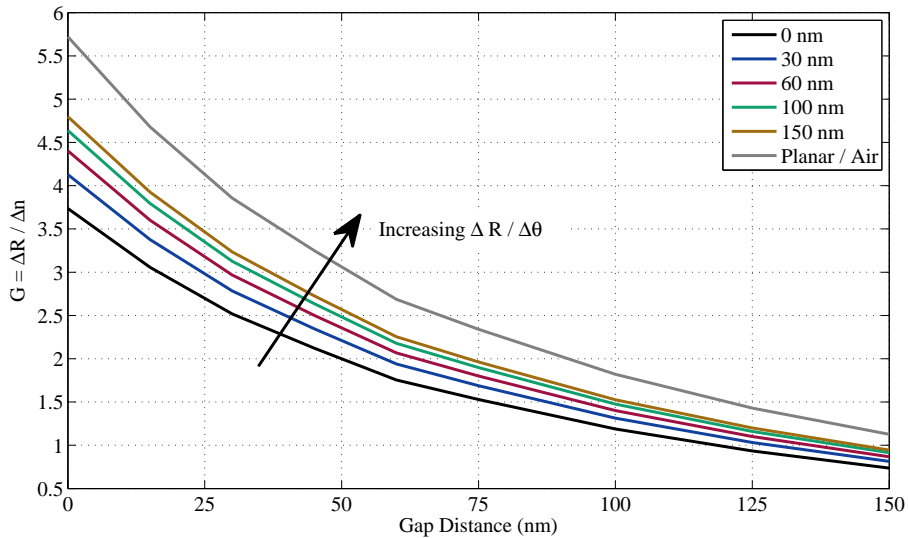


Figure 4.6: The effect on the gain factor (4.8) with increasing the gap distance. The individual traces are from varying $\Delta R/\Delta\theta$ as determined from the modelling with the five-layer model. $\Delta R/\Delta n$ comes from Figure 3.17.

The minimum detectable ΔR_{min} was determined to be 1:110. Using (4.9), Δn can be calculated, where $\Delta R/\Delta\theta = 0.469$, and $\Delta\theta/\Delta n = 5.933$ assuming a 30 nm gap

distance.

$$\frac{\Delta R}{\Delta n} = \frac{\Delta R}{\Delta \theta} \frac{\Delta \theta}{\Delta n} \quad (4.9)$$

At an 8 kHz sampling rate, Δn_{min} is 3.29×10^{-3} or has a minimum detectable Δn of 1:304 per pixel with a gap distance of 30 nm between the cell and the surface. This rises to Δn_{min} is 2.45×10^{-3} or minimum detectable Δn of 1:409 per pixel if the cell is directly on the gold surface ($d = 0nm$). The sensor needs to be able to detect a change in Δn of 1.5×10^{-3} . Under these conditions the SNR is 0.456 – 0.612, and is smaller than what we can detect assuming a gap distance of less than 30 nm. However, this minimum detectable refractive index change is per pixel, and the cell will cover more than one pixel. Therefore, it will be possible to average across the entire region of interest (ROI) to increase the SNR and improve the minimum detectable signal.

In Section 2.13 it was determined that the smallest ROI imaged during experiments is likely to be around 48×48 pixels. Assuming the cell is a perfect circle, with a radius of $6.5 \mu m$ (cell area = $133 \mu m^2$), this is magnified to $133 \times 18^2 = 4.31 \times 10^4 \mu m$ on the camera. One pixel is $9.9 \mu m$, which gives an area of $98 \mu m^2$. The number of pixels per cell can be calculated as $4.31 \times 10^4 / 98 = 438$ pixels/cell. The total noise per ROI is now $2300e^-$.

When considering the area and number of pixels the minimum detectable ΔR rises to 4.35×10^{-4} or one part in 2300. Using (4.9), Δn for the entire ROI can be calculated, where $\Delta R / \Delta \theta = 0.469$, and $\Delta \theta / \Delta n = 5.93$ with a 30 nm gap distance. $\Delta n_{min,30}$ is 1.56×10^{-4} or Δn of 1:6400 per ROI with a gap distance of 30 nm between the cell and the surface. The minimum detectable Δn rises to $\Delta n_{min,0}$ is 1.16×10^{-4} or Δn is 1:8580 per ROI if the cell is directly on the gold surface ($d = 0nm$). Both of these minimum detectable signals are for an 8 kHz sampling rate. The sensor needs to be able to detect a change in Δn of 1.5×10^{-3} , which is now about 9 – 12 \times greater than what we can detect assuming the gap distance is less than 30 nm. The sensor should now theoretically, be able to detect the refractive index change of $\Delta n = 1.5 \times 10^{-3}$ up to a gap distance of 150 nm, where $\Delta n_{min,150} = 4.605 \times 10^{-4}$. Under these conditions the SNR is 3.26.

The refractive index unit (RIU) is an arbitrary unit that characterises the sensitivity of an SPR sensor as a change in the refractive index of the medium, given by (3.23).

$\Delta R/\Delta n$ for the sensor based on the five-layer model decreases from 3.74 to 2.78 RIU when the gap distance increases to 30 nm.

Although the sensor should now theoretically, be able to detect the refractive index change during an AP up to a gap distance (d) of 150 nm, the cell/surface distance is never fixed. Additionally, the calculations in Chapter 3 estimating the refractive index change might be incorrect, so it is anticipated that in practice signal averaging may be required to improve the SNR further. Signal averaging is a digital technique that works by splitting the waveform into epochs and summing them with the aim that the noise adds destructively and reduces, while the signal builds up, described in Section 1.6.4. The signal-to-noise ratio increases with the \sqrt{N} , where N is the number of epochs or repeats. Figure 4.7 shows the improvement of the minimum detectable ΔR and Δn after signal averaging. Δn considers gap distances of 0 nm and 30 nm.

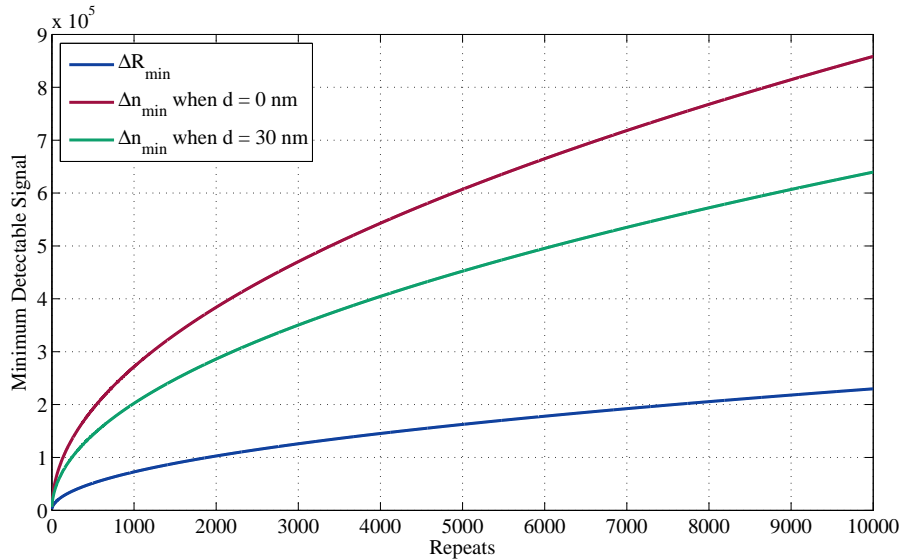


Figure 4.7: Improvement in the minimum detectable ΔR and Δn with $d = 0$ and 30 nm after signal averaging. The SNR improves by \sqrt{N} , where N is the number of repeats. Illustrated in Figure 1.6.

4.2 Temperature Dependence

To ensure that long-term recording could be performed on the cell cultures it was important that the SLED or 590 nm LED would not affect the temperature of the coverslip. If the coverslip temperature was to increase too much over time, then this could irreversibly damage the cell culture. This change in temperature (ΔT) can be calculated using,

$$\Delta T = \frac{Q}{mc} \quad (4.10)$$

where m is the mass of the water (0.5 mg), Q is the heat transferred in the exchange, in joules, and c is the specific heat capacity of water, which is 4.19 joule/gram°C. Assuming the worst case and that all the power from the SLED (1.1 mW) is transferred to heat energy over 20 mins the temperature change will be 0.6 Kelvin. However, splitting the system efficiency will give a more realistic result. Assuming, $\sqrt{7.73 \times 10^{-3}} \times 1.1 \times 10^{-3} = 0.097$ mW, the temperature change will be 0.056 K over 20 mins. These values do not take into account any loss of heat to the environment, for example, via the glass coverslip, glass objective etc. and are the worst case.

To experimentally validate the change in temperature, a thermistor (Fluke 54 II) was thermally bonded to the coverslip, and the LED and SLED were turned on (at different times) and left for 20 minutes. The ambient temperature was monitored as a reference, and the air conditioning was set to 19 °C. Table 4.1 details the results. The largest change in temperature after 20 minutes is less than 1% which can be attributed to noise. Therefore, we can conclude that the LED or SLED does not have a significant impact on the temperature of the coverslip.

4.3 Determination of the Angle of Incidence

As described in Section 2.9.2, the angle of incidence at the sample with respect to distance from the origin is not linear or even $\tan \theta$ as expected but rather $\sin \theta$. This is referred to as the sine condition (Richards and Wolf, 1959). To determine how the angle of incidence changes with respect to the position of the focused SLED at the back focal plane (BFP), the SLED was scanned across the BFP with different solvents on the glass surface. The method is illustrated in Figure 4.8. The focused

Table 4.1: Measured temperature of the coverslip and ambient at the start and after 20 mins of use with SLED or LED. The largest change in temperature after 20 minutes is less than 1%, therefore, the SLED and LED have no significant affect on the temperature of the coverslip.

	Time (mins)	Coverslip Temperature ($^{\circ}\text{C}$)	Ambient Temperature ($^{\circ}\text{C}$)
LED	0	23.5	22.8
	20	23.4	22.7
SLED	0	23.4	23.1
	20	23.4	23.3

SLED was scanned across the BFP using the stepper motor moving the SLED and pair of lenses. The radial position of the focused SLED at the BFP then relates to angle of incidence at the sample plane (Burghardt, 2012). The reflected light intensity detected at the EPIX camera was plotted with respect to the radial position of the SLED along the x -axis. The position where where all light is reflected, i.e., being totally internally reflected was exported and related to the critical angle for each solvent using (3.18). Finally, an expression was derived to relate distance from the origin (position of SLED) for each critical angle. The expression was then compared to $\sin \theta$.

The angle of incidence was varied using a stepper motor moving the focused SLED beam across the BFP of the objective at a rate of 0.1 mm/sec. Images were captured on the EPIX at 24 fps, with an exposure time of 0.124 msec. The resulting scans were processed in MATLAB by aligning the origins, i.e., where the large peak of light intensity is in the middle and all light is transmitted through the sample, Figure 4.9. The refractive index of the glass used is defined in the datasheet as 1.52 at 680 nm. The corresponding frame number (x) for the critical angle of each solvent was manually exported and the distance from the origin was calculated from the time taken ($t = x/fps$) and the speed ($d = s \times t$), Table 4.2. The scans were repeated three times. The means and standard deviation for each solvent are reported in the table. The greatest difference between repeats was 0.04 mm, and with 95%

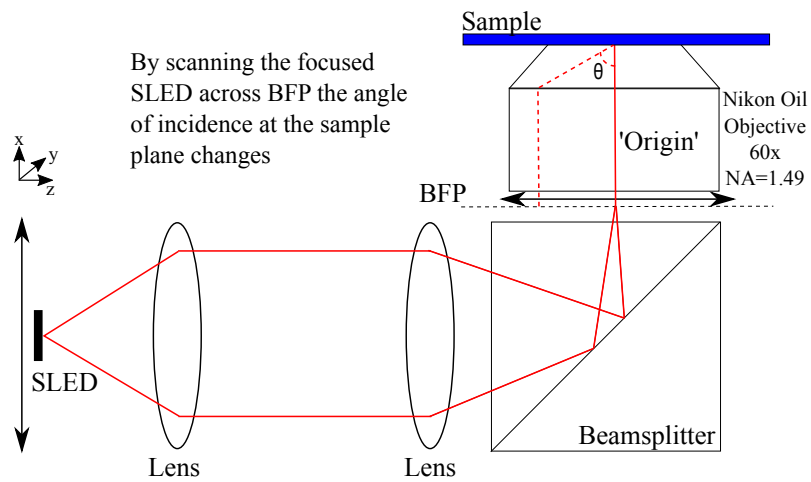


Figure 4.8: Illustration of the method employed to determine the angle of incidence at the sample plane by scanning a focused SLED across the BFP. The SLED and pair of lenses are attached to a stepper motor which moves them along the x -axis. The reflected light intensity detected at the EPIX camera was plotted with respect to the position of the SLED along the x -axis. The position where all light is reflected, i.e., being totally internally reflected was exported and related to the critical angle for each solvent using (3.18) (Burghardt, 2012).

confidence values the difference is less than 1 mm.

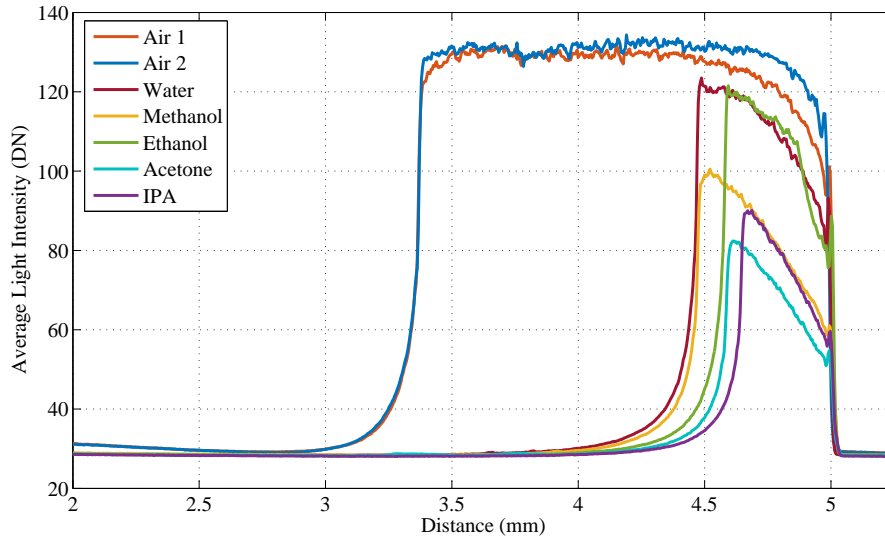


Figure 4.9: Resulting scans with different media on glass. The refractive index of the media changed the critical angle. The focused SLED scans across the BFP. The first increase in light intensity from the y -axis is the position where all light is undergoing total internal reflection, and thus the critical angle. The resulting θ_c corresponds to a distance that is used to plot the curve of the BFP. The average dark noise is around 28 DN for an exposure time of 0.124 ms.

The distance from the origin was plotted against the critical angle (Figure 4.10) to find the curve of the BFP. The fitting was performed using the Curve Fitting Toolbox in MATLAB. The fitting is a second order non-linear Least Squares Polynomial plotted with the 95% confidence bounds. $f(x) = p_1x^2 + p_2x + p_3$, where $p_1 = 1.41$, $p_2 = 7.43$, and $p_3 = 8.89 \times 10^{-3}$. The residuals from the Polynomial fit are in bottom plot, where R-square = 0.9996, SSE = 1.38, and RMSE = 0.588. Other fittings were attempted and the results are in Table 4.3 confirming the Polynomial fit had the best R-square value and smallest SSE and RMSE.

Table 4.2: Table detailing the refractive index, critical angle (θ_c), and measured distance from the origin for each solvent. Refractive Indices are given for a 680 nm wavelength.

Medium	Refractive Index	Calculated θ_c	Distance from origin (mm)
Air	1.000	41.15	3.39 ± 0.0312
Methanol	1.325	60.91	4.48 ± 0.0369
Water	1.333	61.27	4.51 ± 0.0402
Acetone	1.357	63.35	4.56 ± 0.0080
Ethanol	1.361	63.59	4.58 ± 0.0065
IPA	1.381	64.96	4.62 ± 0.0185

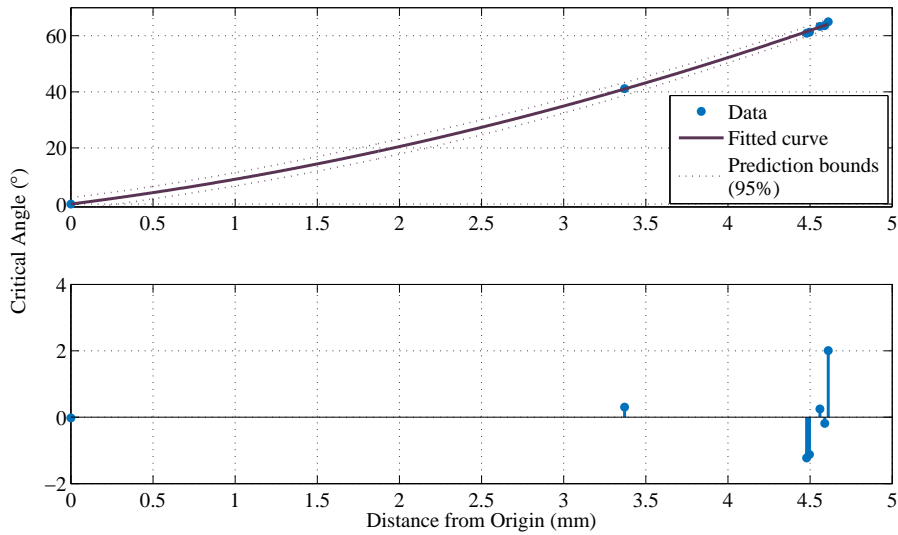


Figure 4.10: Summary from the scans showing the distance from origin vs. critical angle for the different media (top) and residuals (bottom). The fitting is a second order non-linear Least Squares Polynomial shown with the 95% confidence bounds. $f(x) = p_1x^2 + p_2x + p_3$, where $p_1 = 1.41$, $p_2 = 7.43$, and $p_3 = 8.89 \times 10^{-3}$. R-square = 0.9996, SSE = 1.38, and RMSE = 0.588.

Table 4.3: Comparison of the other curve fitting results for determining the angle of incidence. The second order Polynomial fitting was selected because it has the highest Adj R-Square, and smallest RMSE.

	SSE	R-Square	Adj R-Square	RMSE
Fourier	1.38	0.9996	0.9992	0.679
Gaussian	5.62	0.9984	0.9975	1.19
Polynomial (2)	1.38	0.9996	0.9994	0.588
Sum of Sine	28.3	0.9917	0.9875	2.66

The Polynomial fit was plotted against the aforementioned sine condition as a function of angle of incidence in Figure 4.11. The inset image shows the difference between sine and poly, showing that at larger angles the difference between the two fittings is more significant. Therefore, $\sin \theta$ is not a suitable approximation for the determination of the angle of incidence and the polynomial fitting will be used going forward.

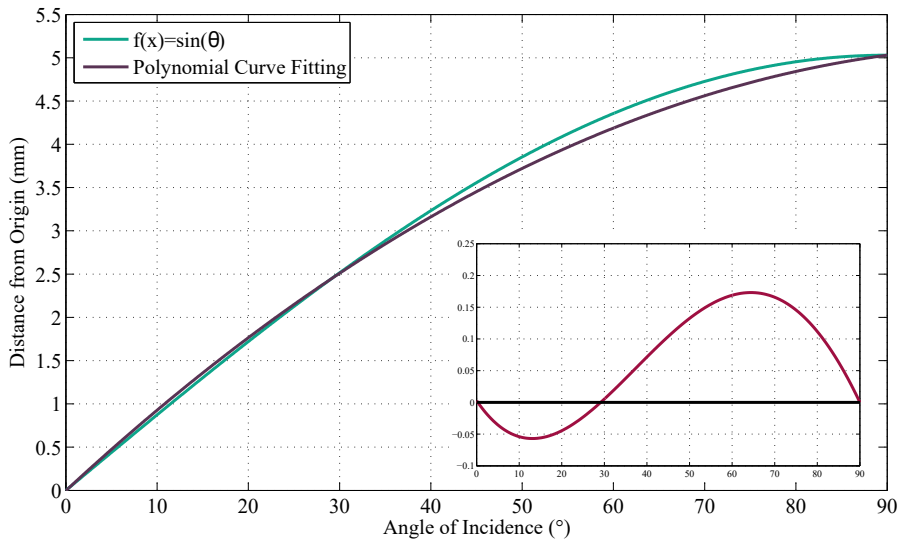


Figure 4.11: Comparison of the polynomial curve fitting with the sine condition, $\sin \theta$ to illustrate how the angle of incidence relates to SLED position. The inset image is the difference between the two fittings (sine - poly).

4.4 Chapter Conclusions

This chapter outlined the measurements performed to characterise and calibrate the custom-built SPM before experiments were performed.

First, the noise floor of the system was determined to evaluate whether the change in the refractive index during an action potential could be detected in principle or what size signal the action potential would have to produce for it to be detected. The noise from both the light source and detector were experimentally measured. The power of the SLED was measured as 1.1 mW, which results in 3.77×10^{15} photons per second. The power incident on the detector with a glass coverslip as the sample and ensuring all the light was undergoing TIR was measured as 8.5 μ W. The noise of the SLED incident on the detector was estimated from the standard deviation over time as 0.226 ± 0.0588 DN. Using the power at the SLED and detector, the optical efficiency was determined to be 7.73×10^{-3} . This large loss can be explained by the number of lossy optical components in the optical pathway of the SPM. The loss is necessary because of the design. The optical pathway as seen in Figure 2.1 shows the SPR response from the SLED to the detector goes through a beamsplitter twice, where the light-source will lose 50% of power each time, a dichroic once, a polariser, and four lenses. The beam splitters and the objective lens give the most substantial losses.

The power arriving at the detector per second per pixel was measured using a 1 mm pinhole as 0.55 μ W in a 0.79 mm² area. The number of photons per second per pixel was calculated considering the pixel area of 98 μ m² as $2.35 \times 10^8 \pm 15300$ (signal \pm shot noise) or at 8 kHz $29.1 \times 10^3 \pm 171$. The shot noise of incident photons at the detector is, therefore, 171 photons/pixel for an 8 kHz sampling frequency and gives the ultimate limit to sensitivity. The noise at an 8 kHz sampling frequency is important because ideally the SPR response will be sampled at a rate equal to this or above.

The quantum efficiency of the image sensor was experimentally measured. The sensor was 50% saturated at an exposure time of 0.18 ms, giving an estimated quantum efficiency of 41.4%. The quantum efficiency is the measure of the effectiveness of the sensor to convert incident photons to electrons. The number of electrons generated

per pixel was calculated by multiplying the number of incident photons per pixel by the quantum efficiency. At an 8 kHz sampling frequency, there was an average of $12.06 \times 10^3 \pm 110$ electrons/sample/pixel. Resulting in an electron shot noise of 110 electrons/sample/pixel.

The illumination was previously found to not be uniform. The dark signal non-uniformity fixed pattern noise of the detector was determined from the standard deviation of the difference between one image that is around 50% saturated, and a corresponding dark image as $3540e^-$ per image. The FPN was improved to $212e^-$ per image when a second image was subtracted from the first to remove common noise.

The read noise was determined from the standard deviation of a differential dark image as $8.36e^-$. The dark noise (σ_d) for the detector was calculated from the standard deviation of a dark image as 0.0354 DN, corresponding to about $5e^-$. Considering the shot noise is 110 electrons/sample/pixel, the dark noise, $5e^-$, and read noise, $8.36e^-$, the total noise (σ) is $110e^-$, and is shot noise limited. The minimum detectable signal (ΔR) was calculated as one part in 109 to achieve an SNR of one for one pixel.

During an action potential, it has been established that the refractive index of the cell membrane will change by $\Delta n = 1.5 \times 10^{-3}$, which gives rise to a theoretical, fractional light intensity change of $\Delta R = \pm 3.1 \times 10^{-3}$. Whether or not the sensor developed can detect this minimum detectable refractive index change is important, so the minimum detectable refractive index change was determined. The theoretical $\Delta\theta/\Delta n$ and $\Delta R/\Delta\theta$ were acquired from the five-layer model from Chapter 3. Both $\Delta\theta/\Delta n$ and $\Delta R/\Delta\theta$ depend on the gap distance between the cell and sensor surface, becoming less sensitive as the gap increases. The gain factor is defined as $\Delta R/\Delta\theta$ multiplied by $\Delta\theta/\Delta n$ and describes the sensitivity considering both terms. Again, it is dependent upon the gap distance and as the gap distance increases, the gain factor increases. The gain factor increases because of the movement of the cell membrane. The cell membrane has a larger refractive index and as it moves away from the surface, the effective bulk refractive index decreases. In this case, a large gain factor is not necessarily a positive because if the cell membrane is outside of the evanescent field of the sensor, i.e, more than 150 nm away from the surface, then the refractive

index change will be undetectable. The gain factor is at a maximum for planar gold with air as the dielectric due to the small refractive index of air.

The minimum detectable Δn was calculated, assuming a 30 nm gap distance as 3.29×10^{-3} or the minimum detectable Δn is 1:304 per pixel at an 8 kHz sampling frequency. If the cell is directly on the gold surface, i.e., has a gap distance of 0 nm then the minimum detectable Δn rises to 2.45×10^{-3} or can discern one part in 409 per pixel at 8 kHz. The sensor needs to detect a Δn of 1.5×10^{-3} , which is currently 0.6–1.2 \times smaller than what we can detect assuming a gap distance of less than 30 nm. More photons are required. For the detector to collect more photons a longer exposure time is required, which is not possible considering the sample rate required. However, during experiments the cell of interest will be covering more than one pixel, so, it will be possible to average across the entire region of interest to increase the SNR and improve the minimum detectable signal.

When considering the area and number of pixels the minimum detectable ΔR rises to 4.352×10^{-4} or one part in 2298. Similarly, Δn_{min} increases to 1.564×10^{-4} or has a minimum detectable Δn of 1:6396 per ROI assuming a gap distance of 30 nm between the cell and the surface. If the cell is directly on the gold surface, this minimum detectable Δn rises to 1.16×10^{-4} or 1:8590 per ROI. Now, the minimum detectable Δn is 9–12 \times greater than what occurs during an AP. Therefore, the sensor should be able to detect the refractive index change of $\Delta n = 1.5 \times 10^{-3}$ up to a gap distance of 150 nm, where $\Delta n_{min,150} = 4.605 \times 10^{-4}$. The actual sensitivity to refractive index changes in an intensity interrogation scheme is experimentally confirmed in Section 5.1.2.

The noise floor of the system has been determined to be low enough to theoretically, be capable of detecting the refractive index change of the cell membrane during an AP. However, it is anticipated that the signal will be small and given that the gap distance is unknown, noise reduction techniques for example, signal averaging may be required to improve the SNR further. The effect of signal averaging on the minimum detectable signals was investigated. The minimum detectable ΔR and Δn increase with the \sqrt{N} , where N is the number of repeats.

To ensure that long-term recording could be performed on the cell cultures, the temperature change of the coverslip was monitored over 20 mins during exposure to

the SLED or 590 nm LED. It was concluded that the LED or SLED do not have a significant impact on the temperature of the coverslip.

The use of a high NA objective lens to excite the surface plasmons results in the angles across the BFP not increasing linearly but instead by $\sin \theta$. This non-linearity is referred to as the sine condition (Richards and Wolf, 1959). To relate SLED position to angle of incidence, scans were performed with different solvents on the glass surface and plotted to derive an expression to relate position on the BFP to angle. The distance from the origin was plotted against the critical angle. The expression follows a second order non-linear Least Squares Polynomial given by $f(x) = p_1x^2 + p_2x + p_3$, where $p_1 = 1.41$, $p_2 = 7.43$, and $p_3 = 8.89 \times 10^{-3}$. The polynomial fitting was compared to the sine condition. The comparison showed that at higher angles, the difference between the fittings was more significant. Therefore, $\sin \theta$ is not an accurate equation for determining the angle of incidence. The derived polynomial equation will be used in the following chapters to convert position to the angle of incidence for the angular SPR responses.

Now that the system has been characterised and calibrated, the angular SPR responses for planar gold are established in the following chapter. The sensitivity to refractive index changes in an intensity modulating SPR scheme is also determined to ensure that the RI change of $\pm 1.5 \times 10^{-3}$ can be detected. After confirming the system is capable of detecting small refractive index changes, primary rat hippocampal neurons are cultured on the sensors, the experimental protocol is developed, and the analysis of the data is described.

CHAPTER 5

PLANAR GOLD SURFACES

In the previous chapters, the modelling of the change in refractive index of the membrane was found, and the noise floor and sensitivity of the system was characterised. The five-layer model was solved using the transfer matrix method. For an estimated refractive index change of $\Delta n = 1.5 \times 10^{-3}$, the theoretical light intensity change will be $\Delta R = \pm 3.1 \times 10^{-3}$, which results in a theoretical $\Delta R/\Delta n$ of 2.067. Chapter 4 calculated the minimum detectable ΔR and Δn signals considering the area and number of pixels of the sensor that the target cell is likely to be covering. The minimum detectable ΔR is one part in 2300, and Δn_{min} is 1.56×10^{-4} or 1:6400 per ROI assuming a gap distance of 30 nm between the cell and the surface. The SPR sensor should, theoretically, considering the noise floor be able to detect the refractive index change of $\Delta n = 1.5 \times 10^{-3}$ up to a gap distance of 150 nm.

This chapter introduces a planar gold sample and characterises the angular SPR response and sensitivity to refractive index changes for the custom-built SPM developed. Finally, hippocampal, primary neurons are plated on the planar gold surfaces and electrophysiology is used to stimulate the cells while simultaneously imaging the optical SPR intensity response. The protocol developed to electrically trigger

and optically record the SPR response from one action potential is explained in detail. Methods to increase the SNR are investigated, including signal averaging. MATLAB code is developed to align, average, and analyse the electrical and optical data. Pseudo-data was created to test the MATLAB code to ensure that it could successfully align and average the electrical and optical data across repeats to reduce the noise. Various statistical tests including temporal and spectral analyses are performed on the datasets to locate signals hidden in noise. The pseudo-data was altered to get standard, positive results for these tests for comparison purposes.

5.1 Planar Gold Characterisation

5.1.1 SPR Response

A sample with a gold film thickness of 50 nm has the optimum SPR response, as shown theoretically in Section 3.1.1. The SPR responses from different gold layer thicknesses (30, 50, and 70 nm) on the glass with air as the dielectric were analysed to illustrate the effect of the metal layer thickness on the strength of the coupling between the incident light and the SPs. The coverslips were prepared following Section 2.4 to gold thicknesses of 30, 50, and 70 nm.

Ellipsometry was used to calculate the thickness of the planar gold. The model assumes three layers: glass/gold/air. A MATLAB function was written to calculate the Ψ ($^\circ$) and Δ ($^\circ$) as a function of wavelength (nm) and thickness of the gold layer (nm) for an isotropic, homogeneous, three-phase system using the Airy formulas. Psi, Ψ is the ratio of the p - and s -polarised light amplitudes, and Delta, Δ is the phase difference induced by the reflection, $\Delta = \delta_1 - \delta_2$, where δ_1 is the phase difference before, and δ_2 is the phase difference after as previously explained in Section 3.2.1. For the glass, using the parameters previously determined in Section 3.2.1, a refractive index of 1.52 was used. The Cauchy model is only valid for visible wavelengths, and the refractive index for the glass is constant. For the refractive index of gold, the analytical model of Etchegoin et al. (2006) is used. For air, the refractive index at standard temperature and pressure is used. Ellipsometry measurements were taken at three different locations on the individual coverslips. A representative measurement on 50 nm gold is shown in Figure 5.1. The 30 nm

coverslips were 34.5 ± 1 nm ($n = 3$). The 50 nm coverslips were 47.3 ± 5 nm ($n = 3$). The 70 nm coverslips were 73.6 ± 5 nm ($n = 3$).

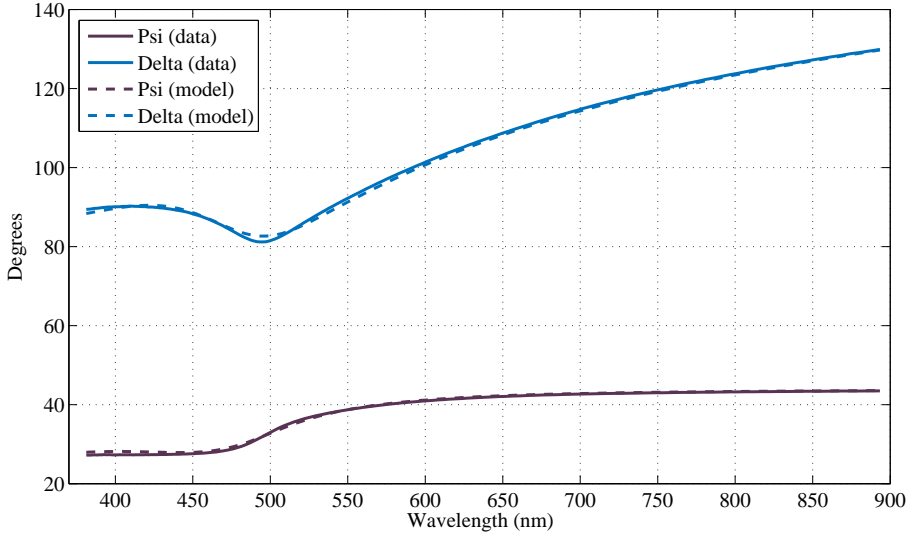
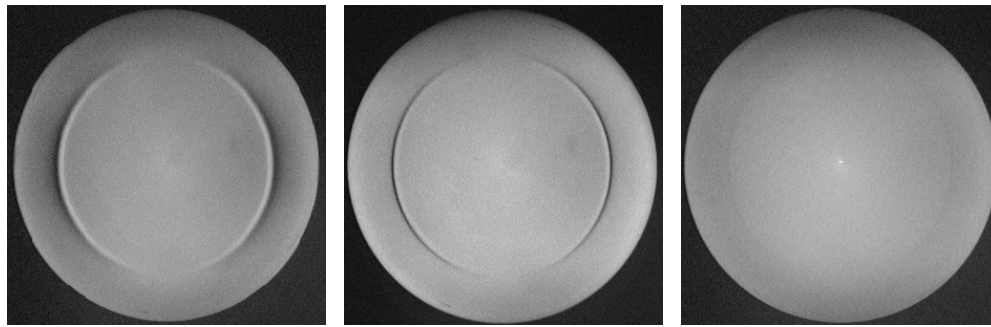


Figure 5.1: Representative ellipsometry figure. The reflected light properties are plotted and a non-linear least squares fittings is performed. The 50 nm coverslips were 47.31 ± 5 nm ($n = 3$).

An oil-objective lens was used to couple the light to the SPs, as previously described in Section 3.1.1. The refractive index of the oil used on the objective was matched to the glass to ensure there was no dispersion at the interface. Images of the BFP were taken using the 640 nm LED to illuminate the BFP of the Nikon oil-objective lens with uniform light. The reflected light intensity was imaged on the Unibrain camera shown in Figures 5.2a, 5.2b, and 5.2c. The radial position of the illumination on the BFP corresponds to the angle of incidence and the azimuthal angle related to the polarisation state. Along the direction where the azimuthal angle is 0° the polarisation state is pure p -polarised light, which changes to pure s -polarised light when the azimuthal angle is $\pm 90^\circ$. The dark semi-circle shows the angle of incidence where the light is coupling with the surface plasmons and is no longer being reflected. There is no dark band in the vertical direction due to the light being pure s -polarised and therefore incapable of exciting SPs. This agrees with the theoretical result presented in Figure 3.4.

A scan across the BFP was performed using the SLED and stepper motor to produce a series of images of the average reflected light intensity with respect to the angle of incidence detected by the EPIX camera. A common region of interest from the image stack was selected using Image-J, and the z -axis profile was exported to a text file. The z -axis profile was imported to MATLAB, and the angle of incidence was calculated using the equation from Section 4.3. The intensity values of the experimental data (y -axis) were normalised and aligned to the theoretical θ_c amplitude. Figure 5.2d show representative angular responses for the different gold thicknesses. The resonance angles are compared in Table 5.1. The experimental angular responses align well with theory showing the SPR sensitivity is highly dependent on the gold film thickness, agreeing with literature (Gwon and Lee, 2010). Figure 5.2d shows the experimental reflectance of the thinner gold film recovers slowly after θ_{sp} , whereas the thicker the gold film the difference between the minimum and maximum reflectance has become smaller, and therefore less sensitive. The difference between theory and the experimental 50 nm θ_{sp} is due to the gold thickness being ~ 48 nm, and the ellipsometry measurements are not exact. The smaller dynamic range of the SPR dip is due to the noise floor from the SPM. The angular response of the sample with a thickness of 70 nm does not show an increase around the critical angle, θ_c . The thick layer of gold reflects $\sim 100\%$ of the incident light to the camera, masking the reflection increase due to the critical angle for glass seen with thinner gold films. A one sample t -test was performed on the experimental θ_{sp} for each thickness compared to their expected theoretical values. None of the θ_{sp} for each thickness were significantly different from their theoretical pair, with p -values of 0.231, 0.171, and 0.173 for the 30, 50, and 70 nm thicknesses, respectively ($n = 3$ for each).

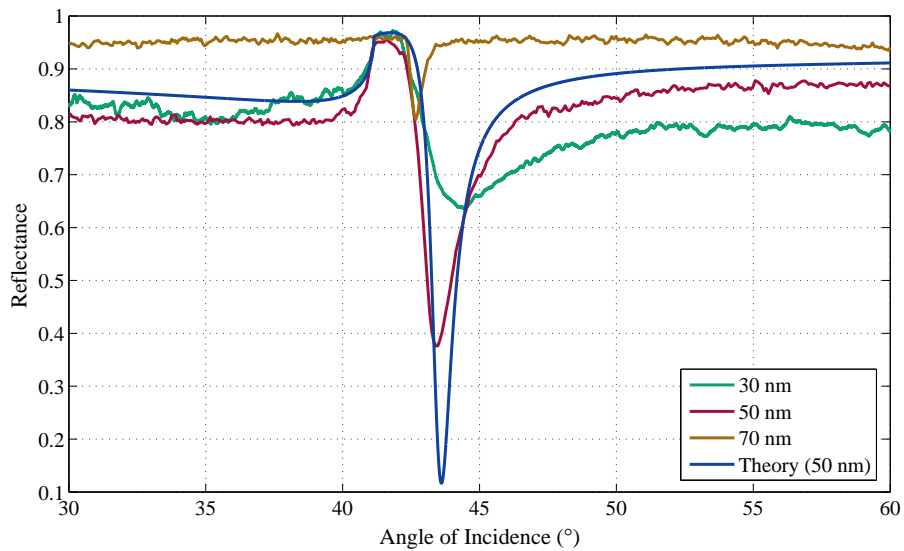
The sensitivity ($\Delta R/\Delta\theta$) is demonstrated in Figure 5.3 where the gradients for each thickness are plotted as a function of the angle of incidence. The gradients of the SPR responses for each of the theoretical and experimental planar samples was calculated using $\Delta\tilde{R} = \Delta\tilde{R}/\Delta\theta$. The angle scan for a gold thickness of 50 nm is the most sensitive regarding sharpness, recovery of the reflectance near θ_{sp} , and has the greatest gradient. Figure 5.3 show that the reflection gradients for the experimental data are comparable, which can be seen in Figure 5.2d. At the beginning of the SPR dip, the gradients are at the steepest and very similar. The theoretical and experimental resonance angles and gradients are summarised in Table 5.1. The



(a) BFP - 30 nm

(b) BFP - 50nm

(c) BFP - 70 nm



(d) Angle scans

Figure 5.2: Representative BFP images and SPR responses for the different thicknesses of gold. Glass/Gold/Air. The experimental responses have been normalised and vertically aligned to theory. The theoretical θ_{sp} is 43.6° . The experimental θ_{sp} for 30 nm is $43.4 \pm 0.17^\circ$, 50 nm is $43.3 \pm 0.16^\circ$, and 70 nm is $42.8 \pm 0.15^\circ$ ($n = 3$ for each). The differences in θ_{sp} are not significant. The difference between theory and the experimental 50 nm SPR response is due to the gold thickness being ~ 48 nm and the ellipsometry measurements are not exact.

experimental gradients of both the 50 and 70 nm planar gold surfaces are less than what was theoretically expected. Differences in thickness or surface roughness could have contributed to this reduced $\Delta R/\Delta\theta$ sensitivity.

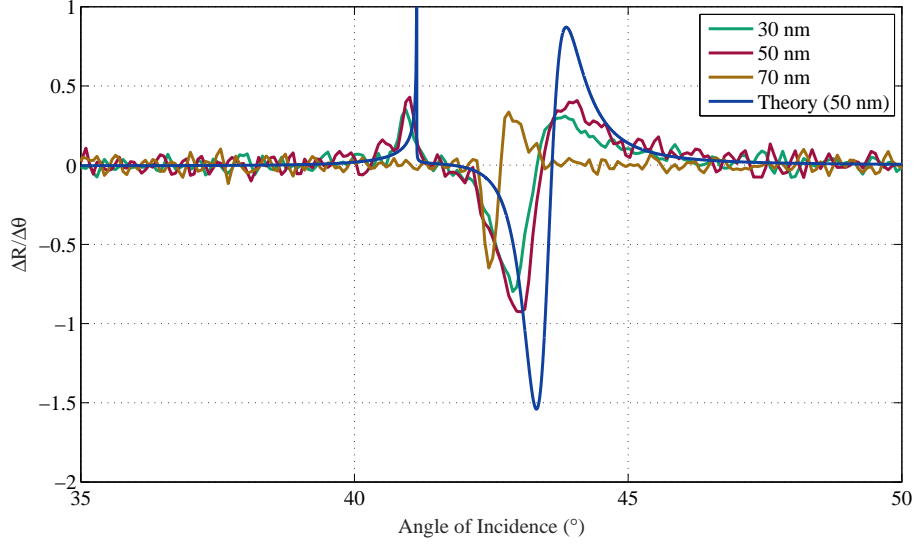


Figure 5.3: Gradient of the angle scans shown in Figure 5.2d calculated using $\Delta\tilde{R} = \Delta\tilde{R}/\Delta\theta$.

Table 5.1: Resonance angles θ_{sp} and gradient maximum amplitude ($\Delta\tilde{R}/\Delta\theta$) values for theoretical (T) and experimental (E) data.

		θ_{sp} (°)	$\Delta\tilde{R}/\Delta\theta$	at Angle (°)
30	T	43.6	0.284	42.9
	E	43.4 ± 0.17	0.798	42.9
50	T	43.6	1.540	42.8
	E	43.3 ± 0.16	0.922	42.97
70	T	43.0	3.037	42.8
	E	42.8 ± 0.15	0.648	42.5

5.1.2 Sensitivity to Refractive Index Changes

The sensor needs to be capable of detecting a refractive index change of $\Delta n = 1.5 \times 10^{-3}$. In an intensity modulation SPR scheme this change in refractive index,

theoretically results in the reflectance changing by $\Delta R = \pm 3.1 \times 10^{-3}$. The sensitivity of the reflection as a function of the refractive index, $\Delta R/\Delta n$ is therefore, 2.067 RIU. The ΔR_{min} and Δn_{min} considering the noise floor and theory are 4.352×10^{-4} (1:2300) and 1.56×10^{-4} (1:6400) per ROI at 8 kHz assuming a gap distance of 30 nm between the cell and the surface, respectively. This results in a $\Delta R/\Delta n$ sensitivity of 2.78 RIU, i.e., when just considering the noise floor, the sensor should be capable of detecting the refractive index change. When the cell moves closer to the surface this sensitivity increases and vice versa. To characterise the sensitivity of the planar gold surfaces on the SPM, the minimum detectable change in refractive index was experimentally determined by changing the bulk refractive index of the dielectric on top of a 50 nm planar gold sample.

The refractive index of salt solutions roughly increases linearly with salinity (S), where $n = 0.0002S + 1.331$, $R^2 = 0.9997$ (Thormählen et al., 1985). Sodium chloride (NaCl) solutions were used at a reference osmolality of 302 mOsm to be comparable with ECS resulting in a reference refractive index of 1.3342. Figure 5.4 illustrates how the refractive index changes with both temperature and salinity.

The concentration of the medium on the surface on the substrate was changed to increase or decrease the refractive index. The concentration values were chosen so that the change in refractive index was at least $\Delta n \sim 0.0002$ and the reference concentration was returned to between each step to ensure that the change in light intensity was not due to drift. The change in refractive index was calibrated with an Abbe Refractometer (Anton Paar, Abbemat 200). The procedure and refractive index values are detailed in Table 2.3. The concentration values were calculated using the following equation:

$$C = \frac{m}{V} = \frac{m}{MV} \quad (5.1)$$

where C is the concentration (mol/L or M), m is the mass (g), M the molar mass (g/mol), and V is the volume of the solution (L). The molar mass of NaCl is 58.44 g/mol.

In an intensity interrogation SPR scheme the reflected light intensity is monitored at a fixed angle, so the position of the angle is important. The sensitivity of the SPR sensor is highest when the slope of the gradient is greatest (Yeatman, 1996). To find the minimum detectable change (sensitivity), the angle of incidence must be

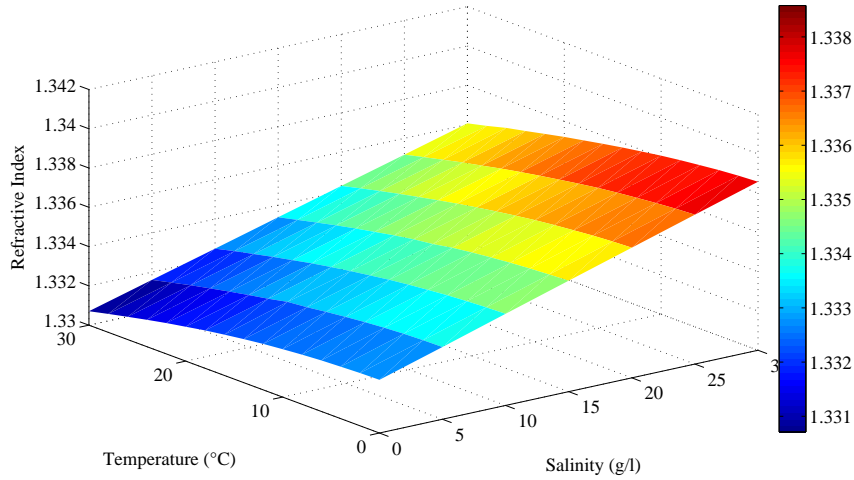
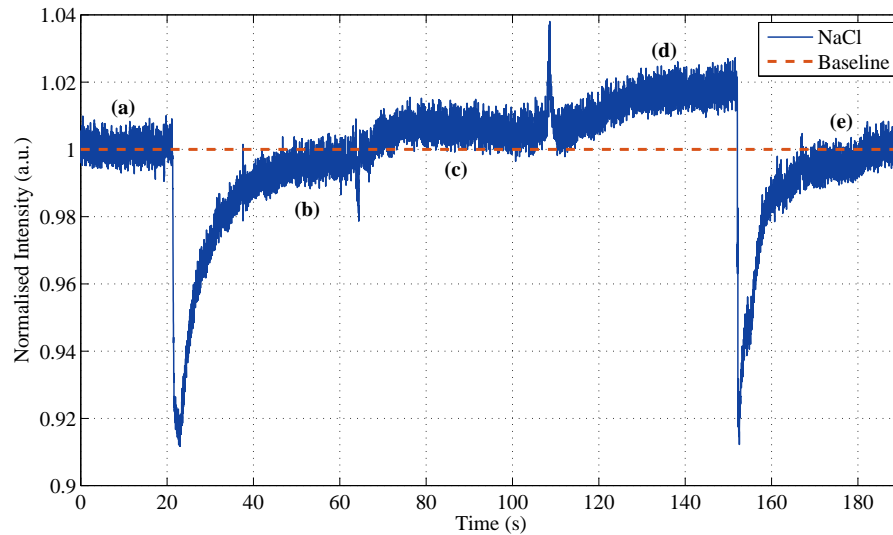


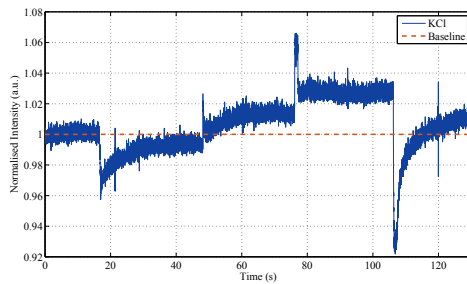
Figure 5.4: Refractive index variation as a function of both temperature and salinity. The colourbar represents the refractive index value. Values from Thormählen et al. (1985).

chosen such that the reflection gradient ($\Delta\tilde{R}$) is at its maximum, shown in Figure 5.2d as around 43° for a gold/air interface. Practically, it is difficult to set this parameter using the stepper motor, so instead, the dynamic range was used. For SPR it is about 30% of the minimum. It is worth noting that there is a trade-off between the steepest part of the curve and the number of photons available because the most sensitive SPR response is around 30% of the maximum. This darker light intensity will mean there are fewer photons available and will equal a smaller SNR. Considering this, the angle of incidence was fixed at around 50% of the difference between θ_{sp} and θ_c .

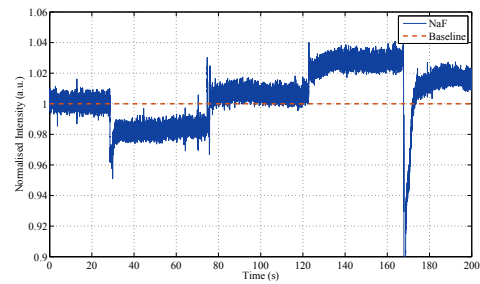
Figure 5.5 shows the time series of an experiment where the concentration of NaCl on the surface on a planar gold film is changed. The y -axis for each experiment was normalised by dividing by the mean of the dataset. When increasing the concentrations, there was an overshoot in the reflected light intensity which quickly stabilises. However, when diluting the concentration, there are long, exponential recoveries to a stable light intensity, up to 30 seconds in some instances. There are three possible explanations for the transients when the concentration is changed; a) diffusion of the solution, b) mechanical waves, and c) temperature sensitivity. (a) the diffusion of



(a) NaCl



(b) KCl



(c) NaF

Figure 5.5: Time series plots of changing the bulk refractive index on the surface of 50 nm planar gold with NaCl (5.5a), KCl (5.5b), and NaF (5.5c). The experiments start with a reference refractive index (a) and then changes the refractive index by at least ± 0.0002 RIU by adding salt solution (d) or water (b). The reference refractive index is returned to between each step (c and e).

the solution across the coverslip will take time to stabilise. The diffusion coefficient for Na^+ ions in water at room temperature was defined in Section 3.3 as $1.33 \times 10^{-5} \text{ cm}^2\text{s}^{-1}$. Using (3.48) the time for the ions to diffuse from the outside of the 19 mm coverslip to the centre is 6.786 seconds. However, it only takes about 1 second on average for the light intensity to stabilise. Also, this does not explain why the long recoveries only occur when diluting the concentration. The long recoveries could be due to the electrostatic interactions between the sodium and/or chloride ions with the water or gold surface. (b) mechanical waves are oscillations of the solution that could be caused by the pipette or movement of the rig. Finally, (c) as mentioned previously the refractive index is very sensitive to temperature so if the solution in the pipette is even slightly different to the bulk solution this could cause the overshoot. Similarly, the average light intensity never returns exactly to the baseline shown in Figure 5.5 of the initial concentration but gradually drifts upwards. The drift could be caused by the variation in temperature or possibly an inherent issue with the light source, which was seen in Section 4.1.1. The concern is that the time it takes for the light intensity to stabilise after a NaCl concentration change takes anywhere from 1 second to 20 seconds. An AP is on the order of 2 ms so if the ion flux interacting with the gold causes the SPR sensor to have a refractory period of up to 20 seconds then this is not suitable for neural activity detection with a high temporal resolution. However, as explained in Section 3.3 it is unlikely that the ion flux during an AP causes a huge refractive index change in the bulk medium because the ions that give rise to the AP occur within 1 nm of the membrane. Also, if the long transients seen are caused by mechanical waves or temperature variations, then SPR is still a viable sensing technique. The experiments were repeated with KCl and NaF to investigate if the anion or cation of the compound alters the transients, Figures 5.5b and 5.5c, respectively. For KCl solutions the light intensity stabilises quickly when the salinity is increased but still suffers from the long, exponential transients when diluting.

The transients when diluting the NaF solutions are faster for the first transition (a – b) taking around ~ 5 seconds. The second transient when diluting is longer but the liquid was disturbed when pipetting so is the likely cause. Therefore, it can be assumed that the chloride cation contributes most to the long transients. The equilibrium potential for Cl^- is -70 mV and very close to the resting membrane potential

for cells. In most neurons, Cl^- ions are not actively transported but passively settle according to the Nernst potential (Kandel, 2012). Thus, the long transients likely caused by Cl^- ions diffusion will not become an issue for detecting AP activity with an SPR sensor. The results from all the experiments are summarised in Figure 5.6.

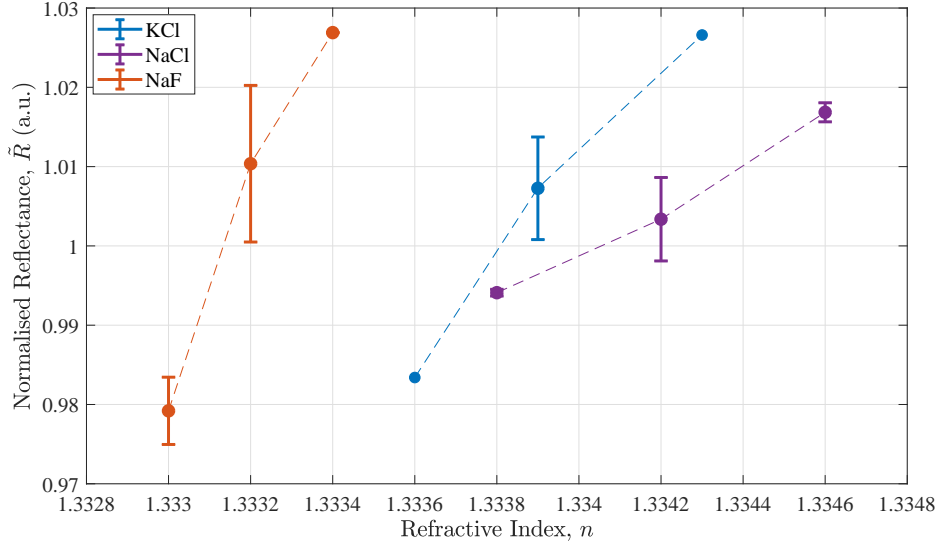


Figure 5.6: Summary of the normalised change in light intensity ($\Delta\tilde{R}$) as a function of the refractive index (n). The large error bars for the reference refractive indices are due to drift during the experiment from either the temperature variation or the light source. The linear fit for NaCl, KCl, and NaF are given in equations (5.2)–(5.4), respectively. The refractive indices were calibrated with a Abbe refractometer.

The large error bars for the reference refractive indices are due to the drift explained previously. The errors between repeats are due to errors in the determination of the salt solution concentrations. When the drift is corrected for the normalised light intensity (\tilde{R}) increases linearly with increasing refractive index, where

$$\tilde{R}_{NaCl} = 28.5n - 37.02, \quad R^2 = 0.9888 \quad (5.2)$$

$$\tilde{R}_{KCl} = 61.973n - 81.664, \quad R^2 = 0.9974 \quad (5.3)$$

$$\tilde{R}_{NaF} = 119.25n - 157.98, \quad R^2 = 0.9946 \quad (5.4)$$

The sensitivity of the sensor is characterised by the refractive index unit (RIU). The RIU was calculated as the ratio of the change in refractive index (Δn) and change

in normalised reflected light intensity ($\Delta\tilde{R}$), using (3.23) as $\Delta R/\Delta n = 28.5, 61.973,$ and 119.25 RIU for NaCl, KCl, and NaF, respectively. The average is 69.908 RIU. The overall sensitivity can be calculated using (3.24) where the noise is $110e^-$ as $2.363 \times 10^{-4} \pm 1.09 \times 10^{-4}$. This experimentally measured $\Delta R/\Delta n$ here is less than what is reported from intensity modulating SPR techniques in literature as 10^{-6} (Sepúlveda et al., 2006; Campbell and Kim, 2007). The level of detection in these sensitivity experiments is limited by the short exposure time (0.124 ms). However, the power of the noise is proportional to the bandwidth. So for the small bandwidth used for these measurements (125 Hz) the total noise power will be reduced and the SNR increased.

Theoretically, a refractive index change of 1.5×10^{-3} at the gradient maximum (69.87°) of the SPR dip will result in the theoretical reflectance changing by $\Delta R = \pm 3.1 \times 10^{-3}$ and $\Delta R/\Delta n$ of 2.067. This $\Delta R/\Delta n$ of 2.067 is on average 30% less than what we can detect, so detecting the refractive index change during an AP should physically be achievable.

5.2 Detection of Neural Activity

The principal question of this thesis is whether or not surface plasmon resonance can be used to detect neural activity in individual cultured neurons. Up to this point, the experiments and theory have determined if this is practically possible by estimating the change in refractive index needed to be detected. The sensitivity of the SPM has been experimentally determined considering the noise floor, and more realistically with a planar gold sensor. In this section, primary, hippocampal neurons are cultured on planar surfaces, and whole-cell patch clamp electrophysiology and SPR is performed simultaneously. The SPR response has been monitored to detect any changes in light intensity and therefore, refractive index. The validation of these SPR responses has been achieved using whole-cell patch clamp. First, the experiment had to be designed to trigger and record one action potential from one neuron.

5.2.1 Triggering and Recording One Action Potential

The first objective was to trigger and record one AP from one neuron successfully. The 50 nm planar gold surfaces were prepared following the methods outlined in Section 2.3.1 and 2.4. A coating or gel is needed to functionalise the metal surface to ensure that the neuronal culture will adhere to the surface and develop. A coating or gel is needed because, at metal surfaces, there are strong polarisation forces that may cause denaturation and loss of specificity of biomolecules needed for cell adhesion (Kasemo, 2002).

The amplitude of the evanescent field decays exponentially with increasing distance from the metal surface. This decrease in relative refractive index sensitivity is e^{2d/l_d} , with d being the distance removed from the sensor. Therefore, objects closest to the surface, resulting in a stronger SPR signal. The cell membrane of living cells *in vitro* are usually separated from the substrate by 20 – 100 nm depending on the adhesion protein or peptide used (Braun and Fromherz, 1998; Giebel et al., 1999; Toma et al., 2014). Therefore, to keep the cell membrane near the metal surface, a 2D planar coating was to be used because a 3D hydrogel (a polymeric material containing a high percentage of water (Kopeček and Yang, 2007)) would potentially keep the cells out of the evanescent field. The cell culture needs a non-toxic surface, and because the cell-surface binding is an interaction between cells and surface-bound proteins the surface needs suitable protein adsorption properties. The surface chemistry of gold can be modified using thiol-containing molecules to form a self-assembled monolayer on the surface (Ulman, 2013; Jans et al., 2009). Thiols on gold, for example, 11-Amino-1-undecanethiol hydrochloride (AUT) make the strongest bond and are known to be very stable (Arya et al., 2009). The gold surfaces were solvent cleaned, and an AUT monolayer was deposited as outlined in Section 2.6.1. After surface functionalisation, the cell culture was plated on the planar gold substrates, following the methods for harvesting, plating, and feeding the cell culture in Section 2.7. On feeding days the cell cultures were imaged using brightfield microscopy with the Nikon Eclipse Ti (10×, NA = 0.25), Figure 5.7a. After at least 14 DIV the cultures were electrically active and stable enough in their extracellular matrix to be prepared for the electrophysiology and SPR experiments. The cell cultures were mounted on a coverslip holder and immersed in extracellular

solution (ECS) before placing on the SPM. The z -axis was adjusted, so the 640 nm LED and SLED were in focus with the BFP and coverslip, respectively. A viable neuron was located by adjusting the x - and y -axis. Images of the neuron selected were taken using transmission (590 nm/EPIX) and reflection microscopy (590 nm/Point Grey), Figures 5.7c and 5.7d, respectively. The SPR image, Figure 5.7b was taken using the SLED reflected off the sample and detected on the EPIX camera. The dark areas are regions where light is coupled to the SPs, and no light is being reflected. The lighter areas are the regions with a different refractive index, assumed to be regions of cell material.

The two ROIs highlighted in Figure 5.7b were selected and used to produce the angle scan shown in Figure 5.8. The figure shows that the regions where cell material is present has a higher θ_{sp} than that of just gold and ECS. The plasmon angle, θ_{sp} for the gold is $70.3 \pm 0.189^\circ$, and θ_{sp} for the cell is $71.5 \pm 0.153^\circ$. Proving that the area where the cell matter is presumed to be has a higher refractive index than that of just gold/ECS. From Section 3.2 the theoretically calculated θ_{sp} for a neuron with a gap distance of 50 nm was approximately 71.3° . This theoretical θ_{sp} is a 0.27° difference from the experimentally measured θ_{sp} and probably due to the neuron being fractionally further away from the gold surface.

To validate that any signal detected using SPR was from an action potential, whole-cell patch clamp was employed to stimulate the target cell while recording the voltage change across the membrane (AP). A procedure to simultaneously invoke an action potential while recording both the electrical and optical intensity responses was developed. Briefly, a patch pipette filled with ICS was tightly sealed onto the target neuron before gently breaking through the membrane to go whole-cell. This tight, giga-ohm seal isolates a patch of the membrane allowing all the ions passing across the membrane during an action potential to flow into the pipette and get recorded by a silver chloride electrode. An action potential was invoked in the target neuron by applying a small current pulse to depolarise the membrane, Figure 5.9.

A master function generator controlled the triggering of the electrophysiology recording/stimulation and SPR recordings. A function generator outputs a 5 Hz pulse to start the electrophysiology protocol while simultaneously triggering the EPIX camera to begin taking images of the SPR response of the neuron at 8 kHz for the

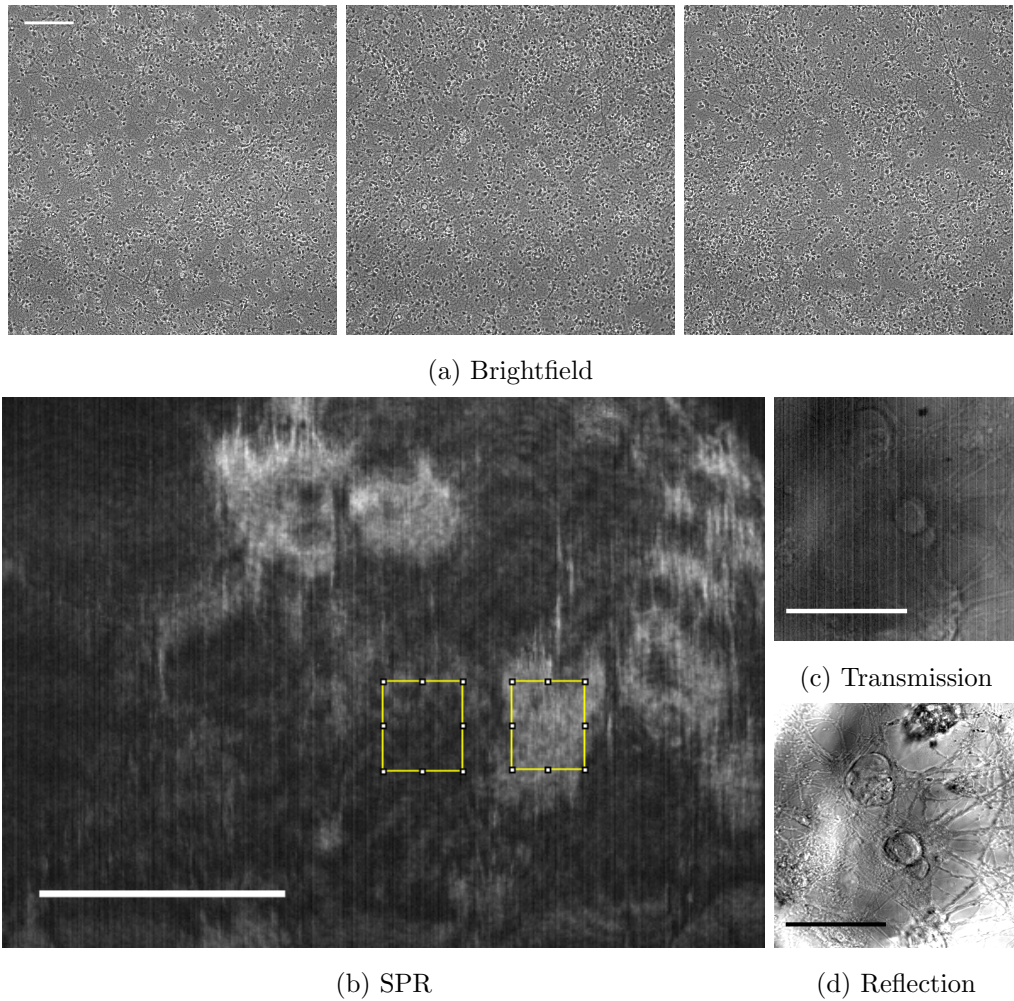


Figure 5.7: Brightfield (5.7a), SPR (5.7b), transmission (5.7c) and reflection (5.7d) images of the sample. Cells were cultured on planar gold and imaged 14 DIV. The dark areas in the SPR image are regions where the light has been coupled to the SPs and less light is being reflected. The lighter areas are the regions with a different refractive index (cell) thus θ_{sp} is at a higher value. The ROIs used for Figure 5.8 are shown. Brightfield images were taken using the Nikon inverted microscope at $10\times$ magnification ($NA = 0.25$) at three different locations on the coverslip with the Hamamatsu camera. The scale bar is $200\ \mu\text{m}$ and consistent across (a). (b), (c), and (d) were taken on the SPM where (b) and (c) were taken using the EPIX camera, and (d) with the Point-Grey. The scale bars on (b), (c), and (d) are $30\ \mu\text{m}$.

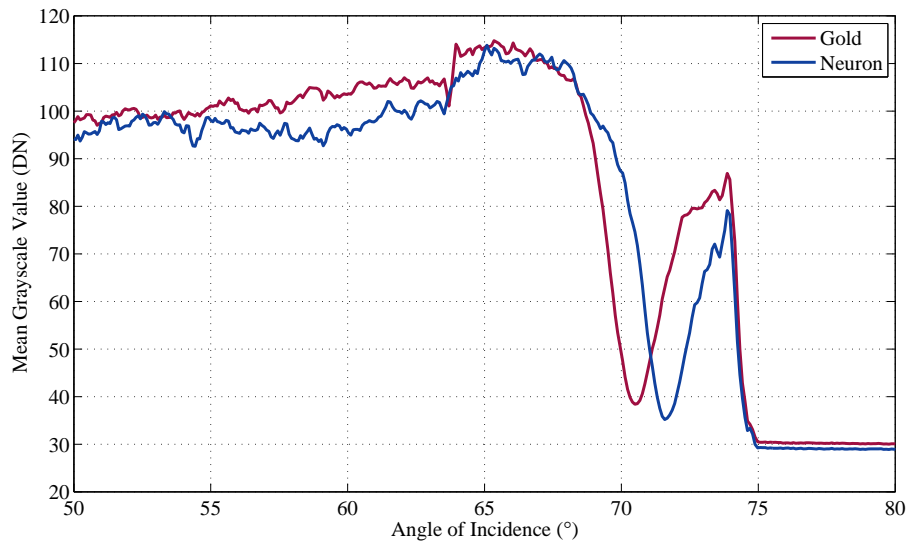


Figure 5.8: Representative angular response for a glass/gold/ECS/cell interface and a region where there was no cell. Critical angle for glass with ECS= $1.37 = 64.2^\circ$. Angular responses were aligned using the critical angle for ECS. θ_{sp} for the gold is $70.3 \pm 0.189^\circ$, and θ_{sp} for the cell is $71.5 \pm 0.153^\circ$ ($n = 3$ for each).

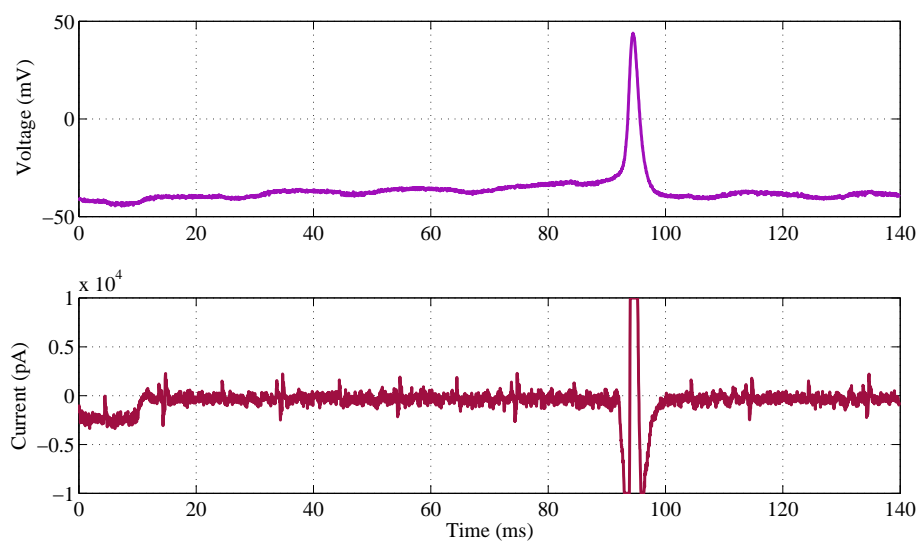


Figure 5.9: Recordings from electrophysiology of the applied current (bottom) and resulting membrane voltage (top). Taken with WINWCP and processed in MATLAB. A current step was applied at $t = 10$ ms. The current step invokes an action potential in the neuron after about 90 ms. Several stimulation and recording protocols were developed because the latency of the AP was not consistent.

duration of the electrophysiology protocol. Detailed methods and settings for the combined electrical and optical recordings can be found in Section 2.13.

MATLAB code was developed to detect the action potentials from the electrophysiology data and analyse the data obtained from the SPR responses. The code first detects spikes in the recorded electrophysiology data using a threshold condition. These spikes correspond to APs. The images captured from monitoring the SPR response were imported into MATLAB, converted from an 8-bit unsigned integer array to double precision numbers in the range of 0 to 1. The matrix of double precision numbers is then transformed to a 1-D vector and reshaped to a 2-D matrix, where pixel \times time. Two regions of interest were selected; one where the neuron of interest was located and a second control area. The control area was subtracted from the neuron ROI to remove any drift, electrical or mechanical noise that might be present and therefore common in both ROIs. The standard deviation of the cell ROI improved on average by a factor of two after the subtraction of a control area. The resulting light intensities as a function of time and pixel number is shown in Figure 5.10. The 2-D matrix was then averaged across all pixels to give the light intensity average as a function of time, Figure 5.11, which will be referred to as the row average. The right-most plot is the resulting histogram of the y -axis values. The histogram of the row average ($\mu = 4.088 \times 10^{-6}$, $\sigma = 1.88 \times 10^{-4}$) was compared to a Gaussian normal ($\mu = 4.85 \times 10^{-6}$, $\sigma = 1.75 \times 10^{-4}$), Figure 5.12. The two distributions are not significantly different from one another as determined by a unpaired t -test; $t(598) = 0.0515$, $p = 0.959$. The D'Agostino-Pearson omnibus test was used to determine if a Gaussian distribution well modelled the data set. The test computes the skewness and kurtosis to quantify how far the distribution is from Gaussian in terms of asymmetry and shape, respectively. The p -value is a sum of these differences, where a large value means that the data is consistent with a Gaussian distribution and a small p -value means the data was sampled from a non-Gaussian distribution. If $p < 0.05$, the dataset does not pass the normality test. Hence, the noise signal was confirmed to be consistent with a Gaussian distribution ($p = 0.984$). The row average was also consistent with a Gaussian distribution ($p = 0.915$).

After examining the SPR responses both visually and after statistical tests it can be concluded that the single AP was not detected optically. It is possible that the level

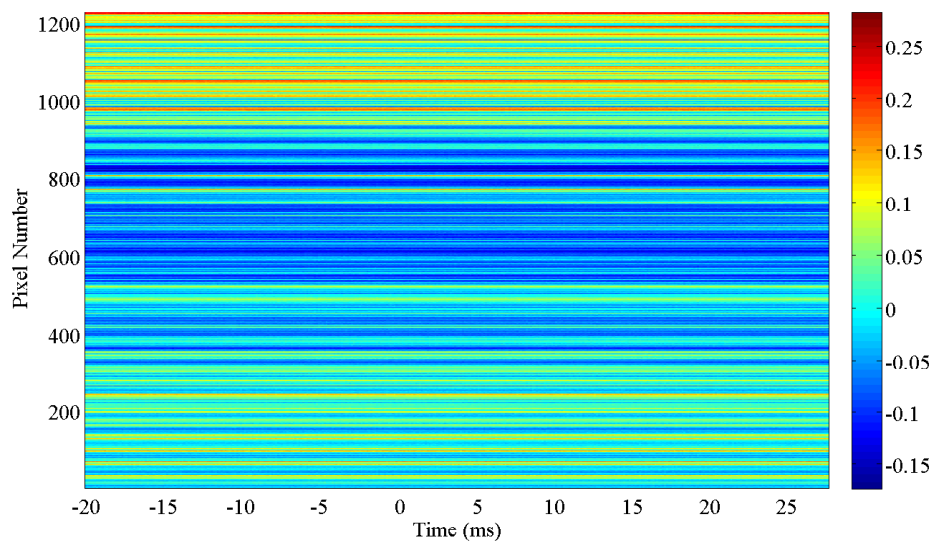


Figure 5.10: Plot of light intensity over time for all pixels in the region of interest for one AP.

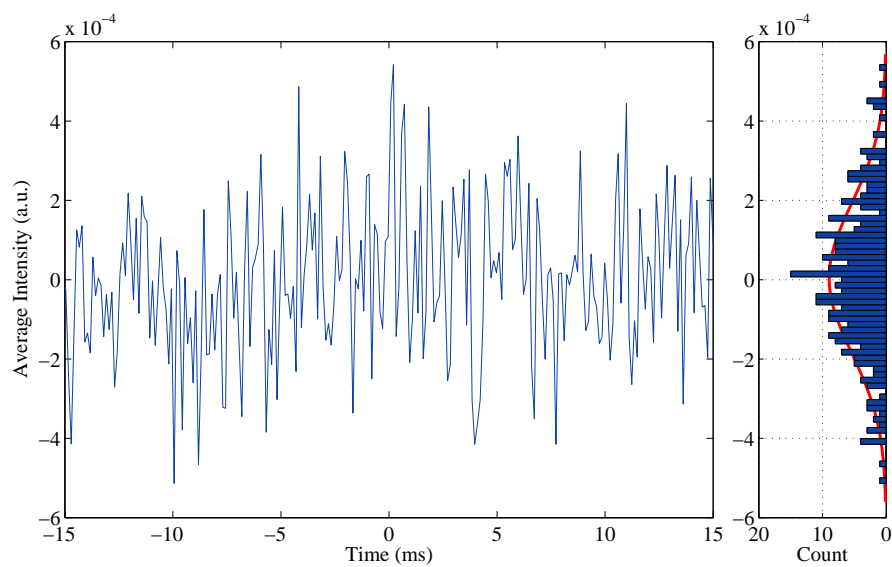


Figure 5.11: The average across all pixels for one action potential. The signal distribution to the right was compared with a Gaussian normal, Figure 5.12.

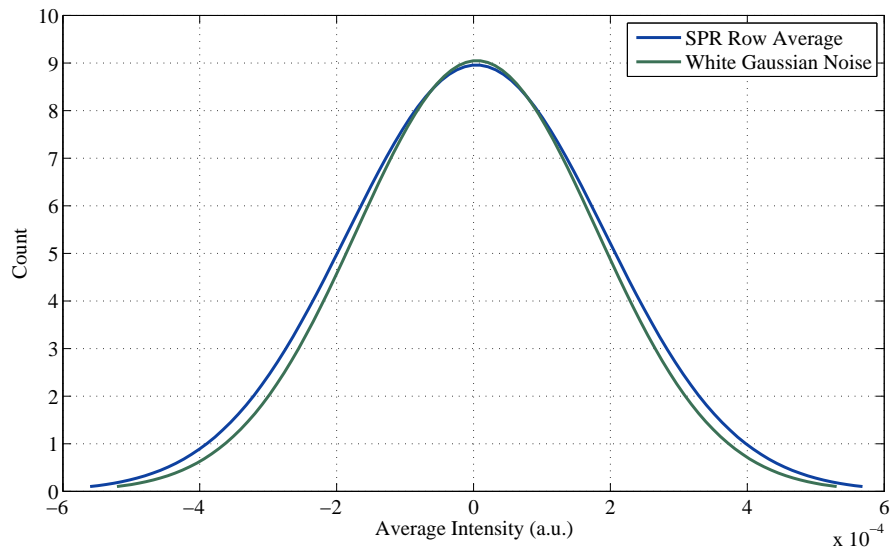


Figure 5.12: Comparison of the average intensity distribution values across all pixels from the SPR images after processing, Figure 5.11 and white Gaussian noise. The row average ($\mu = 4.088 \times 10^6$, $\sigma = 1.88 \times 10^4$) and Gaussian normal ($\mu = 4.85 \times 10^6$, $\sigma = 1.75 \times 10^4$) are not significantly different from one another as determined by an unpaired t -test; $t(598) = 0.0515$, $p = 0.959$.

of the noise present in the SPR recordings masks the light intensity variation caused by the refractive index change. When recording one action potential the noise level, ΔR_n is $4 \times 10^{-4} \pm 9.53 \times 10^{-5}$ ($n = 7$). In Section 3.2 it was determined that for a refractive index change of 1.5×10^{-3} the theoretical reflectance, ΔR_t will change by $\pm 3.1 \times 10^{-3}$. The difference between the theoretical reflectance change and the noise level is $\sim 10^{-1}$, so the noise level is lower than the theoretical light intensity change. However, the theoretical change of the reflectance is very small, and reduces further as the gap distance between the surface and cell gets larger.

To confirm this level of noise was not due to the fixed pattern noise the analysis was performed again but a reference frame was subtracted from the imported images. The standard deviation of the row average reduced to 2.9×10^{-4} from 3.26×10^{-4} . An improvement of 3.6×10^{-5} . The removal of the control area from the ROI will have reduced the FPN and there will just be an averaged "offset" between the two images. Considering the theoretical change of the reflectance is very small, methods of reducing the noise further and increasing the SNR are investigated.

5.2.2 Increasing the SNR

The technique of signal averaging can be used to increase the SNR and was described in Section 1.6.4. Signal averaging is a digital technique that can be used to separate a repetitive signal from noise without distorting the signal. Signal averaging works by splitting the recorded measurements into epochs and summing them. The noise will add destructively and reduce while the signal will add constructively and increase in amplitude. The signal-to-noise ratio increases with the \sqrt{N} , where N is the number of epochs or repeats (Hassan and Anwar, 2010). To improve the SNR, more APs were invoked in the same neuron and then averaged. The process previously described in Section 5.2.1 was followed, but the master function generator was set to output more pulses at 5 Hz with a pulse duration of $62.5 \mu\text{secs}$, described in Section 2.13.

The MATLAB code was improved to perform the signal averaging, and more data analysis techniques were applied to the data. To ensure that the post-processing was able to detect an AP in noise successfully, a method to construct SPR data with APs added separately is proposed and will be described at the same time as the stages of the data processing. The pseudo-data was generated by concealing a

real AP recording in half of the pixels from an SPR recording when no stimulus was present. The amplitude of the electrically recorded AP was scaled to 5.64×10^{-5} mV so that it was undetectable before implementing the algorithm, Figure C.3. The 100 Hz noise that is present in the waveform is an artefact from the SLED and was discussed in Section 4.1.1. First, the electrophysiology data (V_{avg}) was imported as before. The spikes were detected and aligned to the first spike. The times relating to the peak of the spike were saved to align the SPR images (t_0). An average spike waveform was produced by averaging across all spikes, Figure C.2.

The SPR images were imported and processed as before. The regions of interest were selected, and the control was subtracted from the cell area, Figure C.4. Note that the 100 Hz noise waveform present in Figure C.3 has been removed. The image stack (cell – control) was aligned by transforming the images to the frequency domain and aligning each image by the time offsets from the electrophysiology using an FFT, where $\delta(t - t_0) \Leftrightarrow e^{-j\omega t_0}$. The aligned image stack was converted back to the time-domain, and the average was computed over 10 – 1000 repeats, Figure C.5. A response profile was plotted from the average across all the pixels from the ROI resulting in a plot of the average intensity across all pixels in the ROI as a function of time, Figure 5.13. After averaging the AP is now visible demonstrating that the MATLAB code developed is successful at finding a signal hidden in noise by aligning and averaging the SPR images.

The effect of the fixed pattern noise was investigated. A separate method of subtracting the first image from all subsequent images was investigated but the standard deviations of the row average were comparable, where $\sigma = 0.0237$ after subtraction, and $\sigma = 0.0263$ after averaging. The subtraction of a control area and signal averaging remove the FPN.

Statistical, temporal and spectral analyses was performed, but first it was necessary to have a standard, positive result to understand the effects of the different steps and subsequent analyses. A flow chart of the data analysis process, steps, and representative figures is shown in Figure 5.14.

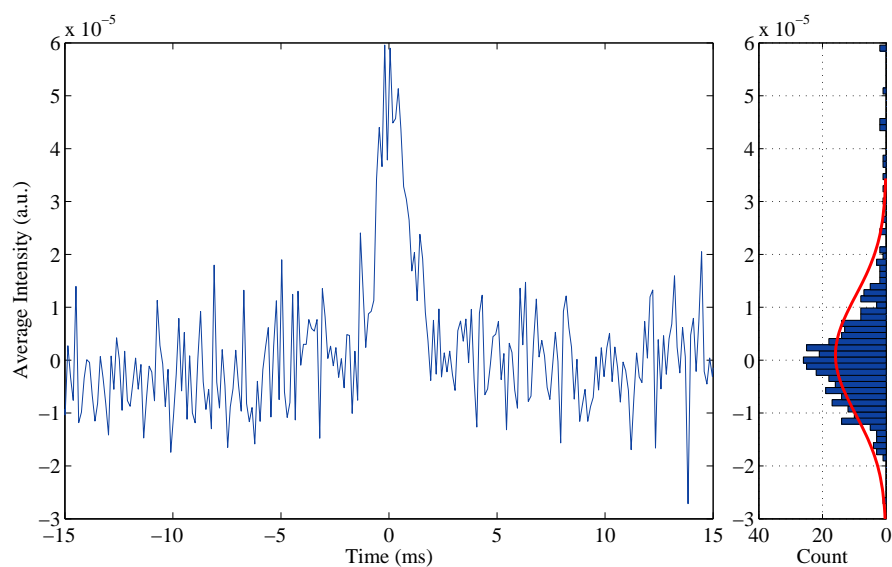


Figure 5.13: The average across all pixels for 500 action potentials from the pseudo data. After averaging the AP is now visible demonstrating that the MATLAB code developed works for aligning and averaging the SPR images. The signal distribution to the right was compared with a Gaussian normal, Figure 5.15.

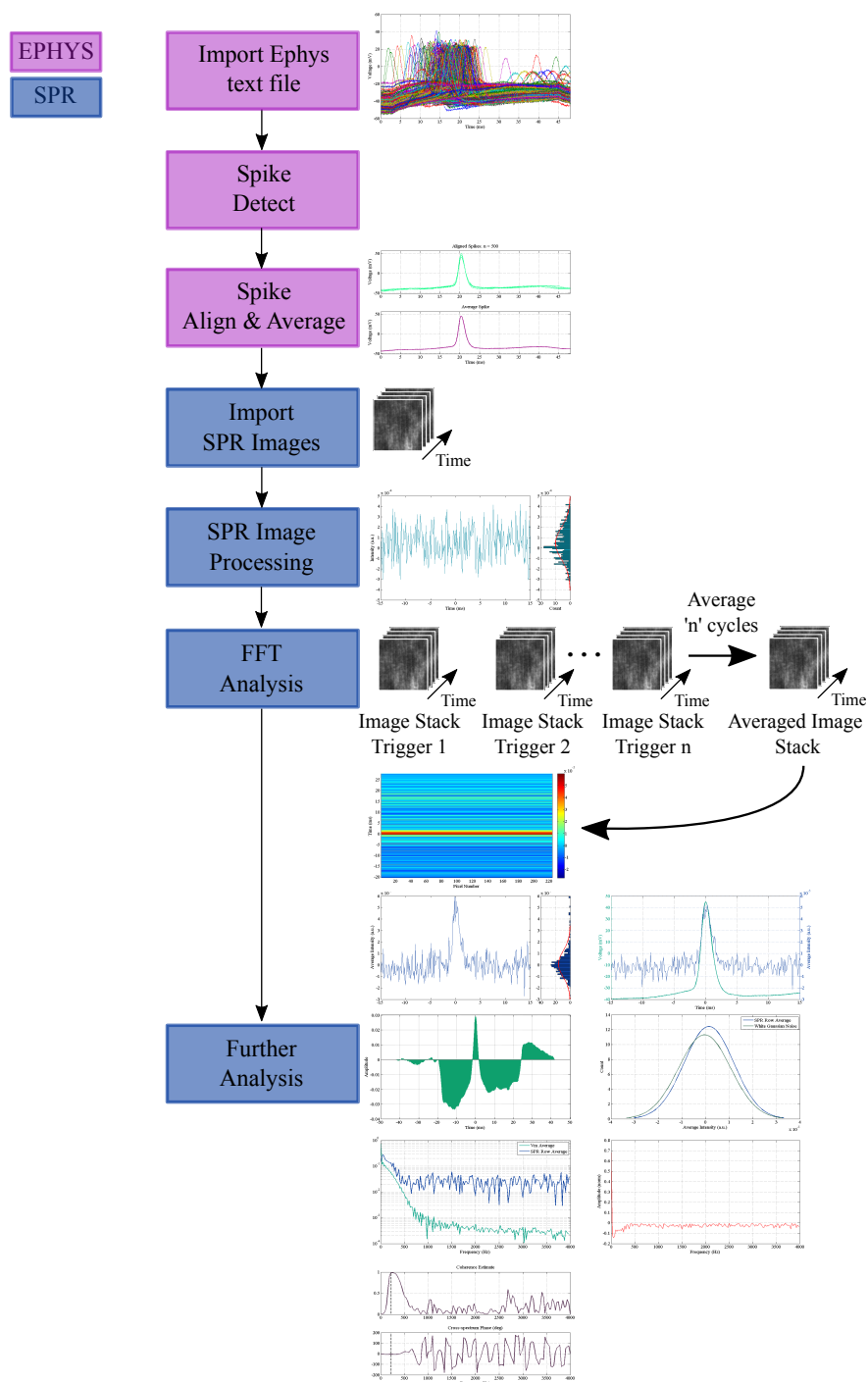


Figure 5.14: Flow chart of the data analysis. The figures are examples from the pseudo-data and were used for comparison with real, experimental data. All the figures not in this chapter can be found in Appendix C.

Measuring Signal Similarities

The various methods of detecting signal similarities were first investigated using the pseudo-data to give a standard result that future results could be compared to. The pseudo-data code was re-run with a large enough AP amplitude that it was detectable by eye before any processing. Signal detection theory was employed to discern between the signal and noise. The statistical, temporal and spectral methods investigated were Gaussian Signal Detection, Cross-correlation, and Power Spectral Density (PSD) analysis.

Signal Detection: Gaussian signal detection is a method of detecting deterministic signals in white Gaussian noise. To determine whether the AP can be detected the distributions of “noise” and “noise + AP” were compared. In Section 1.6.2 it was stated that an ideal system should be shot noise limited. For convenience, it is assumed that for experimentally realistic values the noise can be assumed to be Gaussian.

The real AP was added to the real white Gaussian noise, with a power of 0 dBW (1 W). The AP was scaled to an amplitude of 1.7 mV, so that is only just detectable without any averaging, Figure C.6. The resulting intensity (y -axis) distributions of the “noise” and “noise + AP” are shown in Figure 5.15.

The means of the “noise + AP” and “noise” are 1.46×10^{-6} , and -3.79×10^{-7} , respectively (difference 1.84×10^{-6}). The results from the D’Agostino & Pearson normality test give p -values of 0.265 and <0.0001 for the “noise” and the “noise + AP”, respectively. Therefore, the presence of the AP significantly changes the resulting intensity distribution away from a Gaussian normal. In addition, an unpaired t -test was performed on the two data sets (parametric, two-tailed). The result shows that there was a significant difference between the distributions for “noise” ($\mu = -3.79 \times 10^{-7}$, $\sigma = 6.018 \times 10^{-7}$) and the “noise + AP” ($\mu = 1.46 \times 10^{-6}$, $\sigma = 5.77 \times 10^{-7}$); $t(670) = 2.21$, $p = 0.0273$. Therefore, the addition of the AP to real white Gaussian noise has a significant effect on the resulting distributions and can be used for determining if an AP occurred.

Cross-Correlation: Cross-correlation can be used to quantify the similarity between two signals as a function of the displacement of one to the other. It is a

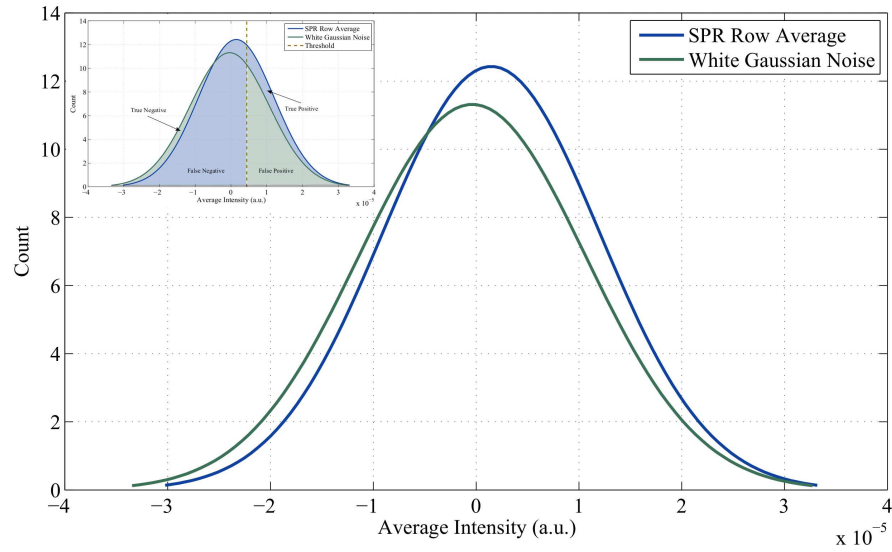


Figure 5.15: Comparison of the pseudo-data values for the intensity (y -axis) from the average across all pixels, Figure 5.13 and white Gaussian noise. The inset image highlights the areas of true positives, negatives, and false positives and negatives, similar to Figure 1.7. An unpaired t -test determined there was a significant difference between the distributions for “noise ($\mu = 3.79 \times 10^7$, $\sigma = 6.018 \times 10^7$) and the “noise + AP” ($\mu = 1.46 \times 10^6$, $\sigma = 5.77 \times 10^7$); $t(670) = 2.21, p = 0.0273$. Therefore, the addition of the AP to real white Gaussian noise has a significant effect on the resulting distributions and can be used for determining if an AP occurred.

technique used to find known signals hidden in noise. The cross-correlation between two signals $u(t)$ and $v(t)$ is

$$w(t) = u(t) \otimes v(t) \quad (5.5)$$

$$= \int_{-\infty}^{\infty} u^*(\tau - t)v(\tau)d\tau \quad (5.6)$$

where u^* is the complex conjugate of u , and τ is the displacement or lag (Bracewell and Bracewell, 1986).

To verify whether an AP has been detected, the electrophysiology data was cross-correlated with the optically recorded SPR response to search for similarities. The electrophysiology data was resampled from 32 kHz to 8 kHz to be the same as the SPR recordings for the cross-correlation to work. The resample function in MATLAB was used which applies an anti-aliasing, low-pass FIR filter to the signal. The resampled electrophysiology data was then cross-correlated with the noisy pseudo-SPR data to determine if there was a match. The peaks in Figure 5.16 show areas where the two data sets are more correlated suggesting that an AP was present. The amplitude of the AP was varied where the top left plot is “noise”, i.e., the amplitude of the AP is so small that it was undetectable after averaging, and the bottom right is detectable by eye after averaging. The peak amplitudes of the cross-correlation were plotted in Figure 5.17 showing the amplitude of the cross-correlation peak increases linearly with increasing AP amplitude, $y = 649.52x + 0.0093$. It is worth noting that for AP amplitudes less than 3.26×10^{-5} mV there are peaks with amplitudes greater than what occurs at $t = 0$, which can be attributed to noise.

FFT Analysis: Spectral coherence between the two signals was also performed to identify any correlations in the frequency domain. It is a statistical method to compare two datasets to estimate the causality between the two signals, i.e., whether the input caused the output. A small value indicates the corresponding frequency components are unrelated while values towards '1' indicates correlation. The power spectrum (PSD) of the respective signals was plotted to display the power present at each frequency. Figure 5.18 confirms that the “AP” and “noise + AP” have perfectly correlated components around 220 Hz with no phase difference. These analysis figures will be used as a gold standard for comparison with real, experimental datasets.

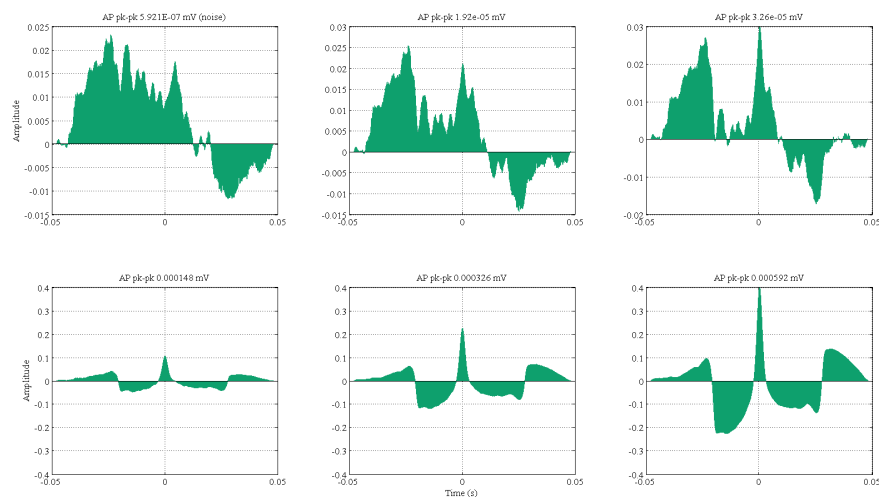


Figure 5.16: Resulting figures from the cross correlation of “AP” and “noise + AP” for increasing amplitudes of AP hidden in noise.

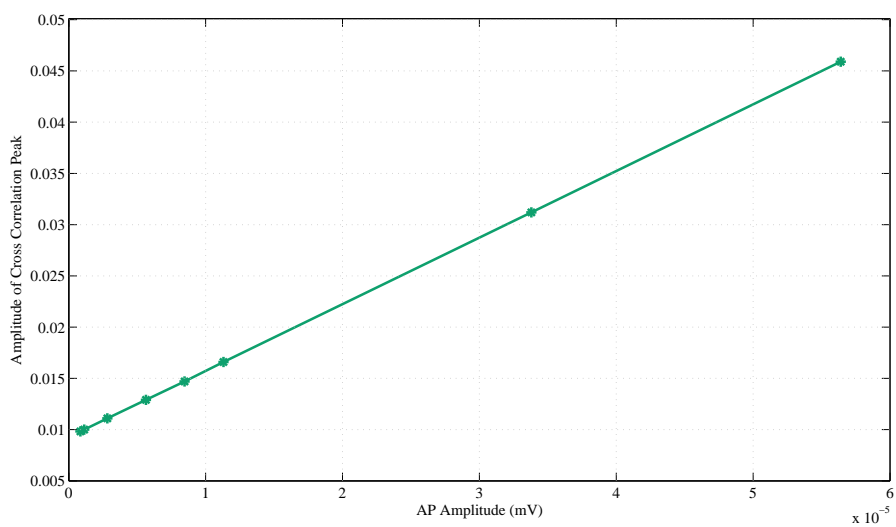


Figure 5.17: Summary of the peak of the cross correlation as a function of the AP amplitude, $y = 649.52x + 0.0093$. $R^2 = 1$.

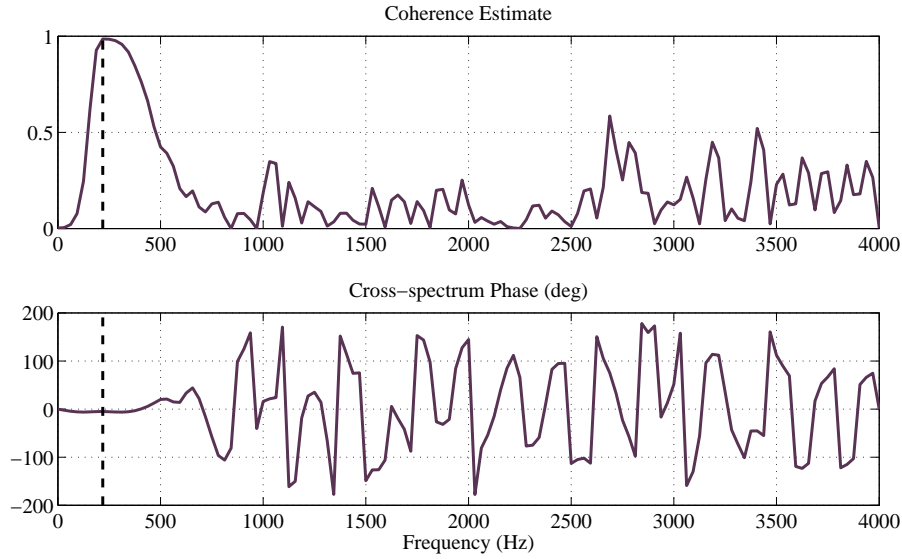


Figure 5.18: Spectral coherence estimate for “AP” and “noise + AP”. The peak at ‘1’ implies the two signals have perfectly correlated components around 220 Hz. The corresponding phase lag is zero degrees.

5.2.3 Planar Results

In total 4,860 APs were successfully stimulated, imaged and analysed over 16 separate events. Figure 5.7a shows images of a representative culture two weeks *in vitro*. As described in the previous section there are four different analysis methods for determining if an action potential was detected; visual inspection of the time aligned and averaged recordings, cross-correlation, comparison of histograms, and spectral coherence. Examples of these from 1000 repeats are given in Figures 5.19 – 5.23, respectively. Figure 5.19 shows the aligned and averaged electrically recorded voltages. Every cell responds differently to stimulation and after a number of triggers becomes fatigued, and the AP changes shape. It can be seen in Figure 5.19 where the amplitude of the AP begins to reduce towards the end of the experiment. The traces from the start of the experiment are dark blue and change to a lighter shade over time. Also, the spike amplitude decreases by 50 mV and the resting membrane potential gradually increases by about 20 mV.

There is no obvious increase in the average light intensity around $t = 0$ for 1000 trig-

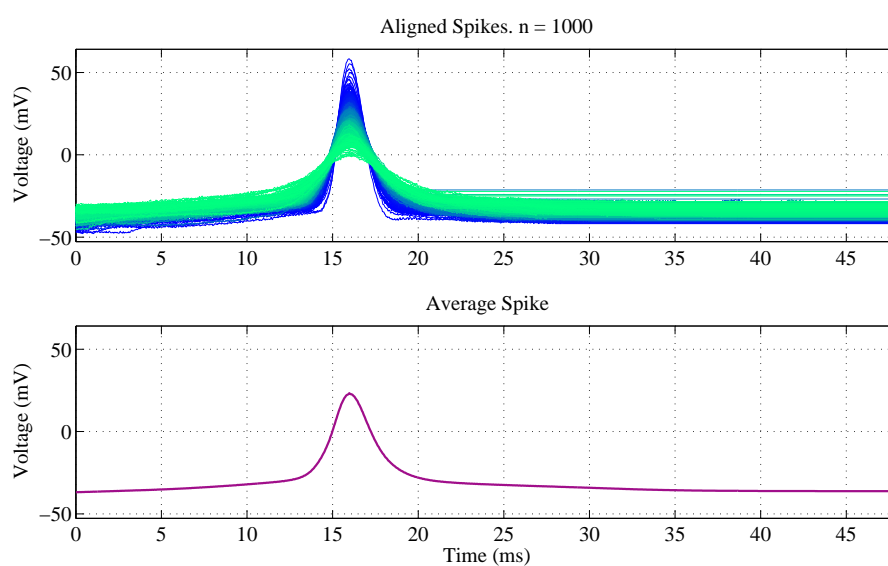


Figure 5.19: Processed electrophysiology voltage recordings for 1000 triggered APs on planar gold surfaces. The spikes are detected using a threshold condition. The first spike is used as a reference and the subsequent action potentials are aligned to it to give the top plot. Bottom plot: The aligned APs are averaged to give the standard voltage waveform for further analysis.

gered APs on planar gold surfaces when visually inspecting the time series average light intensity, Figure 5.20.

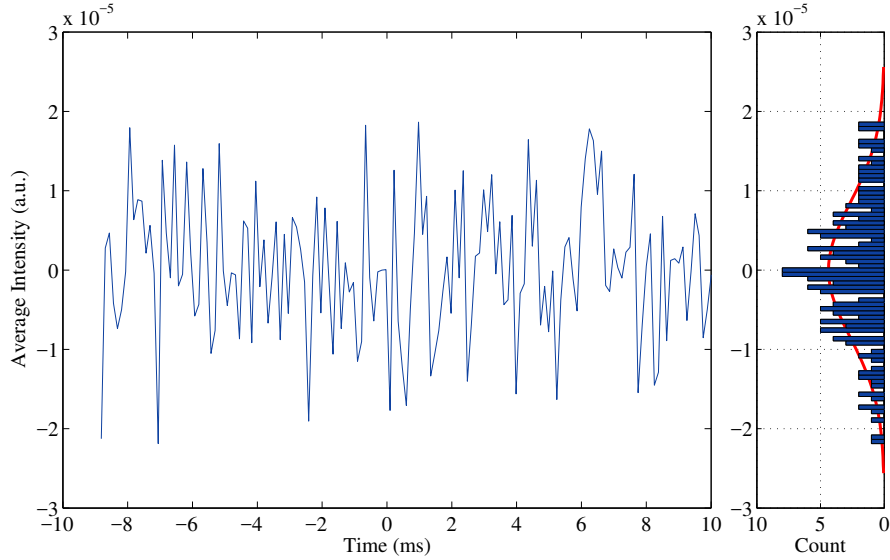


Figure 5.20: The average across all pixels for 1000 action potentials from the planar results. The signal distribution to the right was compared with a Gaussian normal, Figure 5.22.

The cross-correlation amplitude at $t = 0$, Figure 5.21 is around -2.5×10^{-5} . Therefore, it can be determined that there is no correlation between the electrically recorded voltage and optical SPR recording.

Statistical tests were performed on Figure 5.22 by comparing the histogram of the SPR response to that of white Gaussian noise for 1000 repeats. An unpaired t -test determined there was no statistically significant difference between the distributions for noise ($\mu = 2.93 \times 10^8$, $\sigma = 9.72 \times 10^6$) and the SPR response ($\mu = 0$, $\sigma = 8.54 \times 10^6$); $t(344) = 0.0298$, $p = 0.976$. Both the SPR response and noise distributions pass a D'Agostino & Pearson normality test with p -values of 0.866 and 0.179, respectively.

Spectral coherence between the electrical and optical signals was also performed to identify if there were any correlations in the frequency domain. The power spectrum of the respective signals was plotted to display the power present at each frequency. Figure 5.23 confirms that the signals have a maximum correlation around 0.3 at 1.8

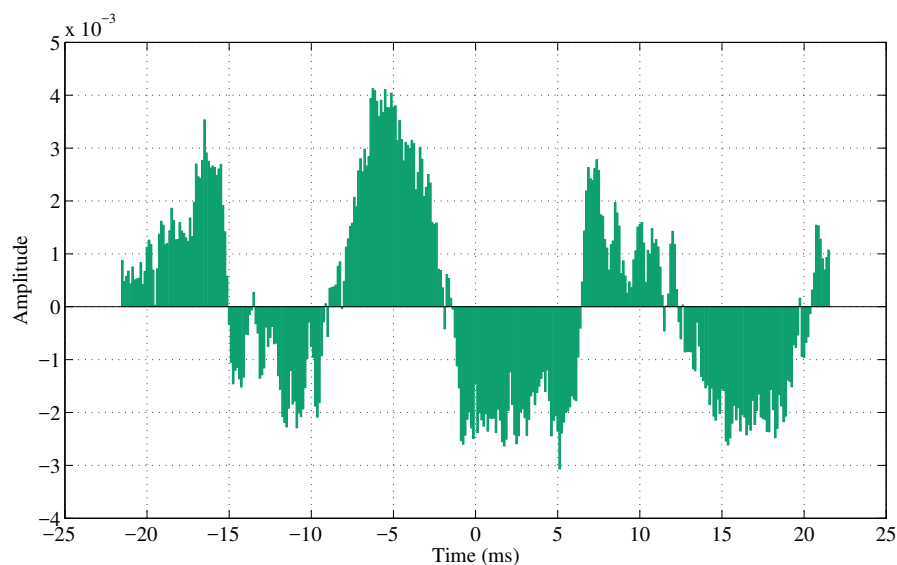


Figure 5.21: Representative figure computing the cross correlation amplitude between the SPR response and electrically recorded membrane voltage for 1000 AP repeats on a planar gold sensor. The amplitude is around -2.5×10^{-5} .

kHz. Comparing this to the reference spectral coherence in Figure 5.18, the perfectly correlated components were around 220 Hz with no phase difference. For 1000 APs at 220 Hz the coherence estimate is around 0 with no phase lag.

Figure 5.24 summarises the cross-correlation amplitude for the different number of repeats up to 1000. A one-way ANOVA was performed between the number of triggers. There were no statistically significant difference between group means as determined by one-way ANOVA; $F(6, 6) = 3.46$, $p = 0.0781$. Also, the average across repeats for the number of triggers was used to perform a single-sample t -test. The single-sample t -test was performed across all the amplitudes to determine if a statistically significant difference existed between the different amount of triggers to that of a true negative as determined by the pseudo-data as 0.005. There was no statistically significant difference between the amount of repeats and the cross-correlation amplitude when no AP was stimulated or detected, i.e., a true negative ($\mu = 0.00258$, $\sigma = 0.0344$); $t(12) = 0.253$, $p = 0.8046$.

Similarly, after comparing the distributions from the SPR row average using a one

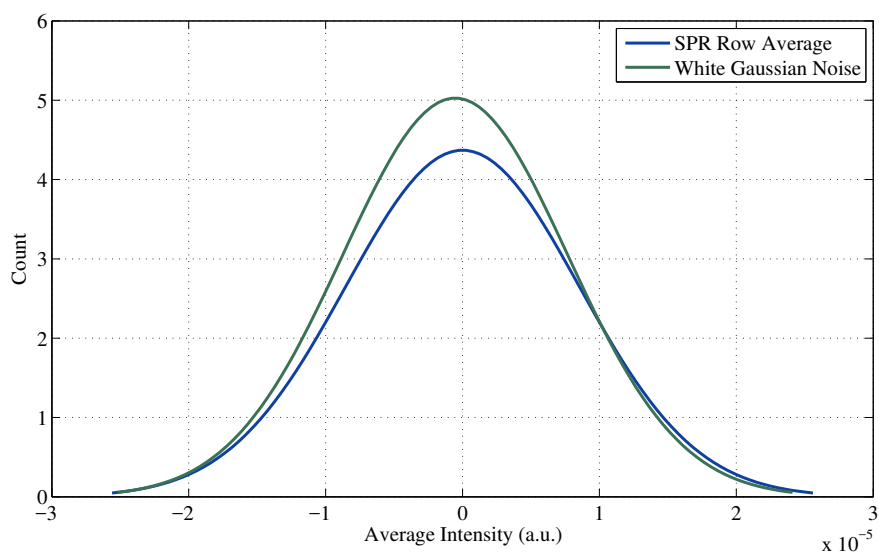


Figure 5.22: Representative figure comparing the histogram of the SPR response to that of white Gaussian noise for 1000 repeats. An unpaired t -test determined there was a no significance difference between the distributions for noise ($\mu = 2.93 \times 10^8$, $\sigma = 9.72 \times 10^6$) and the SPR response ($\mu = 0$, $\sigma = 8.54 \times 10^6$); $t(344) = 0.0298$, $p = 0.976$. Both the SPR response and noise distributions pass a D'Agostino & Pearson normality test with p -values of 0.866 and 0.179, respectively.

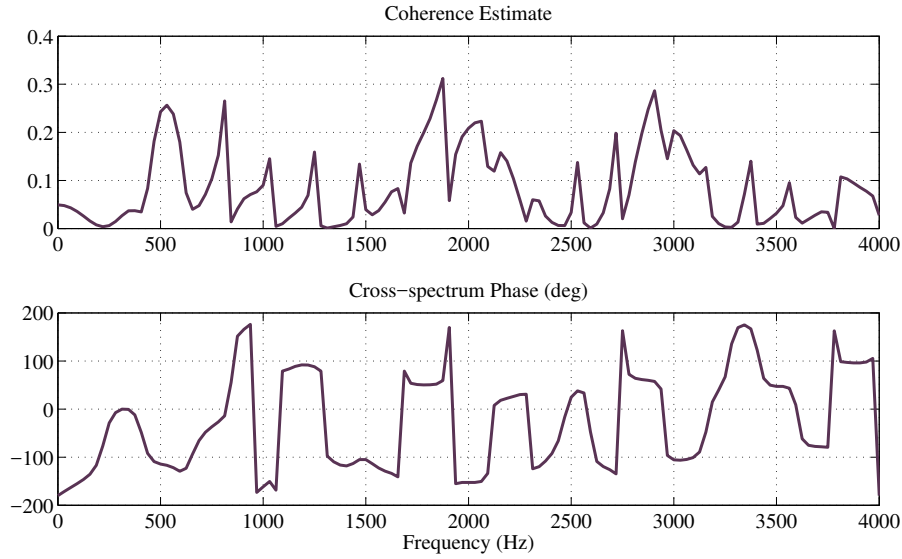


Figure 5.23: Spectral coherence estimate for the relation between the SPR response and electrically recorded membrane voltage for 1000 AP repeats on a planar gold sensor.

sample t -test. It was found there was no statistically significant difference between the amount of repeats ($\mu = -5.83 \times 10^{-6}$, $\sigma = 6.87 \times 10^{-6}$) and the average intensity as determined by the peak of the histogram distribution (-1.17×10^{-7}) when no AP was stimulated or detected; $t(6) = 1.86$, $p = 0.137$.

The estimate of the spectral coherence for each repeat was computed, and it could be seen visually that at no frequency there was a correlation of more than 0.5, i.e., there was no causality between the intracellular recorded voltage and SPR response.

Therefore, it can be concluded to a high certainty that the planar gold SPR sensors did not detect any action potentials up to 1000 repeats and down to a noise floor of 7.57×10^{-6} . The standard deviation of the noise was taken for each experiment after one AP and then after averaging to compare the improvement in noise, Table 5.2. The mean of the standard deviations and error bars (σ) are plotted with theory in Figure 5.25. The experimental noise levels followed theory very closely and after averaging the noise was significantly reduced. The largest improvement in noise occurs between 10 and 100 averages.

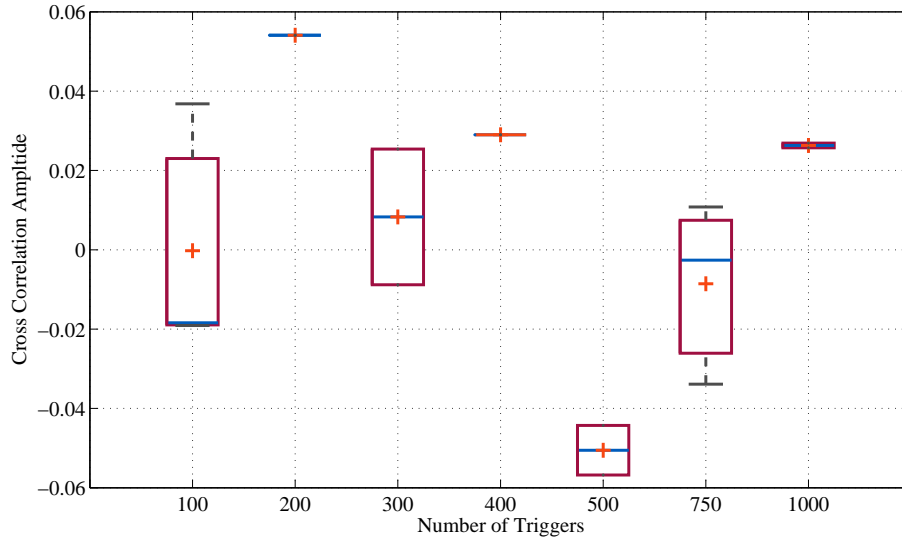


Figure 5.24: Summary of the resultant amplitude from the cross correlation analysis for the planar sensors for the different repeats. There is no statistically significant difference between the amount of repeats and the cross-correlation amplitude for a true negative ($\mu = 0.01078$, $\sigma = 0.03396$); $t(6) = 0.4501$, $p = 0.6684$.

Table 5.2: Estimated noise floor from the planar repeats. The estimated noise floor was calculated from the standard deviation of the row average. The standard deviation is from the repeat of the experiment (n).

Repeats	Est. Noise Floor	Standard Deviation	n
1	2.67×10^{-4}	6.46×10^{-5}	16
10	8.00×10^{-5}		1
100	3.10×10^{-5}	1.25×10^{-5}	2
200	1.71×10^{-5}	1.26×10^{-5}	2
300	1.90×10^{-5}	1.64×10^{-5}	2
400	2.58×10^{-5}		1
500	1.07×10^{-5}		1
750	9.33×10^{-6}		1
1000	7.57×10^{-6}	4.81×10^{-7}	2

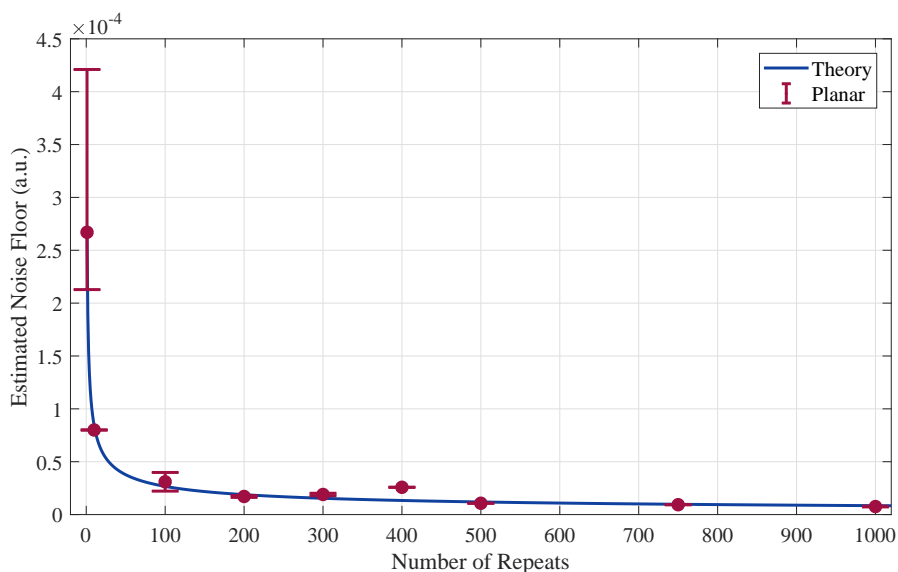


Figure 5.25: Estimated noise floor from the planar repeats compared with theory ($1 / \sqrt{N}$). The standard deviation of the row average was exported for each repeat on the planar surfaces and fit to theory.

The upper limit of repeats to average over was determined by the EPIX camera and the neuron itself. Attempting to trigger more than 1000 APs using the EPIX camera would always result in missed frames from the images. Also after 1000 APs were stimulated in the neuron, the neuron would become fatigued, and the AP would change shape as can be seen in Figure 5.19. This reduction in spike shape made the images harder to align and could mean that the refractive index change of the neuron membrane during the AP would also reduce. If the refractive index change of the cell membrane was smaller, then the light intensity change would decrease and result in a reduced SNR.

5.3 Chapter Conclusions

This chapter introduced a planar gold sample and characterised the SPR response and sensitivity for the SPM developed. The resonance angles were compared and the experimental angular responses align well with theory showing the SPR sensitivity is highly dependent on the gold film thickness. The reflectance of the thinner gold film

recovers slowly after θ_{sp} , whereas the thicker the gold film the difference between the minimum and maximum reflectance amplitude has become smaller, and therefore less sensitive. None of the experimental θ_{sp} for each thickness were significantly different from their respective theoretical θ_{sp} . The gradients of the SPR responses for each of the theoretical and experimental planar samples was calculated using $\Delta\tilde{R} = \Delta\tilde{R}/\Delta\theta$. The angular response for a gold thickness of 50 nm was the most sensitive in terms of sharpness, recovery of the reflectance amplitude near θ_{sp} , and has the greatest gradient. Confirming a 50 nm gold layer is optimum at 680 nm.

The sensitivity of the gold planar surfaces was characterised by using different salt solutions to change the bulk refractive index of the dielectric in an intensity interrogation scheme. The refractive index unit (RIU) was calculated as the ratio of the change in refractive index (Δn) and change in normalised reflected light intensity ($\Delta\tilde{R}$) as $\Delta\tilde{R}/\Delta n = 28.5, 61.97, \text{ and } 119.25$ RIU for NaCl, KCl, and NaF, respectively. The average $\Delta\tilde{R}/\Delta n$ is 69.9. The refractive index change during an AP was theoretically determined to be $\Delta n = \pm 1.5 \times 10^{-3}$ resulting in the theoretical reflectance changing by $\Delta R = \pm 3.1 \times 10^{-3}$ and giving a required $\Delta R/\Delta n$ of 2.067. This $\Delta R/\Delta n$ of 2.067 is on average 30% less than what we can detect. Therefore, detecting the refractive index change during an AP should physically be achievable.

Finally, primary rat hippocampal neurons were plated on the planar gold surfaces and electrophysiology was used to stimulate the cells while imaging the optical response. The protocol to trigger and record the voltage and SPR response of one action potential simultaneously was developed. The results showed no variation in the light intensity at the time of an AP being invoked. Methods of minimising noise in post-processing by signal averaging was investigated and confirmed to be effective, closely following theory. MATLAB code was developed to analyse the recorded electrical and optical data, and to reduce the noise level further. Any electrical or mechanical noise that was present was removed by subtracting a control area from the cell ROI. On average the standard deviation of the intensity profile of the row average was improved by a factor of two. Pseudo-data was created to test the MATLAB code to ensure that it was able to align and average across repeats. Similarly, the pseudo-data was used to get standard, positive results of the statistical, temporal, and spectral analyses.

It can be concluded that the planar gold SPR sensors were unsuccessful at detecting any action potentials up to 1000 repeats, and down to a noise floor of 7.57×10^{-6} . The noise floor is three orders of magnitude smaller than the theoretical light intensity change expected, $\Delta R = \pm 3.1 \times 10^{-3}$. The hypothesis for the planar surfaces not successfully detecting AP activity is that the refractive index change is localised to the cell membrane, which is a small area on a relatively large gold surface. The large surface area of gold could average the SPR response and reduce the SNR. A method of decreasing the sensor size and localising the SPR signal is investigated in the next chapter.

CHAPTER 6

MICROSTRUCTURES

In the previous chapter, an experimental protocol and analysis method to detect neural activity was developed and validated. The planar gold sensors were unsuccessful at detecting action potentials from cultured neurons. One possible explanation is that a large area of gold will average the refractive index changes of the signal because of diluting effects on the electrons across the surface (Yanase et al., 2010). As discussed previously in Section 3.1 a plasmon needs about four times the propagation length L_x for a full decay or build up (Schasfoort and Tudos, 2008). This suggests that SPs with distances larger than L_x are completely independent of each other and can be considered as separate sensing areas, as long as they are significantly larger than L_x^2 . For example, SPs on gold, excited at 680 nm in water, L_x is 18.27 μm resulting in $L_x^2 \approx 330 \mu\text{m}^2$. The entire 19 mm coverslip used in this work has a total sensing area of $\sim 280 \mu\text{m}^2$ implying that there will only be one available sensing area and therefore, only able to detect the SPR response from one cell at a time. If there is only one sensor area, then it would not be suitable for detecting every action potential from every neuron. To improve localisation and achieve single-cell resolution a new sensor was required that reduced the sensing area to that of one cell.

To design this new sensor first, it was necessary to establish the size and morphology of the cell. Once this was known, the photomask could be designed so that each cell could completely cover at least one gold structure, while considering the effect of spatial constriction of the propagation length on the quality of the plasmon. The photolithography protocol was optimised, so the procedure was reproducible and less susceptible to external factors. The microstructures were characterised by their size, morphology, height, and angular SPR response. The microstructures sensitivity to refractive index changes was also investigated. The microstructures fabricated were predominantly glass and previously, for planar gold AUT was used for the adhesion layer. However, AUT does not adhere to glass so a new adhesion protocol was required. Neurons are notorious for their sensitivity to the condition of the substrate so a cell viability assay was performed using two different adhesion protocols, PEI and PLL and compared to AUT on glass. Finally, once cells were successfully cultured on the microstructures the experiments from Section 5.2 were repeated and analysed to determine if the new sensor that was developed was capable of detecting neural activity.

6.1 Photomask Design

6.1.1 Cell Morphology

To successfully design a sensing platform for cells it was necessary to find the size and morphology of the cells. Brightfield images of cells 2 DIV were taken using the Nikon Ti (10 \times , NA = 0.25) and imported to Image-J, Figure 6.1a. First, a threshold image was created in Image-J to measure the area, circularity, Feret diameter, and minimum Feret diameter of the cells (see Figure 6.1b). The area is given in calibrated square units (μm in this instance). The circularity was calculated using (6.1), with a value of ‘1’ indicating a perfect circle and a value approaching ‘0’ indicates an increasing elongated shape. The Feret diameter is the longest distance between any two points along the selection boundary, also known as the maximum caliper. Conversely, the minimum Feret diameter is the minimum caliper.

$$\text{Circularity} = 4\pi \frac{\text{Area}}{\text{Perimeter}^2} \quad (6.1)$$

Particles less than $80 \mu\text{m}^2$ were considered to be debris so were excluded from the analysis. N_{total} was 1074, the results can be found in Table 6.1. The average Feret diameter for a cell was found to be between 10.3 and $16.4 \mu\text{m}$, which agrees with values reported in literature for a typical mammalian cell (Meitzen et al., 2011).

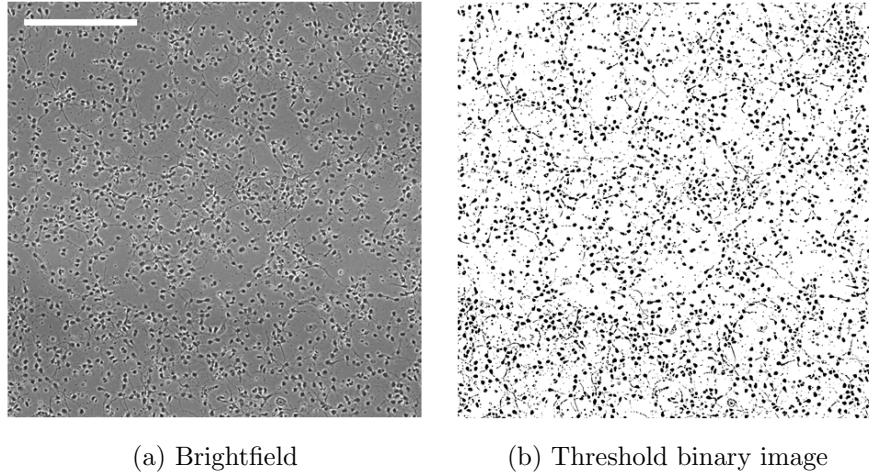


Figure 6.1: Microscopy and threshold binary image of primary rat hippocampal neurons 2 DIV taken with the Nikon Inverted Microscope ($10\times$, $\text{NA} = 0.25$) and the Hamamatsu camera. The scale bar is $200 \mu\text{m}$ and consistent across both images.

Table 6.1: Results from the analysis of cell morphology of cultured neurons at 2 DIV. The means and standard deviation for the area, feret, min feret, and circularity are reported and have been used to design the microstructures ($N_{total} = 1074$).

Parameter	Mean \pm Std Dev	
Area	111.6 ± 19.5	μm^2
Feret	16.4 ± 3.33	μm
MinFeret	10.6 ± 1.29	μm
Circularity	0.735 ± 0.135	μm

6.1.2 Design

The photomask was designed such that the lengths of the metal microstructures were tailored to both Nyquist criteria and the SP propagation length, the latter being approximately $18.3 \mu\text{m}$. The Nyquist criteria states that to ensure each cell

fully covers at least one gold microstructure the spacing of the structures needs to be half the size of the cell or smaller (Nyquist, 1928; Shannon, 1949). The diameter of the cell was assumed to be about $13\ \mu\text{m}$, so the spacing needed to be at least $6.5\ \mu\text{m}$. The dimensions of the contact aligner only allowed a 3×3 inch mask to be used. No features should be within 10 mm of the mask edge giving a usable area of 5.62 cm. The resolution of contact lithography is limited to the wavelength of the radiation used, where the wavelength used is 365 nm (Levinson, 2005). The minimum feature size achievable was $\sim 2\ \mu\text{m}$. Taking these issues into consideration, the geometries chosen to be investigated are in Table 6.2, each with $2\ \mu\text{m}$ between each metal strip. The area of each pattern was restricted to 0.5 mm.

Table 6.2: Dimensions of structures on Photomask in μm . The pitch was $2\ \mu\text{m}$.

2×2		
2×6	6×6	
2×10	6×10	10×10
2×16	6×16	10×16

6.2 Optimisation of Photolithography Protocol

Patterning coverslips using photolithography was a lengthy process that can take on average about 20 hours to fabricate ten sensors (Appendix A.3). Optimisation of the photolithography protocol was performed to increase reproducibility, and minimise variability in response to noise factors, including temperature, humidity, age/quality of the resist and developer, and the distance between the coverslip and photomask.

The usual steps for the image reversal process are: photoresist coating, pre-bake, exposure, reversal bake, flood exposure, development, and lift-off (Levinson, 2005). The methodology is described in more detail in Appendix D.1.2. The standard physics clean room protocol for image reversal processing was used as a starting point. However, this process was optimised for use with Gallium Arsenide, which has different optical properties to that of the coverglass used. This resulted in all the gold and photoresist being removed during lift off. The reversal bake was optimised separately according to the photoresist datasheet. The other parameters that had

the most significant impact on the outcome were the exposure time, flood exposure time, and development time. These steps were optimised with the experimental runs, designed using a Taguchi array. A Taguchi array is method of experimental design where at each level of a particular parameter, all levels of each of the other parameters are tested at least once (Taguchi, 1986).

6.2.1 Reversal Bake Optimisation

The reversal bake was optimised as per the datasheet (Sheet, 2004). Eight, clean coverslips were coated in photoresist (AZ 5214E) and prebaked 110°C for 50 seconds. These coverslips were subjected to different reversal-bake temperatures (115, 120, 125, and 130°C) for 2 mins. A 30 secs flood exposure was applied then the coverslips were immersed in concentrated AZ 726 MIF developer for 1 min. On some of the coverslips the resist was removed, on others, the resist remained thermally cross-linked. The optimum reversal bake temperature is 5 – 10°C below the temperature where the crosslinking starts (Gogolides et al., 1996). The reversal bake optimisation resulted in an optimised thermal bake temperature of 120°C. To maintain a consistent, repeatable process, this temperature was kept constant within $\pm 1^\circ\text{C}$.

6.2.2 Experimental Design

To save time and material cost, an orthogonal Taguchi array was implemented to optimise the remaining parameters. An orthogonal Taguchi array is where at each level of a particular parameter, all levels (L) of each of the other parameters ($P - 1$) are tested at least once (Taguchi, 1986). The orthogonal Taguchi array ensures there are no unnecessary repeats and is less costly than a full factorial analysis where every possible combination is run ($N = L^P = 3^3 = 27$ runs). The required number of runs for an orthogonal Taguchi array is the number of levels \times each level of each parameter tested three times. Therefore, $3 \times 3 = 9$. The runs are shown in Table 6.3.

The remaining independent variables; exposure, flood exposure, and development times were optimised using the Taguchi array defining each experimental run. Each run was performed on three different coverslips. The coverslips were initially solvent cleaned and treated with MPTS following the methods in Section 2.3.1. Each coverslip had a drop of AZ 5412E image reversal photoresist spun on at 4000 rpm for

Table 6.3: Experimental runs designed using a standard three level Taguchi array. Where P1 is exposure time (2.0, 2.5, 3.0 seconds), P2 is flood exposure time (20, 25, and 30 seconds), and P3 is development time (20, 25, and 30 seconds).

Run	P1	P2	P3
1	1	1	1
2	1	2	2
3	1	3	3
4	2	1	2
5	2	2	3
6	2	3	1
7	3	1	3
8	3	2	1
9	3	3	2

30 seconds to give a uniform layer of $1.4 \mu\text{m}$. Next, the coverslips were pre-baked at 110°C for 50 seconds and then subjected to a specified exposure time. In the previous section, the reversal bake was optimised, so each coverslip was subjected to a reversal bake of 120°C for two mins before undergoing different flood exposure times. Finally, the coverslips were submerged in the developer for different times. The microstructures were inspected under a microscope (Olympus, $10\times$, $\text{NA} = 0.25$) after development to check the pattern and qualitatively assess the condition. If the pattern looked clear of resist and in good condition, then it was considered a successful attempt. The percentage of successfully patterned structures (out of 9) was calculated for each three coverslips, Table 6.4.

The goal of the optimisation process was to minimise the variability in the photolithography success rate in response to noise factors while maximising variability in response to the controlled steps. The noise factors in the process included the temperature, age/quality of the resist and developer, and the distance between the coverslip and photomask. The latter was improved by removing the photoresist edge beads before the pre-bake with a cotton-wool bud soaked in acetone. The variability can be quantified by calculating the signal-to-noise ratio. A larger SNR means less variability. Taguchi (1986) proposed four SNR ratios; “smaller-the-better”, “larger-

Table 6.4: Populated version of Table 6.3 and results giving the average number of successful attempts for each run. $n = 6$ for each level.

Exposure Time (s)	Flood Exposure Time (s)	Development Time (s)	Successful Attempts
2.0	20	20	0/6
2.0	25	25	4/6
2.0	30	30	1/6
2.5	20	25	3/6
2.5	25	30	2/6
2.5	30	20	0/6
3.0	20	30	2/6
3.0	25	20	0/6
3.0	30	25	5/6

the-better”, “nominal-is-best”, and “signed target”. As a larger number of successful attempts is desirable, the “larger-the-better” concept was adopted. The SNR was calculated using (6.2) where a large SNR means a smaller response variation.

$$\text{SNR} = -10 \log_{10} \left(\frac{1}{n} \sum \frac{1}{y^2} \right) \quad (6.2)$$

where n is the number of repeats, and y is the measured value in the run. Figure 6.2 displays the resulting SNRs for each parameter. Based on the figure the optimal photolithography parameters are 3 seconds exposure time, 30 seconds flood exposure time, and 25 seconds development time. The development time has the most variance between different values, and after developing for just 20 seconds, no patterns were visible.

The effect of the protocol parameters were tested with a one-way ANOVA, between the different parameter and average success rate. The means, median, upper, and lower quartiles for the exposure time, flood exposure time, and development time were plotted and are shown in Figure 6.3a, 6.3b, and 6.3c, respectively. There was a statistically significant difference between the different development times as

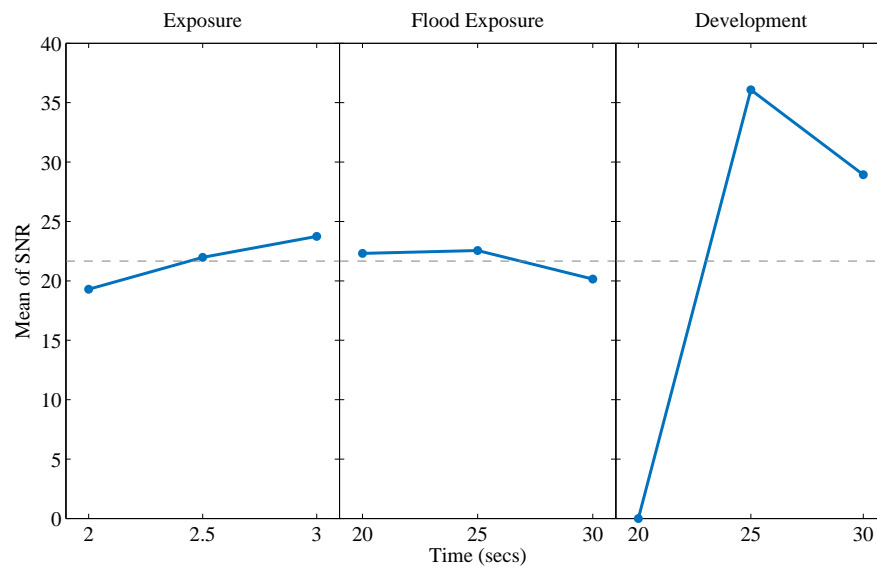


Figure 6.2: S/N Ratios to quantify the variability of the independent parameters from the Taguchi array (Taguchi, 1986). More successful attempts are desirable therefore the “larger-the-better” concept was adopted. The SNR was calculated using (6.2). The largest SNR ratios give the the optimal photolithography parameters as an exposure time of 3 seconds, 25 seconds flood exposure time, and 25 seconds development time. The reference line is the overall mean at 21.6.

determined by the one-way ANOVA; $F(2, 24) = 59.9$, $p < 0.0001$. There was no statistically significant difference between the different exposure times; $F(2, 24) = 0.767$, $p = 0.476$, or flood exposure times; $F(2, 24) = 0.0137$, $p = 0.986$. Therefore, the development time has the most effect on the outcome, followed by the exposure time. The flood exposure time has the smallest effect. The 20 and 25-second flood exposure times have higher SNRs but the microstructures were distorted with more curvature at the edges, and on average smaller than the desired size. The mean of successful attempts for the 30 second flood exposure time was lower because the results had the most variance. The most successful attempts were with Run 9, where the exposure time was 3 seconds, 30 seconds of flood exposure, and a 25 second development time. This protocol was the only run to fabricate structures smaller than $6 \mu\text{m}$ successfully. Given this, the final parameters were decided as an exposure time of 3 seconds, a flood exposure of 30 seconds, and 25 seconds of development.

6.3 Microstructure Characterisation

Brightfield microscopy was used to inspect the microstructures morphology and profilometry to measure the height of the gold layer, which is critical for a good SPR response. The SPR response for each microstructure was confirmed, and their sensitivity to refractive index changes was characterised to ensure that they exhibit plasmonic properties and could be used to detect electrical activity. Finally, the structure's resistance to chemical and mechanical cleaning methods was investigated so they could be reused and ultimately increase reproducibility.

6.3.1 Microscopy

Brightfield images at $10\times$ magnification were taken of the microstructures using an Olympus microscope ($\text{NA} = 0.25$), shown in Figure 6.4. The microstructures smaller than $6 \mu\text{m}$ were very rarely successful, with the distance between the coverslip and the photomask being crucial. If the contact between the coverslip and mask was not perfect, the structures would not develop. Occasionally, even after optimisation, the microscopy images would reveal defeats including rounded edges and gaps between structures of more than $2 \mu\text{m}$. The former most likely due to under- or overexposure

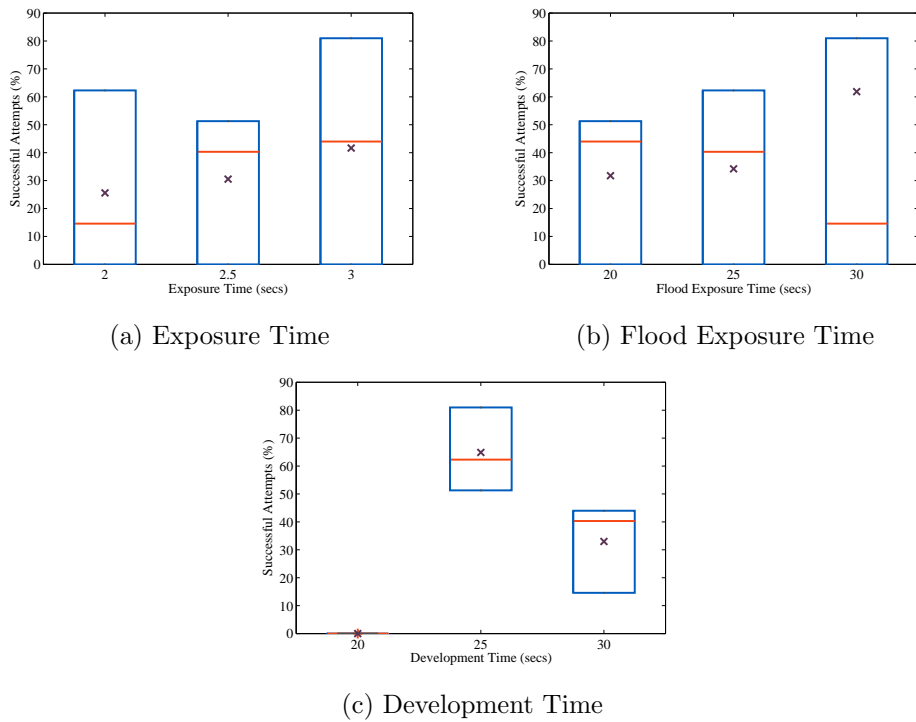


Figure 6.3: Results from the one-way ANOVA for each variable vs. the average number of successful attempts. The crosses are the average success rate for each variable. There was a statistically significant difference between the different development times; $F(2, 24) = 59.9$, $p < 0.0001$. There was no statistically significant difference between the different exposure; $F(2, 24) = 0.767$, $p = 0.476$, and flood exposure times; $F(2, 24) = 0.0137$, $p = 0.986$. Therefore, the photolithography process is most dependent on the development time.

and the latter by the distance between the coverslip and photomask being too large and UV light exposing larger areas.

6.3.2 Profilometry

Profilometry measurements of each microstructure were taken after lift-off. Ellipsometry was used to calculate the thickness of the planar gold references. The average height of the microstructures was 47.7 ± 1.1 nm ($n = 9$). The average thickness of the planar gold references was 47.4 ± 1.5 nm ($n = 9$), i.e., the ellipsometry measurements give similar results to the profilometry measurements.

6.3.3 SPR Response

Images of the BFP were taken using the 640 nm LED to illuminate the BFP of the Nikon oil-objective lens with uniform light. The reflected light intensity was imaged on the Unibrain camera shown in Figures 6.5a, 6.6a, 6.7a, 6.8a, and 6.9a. The radial position of the illumination on the BFP corresponds to the angle of incidence and the azimuthal angle related to the polarisation state. Along the direction where the azimuthal angle is 0° the polarisation state is pure p -polarised light, which changes to pure s -polarised light when the azimuthal angle is $\pm 90^\circ$. The representative BFP's look more like glass than 50 nm gold from Figure 5.2b. However, there does appear to be a faint darker semi-circle after the critical angle for glass showing that some light is coupling with the surface plasmons. This can be explained because the structures are at most one-third gold, the rest is glass.

The SLED was scanned across the BFP of each of the microstructures to increase the angle of incidence. A series of images was produced of the average reflected light intensity with respect to the angle of incidence detected by the EPIX camera. A plot of the angular SPR response was created using Image-J to export the z -axis profiles for different regions of interest; one of glass as a reference and the other of a gold structure. The z -axis profiles were imported to MATLAB, and the angle of incidence was calculated using the equation from Section 4.3.

Figures 6.5b, 6.6b, 6.7b, 6.8b, and 6.9b show representative angular responses for the planar gold reference, and each of the microstructures, with air as the dielectric. All the structures exhibit noticeable SPR dips just after the critical angle ($\theta_c = 41.2^\circ$).



Figure 6.4: Representative brightfield images (Olympus, $10\times$, $NA = 0.25$) of the nine microstructures post lift-off. The area of each pattern is restricted to 0.5 mm and each image is an area of $600 \times 800\ \mu\text{m}$.

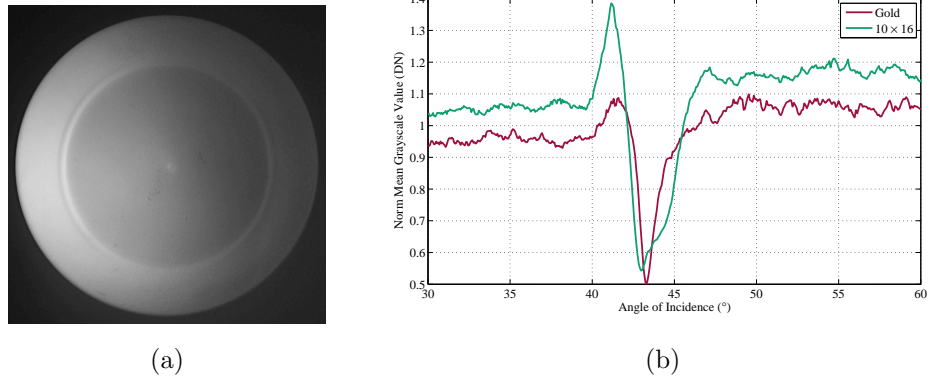


Figure 6.5: Representative BFP image (a) and SPR response (b) for the 10×16 gold microstructures. Glass / Gold / Air. $\theta_{sp} = 42.99 \pm 0.149^\circ$. ($n = 4$). The difference in θ_{sp} between the planar control and gold microstructure is not significant.

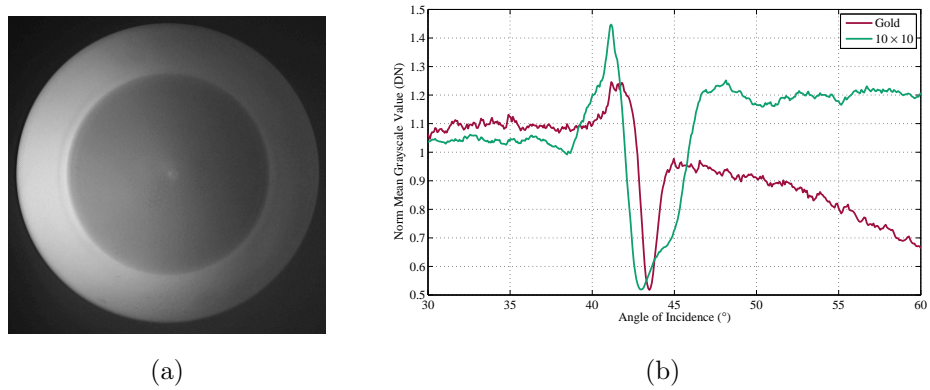


Figure 6.6: Representative BFP image (a) and SPR response (b) for the 10×10 gold microstructures. Glass / Gold / Air. $\theta_{sp} = 43.1 \pm 0.193^\circ$. ($n = 4$). The difference in θ_{sp} between the planar control and gold microstructure is not significant.

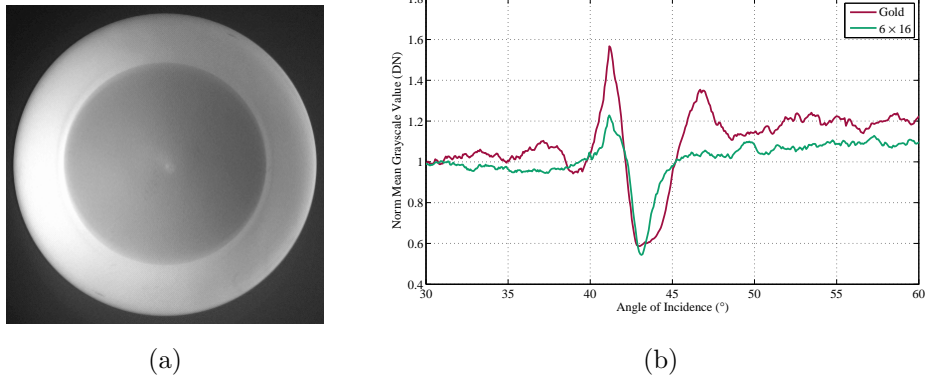


Figure 6.7: Representative BFP image (a) and SPR response (b) for the 6×16 gold microstructures. Glass / Gold / Air. $\theta_{sp} = 43.2 \pm 0.672^\circ$. ($n = 2$). The difference in θ_{sp} between the planar control and gold microstructure is not significant.

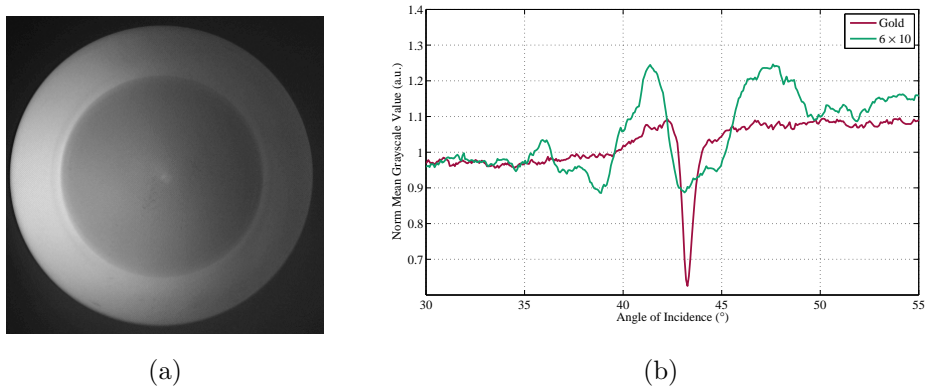


Figure 6.8: Representative BFP image (a) and SPR response (b) for the 6×10 gold microstructures. Glass / Gold / Air. $\theta_{sp} = 42.97 \pm 0^\circ$. ($n = 1$). The difference in θ_{sp} between the planar control and gold microstructure is not significant.

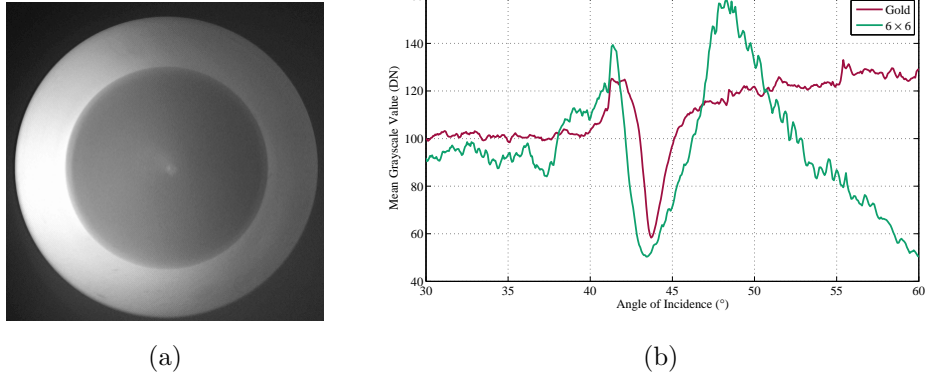


Figure 6.9: Representative BFP image (a) and SPR response (b) for the 6×6 gold microstructures. Glass / Gold / Air. $\theta_{sp} = 43.3 \pm 0^\circ$. ($n = 3$). The difference in θ_{sp} between the planar control and gold microstructure is not significant.

A paired t -test was performed on the structures and their paired planar control, Figure 6.10. There was no statistically significant difference between the resonance angle for the planar controls ($\mu = 43.16^\circ$, $\sigma = 0.223$) and the structures ($\mu = 43.1^\circ$, $\sigma = 0.251$); $t(9) = 0.463$, $p = 0.655$. In addition, an ordinary one-way ANOVA was performed on the datasets for the different structures and planar controls. There was no statistically significant difference between the datasets; $F(5, 17) = 0.533$, $p = 0.749$. Therefore, it can be concluded that the size of the gold microstructure has no significant affect on the resonance angle, θ_{sp} .

In an intensity interrogation SPR scheme, the angle of incidence (θ) is fixed at the angle with the steepest gradient so any change on the surface will result in a large shift in reflected light intensity. The gradients of the SPR responses for each of the microstructures and planar controls was calculated using $\Delta\tilde{R} = \Delta\tilde{R}/\Delta\theta$, see Figure 6.11 and summarised in Table 6.5. As expected the gradient decreases with decreasing strip length, Figure 6.11. The decrease in the gradient amplitude is expected due to the spatial constriction of the SPP (propagation length $\approx 18.27 \mu\text{m}$). Small defects in the microstructures may have also contributed to the poor SPR signal. An analysis of variance showed that the effect of decreasing structure size on the gradient maximum was significant, $F(5, 17) = 2.85$, $p = 0.048$. However, the trade-off between sensitivity to refractive index changes and localisation still needs to be investigated. Then considering both the plasmonic response and Nyquist

criteria an optimum structure size can be selected for detecting electrical activity.

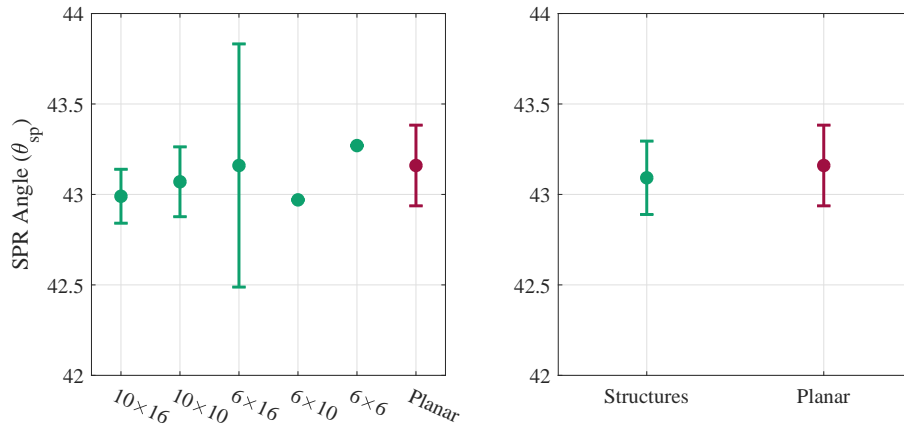


Figure 6.10: θ_{sp} summary for the microstructures and planar controls. Total structures ($n = 14$) and planar controls ($n = 10$).

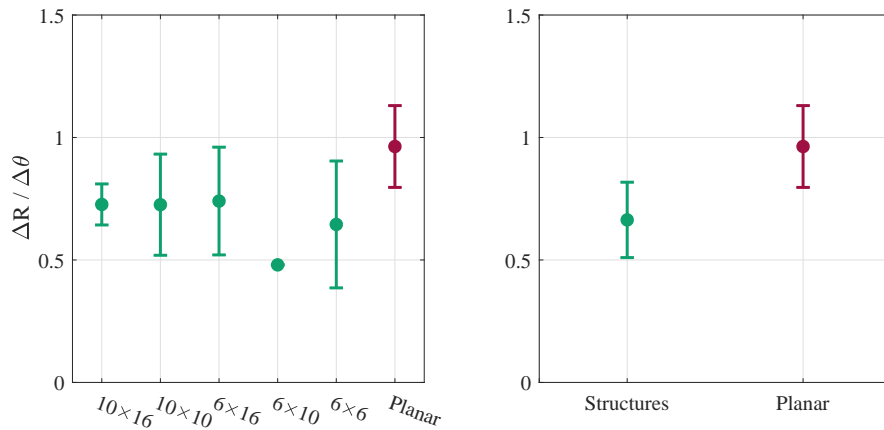


Figure 6.11: Gradient maximum ($\Delta\tilde{R}/\Delta\theta$) summary for the microstructures and planar controls. Total structures ($n = 13$) and planar controls ($n = 10$).

Sensitivity to Refractive Index Changes

To characterise the sensitivity of the microstructures to refractive index changes, the minimum detectable change in refractive index was experimentally determined by changing the bulk refractive index of the dielectric. The experiments from Section 5.1.2 were repeated. Sodium chloride (NaCl) solutions were used at a reference osmolality of 302 mOsm to be comparable with ECS resulting in a reference refractive

Table 6.5: SPR angle (θ_{sp}) and gradient maximum ($\Delta\tilde{R}/\Delta\theta$) for the 50 nm planar controls and microstructures.

	SPR Angle ($^\circ$)	$\Delta R/\Delta\theta$
Planar ($n = 10$)	43.2 ± 0.223	0.963 ± 0.167
10×16 ($n = 4$)	43.0 ± 0.149	0.727 ± 0.084
10×10 ($n = 4$)	43.1 ± 0.193	0.726 ± 0.207
6×16 ($n = 2$)	43.2 ± 0.672	0.741 ± 0.220
6×10 ($n = 1$)	43.0 ± 0	0.480 ± 0
6×6 ($n = 3$)	43.3 ± 0	0.645 ± 0.259

index of 1.3342.

The concentration of the medium on the surface on the substrate was changed to increase or decrease the refractive index. The concentration values were chosen so that the change in refractive index was at least $\Delta n \sim 0.0004$ and the reference concentration was returned to between each step to be sure that the change in light intensity was not due to drift. The change in refractive index was calibrated with an Abbe Refractometer (Anton Paar, Abbemat 200). These values are shown in Table 2.3.

Figure 5.5 shows the time series of an experiment where the concentration of NaCl on the surface on a 10×16 gold microstructure is changed. The y -axis for each experiment was normalised by dividing by the mean of the dataset. The sensitivity experiments were repeated on the 10×10 and 6×6 gold microstructures.

The results from all the experiments are summarised in Figure 6.13. The large error bars for the reference refractive indices are due to the drift explained previously in Section 5.1.2. The errors between repeats are due to errors in the determination of the salt solution concentrations. The normalised light intensity (\tilde{R}) increases linearly (with drift corrected for) with increasing refractive index (n), where

$$\tilde{R}_{10 \times 16} = 28.5n - 34.35, \quad R^2 = 0.9986 \quad (6.3)$$

$$\tilde{R}_{10 \times 10} = 26.37n - 36.85, \quad R^2 = 0.9928 \quad (6.4)$$

$$\tilde{R}_{6 \times 6} = 19.23n - 24.66, \quad R^2 = 0.5849 \quad (6.5)$$

The refractive index unit (RIU) characterises the sensitivity of the sensor. The RIU was calculated as the ratio of the change in refractive index (Δn) and change in normalised reflected light intensity ($\Delta\tilde{R}$), using (3.23). The average RIU for each microstructure are summarised in Table 6.6. the average sensitivity of planar gold was determined to be 69.908 RIU. As expected, the sensitivities of the microstructures are smaller than that of planar gold, which agrees with the gradient measurements. If the gradient $\Delta R/\Delta\theta$ is smaller, the sensitivity to refractive index should be less. Theoretically, a change of $\Delta n = 1.5 \times 10^{-3}$ at the gradient maxima (69.87°) of the SPR dip will result the theoretical reflectance changing by $\Delta R = \pm 3.1 \times 10^{-3}$ and a required $\Delta R/\Delta n$ of 2.067. This required theoretical reflectance is about on average 10% less than what can be detected. Therefore, detecting the refractive index change during an AP should be achievable on the 10×16 , 10×10 , and 6×6 microstructures. It is important to note that this sensitivity is across the bulk substrate and it is still possible that the localised refractive index changes in the cell membrane will result in a larger SPR signal as the cell engulfs the gold structure.

The sensitivities for the 10×16 gold microstructure ($\Delta\tilde{R}/\Delta n = 28.5$ RIU) and 10×10 gold microstructure ($\Delta\tilde{R}/\Delta n = 26.37$ RIU) are comparable. The average size of a cell is $\sim 13 \mu\text{m}$, so the $16 \mu\text{m}$ gold structure will be too large to have a cell engulfing the entire sensing pad. Considering both the plasmonic response and Nyquist criteria the $10 \times 10 \mu\text{m}$ sensor is selected as the optimum structure size and will be used in the following experiments attempting to detect neural activity.

Table 6.6: The sensitivities for the 10×16 , 10×10 , and $6 \times 6 \mu\text{m}$ microstructures.

Structure Size (μm)	$\Delta\tilde{R}/\Delta n$	
10×16	28.5	$n = 3$
10×10	26.37	$n = 3$
6×6	19.23	$n = 2$

6.3.4 Chemical and Mechanical Resistance

The length of time it took to produce ten microstructures was approximately 20 hours. The surface functionalisation and cell preparation required to get to the final experiments took a further three weeks (see Appendix A.3). As previously mentioned

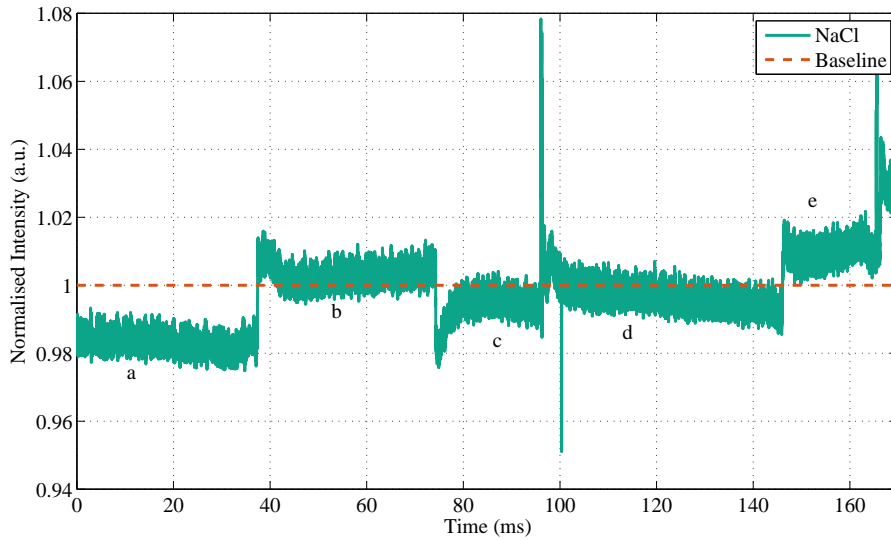


Figure 6.12: Time series plots changing the bulk refractive index on the surface of the gold microstructures with NaCl. The experiments begin with water (a) and the concentration is increased to a reference refractive index (b). The refractive index is changed by at least ± 0.0004 RIU by adding salt solution (e) or water (c). The reference refractive index is returned to between each step (d).

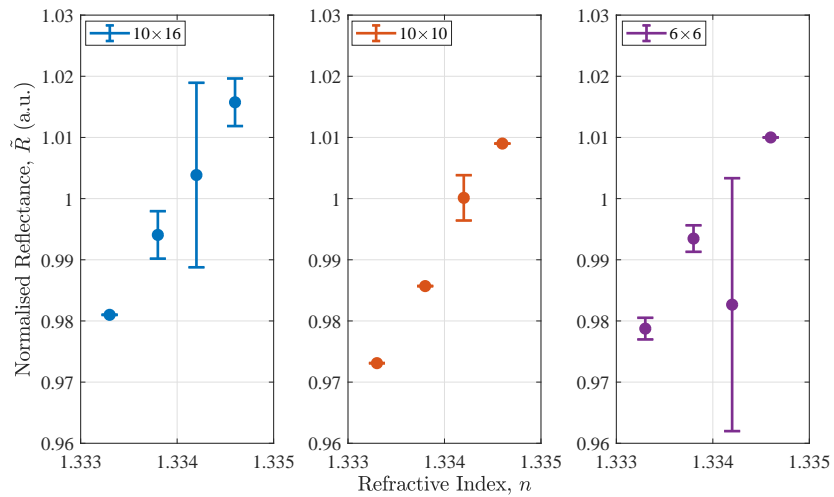


Figure 6.13: Summary of the normalised change in light intensity as a function of the refractive index for each of the microstructures. The large error bars for the reference \tilde{R} refractive indices are due to drift during the experiment from either temperature variation or the light source.

even after optimisation the photolithography process was at best 81% effective and was sensitive to a number of external, uncontrollable factors. Therefore, it was be useful to know if the structures could withstand robust cleaning methods to remove the cell matter and objective-oil so they could be reused.

The gold structures could withstand immersion in Terg-a-zyme enzyme detergent and subsequent solvent cleaning, but both of these methods were not strong enough to remove cell matter. Piranha treatment was performed on the structures. However, this cleaning method caused the gold to lift-off, and was therefore not suitable. Therefore, it was not possible to reuse the microstructures after cell-based experiments.

6.4 Microstructure Functionalisation

6.4.1 Cell Viability

The microstructures being developed are predominantly glass with at most one-third of the area consisting of gold. AUT was used for the adhesion layer on gold but AUT does not adhere to glass so a new adhesion protocol was required. Two, well-established adhesion protocols were investigated; Poly-L-lysine and Polyethyleneimine. Poly-L-lysine (PLL) is the industry standard for cell attachment to glass or plastic (Yavin and Yavin, 1974; Mazia et al., 1975). PLL is a polymer that binds to the surface through electrostatic interactions and covers the surface with positively charged amino acids. The positive amino acid interacts with the negatively charged membrane proteins to promote adhesion. Polyethyleneimine (PEI) is another polymer that is richer in amino acids than PLL and has been proven to provide a stronger attachment between the cell and the surface (Wiertz, 2010; Sun et al., 2012).

The viability of each adhesion protocol was assessed with a live/dead cell viability assay performed on neurons cultured on AUT, PLL, and PEI treated surfaces. The live/dead cell viability assay determines the viability of cells in a population. Calcein (Excitation/Emission 494/517 nm) and Propidium Iodide (Excitation/Emission 536/617 nm) were used to stain the live and dead neurons at 12 DIV, respectively. Propidium Iodide stains the condensed DNA that dead cells leave behind. Representative fluorescent images for the cultures are shown in Figures 6.14 and 6.15 for

the AUT treated, and PEI treated surfaces, respectively.

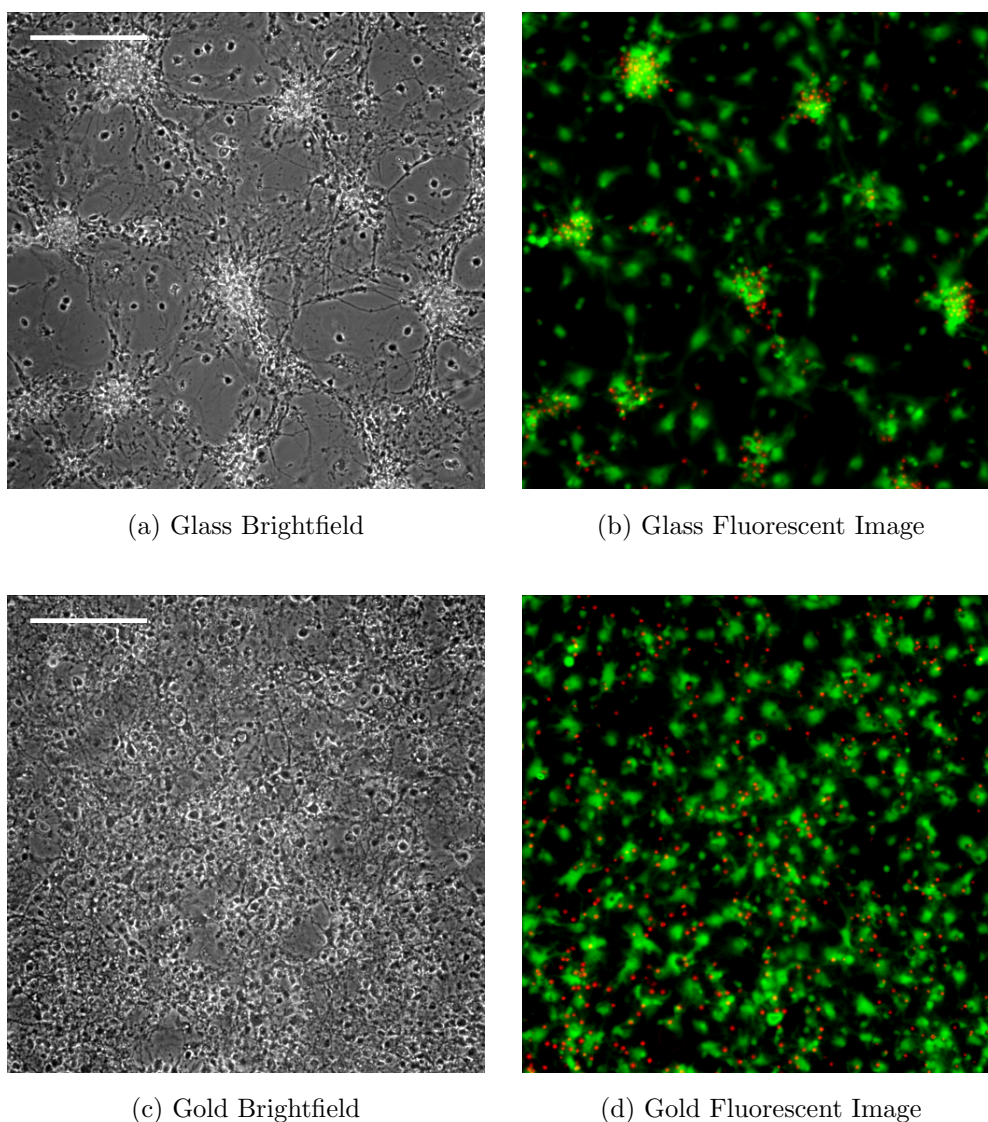


Figure 6.14: Brightfield and fluorescent images from the cell viability assay for AUT treated surfaces at 12 DIV using the Nikon Eclipse Ti-U inverted microscope ($10\times$, $NA = 0.25$). The live cells (green) were stained with Calcein. The dead cells (red) were stained with Propidium Iodide. The brightfield images and the fluorescent images were taken using the QuantEM EMCCD camera. Scale bar is $200\ \mu\text{m}$ long and is consistent across all images. The images were processed in Image-J where the colour was added. As expected the cells on AUT-treated glass have fasciculated.

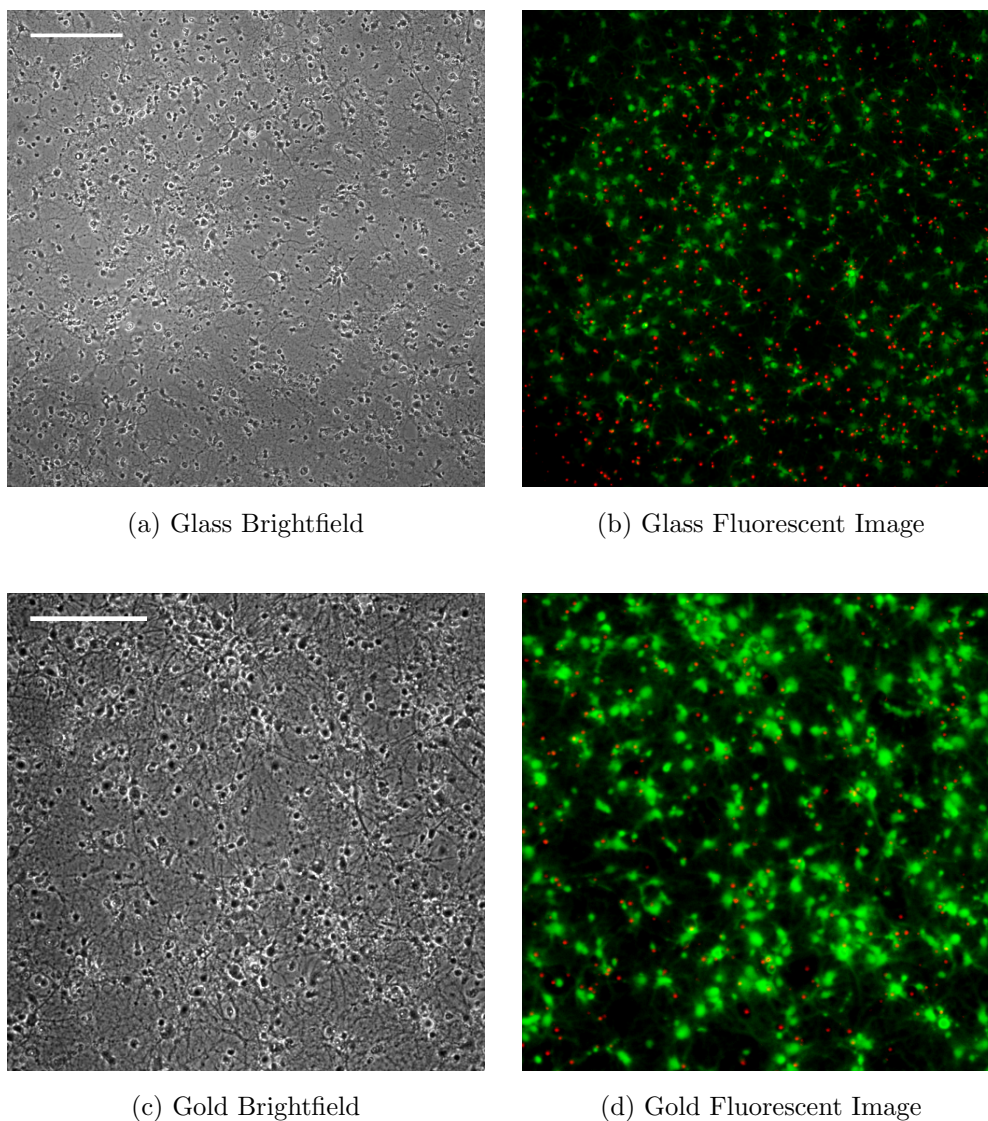


Figure 6.15: Brightfield and fluorescent images from the cell viability assay for PEI treated surfaces. The methods and imaging settings for the live and dead cells are the same as the AUT treated surfaces. The brightfield and fluorescent images on glass were taken using the Hamamatsu camera while the gold were with the QuantEM camera. The scale bar is $200\ \mu\text{m}$ long and is consistent across both the brightfield and fluorescent images. PEI is demonstrated to be suitable for culturing primary, hippocampal neurons on both glass and gold.

The number of live and dead cells were counted for a quarter of the field of view using the Nikon 10 \times objective ($NA = 0.25$) for three different samples and then assumed to be equal across the entire field of view. The cells on the PLL surfaces, Figure 6.16 came away from the surface within five days of plating so were not analysed. The ratio of live and dead between the two cell adhesion methods (AUT and PEI) on gold was calculated and are comparable, Figure 6.17.

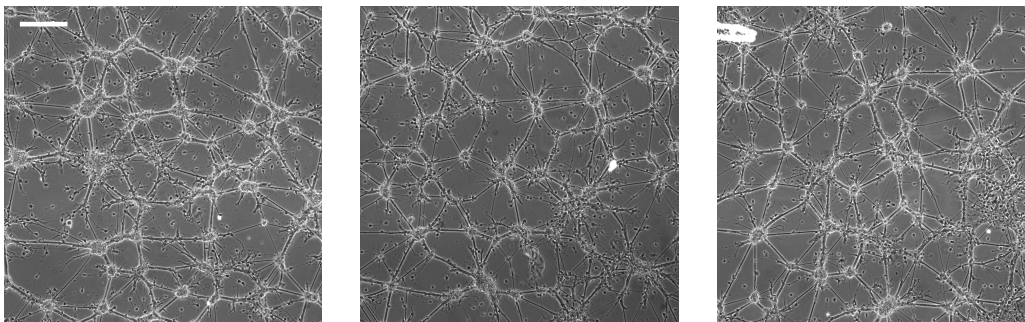


Figure 6.16: Brightfield images of the cells on the PLL surfaces 5 DIV. Scale bar is 200 μm long and is consistent across all images.

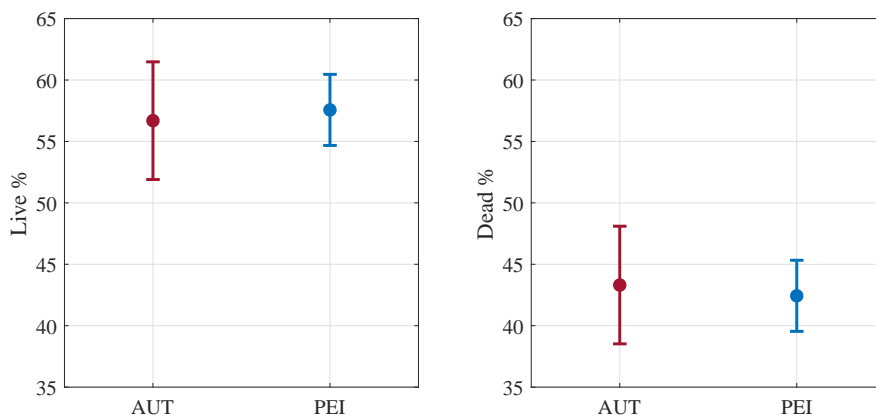


Figure 6.17: Live (left) and dead (right) cell viability assay summary on gold using AUT and PEI as the adhesion method ($n = 3$ for each). There is no statistically significant difference between the distributions for “AUT Live” ($\mu = 56.69$, $\sigma = 4.789$) and the “PEI Live” ($\mu = 57.57$, $\sigma = 2.894$); $t(4) = 0.2714$, $p = 0.7995$.

An unpaired t -test was performed on the two adhesion methods datasets for gold surfaces (parametric, two-tailed). The result shows that there was no statistically

significant difference between the distributions for “AUT Live” ($\mu = 56.69$, $\sigma = 4.789$) and the “PEI Live” ($\mu = 57.57$, $\sigma = 2.894$); $t(4) = 0.2714$, $p = 0.7995$. Similarly, for the distributions for “AUT Dead” ($\mu = 43.31$, $\sigma = 4.789$) and the “PEI Dead” ($\mu = 42.43$, $\sigma = 2.894$).

A summary of the two adhesion methods on glass was not possible because on the AUT-treated surfaces the neurons had fasciculated as expected, making it difficult to count the number of live/dead cells reliably. Therefore, PEI is a suitable alternative for AUT on samples with both glass and gold areas. This confirmed that PEI could be used for future cell platings. Primary hippocampal neurons were cultured on the microstructures and imaged at 14 DIV to confirm. Visual inspection of the neurons cultured on the microstructures showed there was no difference between the neurons on the structures and those on the unpatterned glass.

6.4.2 Effect of PEI Layer on SPR Signal

To ensure the PEI layer would not have an adverse effect on the SPR response a control experiment was performed on planar gold. The PEI was applied as described in Section 2.6.2. The SPR angular response was recorded and compared to that of planar gold from the same evaporation ($n = 3$).

The response angle, θ_{sp} for the PEI-treated gold coverslips was 43.02 ± 0.112 compared to the planar gold controls, 43.1 ± 0.0318 . The addition of the PEI layer does not significantly affect the SPR angle as determined by a unpaired t -test; $t(3) = 0.5755$, $p = 0.6053$. Similarly, the amplitude of the gradient maximum is not significantly different between the planar controls ($\mu = -8.268$, $\sigma = 0.1782$) and the PEI-treated coverslips ($\mu = -8.93$, $\sigma = 1.47$); $t(3) = 0.601$, $p = 0.5904$.

6.5 Detection of Neural Activity

In this section, primary, hippocampal neurons are cultured on the 10×10 microstructures, and whole-cell patch clamp electrophysiology and SPR is performed simultaneously, i.e., repeating the experiments from Section 5.2 on the microstructures. The 10×10 microstructures were selected because they were smaller than the average size of a cell, and the gradient maximum amplitude and sensitivity was not too dissimilar from that of planar gold. The 10×10 microstructures resulted in an

optimum trade-off between size and sensitivity to refractive index changes. The SPR intensity response is monitored throughout the experiments to detect any changes in light intensity and therefore, refractive index. The validation of these detected SPR responses was achieved using whole-cell patch clamp.

6.5.1 10×10 Microstructure

The gold microstructures were solvent cleaned, and a PEI monolayer was deposited as outlined in Section 2.6.2. After surface functionalisation, the cell culture was plated on the gold microstructures, following the methods for harvesting, plating, and feeding the cell culture in Section 2.7. On feeding days the cell cultures were imaged using brightfield microscopy with the Nikon Eclipse Ti ($10\times$, $NA = 0.25$), Figure 6.18a. After at least 14 DIV the cultures were electrically active and stable enough in their extracellular matrix to be prepared for the electrophysiology and SPR experiments.

The cell culture was mounted on a coverslip holder and immersed in ECS before placing on the SPM. The z -axis of the sample stage was adjusted, so the 640 nm LED and SLED were in focus with the BFP and coverslip, respectively. A viable neuron was located by adjusting the x - and y -axis and images were taken using transmission (590 nm/EPIX) and reflection microscopy (590 nm/Point Grey), Figures 6.18d and 6.18c, respectively. A scanning electron microscope image (SEM) was taken to show the cells on the microstructures 14 DIV. The cells were prepared by washing the coverslips $3\times$ with phosphate buffered saline, and fixed using ice cold methanol for 5 minutes.

The SPR angular response was taken using the SLED and stepper motor to scan across the range of angles. The reflected light intensity was detected using the EPIX camera, Figure 6.19. The figure shows that the regions where cell material is present has a higher θ_{sp} than that of just gold and ECS. The plasmon angle, θ_{sp} for the gold microstructures is $70.7 \pm 0.41^\circ$, and θ_{sp} for the cell is $71.1 \pm 0.14^\circ$. This is comparable to the respective plasmon angles from Section 5.2.1, where θ_{sp} for the gold was $70.3 \pm 0.189^\circ$, and for the cell was $71.5 \pm 0.153^\circ$.

The protocol and MATLAB code from Section 5.2 was used. The data from 400 triggers and above will be discussed in the following sections.

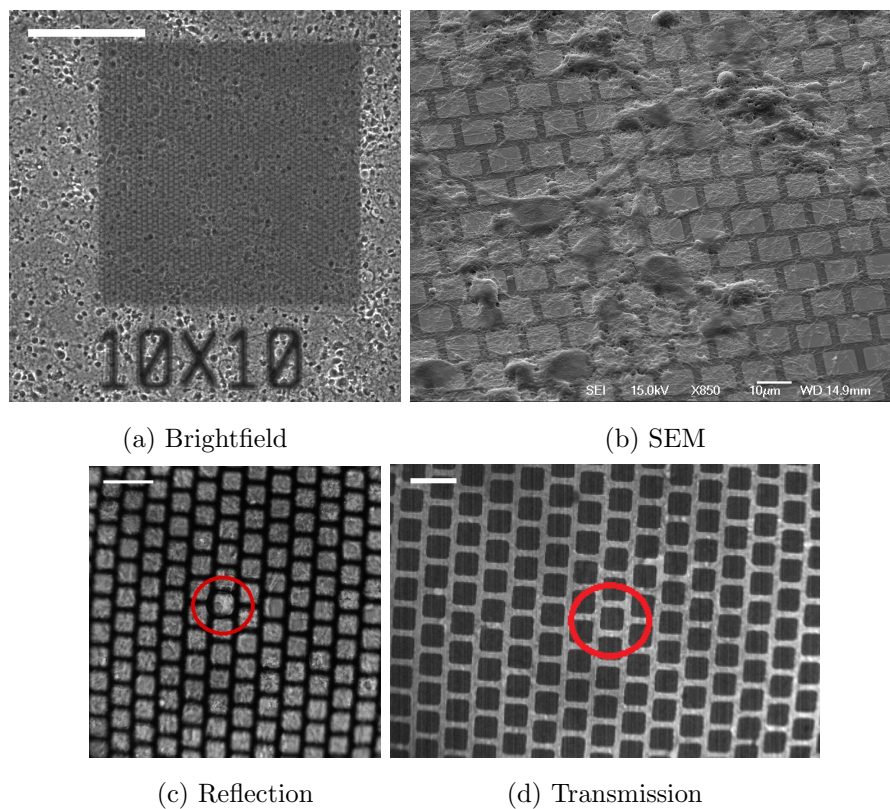


Figure 6.18: Brightfield (6.18a), SEM (6.18b), reflection (6.18c), and transmission (6.18d) images of the sample. Cells were cultured on microstructures and imaged 14 DIV. Brightfield images were taken using the Nikon inverted microscope at $10\times$ magnification ($NA = 0.25$) - the scale bar is $100\ \mu\text{m}$. The scale bar for the reflection and transmission images is $20\ \mu\text{m}$. The red circles highlight where the neuron of interest is. The SEM images were taken using fixed cells.

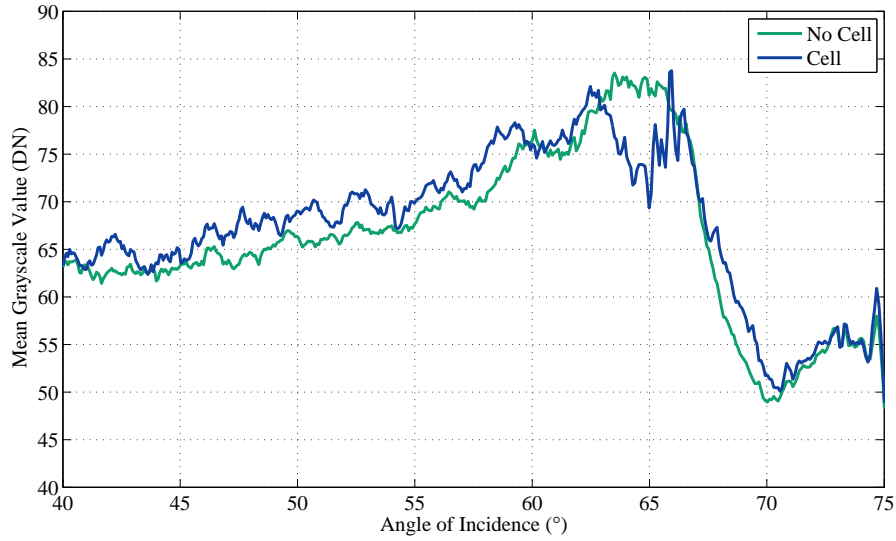


Figure 6.19: Representative angular response for a glass/gold microstructure/ECS/cell interface and a region where there was no cell. θ_{sp} for the gold microstructure is $70.7 \pm 0.41^\circ$, and θ_{sp} for the cell is $71.1 \pm 0.14^\circ$ ($n = 3$).

400 Action Potentials

400 action potentials were invoked in the neuron of interest, and the SPR response was monitored on the EPIX camera. As before, the electrophysiology voltage recordings were imported to MATLAB, the spikes were aligned, and an average spike waveform was produced, Figure 6.20.

The SPR images were imported and processed as before. The regions of interest were selected, and the control was subtracted from the cell area. The image stack (cell – control) was aligned by transforming the images to the frequency domain and aligning each image by the time offsets from the electrophysiology using an FFT. The aligned image stack was converted back to the time-domain, and the average was computed over the 400 triggers. A response profile was plotted from the average across all the pixels from the ROI resulting in a plot of the average intensity across all pixels in the ROI as a function of time, Figure 6.21. After averaging there is no visible increase in light intensity at $t = 0$. For every set of data, a control area of a gold structure without the neuron of interest was analysed.

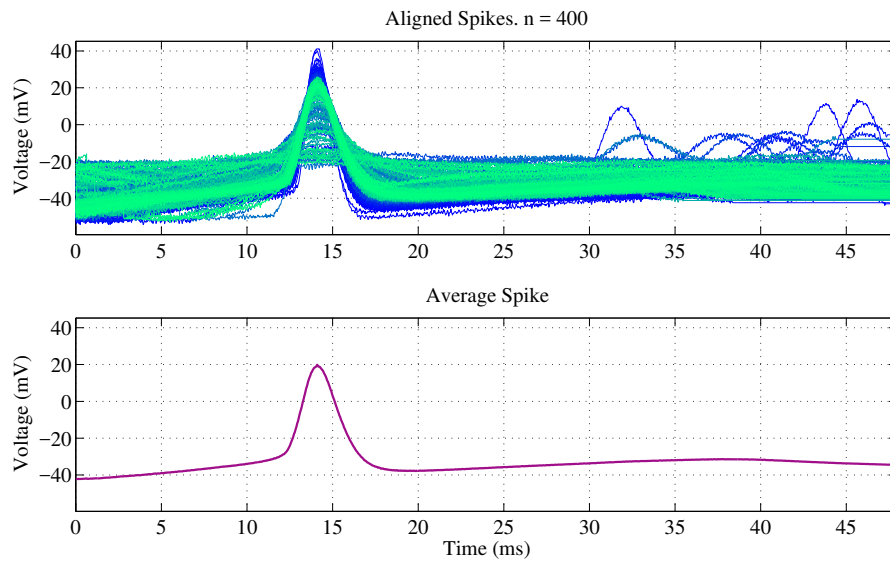


Figure 6.20: Processed electrophysiology voltage recordings from the microstructures ($n = 400$). The spikes were detected using a threshold condition. Multiple spikes in the same time epoch were ignored. The first spike is used as a reference and the subsequent action potentials are aligned to it to give the top plot. The initial spike time ($t_{AP} = 14.1$ msec) is stored as are the time differences (Δt). Bottom plot: The aligned APs are averaged to give the standard voltage waveform for further analysis.

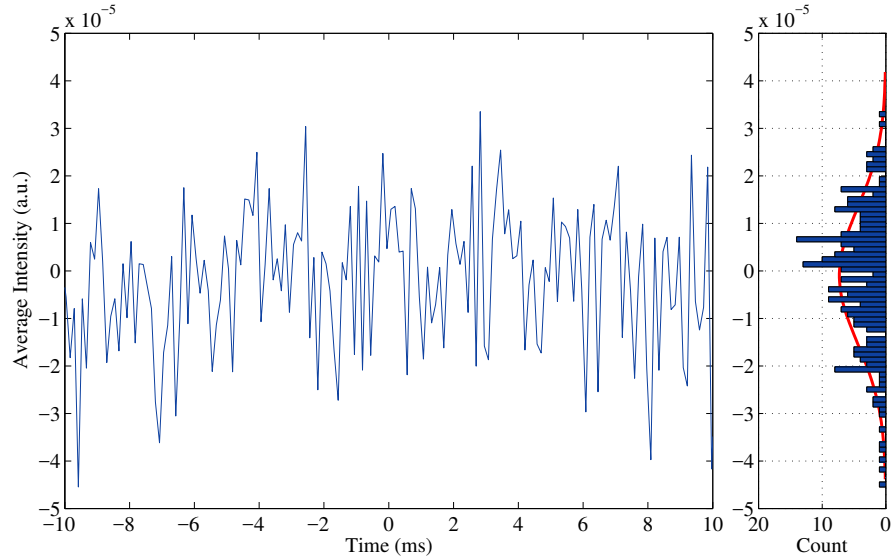


Figure 6.21: Time series plot of the average intensity as a function of time averaged across all pixels in the ROI. The histogram to the left is the distribution of the intensities (y -axis) and is compared to a Gaussian normal.

As described in Section 5.2.2, there are three different analysis methods for determining if an action potential was detected; cross-correlation, comparison of histograms, and spectral coherence. The cross-correlation between the intracellular voltage recording and the optical SPR response was calculated. There was a peak at $t = 0$ of 0.0116, which could potentially be attributed to a $3.54 \mu\text{V}$ AP using Figure 5.17. The control area is shown in the inset of Figure 6.22. The control area (Median = -0.00573) is significantly different from that of the cell area (Median = 0.01058) as determined by a Mann-Whitney U Test; $U = 138000$, $p = < 0.001$. This Mann-Whitney U test is similar to the t -test but does not require the assumption of normal distributions (Hettmansperger and McKean, 2010). The visible difference and statistical confirmation seems promising and maybe the SPR detected a change in light intensity at $t = 0$.

The D’Agostino & Pearson normality test was performed on the distributions of the “noise” ($\mu = -1.03 \times 10^{-7}$, $\sigma = 1.42 \times 10^{-5}$) and the SPR response ($\mu = -9.98 \times 10^{-7}$, $\sigma = 1.43 \times 10^{-5}$) from Figure 6.23. As expected, the white Gaussian noise does not deviate from a Gaussian normal. However, the SPR row average

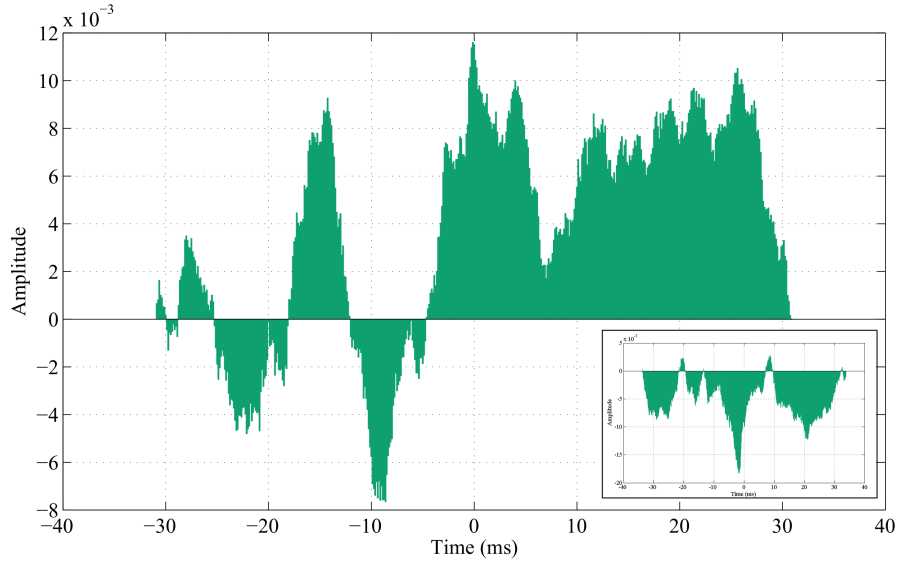


Figure 6.22: Cross-correlation results for 400 APs on the 10×10 microstructure. The peak at $t = 0$ is at 0.0116 and could be attributed to a $3.54 \mu\text{V}$ AP using Figure 5.17. The inset figure is the control area where the peak is at -0.0183 .

does ($p = 0.0387$), where the kurtosis is comparable to the noise. The skewness was -0.398 , which is evident in the figure, so the SPR row average for 400 APs on the 10×10 microstructure has an asymmetrical distribution with a long tail to the left, i.e., more points above zero. The presence of one or a few outliers might have caused the normality test to fail, so an outlier test was run. The Grubbs ($\alpha = 0.2$) method was used. The Z ratio (6.6) is calculated as the difference between the outlier and the mean (μ) divided by the standard deviation (σ) for all the values (Y) in the dataset. When Z is large, the value is far from the others, i.e., an outlier.

$$Z = \frac{|\mu - Y|}{\sigma} \quad (6.6)$$

The Grubb's test found zero outliers with a probability of mistakenly identifying an outlier of 2%. Considering the signal row average deviates from a Gaussian normal and no outliers could be identified, further statistical tests were performed. The standard deviations between the datasets were comparable and because the p -value from the D'Agostino & Pearson normality test was close to insignificant, an unpaired t -test was still performed, even though this assumes a Gaussian distribution. The

SPR row average and Gaussian noise are not significantly different from one another; $t(494) = 0.699$, $p = 0.485$.

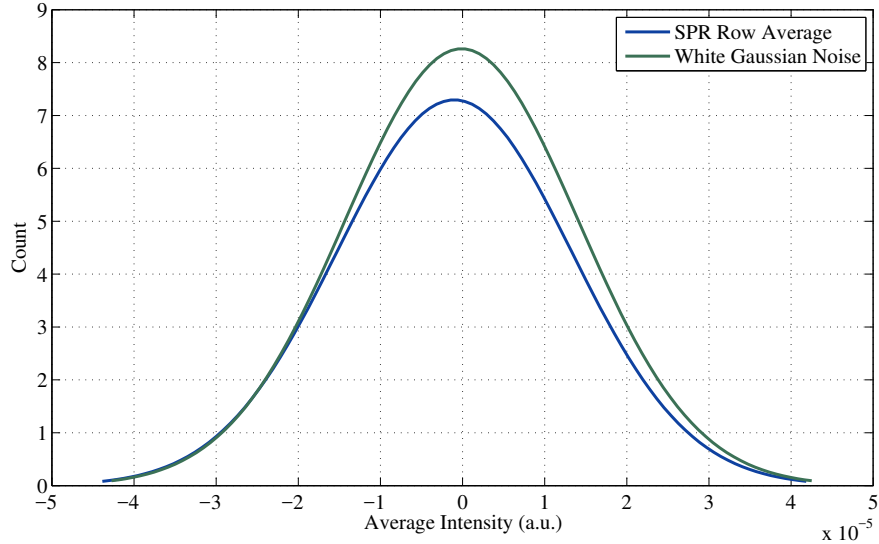


Figure 6.23: Comparison of the intensity (y -axis) values from the average across all pixels, Figure 6.21 and white Gaussian noise. The row average ($\mu = -1.03 \times 10^{-7}$, $\sigma = 9.023 \times 10^{-7}$) and Gaussian noise ($\mu = -1.03 \times 10^{-7}$, $\sigma = 9.023 \times 10^{-7}$) are not significantly different from one another as determined by a unpaired two-tailed t -test ($t(494) = 0.699$, $p = 0.485$).

Spectral coherence between the two signals was performed to identify any correlations in the frequency-domain, Figure 6.24. The pseudo-data from Section 5.2.2 showed that the “AP” and “noise + AP” have perfectly correlated components around 220 Hz with no phase lag. The resulting figure from 400 APs shows a 67% correlation between the voltage and optical recordings at 2.22 kHz with a corresponding phase difference of 77.02° . At the same point from the pseudo-data, Figure 5.18, the coherence estimate was around 0%, also with a phase difference of approximately 75%. The peak in the pseudo-data was at 220 Hz. At 220 Hz from the 400 APs data, there is a 39.8% correlation with 24.76° phase difference. It is probable that the optical signal was not correlated to the electrical and these peaks are just coincidence.

The cross-correlation and deviation from a Gaussian normal showed promising re-

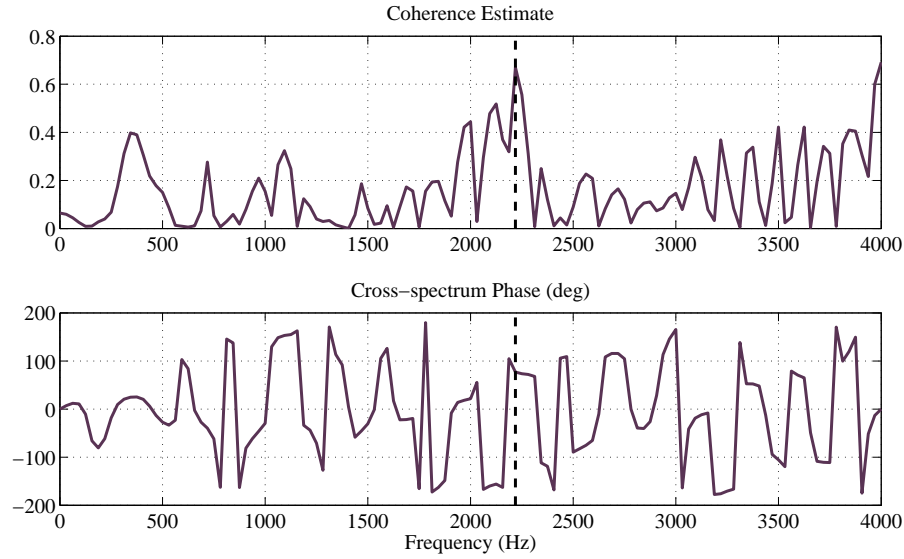


Figure 6.24: Spectral coherence estimate for the relation between the SPR response and electrically recorded membrane voltage for 400 AP repeats on the 10×10 microstructure.

sults. However, the insignificant t -test between the SPR recordings and noise distributions, and the inconclusive spectral coherence results were less so. The experiments were repeated in two more separate events with 400 triggers and 700 triggers. The triggering of 400 APs was repeated from another plating. As before, after averaging there was no noticeable increase in light intensity in the time series. The cross-correlation amplitude at $t = 0$ was 0.00828, which is closer to the cross-correlation amplitude for a true negative (0.005) than that from the previous experiment. The D’Agostino & Pearson normality test was performed on the distributions of the “noise” ($\mu = -1.38 \times 10^{-6}$, $\sigma = 2.25 \times 10^{-5}$) and the SPR response ($\mu = -4.96 \times 10^{-6}$, $\sigma = 2.32 \times 10^{-5}$). As expected, the white Gaussian noise does not deviate from a Gaussian normal nor does the SPR response, where the p -values are 0.068 and 0.191, respectively. Comparing the histograms for the SPR response and noise did not show that the distributions were statistically different from one another; $t(336) = 1.44$, $p = 0.152$. The coherence estimate showed no frequencies where the signals were correlated by more than 50%. Therefore, it can be concluded with a high degree of certainty that for this run of 400 repeats there was no action

potential detected.

Due to the inconclusive results from the 400 APs, more APs were triggered on a different 10×10 microstructure in case the SNR was a fraction too small. Increasing the number of repeats by 300 to 700 would increase the SNR by around 17. After averaging across 700 APs, there was no obvious increase in light intensity in the time series. The cross-correlation amplitude at $t = 0$ was -0.0242 . The D'Agostino & Pearson normality test was performed on the distributions of the "noise" ($\mu = 9.84 \times 10^{-8}$, $\sigma = 1.54 \times 10^{-5}$) and the SPR response ($\mu = 3.1 \times 10^{-6}$, $\sigma = 1.38 \times 10^{-5}$). The white Gaussian noise does not deviate from a Gaussian normal nor does the SPR response, where the p -values are 0.167 and 0.161, respectively. An unpaired t -test was performed. The SPR row average and Gaussian noise are not significantly different from one another; $t(362) = 1.96$, $p = 0.0504$ but are very close to being significant. The coherence estimate showed no frequencies where the signals were correlated by more than 50%. Again, it can be concluded with a high degree of certainty that for this run of 700 repeats there was no action potential detected.

Summary

In total, 2,160 APs were triggered over ten separate events. Figure 6.25 summaries the cross-correlation amplitude for the different number of repeats up to 700 on the microstructures. A one-way ANOVA was performed between the number of triggers. There was no statistically significant difference between group means as determined by one-way ANOVA; $F(4, 5) = 0.662$, $p = 0.645$. Also, the average across repeats for the number of triggers was used to perform a single-sample t -test. The single-sample t -test was performed across all the amplitudes to determine if a statistically significant difference existed between the different amount of triggers to that of a true negative (0.005) as determined by the pseudo-data. There was no statistically significant difference between the amount of repeats and the cross-correlation amplitude when no AP was stimulated or detected ($\mu = 0.0592$, $\sigma = 0.0963$); $t(9) = 1.78$, $p = 0.109$.

The experiment that was described in the previous section for 400 APs was an outlier, but it is impossible to tell whether it was a processing/analysis error or whether the SPR response did detect a change in light intensity during the action potential. The number of independent variables that can affect the possibility of

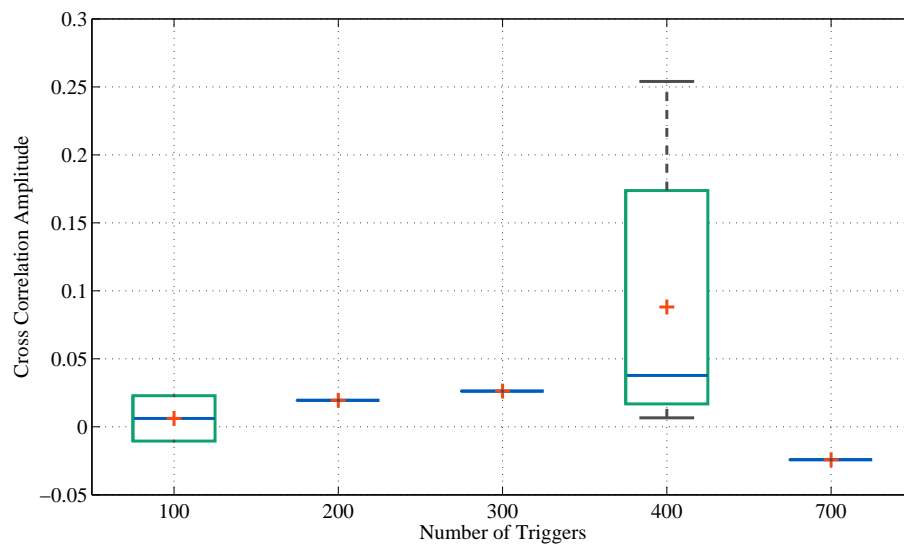


Figure 6.25: Summary of cross correlation amplitudes for the different number of repeats 10×10 microstructure. There were no statistically significant difference between group means as determined by one-way ANOVA; $F(4, 5) = 0.662$, $p = 0.645$.

detecting electrical activity are numerous. For example, the distance between the neuron and gold surface is rarely reproducible, the size of the cell will also affect the refractive index change (or the birefringence), and finally, if there are any defects on the gold structure the sensitivity of the sensor will be reduced.

The standard deviation of the noise was taken for each experiment for one AP and then after averaging to compare the improvement in noise, Table 6.7. The mean of the standard deviations and errorbars (σ) are plotted with theory in Figure 6.26. The experimental noise levels followed theory very closely and after averaging the noise was greatly reduced. The greatest improvement in noise occurs after 10 to 100 averages. The reduction in noise is minimal after 400/700 repeats.

Table 6.7: Estimated noise floor from the microstructure repeats. The estimated noise floor was calculated from the standard deviation of the row average. The standard deviation is from the repeat of the experiment (n).

Repeats	Est. Noise Floor	Standard Deviation	n
1	4.00×10^{-4}	$\pm 9.53 \times 10^{-5}$	10
10	1.01×10^{-4}	$\pm 1.43 \times 10^{-6}$	5
100	3.96×10^{-5}		1
200	4.98×10^{-5}		1
300	1.71×10^{-5}		1
400	2.10×10^{-5}	5.81×10^{-6}	2
700	1.37×10^{-5}		1

6.6 Chapter Conclusions

To successfully design a sensing platform for cells it was first necessary to find the size and morphology of the cells. Brightfield images of cells 2 DIV were taken, and the average diameter of a cell was found to be between 10.27 and 16.35 μm , agreeing with values reported in literature (Meitzen et al., 2011).

The geometries chosen to be investigated were 6×6 , 6×10 , 6×16 , 10×10 , and $10 \times 16 \mu\text{m}$, each with 2 μm spacing between each strip. The area of each pattern was restricted to 0.5 mm. The photolithography process was optimised to minimise

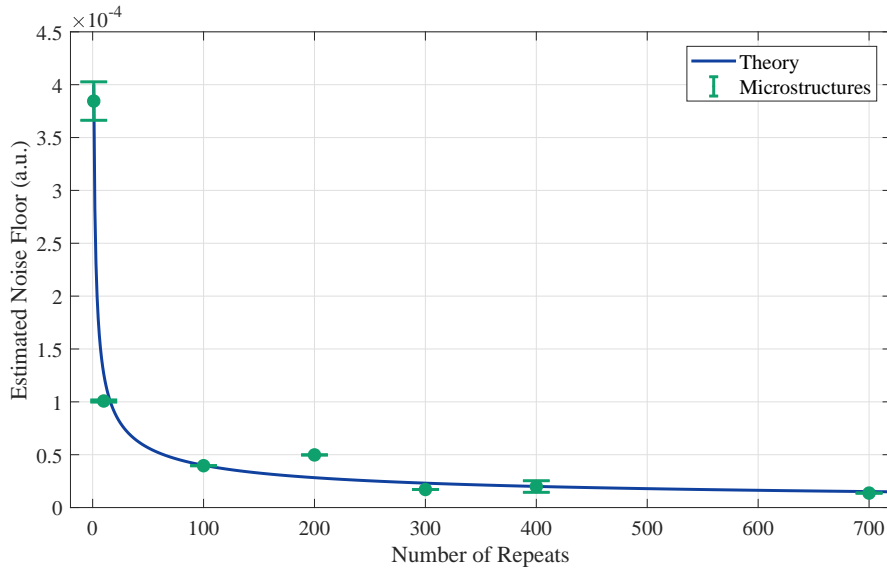


Figure 6.26: Estimated noise floor from the microstructure repeats compared with theory ($1 / \sqrt{N}$). The standard deviation of the row average was exported for each repeat on the 10×10 microstructure and normalised.

the variability in the success rate in response to noise factors while maximising variability in response to the controlled steps.

Gold microstructures were fabricated using photolithography, and their properties studied. Brightfield microscopy was used to investigate their morphology and profilometry to measure the thickness of the gold layer. The angular response for all the microstructures showed a decrease in reflected light intensity on the gold structures past the critical angle demonstrating light was able to couple with surface plasmons. The SPR dip was observed for all the microstructures with the SPR dip becoming less sensitive with respect to the gradient amplitude, and broader as the length decreased compared to the SPR dip of the planar gold reference. The SPR angle does not change significantly depending on the gold structure length.

The amplitude of gradient ($\Delta R / \Delta \theta$) decreases with decreasing strip length. This is expected due to the spatial constriction of the SPP, where the propagation length is $\approx 18.27 \mu\text{m}$. Small defects in the microstructures may have also contributed to the poor SPR signal. The change in the maximum gradient amplitude significantly

changed when the structure size was decreased, which can also be attributed to the spatial constriction of the SPP.

The trade-off between sensitivity to refractive index changes and localisation was then investigated by determining the sensitivity of the microstructures. The sensitivity of the gold microstructures was characterised by using different salt solutions to change the bulk refractive index of the dielectric in an intensity interrogation scheme. The refractive index unit (RIU) was calculated as the ratio of the change in refractive index (Δn) and change in normalised reflected light intensity ($\Delta \tilde{R}$) as $\Delta \tilde{R}/\Delta n = 28.5$ RIU for the 10×16 microstructure, 26.4 RIU for the 10×10 , and 19.2 RIU for the 6×6 μm microstructure. As expected, the sensitivity is less than that of planar gold by about $2 - 3\times$, which agrees with the gradient measurements, so where the gradient was smaller, the sensitivity was smaller. The light intensity change during an AP due to a refractive index change of 1.5×10^{-3} was theoretically determined to be $\Delta R = \pm 3.1 \times 10^{-3}$ at the gradient maximum and $\Delta R/\Delta n$ of 2.067. This theoretical $\Delta R/\Delta n$ is about on average 10% less than what we can detect. So, detecting the refractive index change during an AP should physically be achievable. These sensitivity experiments were changing the bulk refractive index, and only the cell-membrane localised refractive index changes of the neuron engulfing the gold structure are of interest. The sensitivities for the 10×16 gold microstructure and 10×10 gold microstructure are comparable, so considering both the plasmonic response and Nyquist criteria, the 10×10 μm sensor was selected as the optimum structure size for neural activity detection.

The development of the microstructures changed the composition and morphology of the sensors from that of planar gold. An alternative to the previously used surface functionalisation method was required. A live/dead cell viability assay was performed on neurons cultured on AUT, PLL, and PEI treated surfaces to ensure a healthy, confluent cell culture on the sensors. PEI was determined to be a suitable alternative for AUT on samples with both glass and gold areas. To ensure the PEI layer would not have a negative effect on the SPR response a control experiment was performed and the addition of the PEI layer was found not to affect the SPR response significantly.

Primary rat hippocampal neurons were plated on the planar gold surfaces and elec-

trophysiology was used to stimulate the cells while imaging the optical response. The cross-correlation and deviation from a Gaussian normal for 400 repeats on the 10×10 microstructure showed promising results. The cross-correlation peak at $t = 0$ was 0.0116, which could potentially be attributed to a $3.54 \mu\text{V}$ AP. However, the t -test between the SPR recordings and noise distributions were statistically insignificant, and the spectral coherence results were inconclusive. The latter had one peak at 67% around 2.2 kHz with a 77° phase difference. This coherence estimate was compared to that from the pseudo-data. The coherence estimate for the pseudo-data at 2.2 kHz was around 0%, also with a phase difference of around 75%. The peak in the pseudo-data was at 220 Hz and at 220 Hz from the 400 APs data, there is a 39.8% correlation with 24.76° phase difference. It is probable that the optical signal was not correlated to the electrical and these peaks are just coincidence.

More APs were triggered because if the SNR was just a fraction too low, then more averages could reveal the signal. Another 300 repeats would increase the SNR by about 17, so, 700 APs, were triggered and analysed. After averaging across 700 APs the time series showed there was no obvious increase in light intensity. The white Gaussian noise does not deviate from a Gaussian normal nor does the SPR response and are not significantly different from one another. The coherence estimate showed no frequencies where the signals were correlated by more than 50%.

It can be concluded to a high degree of certainty that no action potentials were detected by the $10 \times 10 \mu\text{m}$ gold microstructure SPR sensors up to 700 repeats and down to a noise floor of about 10^{-5} . However, there is a difference between the responses from planar gold surfaces and those from the 10×10 microstructures.

DISCUSSIONS AND CONCLUSIONS

The work in this thesis set out to develop a sensor that could detect neural activity with single-cell resolution from a large network for an extended period of time. The technologies that currently exist, however, are limited in this aim, as discussed in Section 1.3. It was concluded that the technology to be developed needed to be non-invasive to the cell and label-free to allow long-term recording. 2D *in vitro* cultures were used to ensure a small gap distance between the sensor and culture to encourage single-cell selectivity. To achieve this goal, the project was divided into four sections corresponding to the experimental chapters.

Modelling of the Light Intensity Change During an AP

In Chapter 3 the theory of SPR sensors was introduced, and the model of the sensor and cell system was formulated. The assumptions and determination of parameters for each layer were outlined resulting in a five-layer model consisting of glass/gold/extracellular solution/cell membrane/cytosol. The transfer matrix method was used to analyse the wave propagation through each layer in the model, giving the standard SPR response. The effect of the cell/substrate distance was investigated so the gap distance was increased, and the transfer matrix was solved

to give the angular response. As the gap distance increases the angle of resonance decreases exponentially. This is because the gold surface senses the bulk refractive index, meaning the extracellular solution, membrane, and cytosol layers combine. Increasing the gap distance and moving the higher refractive index membrane away from the gold surface decreases the bulk refractive index and consequently decreases the resonant angle. The response will, therefore, be stronger the closer the cell is to the surface. A refractive index change of $\Delta n = 1.5 \times 10^{-3}$ was calculated by considering the rearrangement of dipoles during electrical activity. This Δn value was used for the following calculations. The gap distance between the cell and gold surface was fixed at 50 nm, and the refractive index of the membrane was changed by $\pm\Delta n$. In an intensity modulation SPR scheme, the detector is fixed at the 50% point, or the angle where the reflection gradient is at a maximum and the change in reflected light intensity is detected. So changing by $\pm\Delta n$ at the 50% point of the SPR dip resulted in the theoretical reflectance changing by $\Delta R = \pm 3.1 \times 10^{-3}$.

The work of Clay (2017) was developed by determining the effect of ion flux during an AP on the plasma frequency of the gold layer. The effect on the plasma frequency was $\Delta\omega_p \approx 2 \times 10^9$ rad/s. With this, the analytical model for the dielectric function of gold (3.10) and the previously computed theoretical SPR response for a three-layer model were solved. It was found that just considering the ion flux the SPR angle remains around 44.89° , but the amplitude of the gradient maximum changes by $\Delta R/\Delta n = -1.203 \times 10^{-6}$. This $\Delta R/\Delta n$ is three orders of magnitude smaller than that calculated considering the refractive index change. However, as long as the cell membrane is in the evanescent field, the larger refractive index change will be detected. Also, considering the evanescent field the movement of ions will occur one nanometer closer to the surface (Alberts, 2017) it is likely they will contribute to the light intensity change. Taking this into account a refractive index change of $\Delta n = 1.5 \times 10^{-3}$ needs to be detected. This refractive index change results in a reflection change of $\Delta R = \pm 3.1 \times 10^{-3}$. In the following chapters, it was confirmed that this reflection change could be detected by measuring the noise floor of the system and the gold and microstructure's sensitivities were determined.

Characterising the System Noise

Chapter 4 characterised and calibrated the custom-built SPM before experiments were performed. Firstly, to determine the noise floor of the system and therefore, the minimum detectable signal to ensure the detection of the change in refractive index determined in Chapter 3 was achievable. The effect of the SLED and LED on the temperature of the coverslip was investigated, and finally, the BFP was calibrated to relate radial position to the angle of incidence for further angular SPR responses.

The noise floor of the system was determined, to evaluate whether the change in refractive index during an action potential could be detected, or what size signal (ΔR) the action potential would have to produce for it to be detected. The noise from both the light source and detector were experimentally measured. The power of the SLED was measured as 1.1 mW, which results in 3.77×10^{15} photons per second. The power at the detector was measured as $8.5 \mu\text{W}$, and thus the optical efficiency is 7.73×10^{-3} . The relatively large loss can be explained by the lossy optical components in the optical pathway of the custom-built SPM. The loss is necessary because of the design and the lossiest components are the beam splitters and the objective lens. The light travels through both of them twice.

Three main sources of noise affect the performance of the detector, these are the signal shot noise, fixed pattern noise, and read noise. The signal shot noise is related to the interaction of photons with the detector, and the read noise defines the noise arising from the electronic components associated with converting the incident photons to electrons. To find the signal shot noise, the power at the detector through a pinhole was measured, and the number of incident photons per pixel was estimated. The shot noise is what limits the sensitivity of the system and at 8 kHz for one pixel is 171 photons.

The number of electrons per pixel can be calculated by multiplying the number of incident photons by the quantum efficiency. The quantum efficiency defines how efficient the sensor is at converting incident photons to electrons, it is quoted in the specifications as 45% and this value was experimentally confirmed. The quantum efficiency was measured by comparing the number of electrons as a function of the exposure time to the half-full well capacity of the pixel. The sensor was 50% saturated at an exposure time of 0.18 ms, resulting in the sensor having a quantum

efficiency of 41.4%. Taking the quantum efficiency as 41.4%, the number of electrons per pixel at 8 kHz will be $12.06 \times 10^3 \pm 110$ electrons/pixel. Therefore, the *signal shot noise* at 8 kHz (σ_s) is 110 electrons/pixel.

The illumination was previously found to not be uniform so the fixed pattern noise of the detector was quantified. The standard deviation of a differential image was calculated; one image that is around 50% saturated had a corresponding dark image subtracted from it. The *FPN* was $3540e^-$ per image, which could be improved to $212e^-$ per image when a second image was subtracted from the first to remove noise common in both.

The *read noise* was determined from the standard deviation from the difference of two dark images as $8.36e^-$. The dark noise (σ_d) for the detector was calculated from the standard deviation of a dark image as 0.0354 DN, corresponding to about $5e^-$. Considering the shot noise is 110 electrons/sample/pixel, the dark noise, $5e^-$, and read noise, $8.36e^-$, the total noise (σ) is $110e^-$, and is shot noise limited. The minimum detectable signal (ΔR) was calculated as one part in 109 with an SNR of one for one pixel at 8 kHz.

In Chapter 3 the refractive index change of a cell membrane during an action potential was estimated as $\Delta n = 1.5 \times 10^{-3}$. It was necessary to estimate the minimum detectable refractive index of the sensor considering the noise floor. Assuming a 30 nm gap distance between the cell and the sensor the minimum detectable Δn of the SPR system is 3.29×10^{-3} or 1:3024 per pixel at 8 kHz. As the cell got closer to the surface, this minimum detectable signal increased and vice versa. Currently, on a pixel per pixel basis the SPR system is not able to detect the refractive index change of $\Delta n = 1.5 \times 10^{-3}$. However, the cell will be covering a number of pixels so the response can be averaged across the entire region of interest to increase the SNR and improve the minimum detectable signal.

Averaging across the area and number of pixels, the minimum detectable ΔR rises to one part in 2298. Δn_{min} increases to 1.56×10^{-4} or one part in 6400 per ROI assuming a gap distance of 30 nm between the cell and the surface. This minimum detectable Δn rises to 1.16×10^{-4} or 1:8580 per ROI if the cell is directly on the gold surface. The minimum detectable Δn after averaging across the entire cell ROI is 9 – 12 \times greater than what occurs during an AP. The sensor is capable of

detecting the refractive index change of $\Delta n = 1.5 \times 10^{-3}$ up to a gap distance of 150 nm just considering the noise floor. However, the actual sensitivity of the sensors to refractive index changes in an intensity interrogation scheme was determined in Section 5.1.2 for planar gold and in Section 6.3.3 for the microstructures .

The noise floor of the system and estimated minimum detectable signals have determined that the SPM should be able to detect the refractive index change during an AP. However, the gap distance is not fixed and because the signal will be small the affect of averaging across a number of repeats was investigated to improve the SNR further. The minimum detectable ΔR and Δn increase with the \sqrt{N} , where N is the number of repeats.

As a control, to ensure that long-term recording could be performed the temperature of the coverslip was monitored over 20 mins during exposure to the SLED or 590 nm LED. It was confirmed that the actual change in temperature was much lower than what was calculated theoretically. Therefore, the LED or SLED does not have a significant impact on the temperature of the coverslip and long-term experiments could be performed.

The various techniques for exciting surface plasmons were discussed in Section 3.1.1. The Kretschmann ATR, Otto, and high NA objective lens configurations were introduced along with their advantages and disadvantages. Using a prism based configuration such as the Kretschmann ATR or Otto introduces spatial distortions, whereas using a high NA objective lens to excite surface plasmons overcomes the distortions by keeping the object plane parallel to the image plane (Huang et al., 2007). However, using a high NA objective lens results in the relationship between position of the focused SLED on the BFP and the angle of incidence on the sample plane not increasing linearly but instead by $\sin \theta$. The position of the SLED on the BFP and resulting angle of incidence was calibrated by using different solvents of different refractive indices on the glass to derive an expression to relate distance from the origin on the BFP to angle of incidence. This equation was used to convert the distance to an angle of incidence for the angular SPR responses.

Detecting Electrical Activity with Planar Gold SPR Sensors

Chapter 5 introduced a planar gold sample and characterised the SPR response and sensitivity for the custom-built SPM developed. Planar gold samples were prepared to three different thicknesses, 30, 50, and 70 nm to demonstrate the effect of the metal thickness on the angular SPR response. The resonance angles, θ_{sp} do not differ significantly from theory, showing that the sensitivity of SPR sensors are highly dependent on the gold film thickness. The reflectance of the thinner gold film was shown to recover slowly after the plasmon angle, whereas the thicker the gold layer the difference between the minimum and maximum reflectance became smaller, and therefore less sensitive. The gradients of the SPR responses for each of the theoretical and experimental planar samples was calculated. The angular response for a gold thickness of 50 nm was the most sensitive regarding sharpness, recovery of the reflectance near θ_{sp} , and has the greatest gradient. Confirming a 50 nm gold layer is optimum at 680 nm and was, therefore, used for the rest of the experimental work.

Next, the sensitivity of the gold planar surfaces was characterised. It was important to ensure that the gold surfaces were capable of detecting the theoretical light intensity change of $\Delta R = \pm 3.1 \times 10^{-3}$ as calculated in Chapter 3, especially knowing that the noise floor was less than what we needed to detect from Chapter 4. The sensitivity of the gold surfaces was measured by changing the bulk refractive index on the surface of the gold using different salt solutions. The refractive index unit was calculated as the ratio of the change in refractive index and change in normalised reflected light intensity and the result was less than that in literature for an intensity modulation SPR scheme (Sepúlveda et al., 2006; Campbell and Kim, 2007). The level of detection in these sensitivity experiments is limited by the short exposure time (0.124 ms). However, the power of the noise is proportional to the bandwidth. So for the small bandwidth used for these measurements (125 Hz) the total noise power will be reduced and the SNR increased.

Finally, primary rat hippocampal neurons were plated on the planar gold surfaces and electrophysiology was used to stimulate the cells while imaging the optical SPR intensity response. Up to this point in the thesis, the experiments and theory have determined that the detection of the estimated refractive index change is practically

possible by experimentally determining what the SPM and planar gold sensors can detect in terms of noise and sensitivity.

A protocol to monitor the SPR response while simultaneously stimulating the target neuron was developed. No action potential was detected from just one triggering event. The electrical and optical recordings were compared visually, and the light intensity distribution of the optical recording was compared to that of white Gaussian noise. The noise level should have been low enough but it is possible that the neuron had a larger gap distance thus reducing the SNR. Methods to minimise the noise further in post-processing were explored including signal averaging and subtracting a control area from the cell ROI. Pseudo-data was created to test the MATLAB code to ensure a positive result after signal averaging. The improvements from signal averaging closely following theory of $1/\sqrt{N}$, where N is the number of triggers. Similarly, subtracting a control area from the cell ROI was successful in removing any electrical or mechanical noise that was present, where the standard deviation on average improved by a factor of two. Several statistical tests were explored as a way of detecting signals hidden in noise including the comparison of the signal distribution to that of white Gaussian noise, cross-correlation, and spectral coherence. The last two measure correlation between the electrical and optical signals in the time and frequency domain, respectively. The pseudo-data was used to get standard positive result for the statistical analyses.

It was concluded that no action potentials were detected on planar gold SPR sensors up to 1000 repeats and down to a noise floor of 7.57×10^{-6} . Note, the noise level is three orders of magnitude smaller than the theoretical light intensity change expected, $\pm 3.1 \times 10^{-3}$. The hypothesis for the planar surfaces not successfully detecting AP activity was that a large area of gold could average the SPR response. A method of decreasing the sensor size and localising the SPR signal was investigated.

Detecting Electrical Activity on Gold Microstructure Sensors

Gold microstructures were fabricated using photolithography, and their properties studied. Bright-field microscopy was used to investigate their morphology, and profilometry to measure the thickness of the gold layer. The photolithography protocol was optimised to increase reproducibility, and minimise variability in response to noise factors.

The angular response for all five of the microstructures examined (10×16 , 10×10 , 6×16 , 6×10 , and $6 \times 6 \mu\text{m}$) showed a decrease in reflected light intensity on the gold structures past the critical angle, demonstrating light was able to couple with surface plasmons. The SPR dip was observed for all the microstructures with the SPR dip becoming less sensitive with respect to the gradient, and broader as the structure length decreases compared to the SPR dip of the planar gold reference. The SPR angle did not change significantly depending on the gold structure length. The gradients of the SPR responses for each of the microstructures and respective planar controls were calculated in the same way as planar gold. As expected, the gradient decreased with decreasing strip length due to the spatial constriction of the SPP (propagation length $\approx 18.27 \mu\text{m}$). The poor SPR signal could also be attributed to defects in the microstructures. An analysis of variance showed that the effect of decreasing structure size on the gradient maximum was significant.

The trade-off between sensitivity to refractive index changes and localisation was then investigated by determining the sensitivity of the microstructures. The sensitivity of the largest gold microstructure was smaller than that of planar gold by approximately two orders of magnitude. This agrees with the gradient measurements from the angular SPR responses, where the amplitude of the gradient maximum was smaller, the sensitivity was smaller. It was realised that the sensitivity of the two largest microstructures, 10×16 and $10 \times 10 \mu\text{m}$ were comparable and had $\Delta R/\Delta n$ sensitivities that were capable of detecting the theoretically determined change in light intensity from an action potential. However, the sensitivity experiments only consider the change in refractive index of the bulk medium, it is anticipated that the sensitivity to refractive index changes in a small area engulfing the gold structure might still be amplified. So, considering both the plasmonic response and Nyquist criteria the $10 \times 10 \mu\text{m}$ microstructure was selected as the optimum structure size for neural activity detection.

The characterisation steps showed that the photolithography produced microstructures exhibited plasmonic properties that are comparable with planar gold and could be used to detect individual action potentials in neurons. However, the microstructures developed were predominantly glass with at most one-third of the area consisting of gold. AUT had been used for the culture of the primary hippocampal neurons on planar gold surfaces but is unable to bind to glass, so a new surface treatment was

required. Cells were cultured on both glass and gold using three different surface treatments, AUT, PEI, and PLL and a live/dead cell viability assay was performed to ensure a healthy, confluent cell culture. The cells on the PLL surfaces came away from the surface within five days of plating and therefore, not analysed. The ratio of live and dead cells between AUT and PEI on gold were calculated and were comparable. The cells cultured with AUT on glass fasciculated and came away from the surface, as expected. PEI was chosen as the cell adhesion method going forward and has been shown in literature to provide a stronger attachment between the cell and the surface (Wiertz, 2010; Sun et al., 2012). The effect of the SPR response before and after the addition of the PEI layer was investigated. The PEI was found not to affect the SPR response significantly.

Primary rat hippocampal neurons were plated on the planar gold surfaces and electrophysiology was used to stimulate the cells while imaging the optical response with an identical protocol to that from the planar gold experiments. Analysis and statistics were performed. 400 triggered events on the 10×10 microstructure showed promising results. The cross-correlation peak for the 400 repeats at $t = 0$ was 0.0116, which could have potentially be attributed to a $3.54 \mu\text{V}$ AP. The response from the optical SPR recordings also deviated from a Gaussian normal with no apparent outliers. However, the t -test between the SPR recordings and noise distributions was insignificant, and the spectral coherence results were inconclusive.

To be sure, 700 APs were triggered and analysed on a different 10×10 microstructure from a separate plating. If the SNR was just a fraction too low then another 300 repeats would increase the SNR by about 17. After averaging across 700 APs, the time series showed there was no obvious increase in light intensity around $t = 0$. The SPR response did not deviate from a Gaussian normal and the SPR response and white Gaussian noise were not significantly different from one another. Additionally, the coherence estimate showed no frequencies where the signals were correlated by more than 50%.

Therefore, It can be concluded to a high degree of certainty that no action potentials were detected by the 10×10 gold microstructure SPR sensors up to 700 repeats and down to a noise floor of about 10^{-5} .

7.1 Conclusions

Unfortunately, it can be concluded to a high degree of certainty that the planar gold surfaces detected no action potentials up to 1000 repeats and the 10×10 gold microstructure SPR sensors up to 700 repeats and down to a noise floor of around 10^{-6} . However, there is a difference between the responses from planar gold surfaces and those from the 10×10 microstructures.

Figure 7.1 compares the cross correlation amplitudes of both the planar gold and microstructures across all the repeats. An unpaired t -test determined there was a no significance difference between the distributions for cross-correlation amplitudes for the planar gold ($\mu = 0.00258$, $\sigma = 0.0344$) and the microstructures ($\mu = 0.0542$, $\sigma = 0.0963$) across all repeats; $t(21) = 1.972, p = 0.062$. The outlier on the microstructure boxplot is due to the 400 repeat experiment previously discussed.

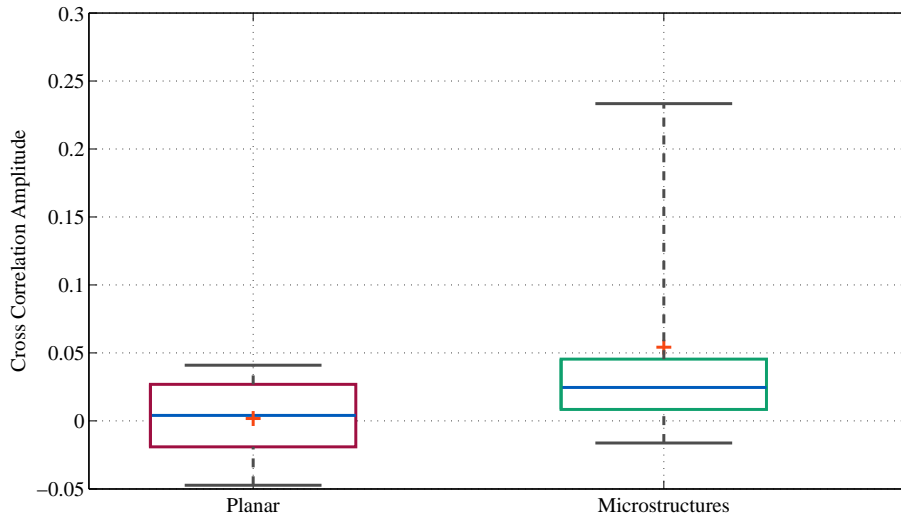


Figure 7.1: The cross correlation amplitudes of both the planar gold ($\mu = 0.00258$, $\sigma = 0.0344$) and microstructures ($\mu = 0.0542$, $\sigma = 0.0963$) across all the repeats. An unpaired t -test determined there was a no significance difference between the distributions for cross-correlation amplitudes for the planar gold and the microstructures across all repeats; $t(21) = 1.972, p = 0.062$.

The reduction in noise for both the planar surfaces and microstructures closely

followed theory. However, this technique is not suitable in its current form for the goal of this PhD thesis. This thesis aimed to develop a sensor with single-cell, single-event resolution over a large network for long-term recording. To understand brain function, it is necessary for the sensor to detect every action potential from every neuron in a population to observe correlations in space and time between stimulus and response. The need to average over such a large number of repeats stops this imaging technique having single-event resolution, resulting in a poor temporal resolution. It is unfortunate that this was not possible. This work could lead to further interesting research and investigation in order to enhance the capabilities of the system, which does have a lot of potential.

7.2 Potential Future Work

Although the overall goal of this PhD work attempting to detect the refractive index change of the cell membrane during electrical activity was unsuccessful, some important discoveries and improvements can be made to enhance the experimental process and sensitivity of the sensors.

A first step would be to streamline and minimise error in the experimental process. The entire process took approximately two months from the start of fabrication to the cell culture being mature enough for experimentation. For example, improving the attachment between the neuronal culture and the gold structure. One of the problems throughout these experiments was finding a neuron that was engulfing a gold microstructure. It was important that the neuron was over a gold structure to ensure a stronger signal. However, a lot of the time the cells were only 50% over a structure. A solution could be to confine the cell growth to the gold microstructure. A poly(ethylene glycol) PEG could be used to create a ‘non-fouling’ surface on the glass (Lan et al., 2005).

A quicker, easier, more reproducible way of fabricating the structures would help to streamline the experimental process. The photolithography fabrication protocol takes about 20 hours to produce approximately 12 surfaces. Even after optimisation, the protocol was not perfectly reproducible, especially with the smaller structures. E-beam lithography could be used for the smaller structures or possibly a planar gold surface could be evaporated, and the 2 μm spacings etched into the gold. Each

coverslip could only fit one or two patterns. When using for the SPR experiments, the structures towards the edge of the coverslip could not be reached by the objective lens on the SPR setup and attempting to, would cause a leak and the sample would be unusable.

Although it was theoretically possible to detect the small refractive index change of the cell membrane the sensitivity of the sensor could be improved by using a thin layer of graphene. Wu et al. (2010) used the Kretschmann configuration to detect the refractive index changes near the sensor surface. They showed that with ten graphene layers on a thin gold film improved the sensitivity to refractive index changes by 25% compared to the gold only case. This improved sensitivity has been attributed to an increased adsorption of biomolecules on the graphene layer. Singh et al. (2015) developed an SPR immunosensor using a single graphene layer on gold film improving the SPR sensor performance by 80% compared to a planar gold control. He et al. (2017) used a graphene-based SPR chip to detect folic acid protein in serum for cancer biomarker detection. They were able to detect folic acid protein binding to receptors on the surface of the sensor with concentrations between 10 fM and 1 pM in serum. Enhanced SPR sensitivity has been demonstrated where the addition of a layer of graphene changed the propagation constant of the SPP, therefore, amplifying the refractive index change near the graphene/sensing medium interface (Gosciniak and Tan, 2013). Enhanced SPR sensitivity has also been shown using fibre-optic biosensors (Song et al., 2010; Rodrigo et al., 2015). It has also been reported that surface plasmons can be excited in graphene without a metal layer (Constant et al., 2016).

FIN.

BIBLIOGRAPHY

- P. N. Abadian, C. P. Kelley, and E. D. Goluch. Cellular analysis and detection using surface plasmon resonance techniques. *Analytical Chemistry*, 86(6):2799–2812, 2014.
- E. Abbe. Beiträge zur theorie des mikroskops und der mikroskopischen wahrnehmung. *Archiv für Mikroskopische Anatomie*, 9(1):413–418, 1873.
- M. B. Ahrens, M. B. Orger, D. N. Robson, J. M. Li, and P. J. Keller. Whole-brain functional imaging at cellular resolution using light-sheet microscopy. *Nature Methods*, 10(5):413–420, 2013.
- T. Akimoto, S. Sasaki, K. Ikebukuro, and I. Karube. Refractive-index and thickness sensitivity in surface plasmon resonance spectroscopy. *Applied Optics*, 38(19):4058–4064, 1999.
- T. Akkin, D. P. Davé, T. E. Milner, and H. G. Rylander III. Detection of neural activity using phase-sensitive optical low-coherence reflectometry. *Optics Express*, 12(11):2377–2386, 2004.
- T. Akkin, D. Landowne, and A. Sivaprakasam. Detection of neural action potentials using optical coherence tomography: intensity and phase measurements with and without dyes. *Frontiers in Neuroenergetics*, 2:22, 2010.

- B. Alberts. *Molecular biology of the cell*. Garland Science, 2017.
- M. B. Ali, F. Bessueille, J.-M. Chovelon, A. Abdelghani, N. Jaffrezic-Renault, M. Maaref, and C. Martelet. Use of ultra-thin organic silane films for the improvement of gold adhesion to the silicon dioxide wafers for (bio) sensor applications. *Materials Science and Engineering: C*, 28(5):628–632, 2008.
- B. D. Anson and W. M. Roberts. A novel voltage clamp technique for mapping ionic currents from cultured skeletal myotubes. *Biophysical Journal*, 74(6):2963–2972, 1998.
- H. Aouani, J. Wenger, D. Gérard, H. Rigneault, E. Devaux, T. W. Ebbesen, F. Mahdavi, T. Xu, and S. Blair. Crucial role of the adhesion layer on the plasmonic fluorescence enhancement. *ACS Nano*, 3(7):2043–2048, 2009.
- S. K. Arya, P. R. Solanki, M. Datta, and B. D. Malhotra. Recent advances in self-assembled monolayers based biomolecular electronic devices. *Biosensors and Bioelectronics*, 24(9):2810–2817, 2009.
- D. Axelrod. Total internal reflection fluorescence microscopy in cell biology. *Traffic*, 2(11):764–774, 2001.
- H. Baac, S. B. Jun, J. N. Turner, W. Shain, K. L. Smith, M. L. Shuler, and S. J. Kim. Extracellular optical recording configuration for neuronal action potential detection by using surface plasmon resonance: preliminary experiment. In *Neural Engineering, 2005. Conference Proceedings. 2nd International IEEE EMBS Conference on*, pages 332–335. IEEE, 2005.
- A. H. Badreddine, T. Jordan, and I. J. Bigio. Real-time imaging of action potentials in nerves using changes in birefringence. *Biomedical Optics Express*, 7(5):1966–1973, 2016.
- D. L. Bailey, D. W. Townsend, P. E. Valk, and M. N. Maisey. *Positron emission tomography*. Springer, 2005.
- S. Baillet. Magnetoencephalography for brain electrophysiology and imaging. *Nature Neuroscience*, 20(3):327, 2017.
- B. J. Baker, E. K. Kosmidis, D. Vucinic, C. X. Falk, L. B. Cohen, M. Djuricic,

- and D. Zecevic. Imaging brain activity with voltage-and calcium-sensitive dyes. *Cellular and Molecular Neurobiology*, 25(2):245–282, 2005.
- D. J. Bakkum, U. Frey, M. Radivojevic, T. L. Russell, J. Müller, M. Fiscella, H. Takahashi, and A. Hierlemann. Tracking axonal action potential propagation on a high-density microelectrode array across hundreds of sites. *Nature Communications*, 4:2181, 2013.
- M. W. Barnett and P. M. Larkman. The action potential. *Practical Neurology*, 7(3):192–197, 2007.
- M. Bear, B. Connors, and M. Paradiso. *Neuroscience: Exploring the Brain*. Philadelphia: Lippincot Williams & Wilkins., 3rd ed. edition, 2006.
- L. Berdondini, K. Imfeld, A. Maccione, M. Tedesco, S. Neukom, M. Koudelka-Hep, and S. Martinoia. Active pixel sensor array for high spatio-temporal resolution electrophysiological recordings from single cell to large scale neuronal networks. *Lab on a Chip*, 9(18):2644–2651, 2009.
- Y. Bledi, A. Domb, and M. Linal. Culturing neuronal cells on surfaces coated by a novel polyethyleneimine-based polymer. *Brain Research Protocols*, 5(3):pp.282–289, 2000.
- F. E. Bloom, N. C. Spitzer, F. Gage, and T. Albright. *Encyclopedia of Neuroscience: Volume One*, volume 1. Academic Press, 2009.
- C. F. Bohren and D. R. Huffman. *Absorption and scattering of light by small particles*. John Wiley & Sons, 1983.
- T. Bonhoeffer and M. Hübener. Intrinsic optical imaging of functional map development in mammalian visual cortex. *Cold Spring Harbor Protocols*, 2016(6):pdb–top089383, 2016.
- M. Born and E. Wolf. *Principles of Optics: Electromagnetic Theory of Propagation, Interference and Diffraction of Light*. Elsevier, 2013.
- R. N. Bracewell and R. N. Bracewell. *The Fourier Transform and Its Applications*, volume 31999. McGraw-Hill New York, 1986.

BIBLIOGRAPHY

- D. Braun and P. Fromherz. Fluorescence interferometry of neuronal cell adhesion on microstructured silicon. *Physical Review Letters*, 81(23):5241, 1998.
- S. M. Breedlove, N. V. Watson, and M. R. Rosenzweig. *Biological Psychology*. Sinauer Associates Sunderland, 2010.
- T. P. Burghardt. Measuring incidence angle for through-the-objective total internal reflection fluorescence microscopy. *Journal of Biomedical Optics*, 17(12):126007, 2012.
- B. Burle, L. Spieser, C. Roger, L. Casini, T. Hasbroucq, and F. Vidal. Spatial and temporal resolutions of eeg: Is it really black and white? a scalp current density view. *International Journal of Psychophysiology*, 97(3):210–220, 2015.
- M. Butz and A. van Ooyen. A simple rule for dendritic spine and axonal bouton formation can account for cortical reorganization after focal retinal lesions. *PLoS Computational Biology*, 9(10):e1003259, 2013.
- G. Buzsáki, C. A. Anastassiou, and C. Koch. The origin of extracellular fields and currentseeg, ecog, lfp and spikes. *Nature Reviews Neuroscience*, 13(6):407–420, 2012.
- C. T. Campbell and G. Kim. Spr microscopy and its applications to high-throughput analyses of biomolecular binding events and their kinetics. *Biomaterials*, 28(15):2380–2392, 2007.
- N. A. Campbell, J. B. Reece, L. Urry, M. Cain, S. Wasserman, P. Minorsky, et al. *Biology*, 1996.
- A. Chandekar, S. K. Sengupta, and J. E. Whitten. Thermal stability of thiol and silane monolayers: A comparative study. *Applied Surface Science*, 256(9):2742–2749, 2010.
- T.-W. Chen, T. J. Wardill, Y. Sun, S. R. Pulver, S. L. Renninger, A. Baohan, E. R. Schreiter, R. A. Kerr, M. B. Orger, V. Jayaraman, et al. Ultrasensitive fluorescent proteins for imaging neuronal activity. *Nature*, 499(7458):295, 2013.
- A. M. Chiarelli, A. Di Vacri, G. L. Romani, and A. Merla. Fast optical signal in visual

BIBLIOGRAPHY

- cortex: Improving detection by general linear convolution model. *Neuroimage*, 66: 194–202, 2013.
- M. S. Chow, S. L. Wu, S. E. Webb, K. Gluskin, and D. Yew. Functional magnetic resonance imaging and the brain: A brief review. *World Journal of Radiology*, 9 (1):5, 2017.
- B. A. Clark and B. Barbour. Currents evoked in bergmann glial cells by parallel fibre stimulation in rat cerebellar slices. *The Journal of Physiology*, 502(2):335–350, 1997.
- R. C. Clay. *Computer models to simulate ion flow in neurons*. PhD thesis, University of Nottingham, 2017.
- L. Cohen, R. Keynes, and B. Hille. Light scattering and birefringence changes during nerve activity. *Nature*, 218(5140):438–441, 1968.
- L. Cohen, B. Hille, and R. Keynes. Light scattering and birefringence changes during activity in the electric organ of electrophorus electricus. *The Journal of Physiology*, 203(2):489–509, 1969.
- L. Cohen, R. Keynes, and D. Landowne. Changes in light scattering that accompany the action potential in squid giant axons: potential-dependent components. *The Journal of Physiology*, 224(3):701–725, 1972a.
- L. Cohen, R. Keynes, and D. Landowne. Changes in axon light scattering that accompany the action potential: current-dependent components. *The Journal of Physiology*, 224(3):727–752, 1972b.
- T. J. Constant, S. M. Hornett, D. E. Chang, and E. Hendry. All-optical generation of surface plasmons in graphene. *Nature Physics*, 12(2):124, 2016.
- R. Cossart, D. Aronov, and R. Yuste. Attractor dynamics of network up states in the neocortex. *Nature*, 423(6937):283–288, 2003.
- J. C. Dainty. *Laser Speckle and Related Phenomena*, volume 9. Springer science & business Media, 2013.
- H. E. de Bruijn, R. P. Kooyman, and J. Greve. Choice of metal and wavelength for

- surface-plasmon resonance sensors: some considerations. *Applied Optics*, 31(4): 440.1–442, 1992.
- K. Deisseroth. Optogenetics: 10 years of microbial opsins in neuroscience. *Nature Neuroscience*, 18(9):1213, 2015.
- Y. Deng and D. Chu. Coherence properties of different light sources and their effect on the image sharpness and speckle of holographic displays. *Scientific Reports*, 7(1):5893, 2017.
- M. Dipalo, H. Amin, L. Lovato, F. Moia, V. Caprettini, G. C. Messina, F. Tantussi, L. Berdondini, and F. De Angelis. Intracellular and extracellular recording of spontaneous action potentials in mammalian neurons and cardiac cells with 3d plasmonic nano-electrodes. *Nano Letters*, 2017.
- P. Drude. Zur elektronentheorie der metalle. *Annalen der Physik*, 306(3):566–613, 1900.
- F. A. Duck. *Physical Properties of Tissues: A Comprehensive Reference Book*. Academic press, 2013.
- J. Dunlop, M. Bowlby, R. Peri, D. Vasilyev, and R. Arias. High-throughput electrophysiology: an emerging paradigm for ion-channel screening and physiology. *Nature Reviews: Drug Discovery*, 7(4):358, 2008.
- P. G. Etchegoin, E. Le Ru, and M. Meyer. An analytic model for the optical properties of gold. *The Journal of Chemical Physics*, 125(16):164705, 2006.
- B. Eversmann, M. Jenkner, F. Hofmann, C. Paulus, R. Brederlow, B. Holzapfl, P. Fromherz, M. Merz, M. Brenner, and M. e. a. Schreiter. A 128 x 128 cmos biosensor array for extracellular recording of neural activity. *IEEE Journal of Solid-State Circuits*, 38(12):2306–2317, 2003. doi: 10.1109/jssc.2003.819174.
- C. Fang-Yen, M. C. Chu, H. S. Seung, R. R. Dasari, and M. S. Feld. Noncontact measurement of nerve displacement during action potential with a dual-beam low-coherence interferometer. *Optics Letters*, 29(17):2028–2030, 2004.
- C. M. Fang-Yen, S. Oh, S. Song, S. Seung, R. R. Dasari, and M. S. Feld. Differential heterodyne mach-zehnder interferometer for measurement of nanometer-scale

- motions in living cells. In *Biomedical Topical Meeting*, page MD9. Optical Society of America, 2006.
- L. Fenno, O. Yizhar, and K. Deisseroth. The development and application of optogenetics. *Annual review of neuroscience*, 34, 2011.
- I. Ferezou, S. Bolea, and C. C. Petersen. Visualizing the cortical representation of whisker touch: voltage-sensitive dye imaging in freely moving mice. *Neuron*, 50(4):617–629, 2006.
- A. J. Foust and D. M. Rector. Optically teasing apart neural swelling and depolarization. *Neuroscience*, 145(3):887–899, 2007.
- A. J. Foust, J. L. Schei, M. J. Rojas, and D. M. Rector. In vitro and in vivo noise analysis for optical neural recording. *Journal of Biomedical Optics*, 13(4):044038, 2008.
- U. Frey, U. Egert, F. Heer, S. Hafizovic, and A. Hierlemann. Microelectronic system for high-resolution mapping of extracellular electric fields applied to brain slices. *Biosensors and Bioelectronics*, 24(7):2191–2198, 2009.
- D. Gardner. Characterizing digital cameras with the photon transfer curve. *Summit Imaging*, 2012.
- L. J. Gentet, G. J. Stuart, and J. D. Clements. Direct measurement of specific membrane capacitance in neurons. *Biophysical Journal*, 79(1):314–320, 2000.
- K.-F. Giebel, C. Bechinger, S. Herminghaus, M. Riedel, P. Leiderer, U. Weiland, and M. Bastmeyer. Imaging of cell/substrate contacts of living cells with surface plasmon resonance microscopy. *Biophysical Journal*, 76(1):509–516, 1999.
- G. H. Glover. Overview of functional magnetic resonance imaging. *Neurosurgery Clinics*, 22(2):133–139, 2011.
- J. Goense, Y. Bohraus, and N. K. Logothetis. fmri at high spatial resolution: implications for bold-models. *Frontiers in Computational Neuroscience*, 10:66, 2016.
- E. Gogolides, E. Tegou, K. Beltsios, K. Papadokostaki, and M. Hatzakis. Thermal and mechanical analysis of photoresist and silylated photoresist films: Application to az 5214. *Microelectronic Engineering*, 30(1-4):267–270, 1996.

- J. Gosciniaik and D. T. Tan. Graphene-based waveguide integrated dielectric-loaded plasmonic electro-absorption modulators. *Nanotechnology*, 24(18):185202, 2013.
- C. A. Goss, D. H. Charych, and M. Majda. Application of (3-mercaptopropyl) trimethoxysilane as a molecular adhesive in the fabrication of vapor-deposited gold electrodes on glass substrates. *Analytical Chemistry*, 63(1):85–88, 1991.
- B. W. Graf, T. S. Ralston, H.-J. Ko, and S. A. Boppart. Detecting intrinsic scattering changes correlated to neuron action potentials using optical coherence imaging. *Optics Express*, 17(16):13447–13457, 2009.
- G. Gratton, P. M. Corballis, E. Cho, M. Fabiani, and D. C. Hood. Shades of gray matter: Noninvasive optical images of human brain responses during visual stimulation. *Psychophysiology*, 32(5):505–509, 1995.
- C. Grienberger and A. Konnerth. Imaging calcium in neurons. *Neuron*, 73(5):862–885, 2012.
- A. Grinvald, E. Lieke, R. D. Frostig, C. D. Gilbert, and T. N. Wiesel. Functional architecture of cortex revealed by optical imaging of intrinsic signals. *Nature*, 324(6095):361–364, 1986.
- A. Grinvald, D. B. Omer, D. Sharon, I. Vanzetta, and R. Hildesheim. Voltage-sensitive dye imaging of neocortical activity. *Cold Spring Harbor Protocols*, 2016(1):pdb-top089367, 2016.
- H. R. Gwon and S. H. Lee. Spectral and angular responses of surface plasmon resonance based on the kretschmann prism configuration. *Materials Transactions*, 51(6):1150–1155, 2010.
- G. M. Hale and M. R. Querry. Optical constants of water in the 200-nm to 200- μ m wavelength region. *Applied Optics*, 12(3):555–563, 1973.
- M. Hämäläinen, R. Hari, R. J. Ilmoniemi, J. Knuutila, and O. V. Lounasmaa. Magnetoencephalography theory, instrumentation, and applications to noninvasive studies of the working human brain. *Reviews of Modern Physics*, 65(2):413, 1993.
- O. P. Hamill, A. Marty, E. Neher, B. Sakmann, and F. Sigworth. Improved patch-

- clamp techniques for high-resolution current recording from cells and cell-free membrane patches. *Pflügers Archiv European Journal of Physiology*, 391(2):85–100, 1981.
- W. Hansen. Electric fields produced by the propagation of plane coherent electromagnetic radiation in a stratified medium. *Journal of the Optical Society of America*, 58(3):p.380, 1968.
- J. J. Harris, R. Jolivet, and D. Attwell. Synaptic energy use and supply. *Neuron*, 75(5):762–777, 2012.
- S. W. Hasinoff. Photon, poisson noise. In *Computer Vision*, pages 608–610. Springer, 2014.
- U. Hassan and M. S. Anwar. Reducing noise by repetition: introduction to signal averaging. *European Journal of Physics*, 31(3):453, 2010.
- L. He, Q. Pagneux, I. Larroulet, A. Y. Serrano, A. Pesquera, A. Zurutuza, D. Mandler, R. Boukherroub, and S. Szunerits. Label-free femtomolar cancer biomarker detection in human serum using graphene-coated surface plasmon resonance chips. *Biosensors and Bioelectronics*, 89:606–611, 2017.
- E. Hecht. *Optics*. Pearson Education, 2016.
- T. Hedrich, G. Pellegrino, E. Kobayashi, J. Lina, and C. Grova. Comparison of the spatial resolution of source imaging techniques in high-density eeg and meg. *NeuroImage*, 157:531–544, 2017.
- T. P. Hettmansperger and J. W. McKean. *Robust Nonparametric Statistical Methods*. CRC Press, 2010.
- D. Hill and R. Keynes. Opacity changes in stimulated nerve. *The Journal of Physiology*, 108(3):278–281, 1949.
- R. Hine et al. *The Facts on File Dictionary of Biology*. Infobase Publishing, 2009.
- C. Hitzenberger, M. Danner, W. Drexler, and A. Fercher. Measurement of the spatial coherence of superluminescent diodes. *Journal of Modern Optics*, 46(12):1763–1774, 1999.
- X. Hoa, A. Kirk, and M. Tabrizian. Towards integrated and sensitive surface plasmon

BIBLIOGRAPHY

- resonance biosensors: a review of recent progress. *Biosensors and Bioelectronics*, 23(2):151–160, 2007.
- A. L. Hodgkin and A. F. Huxley. Action potentials recorded from inside a nerve fibre. *Nature*, 144(3651):710–711, 1939.
- A. L. Hodgkin and A. F. Huxley. A quantitative description of membrane current and its application to conduction and excitation in nerve. *The Journal of Physiology*, 117(4):500–544, 1952.
- A. L. Hodgkin and B. Katz. The effect of sodium ions on the electrical activity of the giant axon of the squid. *The Journal of Physiology*, 108(1):37–77, 1949.
- A. L. Hodgkin, A. F. Huxley, and B. Katz. Measurement of current-voltage relations in the membrane of the giant axon of loligo. *The Journal of Physiology*, 116(4):424–448, 1952.
- R. Homma, B. J. Baker, L. Jin, O. Garaschuk, A. Konnerth, L. B. Cohen, C. X. Bleau, M. Canepari, M. Djurusic, and D. Zecevic. Wide-field and two-photon imaging of brain activity with voltage and calcium-sensitive dyes. *Dynamic Brain Imaging: Multi-Modal Methods and In Vivo Applications*, pages 43–79, 2009.
- J. Homola. Surface plasmon resonance sensors for detection of chemical and biological species. *Chemical Reviews*, 108(2):462–493, 2008.
- P. Horowitz, W. Hill, and V. Elings. *The Art of Electronics*. Cambridge (UK): Cambridge University Press, 3rd ed. edition, 2015.
- B. Huang, F. Yu, and R. N. Zare. Surface plasmon resonance imaging using a high numerical aperture microscope objective. *Analytical Chemistry*, 79(7):2979–2983, 2007.
- D. H. Hubel et al. Tungsten microelectrode for recording from single units. *Science*, 125(3247):549–550, 1957.
- S. A. Huettel, A. W. Song, G. McCarthy, et al. *Functional magnetic resonance imaging*, volume 1. Sinauer Associates Sunderland, 2004.
- H. C. Hulst and H. C. van de Hulst. *Light scattering by small particles*. Courier Corporation, 1957.

- M. Hutzler, A. Lambacher, B. Eversmann, M. Jenkner, R. Thewes, and P. Fromherz. High-resolution multitransistor array recording of electrical field potentials in cultured brain slices. *Journal of Neurophysiology*, 96(3):1638–1645, 2006.
- M. S. Islam, A. Z. Kouzani, X. J. Dai, and W. P. Michalski. Investigation of the effects of design parameters on sensitivity of surface plasmon resonance biosensors. *Biomedical Signal Processing and Control*, 6(2):147–156, 2011.
- M. M. A. Jamil, M. C. Denyer, M. Youseffi, S. T. Britland, S. Liu, C. See, M. Somekh, and J. Zhang. Imaging of the cell surface interface using objective coupled wide-field surface plasmon microscopy. *Journal of Structural Biology*, 164(1):75–80, 2008.
- J. R. Janesick. *Scientific Charge-Coupled Devices*, volume 83. SPIE press, 2001.
- J. R. Janesick. *Photon Transfer*. SPIE press San Jose, 2007.
- K. Jans, B. Van Meerbergen, G. Reekmans, K. Bonroy, W. Annaert, G. Maes, Y. Engelborghs, G. Borghs, and C. Bartic. Chemical and biological characterization of thiol sams for neuronal cell attachment. *Langmuir*, 25(8):4564–4570, 2009.
- J. Jatschka, A. Dathe, A. Csáki, W. Fritzsche, and O. Stranik. Propagating and localized surface plasmon resonance sensing a critical comparison based on measurements and theory. *Sensing and Bio-Sensing Research*, 7:62–70, 2016.
- B. Johnson, S. T. Peace, A. Wang, T. A. Cleland, and A. Molnar. A 768-channel cmos microelectrode array with angle sensitive pixels for neuronal recording. *IEEE Sensors Journal*, 13(9):3211–3218, 2013.
- N. L. Johnson, S. Kotz, and N. Balakrishnan. Continuous univariate probability distributions,(vol. 1), 1994.
- P. Johnson and R. Christy. Optical constants of transition metals: Ti, v, cr, mn, fe, co, ni, and pd. *Physical Review B*, 9(12):5056, 1974.
- P. B. Johnson and R.-W. Christy. Optical constants of the noble metals. *Physical Review B*, 6(12):4370, 1972.
- S. Kaech and G. Banker. Culturing hippocampal neurons. *Nature Protocols*, 1(5):2406, 2006.

- E. Kandel. *Principles of Neural Science*. New York: McGraw-Hill, 2012.
- B. Kasemo. Biological surface science. *Surface Science*, 500(1):656–677, 2002.
- S. Kedenburg, M. Vieweg, T. Gissibl, and H. Giessen. Linear refractive index and absorption measurements of nonlinear optical liquids in the visible and near-infrared spectral region. *Optical Materials Express*, 2(11):1588–1611, 2012.
- H. E. Keller. Proper alignment of the microscope. In *Methods in Cell Biology*, volume 56, pages 135–146. Elsevier, 1998.
- S. A. Kim, K. M. Byun, J. Lee, J. H. Kim, D.-G. A. Kim, H. Baac, M. L. Shuler, and S. J. Kim. Optical measurement of neural activity using surface plasmon resonance. *Optics Letters*, 33(9):914–916, 2008.
- S. A. Kim, S. J. Kim, H. Moon, and S. B. Jun. In vivo optical neural recording using fiber-based surface plasmon resonance. *Optics Letters*, 37(4):614–616, 2012.
- B. Kolb and R. Gibb. Brain plasticity and behaviour in the developing brain. *Journal of the Canadian Academy of Child and Adolescent Psychiatry*, 20(4):265, 2011.
- B. Kolb and I. Q. Whishaw. Brain plasticity and behavior. *Annual Review of Psychology*, 49(1):43–64, 1998.
- J. Kopeček and J. Yang. Hydrogels as smart biomaterials. *Polymer International*, 56(9):1078–1098, 2007.
- E. Kretschmann and H. Raether. Radiative decay of non radiative surface plasmons excited by light. *Zeitschrift für Naturforschung A*, 23(12):2135–2136, 1968.
- B. Lamprecht, J. Krenn, G. Schider, H. Ditlbacher, M. Salerno, N. Felidj, A. Leitner, F. Aussenegg, and J. Weeber. Surface plasmon propagation in microscale metal stripes. *Applied Physics Letters*, 79(1):51–53, 2001.
- S. Lan, M. Veisoh, and M. Zhang. Surface modification of silicon and gold-patterned silicon surfaces for improved biocompatibility and cell patterning selectivity. *Biosensors and Bioelectronics*, 20(9):1697–1708, 2005.
- D. Landowne. Molecular motion underlying activation and inactivation of sodium channels in squid giant axons. *The Journal of Membrane Biology*, 88(2):173–185, 1985.

- D. Landowne. Measuring nerve excitation with polarized light. *The Japanese Journal of Physiology*, 43:S7–11, 1993.
- A. LaPorta and D. Kleinfeld. Interferometric detection of action potentials. *Cold Spring Harbor Protocols*, 2012(3):pdb-ip068148, 2012.
- M. Lazebnik, D. L. Marks, K. Potgieter, R. Gillette, and S. A. Boppart. Functional optical coherence tomography for detecting neural activity through scattering changes. *Optics Letters*, 28(14):1218–1220, 2003.
- E. Le Ru and P. Etchegoin. *Principles of Surface-Enhanced Raman Spectroscopy: and related plasmonic effects*. Elsevier, 2008.
- J. Lee and S. J. Kim. Spectrum measurement of fast optical signal of neural activity in brain tissue and its theoretical origin. *Neuroimage*, 51(2):713–722, 2010.
- I. Lelong, V. Petegnief, and G. Rebel. Neuronal cells mature faster on polyethyleneimine coated plates than on polylysine coated plates. *J. Neurosci. Res.*, 32(4):pp. 562–568, 1992.
- H. J. Levinson. *Principles of Lithography*, volume 146. SPIE press, 2005.
- C.-T. Li and Y. Li. Color-decoupled photo response non-uniformity for digital image forensics. *IEEE Transactions on Circuits and Systems for Video Technology*, 22(2):260–271, 2012.
- S. Link and M. A. El-Sayed. Size and temperature dependence of the plasmon absorption of colloidal gold nanoparticles. *The Journal of Physical Chemistry B*, 103(21):4212–4217, 1999.
- S. Link and M. A. El-Sayed. Shape and size dependence of radiative, non-radiative and photothermal properties of gold nanocrystals. *International Reviews in Physical Chemistry*, 19(3):409–453, 2000.
- A. Litke, N. Bezayiff, E. Chichilnisky, W. Cunningham, W. Dabrowski, A. Grillo, M. Grivich, P. Grybos, P. Hottowy, S. Kachiguine, et al. What does the eye tell the brain?: Development of a system for the large-scale recording of retinal output activity. *IEEE Transactions on Nuclear Science*, 51(4):1434–1440, 2004.
- X. Liu, Q. Wang, and L. Chen. In situ functionalized self-assembled monolayer

- surfaces for selective chemical vapor deposition of copper. *Applied Surface Science*, 255(6):pp.3789–3794., 2009.
- X.-W. Liu, Y. Yang, W. Wang, S. Wang, M. Gao, J. Wu, and N. Tao. Plasmonic-based electrochemical impedance imaging of electrical activities in single cells. *Angewandte Chemie International Edition*, 2017.
- Z. Liu, J. Xu, X. Wang, K. Nie, and W. Jin. A fixed-pattern noise correction method based on gray value compensation for tdi cmos image sensor. *Sensors*, 15(9):23496–23513, 2015.
- L. S. Live and J.-F. Masson. High sensitivity of plasmonic microstructures near the transition from short-range to propagating surface plasmon. *The Journal of Physical Chemistry C*, 113(23):10052–10060, 2009.
- L. S. Live, M.-P. Murray-Methot, and J.-F. Masson. Localized and propagating surface plasmons in gold particles of near-micron size. *The Journal of Physical Chemistry C*, 113(1):40–44, 2008.
- L. S. Live, O. R. Bolduc, and J.-F. Masson. Propagating surface plasmon resonance on microhole arrays. *Analytical Chemistry*, 82(9):3780–3787, 2010.
- S. Lloyd-Fox, A. Blasi, and C. Elwell. Illuminating the developing brain: the past, present and future of functional near infrared spectroscopy. *Neuroscience & Biobehavioral Reviews*, 34(3):269–284, 2010.
- H. Lodish, A. Berk, S. L. Zipursky, P. Matsudaira, D. Baltimore, and J. Darnell. Molecular cell biology 4th edition. *National Center for Biotechnology Information's Bookshelf*, 2000.
- L. L. Looger and O. Griesbeck. Genetically encoded neural activity indicators. *Current Opinion in Neurobiology*, 22(1):18–23, 2012.
- H. D. Lu, G. Chen, J. Cai, and A. W. Roe. Intrinsic signal optical imaging of visual brain activity: Tracking of fast cortical dynamics. *NeuroImage*, 148:160–168, 2017.
- J. Lu, W. Wang, S. Wang, X. Shan, J. Li, and N. Tao. Plasmonic-based electrochemical impedance spectroscopy: Application to molecular binding. *Analytical Chemistry*, 84(1):327–333, 2011.

- C. Mack. *Fundamental Principles of Optical Lithography: The Science of Microfabrication*. John Wiley & Sons, 2008.
- B. A. MacVicar and D. Hochman. Imaging of synaptically evoked intrinsic optical signals in hippocampal slices. *Journal of Neuroscience*, 11(5):1458–1469, 1991.
- A. K. Mahapatro, A. Scott, A. Manning, and D. B. Janes. Gold surface with sub-nm roughness realized by evaporation on a molecular adhesion monolayer. *Applied Physics Letters*, 88(15):151917, 2006.
- S. A. Maier. *Plasmonics: fundamentals and applications*. Springer Science & Business Media, 2007.
- M. D. Malinsky, K. L. Kelly, G. C. Schatz, and R. P. Van Duyne. Chain length dependence and sensing capabilities of the localized surface plasmon resonance of silver nanoparticles chemically modified with alkanethiol self-assembled monolayers. *Journal of the American Chemical Society*, 123(7):1471–1482, 2001.
- J. Marcum. A statistical theory of target detection by pulsed radar. *IRE Transactions on Information Theory*, 6(2):59–267, 1960.
- A. L. Mattheyses, S. M. Simon, and J. Z. Rappoport. Imaging with total internal reflection fluorescence microscopy for the cell biologist. *J Cell Sci*, 123(21):3621–3628, 2010.
- A. R. Mayer, T. Toulouse, S. Klimaj, J. M. Ling, A. Pena, and P. S. Bellgowan. Investigating the properties of the hemodynamic response function after mild traumatic brain injury. *Journal of Neurotrauma*, 31(2):189–197, 2014.
- K. M. Mayer and J. H. Hafner. Localized surface plasmon resonance sensors. *Chemical Reviews*, 111(6):3828–3857, 2011.
- D. Mazia, G. Schatten, and W. Sale. Adhesion of cells to surfaces coated with polylysine. applications to electron microscopy. *The Journal of Cell Biology*, 66(1):198–200, 1975.
- J. Meitzen, K. R. Pflapsen, C. M. Stern, R. L. Meisel, and P. G. Mermelstein. Measurements of neuron soma size and density in rat dorsal striatum, nucleus

- accumbens core and nucleus accumbens shell: differences between striatal region and brain hemisphere, but not sex. *Neuroscience Letters*, 487(2):177–181, 2011.
- R. Meyer. Light scattering from biological cells: dependence of backscatter radiation on membrane thickness and refractive index. *Applied Optics*, 18(5):p.585, 1979.
- G. Mie. Beiträge zur optik trüber medien, speziell kolloidaler metallösungen. *Annalen der Physik*, 330(3):377–445, 1908.
- K. Moutzouris, M. Papamichael, S. C. Betsis, I. Stavrakas, G. Hloupis, and D. Triantis. Refractive, dispersive and thermo-optic properties of twelve organic solvents in the visible and near-infrared. *Applied Physics B*, 116(3):617–622, 2014. ISSN 1432-0649.
- J. Müller, M. Ballini, P. Livi, Y. Chen, M. Radivojevic, A. Shadmani, V. Viswam, I. L. Jones, M. Fiscella, R. Diggelmann, et al. High-resolution cmos mea platform to study neurons at subcellular, cellular, and network levels. *Lab on a Chip*, 15(13):2767–2780, 2015.
- T. Murphy. Statistics of photon arrival time. *APOLLO Project Document*,, 2001.
- E. Neher and B. Sakmann. Single-channel currents recorded from membrane of denervated frog muscle fibres. *Nature*, 260(5554):799–802, 1976.
- G. G. Nenninger, M. Piliarik, and J. Homola. Data analysis for optical sensors based on spectroscopy of surface plasmons. *Measurement Science and Technology*, 13(12):2038, 2002.
- H. H. Nguyen, J. Park, S. Kang, and M. Kim. Surface plasmon resonance: a versatile technique for biosensor applications. *Sensors*, 15(5):10481–10510, 2015.
- E. Niedermeyer and F. L. da Silva. *Electroencephalography: basic principles, clinical applications, and related fields*. Lippincott Williams & Wilkins, 2005.
- A. G. Notcovich, V. Zhuk, and S. Lipson. Surface plasmon resonance phase imaging. *Applied Physics Letters*, 76(13):1665–1667, 2000.
- H. Nyquist. Certain topics in telegraph transmission theory. *Transactions of the American Institute of Electrical Engineers*, 47(2):617–644, 1928.
- M. E. J. Obien, K. Deligkaris, T. Bullmann, D. J. Bakkum, and U. Frey. Revealing

- neuronal function through microelectrode array recordings. *Frontiers in Neuroscience*, 8, 2014.
- H. S. Orbach and L. B. Cohen. Optical monitoring of activity from many areas of the in vitro and in vivo salamander olfactory bulb: a new method for studying functional organization in the vertebrate central nervous system. *Journal of Neuroscience*, 3(11):2251–2262, 1983.
- A. Otto. Excitation of nonradiative surface plasma waves in silver by the method of frustrated total reflection. *Zeitschrift für Physik*, 216(4):398–410, 1968.
- O. Palyvoda, C. Chen, and G. Auner. Culturing neuron cells on electrode with self-assembly monolayer. *Biosensors and Bioelectronics*, 22(9-10):pp.2346–2350, 2007.
- R. M. Paredes, J. C. Etzler, L. T. Watts, W. Zheng, and J. D. Lechleiter. Chemical calcium indicators. *Methods*, 46(3):143–151, 2008.
- J. Parvizi and S. Kastner. Promises and limitations of human intracranial electroencephalography. *Nature Neuroscience*, page 1, 2018.
- R. Paschotta. Noise in laser technology. *Optik & Photonik*, 4(2):48–50, 2009.
- R. Paschotta et al. *Encyclopedia of Laser Physics and Technology*, volume 1. Wiley-Vch Berlin, 2008.
- R. Perin, T. K. Berger, and H. Markram. A synaptic organizing principle for cortical neuronal groups. *Proceedings of the National Academy of Sciences*, 108(13):5419–5424, 2011.
- S. Peron, T.-W. Chen, and K. Svoboda. Comprehensive imaging of cortical networks. *Current Opinion in Neurobiology*, 32:115–123, 2015.
- D. S. Peterka, H. Takahashi, and R. Yuste. Imaging voltage in neurons. *Neuron*, 69(1):9–21, 2011.
- A. W. Peterson, M. Halter, A. Tona, K. Bhadriraju, and A. L. Plant. Surface plasmon resonance imaging of cells and surface-associated fibronectin. *BMC Cell Biology*, 10(1):16, 2009.

BIBLIOGRAPHY

- A. W. Peterson, M. Halter, A. Tona, and A. L. Plant. High resolution surface plasmon resonance imaging for single cells. *BMC Cell Biology*, 15(1):35, 2014.
- M. E. Phelps, J. Mazziotta, and H. R. Schelbert. Positron emission tomography and autoradiography: principles and applications for the brain and heart. *Clinical Cardiology*, 1985.
- K. S. Phillips and Q. Cheng. Recent advances in surface plasmon resonance based techniques for bioanalysis. *Analytical and Bioanalytical Chemistry*, 387(5):1831–1840, 2007.
- Photometrics. Read noise: Photometrics whitepaper, 2015. URL <https://www.photometrics.com/resources/whitepapers/read-noise.php>.
- A. Poghosian, S. Ingebrandt, A. Offenhäusser, and M. J. Schöning. Field-effect devices for detecting cellular signals. *Seminars in Cell & Developmental Biology*, 20(1):41–48, 2009.
- S. Potter, D. Wagenaar, T. DeMarse, M. Taketani, and M. Baudry. Advances in network electrophysiology using multi-electrode arrays, 2006.
- S. M. Potter and T. B. DeMarse. A new approach to neural cell culture for long-term studies. *Journal of Neuroscience Methods*, 110(1):17–24, 2001.
- D. Purves, G. Augustine, D. Fitzpatrick, W. Hall, A. LaMantia, and L. White. *Neuroscience*. Sunderland, Massachusetts.: Sinauer Associates, Inc, 5th ed. edition, 2012.
- M. S. Rad, Y. Choi, L. B. Cohen, B. J. Baker, S. Zhong, D. A. Storace, and O. R. Braubach. Voltage and calcium imaging of brain activity. *Biophysical Journal*, 2017.
- H. Radhakrishnan, W. Vanduffel, H. P. Deng, L. Ekstrom, D. A. Boas, and M. A. Franceschini. Fast optical signal not detected in awake behaving monkeys. *Neuroimage*, 45(2):410–419, 2009.
- A. D. Rakić, A. B. Djurišić, J. M. Elazar, and M. L. Majewski. Optical properties of metallic films for vertical-cavity optoelectronic devices. *Applied Optics*, 37(22): 5271–5283, 1998.

- M. Rasigni and G. Rasigni. Optical constants of lithium deposits as determined from the kramers-kronig analysis. *JOSA*, 67(1):54–59, 1977.
- D. M. Rector, G. R. Poe, M. P. Kristensen, and R. M. Harper. Light scattering changes follow evoked potentials from hippocampal schaeffer collateral stimulation. *Journal of Neurophysiology*, 78(3):1707–1713, 1997.
- J. Rheims, J. Köser, and T. Wriedt. Refractive-index measurements in the near-ir using an abbe refractometer. *Measurement Science and Technology*, 8(6):601, 1997.
- B. Richards and E. Wolf. Electromagnetic diffraction in optical systems. ii. structure of the image field in an aplanatic system. *Proceedings of the Royal Society of London A: Mathematical, Physical and Engineering Sciences*, 253(1274):358–379, 1959. ISSN 0080-4630.
- D. Rodrigo, O. Limaj, D. Janner, D. Etezadi, F. J. G. de Abajo, V. Pruneri, and H. Altug. Mid-infrared plasmonic biosensing with graphene. *Science*, 349(6244):165–168, 2015.
- M. Rycenga, C. M. Cobley, J. Zeng, W. Li, C. H. Moran, Q. Zhang, D. Qin, and Y. Xia. Controlling the synthesis and assembly of silver nanostructures for plasmonic applications. *Chemical Reviews*, 111(6):3669–3712, 2011.
- A. Sale, N. Berardi, and L. Maffei. Environment and brain plasticity: towards an endogenous pharmacotherapy. *Physiological Reviews*, 94(1):189–234, 2014.
- B. Salzberg, H. Davila, and L. Cohen. Optical recording of impulses in individual neurones of an invertebrate central nervous system. *Nature*, 246(5434):508–509, 1973.
- B. Salzberg, A. Grinvald, L. Cohen, H. Davila, and W. Ross. Optical recording of neuronal activity in an invertebrate central nervous system: simultaneous monitoring of several neurons. *Journal of Neurophysiology*, 40(6):1281–1291, 1977.
- L. Scaffardi, N. Pellegrini, O. De Sanctis, and J. Tocho. Sizing gold nanoparticles by optical extinction spectroscopy. *Nanotechnology*, 16(1):158, 2004.

- R. B. Schasfoort and A. J. Tudos. *Handbook of surface plasmon resonance*. Royal Society of Chemistry, 2008.
- J. L. Schei, M. D. McCluskey, A. J. Foust, X.-C. Yao, and D. M. Rector. Action potential propagation imaged with high temporal resolution near-infrared video microscopy and polarized light. *Neuroimage*, 40(3):1034–1043, 2008.
- C. Sekirnjak, P. Hottowy, A. Sher, W. Dabrowski, A. M. Litke, and E. Chichilnisky. High-resolution electrical stimulation of primate retina for epiretinal implant design. *Journal of Neuroscience*, 28(17):4446–4456, 2008.
- B. Sepúlveda, A. Calle, L. M. Lechuga, and G. Armelles. Highly sensitive detection of biomolecules with the magneto-optic surface-plasmon-resonance sensor. *Optics Letters*, 31(8):1085–1087, 2006.
- C. E. Shannon. Communication in the presence of noise. *Proceedings of the IRE*, 37(1):10–21, 1949.
- R. Sharpshkar. Ultra low power bioelectronics: Fundamentals, biomedical applications, and bio-inspired system, 2010.
- P. D. Sheet. Az 5214 e image reversal photoresist. *AZ Electronic Materials*, 70, 2004.
- R. Sherman-Gold. *The Axon Guide for Electrophysiology & Biophysics Laboratory Techniques*. Axon Instruments, 1993.
- W. L. Shew, T. Bellay, and D. Plenz. Simultaneous multi-electrode array recording and two-photon calcium imaging of neural activity. *Journal of Neuroscience Methods*, 192(1):75–82, 2010.
- M. Singh, M. Holzinger, M. Tabrizian, S. Winters, N. C. Berner, S. Cosnier, and G. S. Duesberg. Noncovalently functionalized monolayer graphene for sensitivity enhancement of surface plasmon resonance immunosensors. *Journal of the American Chemical Society*, 137(8):2800–2803, 2015.
- L. Sjulson and G. Miesenböck. Optical recording of action potentials and other discrete physiological events: a perspective from signal detection theory. *Physiology*, 22(1):47–55, 2007.

- D. Smetters, A. Majewska, and R. Yuste. Detecting action potentials in neuronal populations with calcium imaging. *Methods*, 18(2):215–221, 1999.
- F. Sohrabi and S. M. Hamidi. Optical detection of brain activity using plasmonic ellipsometry technique. *Sensors and Actuators B: Chemical*, 251:153–163, 2017.
- T. Son, J. Seo, I.-H. Choi, and D. Kim. Label-free quantification of cell-to-substrate separation by surface plasmon resonance microscopy. *Optics Communications*, 2017.
- B. Song, D. Li, W. Qi, M. Elstner, C. Fan, and H. Fang. Graphene on au (111): A highly conductive material with excellent adsorption properties for high-resolution bio/nanodetection and identification. *ChemPhysChem*, 11(3):585–589, 2010.
- H. Sontheimer and M. L. Olsen. Whole-cell patch-clamp recordings. In *Patch-Clamp Analysis*, pages 35–68. Springer, 2007.
- M. E. Spira and A. Hai. Multi-electrode array technologies for neuroscience and cardiology. *Nature Nanotechnology*, 8(2):83–94, 2013.
- N. Spruston, G. Stuart, and M. Häusser. Dendritic integration. *Dendrites*, pages 231–271, 1999.
- G. Stabler, M. Somekh, and C. See. High-resolution wide-field surface plasmon microscopy. *Journal of Microscopy*, 214(3):328–333, 2004.
- N. B. Standen, P. T. Gray, and M. J. Whitaker. *Microelectrode Techniques: The Plymouth Workshop Handbook*. Company of Biologists, 1987.
- S. V. Stehman. Selecting and interpreting measures of thematic classification accuracy. *Remote Sensing of Environment*, 62(1):77–89, 1997.
- J. Steinbrink, M. Kohl, H. Obrig, G. Curio, F. Syre, F. Thomas, H. Wabnitz, H. Rinneberg, and A. Villringer. Somatosensory evoked fast optical intensity changes detected non-invasively in the adult human head. *Neuroscience Letters*, 291(2):105–108, 2000.
- J. Steinbrink, F. C. Kempf, A. Villringer, and H. Obrig. The fast optical signal robust or elusive when non-invasively measured in the human adult? *Neuroimage*, 26(4):996–1008, 2005.

- R. Stepnoski, A. LaPorta, F. Raccuia-Behling, G. Blonder, R. Slusher, and D. Kleinfeld. Noninvasive detection of changes in membrane potential in cultured neurons by light scattering. *Proceedings of the National Academy of Sciences*, 88(21): 9382–9386, 1991.
- Y.-w. Su and W. Wang. Surface plasmon resonance sensing: from purified biomolecules to intact cells. *Analytical and Bioanalytical Chemistry*, pages 1–9, 2018.
- Y. Sun, Z. Huang, W. Liu, K. Yang, K. Sun, S. Xing, D. Wang, W. Zhang, and X. Jiang. Surface coating as a key parameter in engineering neuronal network structures in vitro. *Biointerphases*, 7(1-4):1–14, 2012.
- J. A. Swets. *Signal Detection and Recognition by Human Observers*. John Wiley & Sons, 1964.
- G. Taguchi. *Introduction to quality engineering: designing quality into products and processes*. 1986.
- M. Taketani and M. Baudry. *Advances in Network Electrophysiology*. Springer, 2010.
- R. Tanamoto, Y. Shindo, N. Miki, Y. Matsumoto, K. Hotta, and K. Oka. Electrical stimulation of cultured neurons using a simply patterned indium-tin-oxide (ito) glass electrode. *Journal of Neuroscience Methods*, 253:272–278, 2015.
- I. Tasaki, A. Watanabe, R. Sandlin, and L. Carnay. Changes in fluorescence, turbidity, and birefringence associated with nerve excitation. *Proceedings of the National Academy of Sciences*, 61(3):883–888, 1968.
- I. Tasaki, K. Iwasa, and R. C. Gibbons. Mechanical changes in crab nerve fibers during action potentials. *The Japanese Journal of Physiology*, 30(6):897–905, 1980.
- T. Tateno and J. Nishikawa. A cmos ic-based multisite measuring system for stimulation and recording in neural preparations in vitro. *Frontiers in Neuroengineering*, 7, 2014.
- Y. Tauran, A. Brioude, A. W. Coleman, M. Rhimi, and B. Kim. Molecular recogni-

- tion by gold, silver and copper nanoparticles. *World Journal of Biological Chemistry*, 4(3):35, 2013.
- C. Thomas, P. Springer, G. Loeb, Y. Berwald-Netter, and L. Okun. A miniature microelectrode array to monitor the bioelectric activity of cultured cells. *Experimental Cell Research*, 74(1):61–66, 1972.
- I. Thormählen, J. Straub, and U. Grigull. Refractive index of water and its dependence on wavelength, temperature, and density. *Journal of Physical and Chemical Reference Data*, 14(4):933–945, 1985.
- L. Tian, S. A. Hires, T. Mao, D. Huber, M. E. Chiappe, S. H. Chalasani, L. Petreanu, J. Akerboom, S. A. McKinney, E. R. Schreiter, et al. Imaging neural activity in worms, flies and mice with improved gcamp calcium indicators. *Nature Methods*, 6(12):875–881, 2009.
- K. Toma, H. Kano, and A. Offenhausser. Label-free measurement of cell–electrode cleft gap distance with high spatial resolution surface plasmon microscopy. *ACS Nano*, 8(12):12612–12619, 2014.
- A. Torricelli, D. Contini, A. Dalla Mora, A. Pifferi, R. Re, L. Zucchelli, M. Caffini, A. Farina, and L. Spinelli. Neurophotonics: non-invasive optical techniques for monitoring brain functions. *Functional Neurology*, 29(4):223, 2014.
- A. Ulman. *An Introduction to Ultrathin Organic Films: From Langmuir–Blodgett to Self-Assembly*. Academic press, 2013.
- S. V. Vaseghi. *Advanced digital signal processing and noise reduction*. John Wiley & Sons, 4th ed. edition, 2008.
- A. Villringer and B. Chance. Non-invasive optical spectroscopy and imaging of human brain function. *Trends in Neurosciences*, 20(10):435 – 442, 1997. ISSN 0166-2236.
- R. F. Voss. 1/f (flicker) noise: A brief review. In *33rd Annual Symposium on Frequency Control*. 1979, pages 40–46. IEEE, 1979.
- W. Wang, S. Wang, Q. Liu, J. Wu, and N. Tao. Mapping single-cell–substrate

- interactions by surface plasmon resonance microscopy. *Langmuir*, 28(37):13373–13379, 2012.
- R. A. Weale. A new micro-electrode for electro-physiological work. *Nature*, 167(4248):529–530, 1951.
- T. D. Wickens. *Elementary signal detection theory*. Oxford University Press, USA, 2002.
- R. W. F. Wiertz. *Regulation of in vitro cell-cell and cell-substrate adhesion*. PhD thesis, Twente University Press, 2010.
- K. A. Willets and R. P. Van Duyne. Localized surface plasmon resonance spectroscopy and sensing. *Annu. Rev. Phys. Chem.*, 58:267–297, 2007.
- C.-M. Wu, Z.-C. Jian, S.-F. Joe, and L.-B. Chang. High-sensitivity sensor based on surface plasmon resonance and heterodyne interferometry. *Sensors and Actuators B: Chemical*, 92(1-2):133–136, 2003.
- L. Wu, H. Chu, W. Koh, and E. Li. Highly sensitive graphene biosensors based on surface plasmon resonance. *Optics Express*, 18(14):14395–14400, 2010.
- Y. Yanase, T. Hiragun, S. Kaneko, H. J. Gould, M. W. Greaves, and M. Hide. Detection of refractive index changes in individual living cells by means of surface plasmon resonance imaging. *Biosensors and Bioelectronics*, 26(2):674–681, 2010.
- Y. Yanase, T. Hiragun, K. Ishii, T. Kawaguchi, T. Yanase, M. Kawai, K. Sakamoto, and M. Hide. Surface plasmon resonance for cell-based clinical diagnosis. *Sensors*, 14(3):4948–4959, 2014.
- Y. Yang, X.-W. Liu, H. Yu, Y. Guan, S. Wang, and N. Tao. Imaging action potential in single mammalian neurons by tracking the accompanying sub-nanometer mechanical motion. *bioRxiv*, page 168054, 2017.
- X.-C. Yao, A. Foust, D. M. Rector, B. Barrowes, and J. S. George. Cross-polarized reflected light measurement of fast optical responses associated with neural activation. *Biophysical Journal*, 88(6):4170–4177, 2005.
- R. Yates and D. Goodman. Probability and stochastic processes. a friendly introduction for electrical and computer engineering. 1999, 1999.

- E. Yavin and Z. Yavin. Attachment and culture of dissociated cells from rat embryo cerebral hemispheres on polylysine-coated surface. *The Journal of Cell Biology*, 62(2):540, 1974.
- E. M. Yeatman. Resolution and sensitivity in surface plasmon microscopy and sensing. *Biosensors and Bioelectronics*, 11(6-7):635–649, 1996.
- Y.-J. Yeh, A. J. Black, D. Landowne, and T. Akkin. Optical coherence tomography for cross-sectional imaging of neural activity. *Neurophotonics*, 2(3):035001, 2015.
- A. Zepeda, C. Arias, and F. Sengpiel. Optical imaging of intrinsic signals: recent developments in the methodology and its applications. *Journal of Neuroscience Methods*, 136(1):1–21, 2004.
- J. Zhang, T. Atay, and A. V. Nurmikko. Optical detection of brain cell activity using plasmonic gold nanoparticles. *Nano Letters*, 9(2):519–524, 2009.
- W. Zhou, X. Dai, and C. M. Lieber. Advances in nanowire bioelectronics. *Reports on Progress in Physics*, 80(1):016701, 2016.
- O. Zhuravleva, A. Ivanov, D. Isaev, V. Kurnosov, K. Kurnosov, V. Romantsevich, and R. Chernov. Analysis of the characteristics of laser and superluminescent diodes. *Journal of Applied Spectroscopy*, 72(5):757–762, 2005.
- M. Zochowski, M. Wachowiak, C. X. Falk, L. B. Cohen, Y.-W. Lam, S. Antic, and D. Zecevic. Imaging membrane potential with voltage-sensitive dyes. *The Biological Bulletin*, 198(1):1–21, 2000.

Appendices

APPENDIX A

SUPPLEMENTARY INFORMATION FOR CHAPTER 2

A.1 Materials, Equipment and Software

A.1.1 Chemical, Solvents and Materials

Name	Company	Cat No.
Electrophysiology Solutions		
Calcium Chloride (CaCl ₂)	Sigma-Aldrich	C1016
Calcium Chloride Solution, 1 M	Sigma-Aldrich	21114
D-(+)-Glucose	Sigma-Aldrich	G7021
EGTA (ethylene glycol tetraacetic acid)	Sigma-Aldrich	E3889
HEPES (4-(2-hydroxyethyl)-1-piperazineethanesulfonic acid)	Sigma-Aldrich	83264
Magnesium Chloride (MgCl ₂)	Sigma-Aldrich	M2670
Magnesium Sulfate Solution, 1 M (MgSO ₄)	Sigma-Aldrich	63126
Mg-ATP (Adenosine 5-triphosphate magnesium salt)	Sigma-Aldrich	A9187

APPENDIX A. SUPPLEMENTARY INFORMATION FOR CHAPTER 2

Na ₂ -ATP (Adenosine 5-triphosphate disodium salt hydrate)	Sigma-Aldrich	A2383
Phosphocreatine disodium salt hydrate	Sigma-Aldrich	P7936
Potassium Chloride (KCl)	Sigma-Aldrich	P9541
Potassium Hydroxide (KOH)		
Sodium Bicarbonate (NaHCO ₃)	Sigma-Aldrich	S5761
Sodium Chloride (NaCl)	Sigma-Aldrich	S5886
Sodium Hydroxide (NaOH)	Sigma-Aldrich	71687
Sucrose (HPLC)	Sigma-Aldrich	84097

Surface Functionalisation

AUT (11-amino-1-undecanethiol hydrochloride)	Sigma-Aldrich	674397
MPTS (3-Mercaptopropyl)-trimethoxysilane (95%)	Sigma-Aldrich	175617
Poly(ethyleneimine) solution (PEI)	Sigma-Aldrich	P3143
Poly-L-lysine (PLL)	Sigma-Aldrich	P4707

Cell Prep

B27 Supplement	Invitrogen	17504-044
Deoxyribonuclease (DNAse)	Sigma-Aldrich	D5025-15KU
Dulbeccos Phosphate Buffered Saline (PBS)	Sigma-Aldrich	D8537
Hanks Balanced Salt Solution	Sigma-Aldrich	H9394
L-Glutamine growth factor	Sigma-Aldrich	G7513
Neurobasal media	Invitrogen	21103-049
Penicillin-Streptomycin	Sigma-Aldrich	P0781
Trypsin	Sigma-Aldrich	T1426
Trypsin Inhibitor	Sigma-Aldrich	T9003

Solvents

Acetone	Sigma-Aldrich	32201
---------	---------------	-------

 APPENDIX A. SUPPLEMENTARY INFORMATION FOR CHAPTER 2

Dimethyl sulfoxide (DMSO)		
Ethanol (ACS) 99.5% (200 proof)	Sigma-Aldrich	459844
Ethanol Denatured	Sigma-Aldrich	458600
Isopropanol (HPLC)	Fisher Scientific	10674732
Methanol		
Toluene anhydrous, 99.8%	Sigma-Aldrich	244511
Other		
Immersion oil	Sigma-Aldrich	10976
Sodium Fluoride (NaF)	Sigma-Aldrich	S7920
Sodium Perchlorate (NaClO ₄)	Sigma-Aldrich	410241
Calcein		
Propidium Iodide		
Photolithography		
Image Reversal Photoresist (AZ 5214E)	Microchemicals GmbH	AZ5214E
Developer (AZ 726MIF)	Microchemicals GmbH	AZ726MIF
Materials		
Glass 19 mm diameter coverslips	Karl Hecht GmbH and Co KG (Sond- heim, Germany)	1001-19-15
PDL Coverslips	neuVitro	GG-18-1.5- pdl
Gold wire (99.999 %, 0.25 mm)	Alfa Aesar	Ordered by Physics
Fire-polished Borosilicate glass with fila- ment	Sutter Instruments	BF150-110- 10HP

A.1.2 SPM Components

Name	Information
Super luminescent diode (SLED)	$\lambda = 680$ nm, 1 mW from Superlum Diodes Ltd.
CMOS Camera	Epix SV643M
CCD Camera	Unibrain Inc Fire-iTM
CCD Camera Grasshopper3	Point Grey S3-U3-28S5M-C (mono)
Dichroic 530 nm	Thorlabs
Dichroic 590 nm	Thorlabs
LED	$\lambda = 470$ nm
LED	$\lambda = 590$ nm
LED	$\lambda = 640$ nm
Lens (L1)	$f = 30$ mm achromatic (ACH)
L2	$f = 75$ mm ACH
L3	$f = 50$ mm ACH
L4	$f = 60$ mm ACH
L5	$f = 175$ mm ACH
L6	$f = 100$ mm ACH
L7	$f = 75$ mm ACH
L8	$f = 150$ mm ACH
L9	$f = 60$ mm ACH
L10	$f = 150$ mm ACH
L11	$f = 60$ mm ACH
Oil-Objective Lens	60 \times , NA = 1.49 from Nikon
Water-Objective Lens	60 \times , NA = 1.00 from Nikon

A.1.3 Equipment

Name	Company	Part No.
Camera	Hamamatsu	C13440-20CU ORCA-Flash4.0 V3
Cryoscopic Osmometer	Gonotec	Osmomat 030
DAQ	National Instru- ments	PCI-6221
EMCCD Camera	Photometrics	QuantEM:512SC
Halogen white light source	Ocean Optics	HL-2000
Headstage	Axon Instruments	CV 201
Inverted microscope	Nikon	Eclipse Ti-U
Patch clamp amplifier	Molecular Devices	Axopatch 200a
pH Meter	Hanna Instruments	HI 2210
Photodiode	Thorlabs	PDA100A
Pipette Puller	Sutter Instruments	
Power Meter	Thorlabs	PM100D
Spectrum analyser	Ocean Optics	USB4000
Clean Room		
Ellipsometer	J.A. Woollam	Alpha-SE
Mask aligner	Karl Suss	MBJ3
Plasma Oven	Electronic Diener Plasma System	Zepto
Spin Coater	Solitec	
Stylus profilometer	KLA-Tencor	Alpha Step D-120
Thermal evaporator	Edwards	E306A

A.1.4 Software

Name	Company	Version
Autocad 2015	Autodesk	2015
ImageJ	National Institute of Health	
Inkscape	Inkscape	0.92.1
Microsoft Office	Microsoft	2013
Matlab	Mathworks	R2014a
Minitab	Minitab, Inc	17.2.1
Prism	Graphpad	6
WinWCP	University of Strathclyde	4.9

A.2 Media and Solutions

Neurobasal Medium

500ml Neurobasal medium

1.25ml L-glutamine

10ml B27 supplement

5ml Pen/strep

Store in refrigerator until day of cell prep then store in incubator.

Hanks/HEPES solution

Add 1.19g HEPES to 500 ml Hanks Balanced Salt Solution (HBSS). Adjust pH to 7.3 with 1M sodium hydroxide, then filter sterilise. Store in refrigerator.

Trypsin solution

Dissolve 100 mg trypsin in 10 ml Ca^{2+} and Mg^{2+} free PBS. Filter sterilise. Store at -20°C .

Trypsin inhibitor solution

Add 25 mg of powder to 2.5 ml Ca^{2+} and Mg^{2+} free PBS, filter sterilise. Store at -20°C .

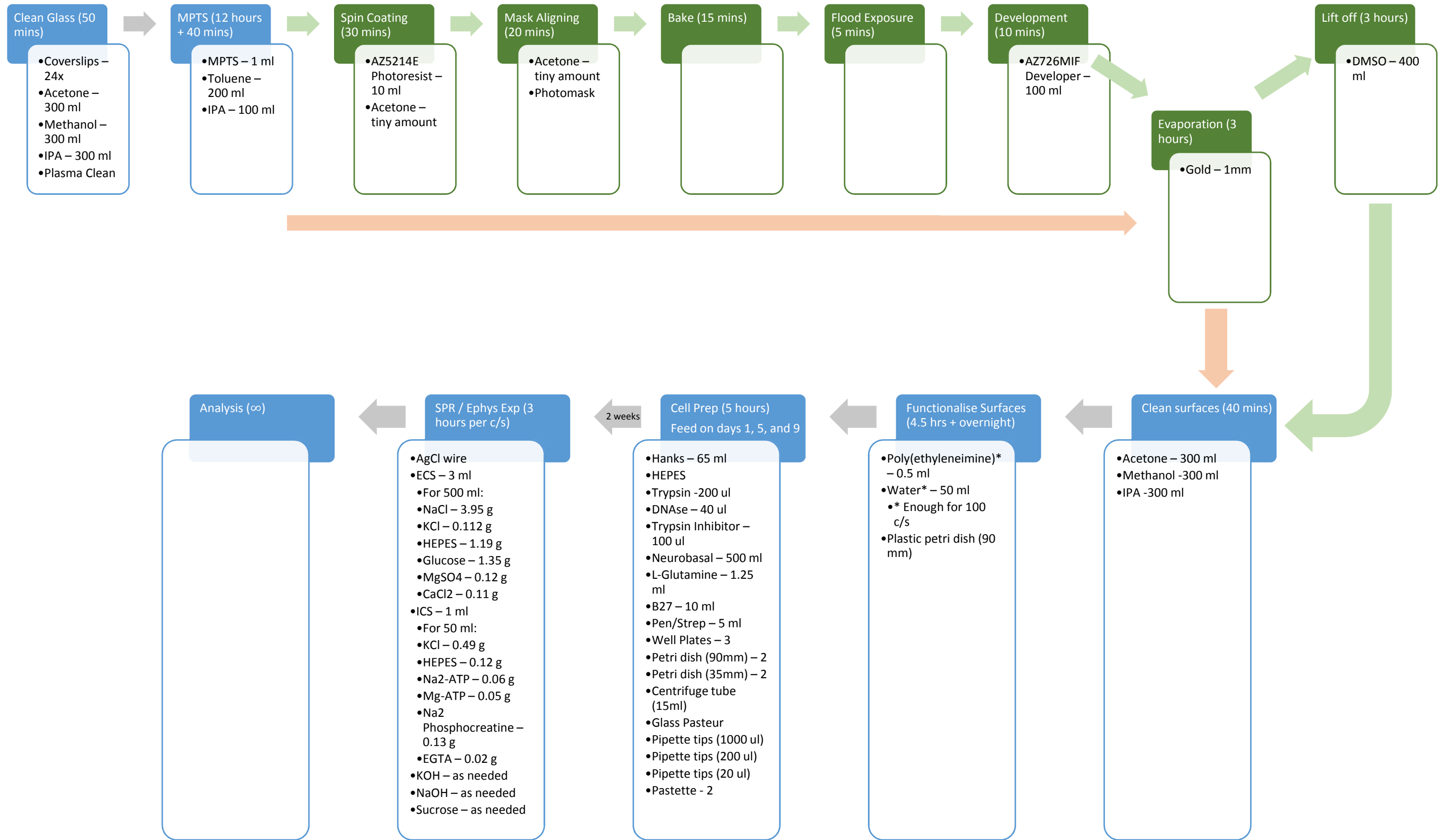
DNase solution

Dissolve 5 mg DNase in 1 ml Ca^{2+} and Mg^{2+} free PBS. Filter sterilise. Store at -20°C .

A.3 Experimental Pipeline

Please see the next page for the experimental pipeline.

Overview of Experimental Pipeline



SUPPLEMENTARY INFORMATION FOR CHAPTER 4

B.1 Specifications

B.1.1 EPIX Camera

Parameter	Specifications
Pixel Architecture	6 transistor pixel
Pixel Size	9.9 μm x 9.9 μm
Resolution	640 (H) x 480 (V)
Frame Rate	250 fps
Fixed Pattern Noise	2.5 % RMS _{p-p} (Min: 10 %, Max: 3.1 %)
Pixel Random Nonuniformity	2.5 % RMS, Max 3.1 %
Conversion Gain	34 $\mu\text{mV}/\text{e}^-$ at output
Saturation Charge	35.000 e ⁻
Sensitivity	3200 V.m ² /W.s 17 V/lux.s (at 550 nm, 180 lux = 1 W/m ²)

Peak Quantum Efficiency \times Fill Factor	45 %
Dark Current (at 21 C)	300 mV/s
Noise Electrons	32 e-
S/N Ratio	43 dB
Parasitic Sensitivity	1/5000
Dynamic Range	61 dB

B.2 Noise and Filters

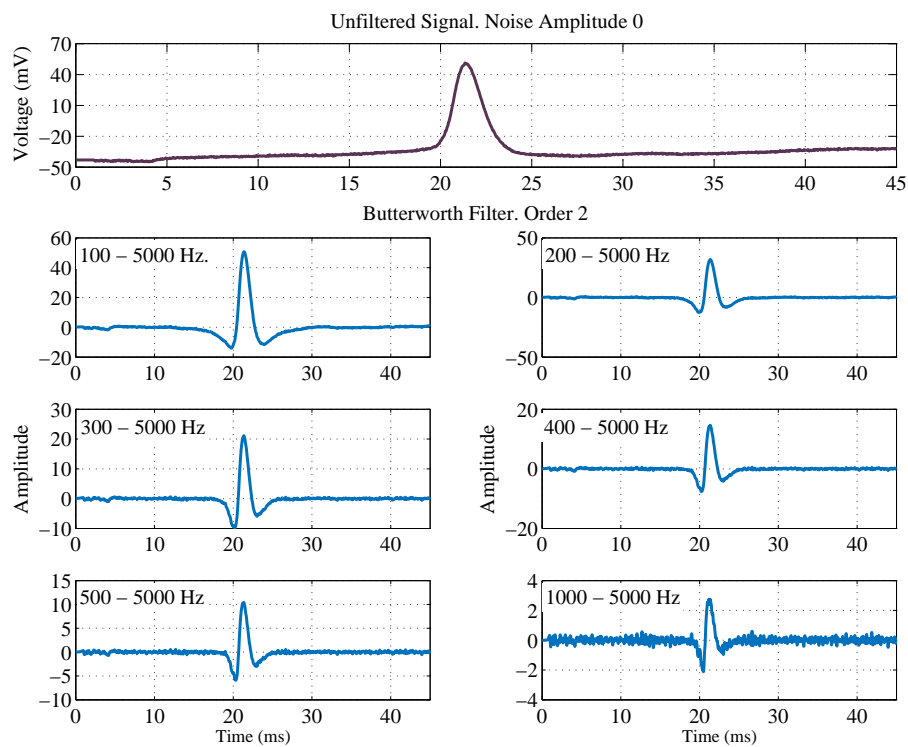


Figure B.1: Effect of filtering on the shape of the action potential. A second order Butterworth bandpass filter was designed and different cut-off frequencies were selected to illustrate the effect.

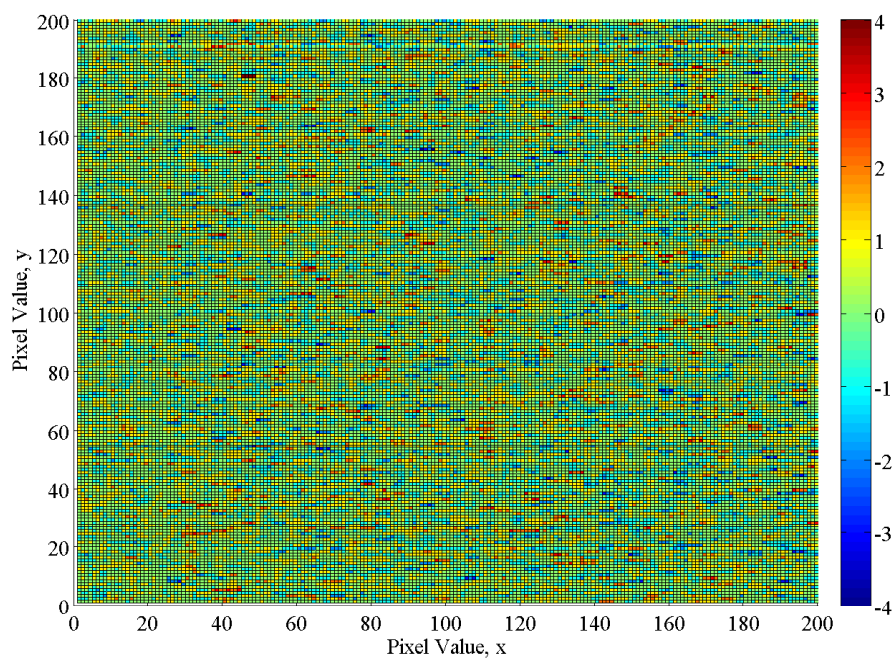


Figure B.2: Difference between the bias images for determining the read noise. The colourbar is the difference in grayscale levels.

APPENDIX C

SUPPLEMENTARY INFORMATION FOR CHAPTER 5

C.1 Figures

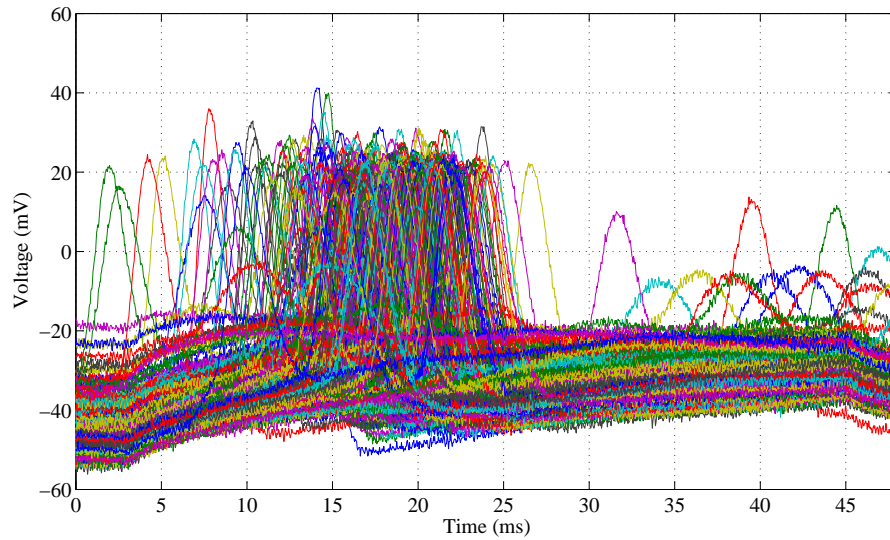


Figure C.1: Raw electrophysiology voltage recordings from the pseudo-data ($n = 500$).

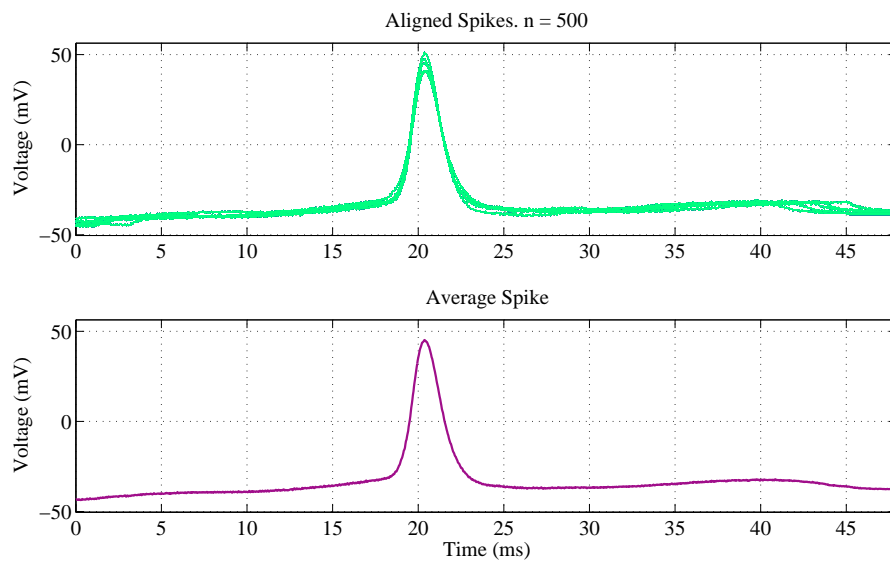


Figure C.2: Processed electrophysiology voltage recordings for the pseudo-data. The spikes are detected using a threshold condition. The first spike is used as a reference and the subsequent action potentials are aligned to it to give the top plot. The initial spike time (t_{AP}) is stored as are the time differences (Δt). Bottom plot: The aligned APs are averaged to give the standard voltage waveform for further analysis.

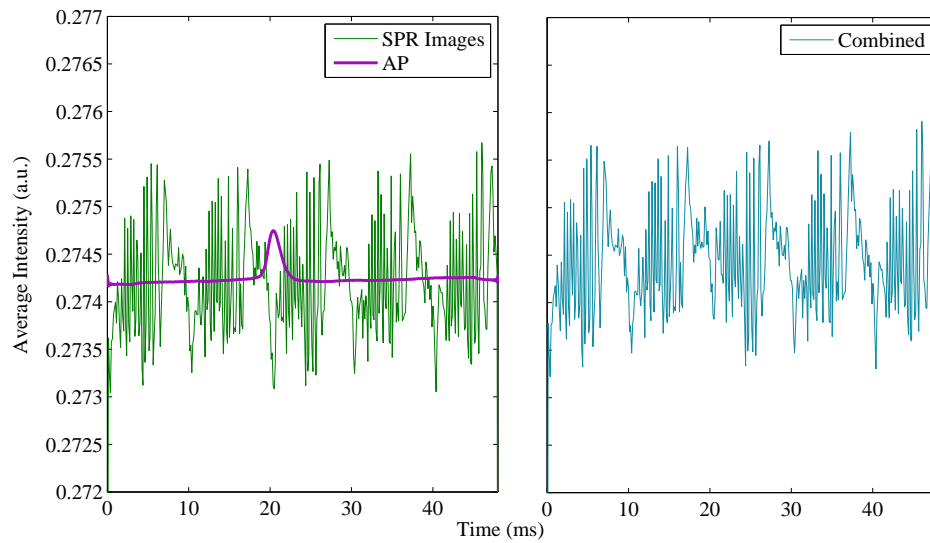


Figure C.3: Left: the raw SPR and voltage recordings. Right: the traces on the left were combined to give the pseudo data. The AP was buried in the noise and is not detectable by eye. The 100 Hz noise that is present is an artefact from the SLED.

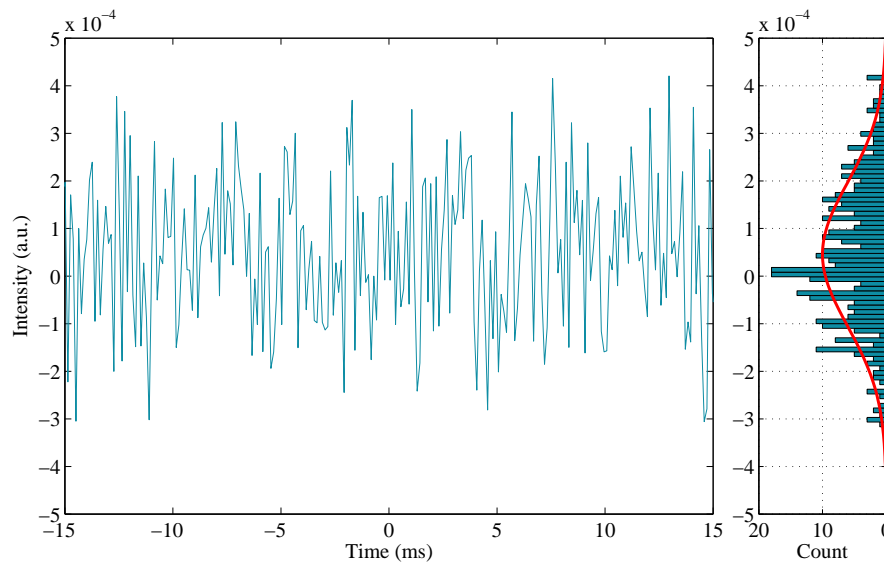


Figure C.4: The average across all pixels for one action potential from the pseudo data after the control area had been subtracted from the ROI where the AP was buried. The AP was buried in the noise and is not detectable by eye. The histogram to the right is the distribution of the y -values.

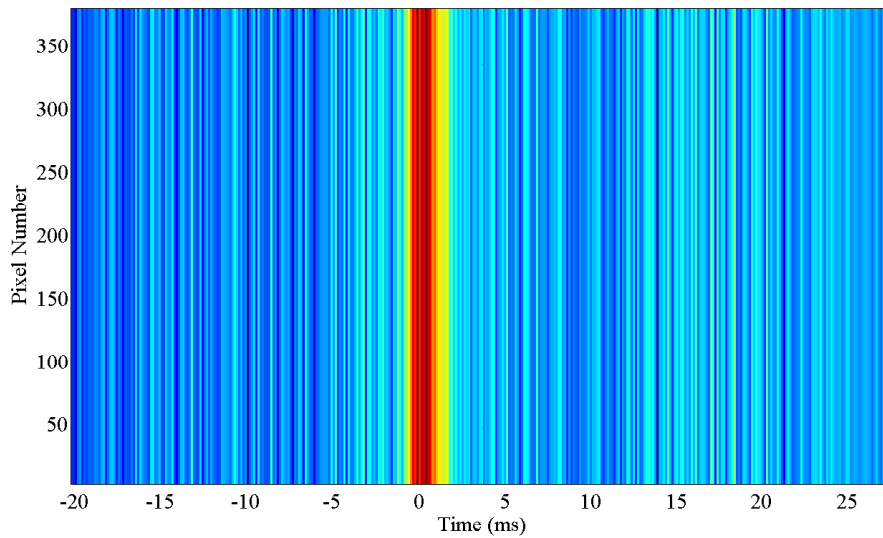


Figure C.5: False colour plot of light intensity over time for all pixels in the region of interest.

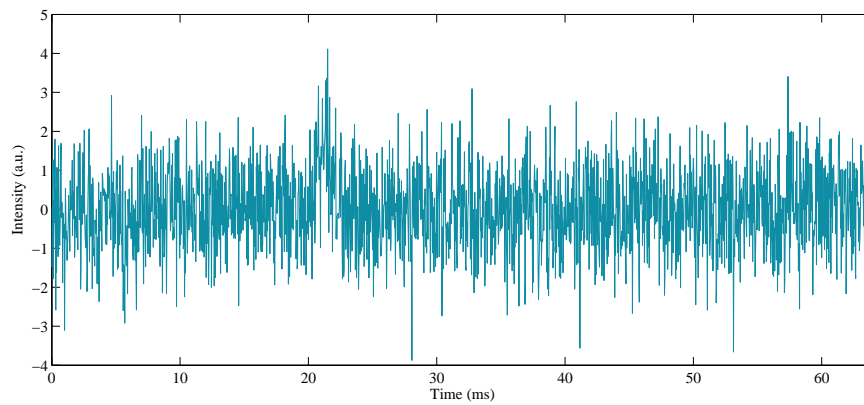


Figure C.6: Time series traces of the pseudo-data created: "Noise + AP". The amplitude of the AP (from mean : max) is 1.698 mV. The power of the noise is 0 dBW i.e. 1 W. Note AP is still evident without any averaging

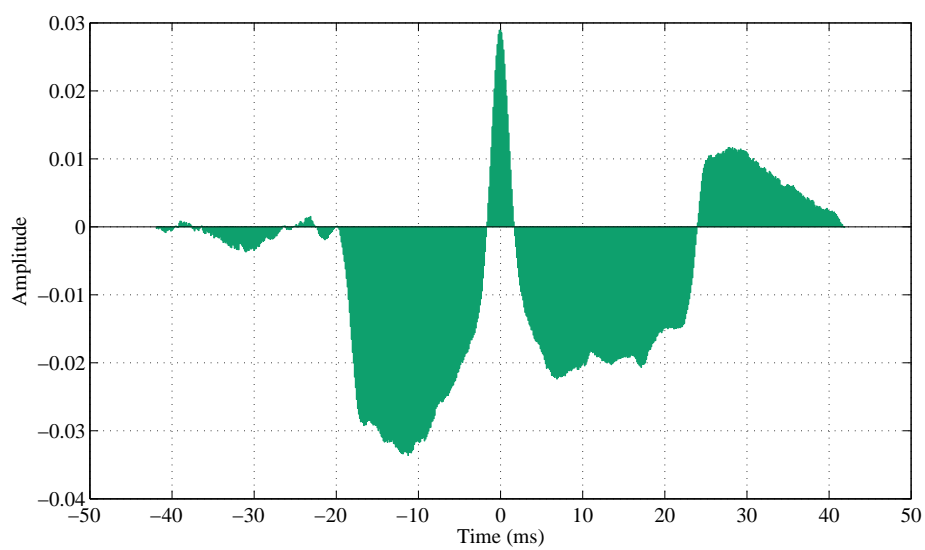


Figure C.7: Cross-correlation standard result from the pseudo-data. This gives a standard for all subsequent analyses from real data to be compared to.

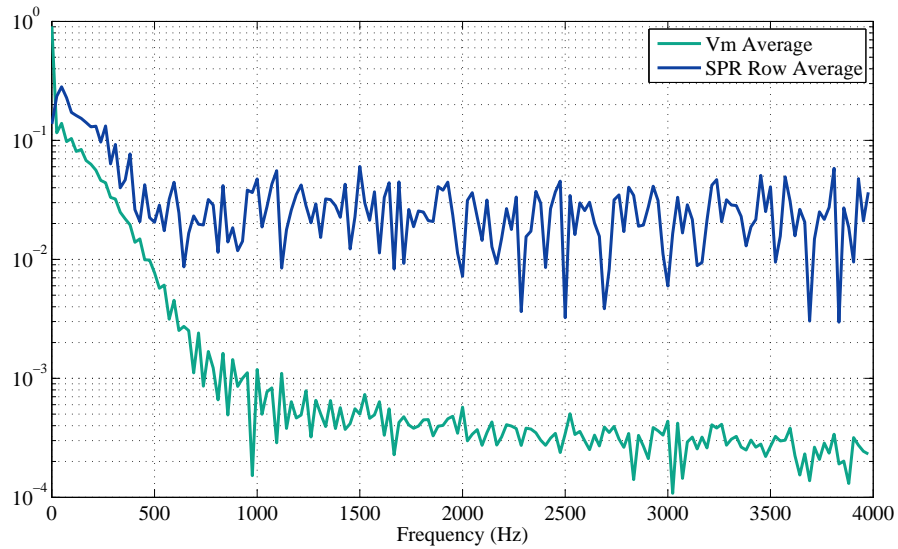


Figure C.8: Frequency domain traces of the average membrane voltage from Figure C.2 and the row average from the optical, SPR recordings, Figure 5.13. The frequencies under 500 Hz have been filtered / deleted as they are not of interest because they cannot be attributed to an action potential. The main frequency of interest should be about 1 kHz corresponding to the 1 ms rise time.

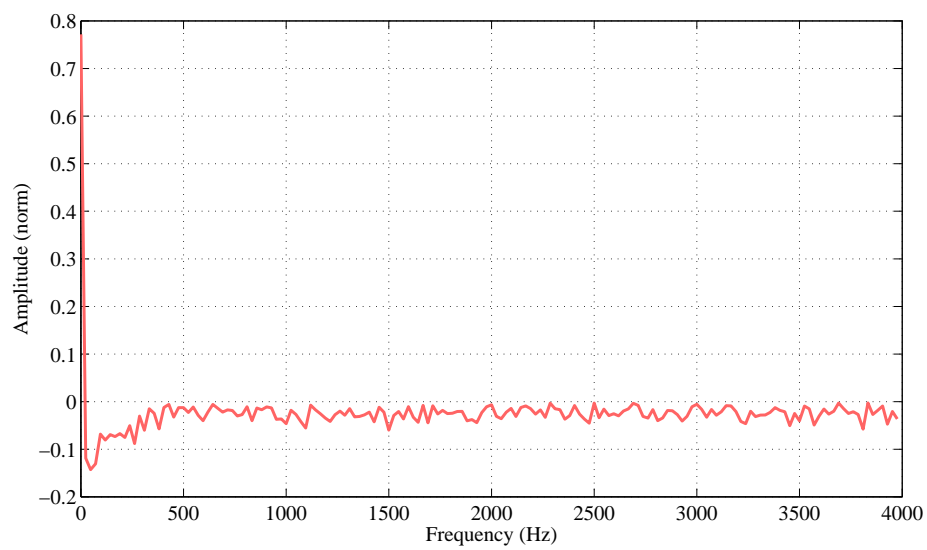


Figure C.9: The two traces from Figure C.8 were normalised and subtracted from one another to see if there were any frequencies where there was a correlation.

SUPPLEMENTARY INFORMATION FOR CHAPTER 6

D.1 Microfabrication Methodology**D.1.1 Gold Deposition onto Glass****Using SAMs as Adhesion Layers**

Gold deposited directly onto glass is not secure and cannot withstand certain cleaning or functionalisation processes. Normally, a thin layer of chromium or titanium (1.5 – 5 nm) is deposited before the gold layer to improve the adhesion. However, this additional layer will have an influence on the SPR signal (Aouani et al., 2009). Alternatively, it is possible to deposit a self-assembled monolayer (SAM), for example (3-Mercaptopropyl)trimethoxysilane (MPTS), to improve the adhesion of the gold layer (Goss et al., 1991; Ali et al., 2008; Mahapatro et al., 2006).

A SAM is a layer of molecular thickness formed by self-organisation of molecules on a solid surface (Arya et al., 2009). The SAM comprises of three parts: a surface-active head group that strongly binds to the surface, an alkyl chain which gives stability to the assembly, and a tail group which adds functionality to the surface.

In the case of MPTS, the trimethoxysilane head group reacts with exposed hydroxyl groups on the SiO₂ substrate that forms a stable silyl ether link, while the thiol tail group binds strongly with the gold layer (Goss et al., 1991). Silane SAMs assembled on SiO₂ are thermally stable to 250-300°C (Chandekar et al., 2010)

Physical Vapor Deposition

Thin metal films can be deposited onto a substrate by physical vapor deposition techniques such as thermal vapor deposition (evaporation). A high purity metal source is placed inside a vacuum ($<10^{-6}$) and a resistive heating element evaporates the metal. The gaseous metal atoms then rise until they reach a cool surface where they condense. Control of the film thickness is difficult and a quartz microbalance (QCM) next to the substrate is used to measure the deposited film thickness in real time.

D.1.2 Photolithography

Photolithography is a process that transfers a 2D image from a photomask onto a thin layer of photosensitive material coated on the surface of a substrate. For biological applications, transparent substrates typically made of glass are better suited as it allows the use of optical techniques.

Types of Resists

There are three types of photoresist: positive, negative, and image reversal. For positive resists, UV light exposes the areas that are to be removed. This exposure changes the chemical structure of the resist so that it becomes more soluble in developer. Positive resist masks leave an exact copy of the mask on the substrate. Negative resists work in the opposite manner. The exposure polymerises the resist, making the resist more difficult to be removed, so the resist remains on the surface where it has been exposed and the developer removes the unexposed resist. Using a negative resist mask results in an inverse pattern of the mask on the substrate. Image reversal resists can be processed in positive or negative mode. If used in the positive mode the process sequence is the same as positive resists. However, if used in the negative mode then an image reversal bake after the exposure and a flood exposure is required.

The different steps for patterning will be discussed in the following subsections focussing on using an image reversal resist. The usual steps for the image reversal process are: substrate preparation, photoresist coating, post-apply bake, exposure, post exposure bake (or reversal bake), flood exposure, development, and removal (Levinson, 2005).

Substrate Preparation

Substrate preparation is important to improve the adhesion of the photoresist to the surface and for a contamination free resist film. Particulate contamination of the substrate introduces defects into the resist pattern. One or more of the following processes can be used to prepare the substrate: cleaning, a dehydration bake and using an adhesion promoter. Chemical or plasma cleaning can remove organic and inorganic films on the surface. Adsorbed water can be removed with a dehydration bake using a temperature of 200 to 400°C for 60 minutes. Measuring the water contact angle (WCA) can test for the amount of adsorbed water on the surface. The WCA should be between 50-70° for good resist adhesion. If the surface is too hydrophilic then there is an increased chance of resist adhesion failure during development. Adhesion promoters chemically react with the surface silanol and replace the -OH group with an organic functional group to improve the photoresist adhesion. Silanes are used for this and are normally spin coated onto the substrate and allowed to dry before coating with photoresist (Mack, 2008).

Photoresist Coating

The resist is deposited onto the substrate using a spin coating process. Spin coating rotates the substrate at a high speed in order to spread out the resist uniformly over the surface. Centrifugal forces push the liquid photoresist to the edge of the substrate which happens until the opposing frictional force of viscosity becomes equal and a uniform, reproducible film of resist is left. The viscosity of the photoresist and the rotational velocity of the substrate determine the thickness of the resist layer (Mack, 2008). An edge bead exists in the outer 1 – 2 mm of the substrate and can be 10 – 30 times thicker than the rest of the resist. Therefore, this edge bead needs to be removed to allow close contact between the photomask and substrate during the first exposure.

Post Apply Bake

The post apply bake is required to dry the substrate as after spin coating the resist will contain about 20 - 40% solvent. By removing the solvent the resist film adhesion improves and makes it harder for particle contamination to occur. The post apply bake is usually between 90 and 120 °C to remove most of the solvent and harden the resist.

Exposure

Contact lithography pushes the photomask against the photoresist-coated substrate and thus offers a high-resolution limit, allowing a minimum feature size on the substrate of about the wavelength of the used radiation (Mack, 2008). The first exposure defines the structure to be patterned and is done with the photomask exposing resist areas to remain after development. Exposing for too long will illuminate dark areas via scattering, diffraction, or reflection. This will result in the structures being larger than expected after development. Exposing for too short a time means the resist closest to the substrate remains rather unexposed resulting in a pronounced undercut.

Reversal Bake

This is the most critical step of the image reversal process. The reversal bake makes the exposed resist areas soluble in developer. The reversal bake temperature needs to be optimised depending on the resist used and the required profile. Typical temperatures are between 110 – 130°C.

Flood Exposure

For image reversal resists a flood exposure step is required between the reversal bake and development. The resist is exposed with no mask. This step is uncritical and makes the areas of resist that were not initially exposed soluble to developer.

Development

The development stage is a critical step in the photolithography process. This stage determines the shape of the photoresist profile (Mack, 2008). The rate of development needed depends on the resist and the reversal bake parameters. If the

reversal bake if too hot or too long can decompose a high amount of the photoactive compound in the resist thus reducing the development rate.

Removal

After the substrates have been patterned and post evaporation the remaining photoresist needs to be removed. Wet or plasma (dry) stripping can remove photoresist. Wet stripping removes resist by dissolution in an organic solvent such as acetone or DMSO. Acetone tends to leaves a residue on the surface so a plasma step is usually followed to completely clean the substrate. Oxygen plasma is highly reactive towards organic polymers, for example the resist but leaves inorganic compounds untouched (Mack, 2008).